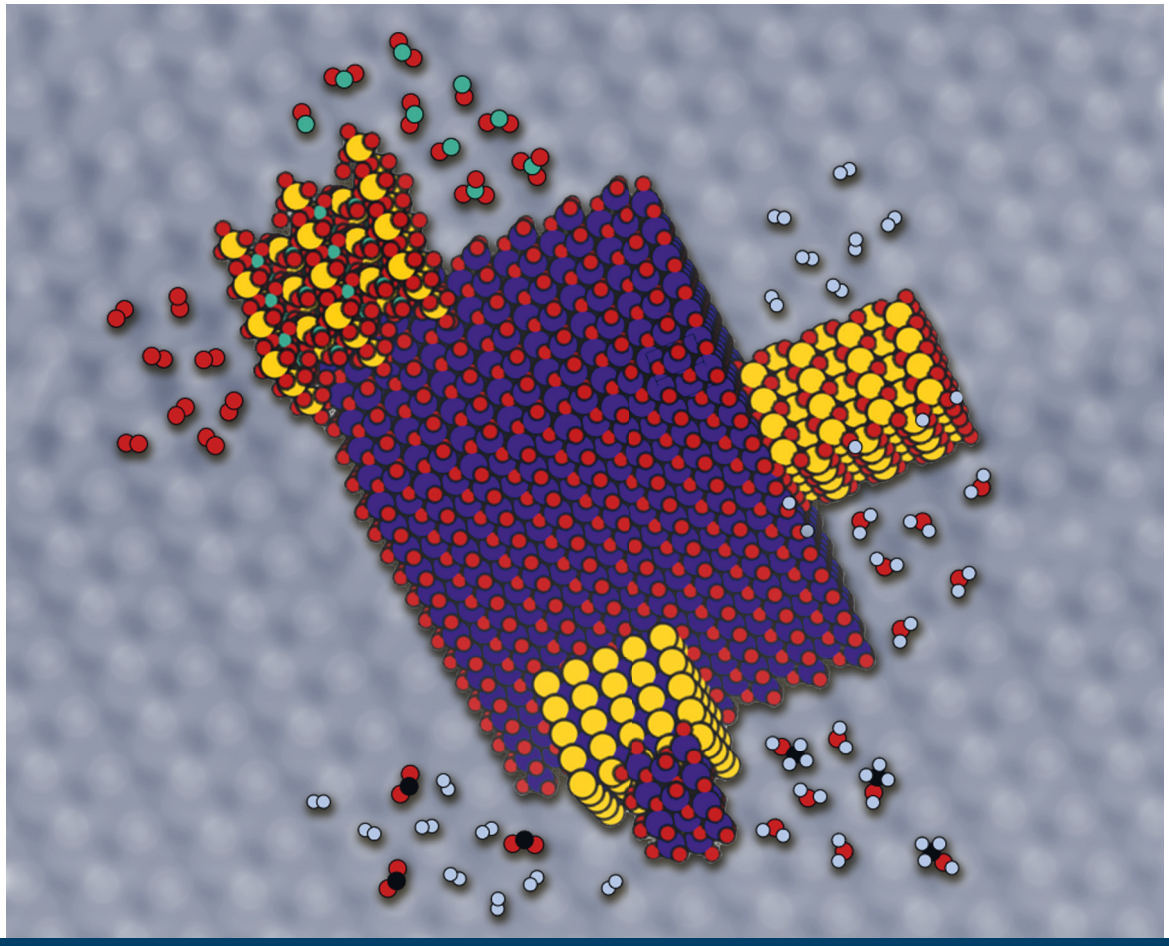

Investigation of Dynamic Material Changes During the Preparation of ZnPd Nanoparticles Supported on ZnO and their Catalytic Application in Methanol Steam Reforming on the Atomic Level

Ansgar Meise

Energie & Umwelt / Energy & Environment
Band / Volume 670
ISBN 978-3-95806-838-4

Mitglied der Helmholtz-Gemeinschaft

JÜLICH
Forschungszentrum

Schriften des Forschungszentrums Jülich
Reihe Energie & Umwelt / Energy & Environment Band / Volume 670

Forschungszentrum Jülich GmbH
Ernst Ruska-Centrum für Mikroskopie und Spektroskopie mit Elektronen (ER-C)
Physik Nanoskaliger Systeme (ER-C-1)

Investigation of Dynamic Material Changes During the Preparation of ZnPd Nanoparticles Supported on ZnO and their Catalytic Application in Methanol Steam Reforming on the Atomic Level

Ansgar Meise

Schriften des Forschungszentrums Jülich
Reihe Energie & Umwelt / Energy & Environment Band / Volume 670

ISSN 1866-1793 ISBN 978-3-95806-838-4

Bibliografische Information der Deutschen Nationalbibliothek.
Die Deutsche Nationalbibliothek verzeichnet diese Publikation in der
Deutschen Nationalbibliografie; detaillierte Bibliografische Daten
sind im Internet über http://dnb.d-nb.de abrufbar.

Herausgeber und Vertrieb:	Forschungszentrum Jülich GmbH Zentralbibliothek, Verlag 52425 Jülich Tel.: +49 2461 61-5368 Fax: +49 2461 61-6103 zb-publikation@fz-juelich.de www.fz-juelich.de/zb
Umschlaggestaltung:	Grafische Medien, Forschungszentrum Jülich GmbH
Druck:	Grafische Medien, Forschungszentrum Jülich GmbH
Copyright:	Forschungszentrum Jülich 2025

Schriften des Forschungszentrums Jülich
Reihe Energie & Umwelt / Energy & Environment, Band / Volume 670

D 82 (Diss. RWTH Aachen University, 2025)

ISSN 1866-1793
ISBN 978-3-95806-838-4

Vollständig frei verfügbar über das Publikationsportal des Forschungszentrums Jülich (JuSER)
unter www.fz-juelich.de/zb/openaccess.

Zusammenfassung

Aufgrund seiner hohen Energiedichte und Nachhaltigkeit gilt Wasserstoff als wichtiger Energieträger in einer nachhaltigen Energiewirtschaft. Bei der Suche nach einem Speichermedium für Wasserstoff hat sich Methanol als vielversprechender chemischer Speicher herauskristallisiert. Die Rückgewinnung erfolgt dabei durch die Reformierung von Methanol- mit Wasserdampf zu Wasserstoff und Kohlendioxid. ZnO-geträgerte, intermetallische ZnPd-Nanopartikel sind aufgrund ihrer hohen CO_2-Selektivität und Aktivität hervorragende Katalysator für die Methanoldampfreformierung. Die guten katalytische Eigenschaften entwickeln sich jedoch erst während der Katalyse. Der Grund für die Verbesserung der katalytischen Eigenschaften scheint eine dynamische Strukturentwicklung des Katalysators zu sein. Die in situ Untersuchung des katalytischen Systems während der Synthese und Katalyse kann die zugrunde liegende strukturellen Veränderungen entschlüsseln.

Die umfassende Arbeit untersucht die Herstellung, die strukturelle Entwicklung und die katalytische Anwendung von ZnPd-Nanopartikeln auf ZnO während der Methanol-Dampfreformierung (MSR) unter Verwendung von in situ-Rastertransmissionselektronenmikroskopie (STEM). Die Herstellungsschritte, einschließlich der Kalzinierung von Palladiumnitrat auf einem Träger und der Reduktion von Palladiumoxid, wurden analysiert. Die Kalzinierung zeigte, dass Palladiumnitrat bei ~170 °C zu Palladiumoxid umgewandelt wird, was zu einem Nanopartikelwachstum mit einem stabilen Größenbereich zwischen 200 und 400 °C führt. Bei Temperaturen über 460 °C zersetzt sich PdO zu elementarem Palladium, was die Partikelbeweglichkeit, Agglomeration und Bildung von ZnO-Nanostäbchen auslöst. Die in situ Reduktion von PdO auf einem Träger führte zur Bildung von intermetallischem ZnPd mittels zwei verschiedener Bildungsmechanismen: durch Wasserstoff-Spillover induzierte ZnO-Migration und Einkapselung von Pd-Nanopartikeln, gefolgt von ZnPd-Keimbildung und Kern-Schale-Strukturbildung. In situ-STEM-Experimente in offenen und geschlossenen Reaktorkonfigurationen veranschaulichten, dass Methanol als starkes Reduktionsmittel für ZnO wirkt, während Wasserstoff und Wasserdampf das System stabilisieren. Unter MSR-Bedingungen unterliegen ZnPd-Nanopartikel Zusammensetzungs- und Morphologieänderungen, einschließlich Zn-Anreicherung und Nanopartikel-Facettierung. Die Bildung von ZnO-Inseln, die in situ erstmals beobachtet wurde, trat bevorzugt auf ZnPd-Facetten und Zn-angereicherten Bereichen auf. Diese Bildung erfordert ein präzises Gleichgewicht zwischen Wasserstoff, Wasser und Methanol und ist daher empfindlich vom chemischen Potenzial abhängig. Die Forschung liefert neue Erkenntnisse über das dynamische Verhalten von ZnPd/ZnO-Katalysatoren unter Betriebsbedingungen, verbessert die Methodik zur Untersuchung von Katalysatoren in Dampfumgebungen und trägt zu einem besseren Verständnis katalytischer Systeme bei.

Abstract

Given its high energy density and sustainability, hydrogen is regarded as a crucial energy carrier in the pursuit of a carbon-free energy economy. In the search for a storage medium of hydrogen, methanol is emerging as a promising chemical storage. The recovery of hydrogen is achieved through the process of methanol steam reforming, whereby methanol and water are transformed into hydrogen and carbon dioxide. The intermetallic ZnPd nanoparticle supported on ZnO has been demonstrated to function as an excellent catalyst for the reforming, due to its high CO_2 selectivity and activity. However, the favourable catalytic performance is first established during catalysis. The reason for the enhancement of the catalytic properties appears to be a dynamic structural evolution of the catalyst, as evidenced by the formation of ZnO patches. The nanostructural dynamics and the underlying cause of the improved catalytic properties can be elucidated by analysing the synthesis and catalysis of the catalytic system in situ.

The comprehensive work studies the preparation, structural evolution, and catalytic application of ZnPd nanoparticles supported on ZnO during methanol steam reforming (MSR), using *in situ* scanning transmission electron microscopy (STEM). The preparation stages, including calcination of supported palladium nitrate and reduction of palladium oxide, were analysed. *In situ* calcination revealed that palladium nitrate transforms into palladium oxide at ~170 °C, leading to nanoparticle growth, with a stable size window between 200-400 °C. At temperatures above 460 °C, PdO decomposes into elemental palladium, triggering particle mobility, agglomeration, and ZnO nanorod formation. Further heating above 660 °C under high vacuum caused ZnO faceting and decomposition, which was facilitated by the evaporation of elemental zinc and oxygen. *In situ* reduction of supported PdO resulted in the formation of intermetallic ZnPd via two distinct formation mechanisms: hydrogen spillover-induced ZnO migration and encapsulation of Pd nanoparticles, followed by ZnPd nucleation and core-shell structure formation. The findings align with those of *ex situ* experiments and existing literature, confirming that the electron beam enhances the reaction but does not activate it. *In situ* STEM experiments in open and closed cell configurations demonstrated that methanol acts as a strong reducing agent for ZnO, while hydrogen and water steam stabilise the system. Under MSR conditions, ZnPd nanoparticles are subject to compositional and morphological changes, including Zn enrichment and nanoparticle faceting. The formation of ZnO patches, which was observed for the first time *in situ*, was found to preferentially occur on ZnPd facets and Zn-enriched areas. This formation requires a precise balance between hydrogen, water, and methanol and thus is sensitively dependent on the chemical potential. The research provides novel insights into the dynamic behaviour of ZnPd/ZnO catalysts under operational conditions, advancing the methodology for studying catalysts in steam environments and contributing to the broader understanding of catalytic systems.

Table of Contents

Zusammenfassung ..... **i**

Abstract ..... **iii**

List of Figures ..... **viii**

Abbreviations ..... **xviii**

1 Motivation **1**

1.1 Research Goals 5

2 Fundamentals **7**

2.1 Zinc Palladium Supported on Zinc Oxide and Methanol Steam Reforming 7

2.2 Evaporation of Liquids 9

2.3 Metal-Support Interactions 11

2.4 Reduction of Metal Oxides – Ellingham Diagram 18

2.5 Transmission Electron Microscopy 20

2.5.1 Transmission Electron Microscopy Mode 20

2.5.2 Scanning Transmission Electron Microscopy Mode 22

2.5.3 Imaging Theory 23

2.5.4 In Situ Gas Transmission Electron Microscopy 26

3 Materials and Methods **29**

3.1 Preparation of Palladium Nitrate Supported on Zinc Oxide 29

3.1.1 Synthesis Protocol 29

3.1.2 Differential Thermal Analysis and Thermogravimetry 29

3.1.3 Inductively-Coupled Plasma/Optical Emission Spectroscopy 30

3.1.4 X-Ray Diffractometry 30

3.2 Transmission Electron Microscopy 31

3.2.1 Environmental Scanning Transmission Electron Microscopy – Open Cell Configuration 31

3.2.2 Micro-Electromechanical System Reactor – Closed Cell Configuration 34

3.2.3 Energy-Dispersive X-ray Spectroscopy 36

3.3 Electron Beam Dosimetry 37

4 Calcination of Palladium Nitrate Supported on Zinc Oxide Using In Situ Scanning Transmission Electron Microscopy **39**

4.1 Experimentals 40

4.2 Results of In Situ Calcination of Supported Palladium Nitrate 42

4.3 Discussions 54

5 Reduction of Zinc Oxide Using Environmental Scanning Transmission Electron Microscopy 59

5.1 Experimentals 60

5.2 Results of Zinc Oxide Reduction Experiment 60

5.3 Discussions 62

6 Reduction of Palladium Oxide Supported on Zinc Oxide Applying Environmental Scanning Transmission Electron Microscopy 65

6.1 Experimentals 66

6.2 Characterisation of Pristine Palladium Oxide Nanoparticles 66

6.3 Reduction of Palladium Oxide at Room Temperature 68

6.3.1 Evaluation of Electron Beam Effects During Reduction 77

6.4 Reduction of Palladium Oxide at 200 °C 78

6.4.1 Evaluation of Beam Effects During Reduction at 200 °C 82

6.5 Discussions 83

7 Methanol Steam Reforming on Zinc Palladium Nanoparticles Supported on Zinc Oxide 93

7.1 Experimentals 93

7.2 Characterisation of Pristine Zinc Palladium Nanoparticles 95

7.3 Reduction in a Pure Hydrogen Atmosphere 97

7.4 Effects of Individual Components 98

7.4.1 Exposure to Water Steam 98

7.4.2 Exposure to Methanol Steam 100

7.4.3 Discussions of Individual Components 103

7.5 Structural Evolution During Methanol Steam Reforming 107

7.5.1 Changes in Morphology of Zinc Palladium Nanoparticles 107

7.5.2 Electron Beam-Assisted Decomposition of Zinc Oxide 109

7.5.3 Discussions of Structural Evolution During Methanol Steam Reforming 112

7.6 Structural Evolution of Supported Zinc Palladium Nanoparticles in a Hydrogen Environment Enriched with Methanol and Water 116

7.6.1 Experimentals – Hydrogen Enrichment with Water and Methanol 116

7.6.2 Discussions of Experimental Feasibility 116

7.6.3 Results of In Situ Experiment in a Hydrogen Environment Saturated with Methanol and Water 117

7.6.4 Discussions of the Effect of Enriched Hydrogen 125

7.7 In Situ Transmission Electron Microscopy Study of Methanol Steam Reforming Employing a Closed Cell Configuration 130

7.7.1 Results of the Pre-reduction of Supported Zinc Palladium Nanoparticles 130

7.7.2 In Situ Results of the Methanol Steam Reforming Experiment 131

7.7.3 Discussions of Methanol Steam Reforming in situ Experiments by Applying a Closed Cell Configuration 134

7.8 Experimental Challenges in the Quantitative Determination of Gas Compositions 135

7.9 Conclusions 137

8 Summary and Implications 139

9 Outlook 141

10 References 143

11 Supporting Information 160

Acknowledgements 173

List of Publications 174

Eidesstaatliche Erklärung 175

List of Figures

Figure 1.1: Storage types of Hydrogen can be classified in physical storage, adsorption and chemical storage. Examples of the specific storage types are illustrated with their respective densities and gravimetric storage capacities. Values are taken from reference. [14] 2

Figure 1.2: a) Pd-Zn phase diagram indicating the existence of the ZnPd intermetallic compound. b) CO_2 selectivity plotted as a function of composition of unsupported ZnPd under MSR conditions. The graphs presented have been taken with the permission of the references[42,43]. 3

Figure 1.3: a) Temporal development of the catalytic performance of freshly reduced ZnPd/ZnO under isothermal MSR conditions at 523 K. b) HRTEM image of a single ZnPd nanoparticle after MSR, with indications of the corresponding lattice spacings for ZnO patches. Figures are taken with permission from reference[37]. 4

Figure 1.4: a) DF-STEM image of a ZnPd particle and b) a related EELS line scan for Pd, Zn and O as well as HAADF intensity profile, dark regions in the figure correspond to Pd-depleted and Zn- and O-rich phases (Z-contrast); c) DF-STEM image of two ZnPd particles and d) related EDX maps showing the elemental distribution of Pd (red), Zn (blue) and O (green). Graphics are taken and modified with permission from reference.[45] 5

Figure 2.1: Sketch illustrating the tetragonal crystal structure of ZnPd. Pd is highlighted in yellow, Zn in blue. The unit cell is marked. Structure is adapted from reference.[46] 7

Figure 2.2: Vapour pressures of methanol (red circles) and water (black squares) plotted as a function of temperature. Values are taken from reference[59,60]. 9

Figure 2.3: Composition of different water and methanol mixtures in liquid and vapour at 40 °C (blue) and 50 °C (red). Data is taken from reference[63]. 10

Figure 2.4: Standard Gibbs energy change of formation for various compounds as a function of temperature displayed in an Ellingham diagram. Figure is adapted from reference. [152–154,156] 19

Figure 2.5: Schematic representation of the electron beam trajectory comparing TEM (left) and STEM mode (right). Individual lenses, apertures and detectors are omitted for simplicity. Diffraction and imaging modes have the same lens settings up to the intermediate lens and are shown separately below. The processing unit digitally recombines the individual signals from the scan into a coherent image. 21

Figure 2.6: Schematic illustration of a transfer function with an envelope damping function (red). The spatial frequency g_1 represents the point information limit of the microscope under the given aberrations. 25

Figure 3.1: Schematic sketch illustrating Bragg's law and the diffraction conditions necessary for constructive interference. The lattice is highlighted in red. X-rays with a wavelength of λ are black. The phase difference that permits constructive interference is indicated in green. 31

Figure 3.2: Schematic illustration of the environmental setup of the HF5000, consisting of a self-constructed vaporizer, a gas supply system and the open cell STEM system. Green colouring indicates an open valve. 32

Figure 3.3: Calibration of the sample pressure assigned to the corresponding column pressure, which is measured at the side column, shown in Figure 3.2. 33
Figure 3.4: Schematic representation of the heater holder and the corresponding MEMS chip. The sample is prepared on the SiN membrane in the centre of the heating spiral. Holder sketch is taken and modified from reference.[194] 34
Figure 3.5: An overview image of the Climate™ *in situ* holder and an exploded view of its tip are shown. A working scheme of the tip illustrates the configuration of the components. Images are taken and modified from reference.[195] 35
Figure 3.6: Schematic illustration of the *in situ* closed cell configuration consisting of a gas supply system, a vaporiser, a MEMS holder inside a TEM and a mass spectrometer. 35
Figure 3.7: Schematic illustration of the inelastic interaction between an electron beam and an electron shell during EDX. The incident electron beam interacts with a shell electron (I), which is excited and subsequently knocked out of its ground state (II), generating an electron hole. An electron from an upper energy level replenishes the hole and emits a photon with an energy ΔE (III), which represents the energy difference between the levels. Such photons are detected during EDX and allocated to an element. Kα, Kβ and Lα transitions are displayed as illustration. 36
Figure 4.1: Heating profile of the *in situ* calcination E-STEM experiment, heating regions of interest and image times are enlarged. 41
Figure 4.2: E-STEM image series of the *in situ* calcination of $Pd(NO_3)_2$/ZnO in oxygen. Upper row: BF image series; middle row: corresponding DF image series; lower row: FFT series of corresponding particle cluster. New reflections appear at temperatures > 170 °C. Figure is taken with permission from reference[200]. 43
Figure 4.3: The DF and SE images of the support-particle structure between $Pd(NO_3)_2$ and ZnO at room temperature are in correspondence, indicating that the majority of the particles is located on the surface. Figure is taken with permission from reference[200]. 43
Figure 4.4: Particle size evolution versus temperature, particle diameter was measured along two perpendicular lines (left); b) Interatomic distances along two directions (right). Figure is taken with permission from reference[200]. 44
Figure 4.5: DTA signal (green), the mass loss (blue) and temperature (black) are plotted as a function of time. The endothermic offset is indicated at 175°C. Figure is taken with permission from reference[200]. 44
Figure 4.6: BF and DF images of pristine sample (top row) and the identical location after calcination at 220 °C in the E-STEM (bottom row). The locations were not exposed to the electron beam during the *in situ* calcination experiment and were imaged solely prior to and following the reaction in vacuum at 60 °C. Figure is taken with permission from reference[200]. 45
Figure 4.7: A series of BF E-STEM images were recorded over a temperature range of 200 to 400 °C. The morphology of the PdO/ZnO particles was found to be largely unaffected by the temperature rise. However, a small increase in size of individual nanoparticles was observed at higher temperatures. Figure is taken with permission from reference[200]. 46

Figure 4.8: A series of SE images was captured at different heating steps between 300 °C and 400 °C. No particle movement or agglomeration was observed. Figure is taken with permission from reference[200]. 47
Figure 4.9: The SE E-STEM image series illustrates the structural changes that occur as a result of the temperature rise during the heating treatment between 300 and 500 °C. The areas of interest are indicated by green circles. Figure is taken with permission from reference[200]. 48
Figure 4.10: The SE E-STEM image series depicts the process of particle merging at 460 °C in an oxygen environment. The time stamps indicate the period after 460 °C was reached. The red dotted lines mark a group of selected particles, illustrating the dynamics of their movement and agglomeration of these particles over time. The insets provide a magnified view of selected regions of interest. Figure is taken with permission from reference[200]. 49
Figure 4.11: The SE images on the left illustrate the impact of varying PdO/ZnO loadings (1%, 3%, 5%) on calcined samples at 500 °C for 180 minutes under ambient conditions. The plot on the right illustrates the corresponding particle size distribution. Figure is taken with permission from reference[200] 49
Figure 4.12: Series of high-resolution BF images of a single particle undergoing structural evolution as a result of heating from 400 to 500 °C. The formation of a nanorod occurs beneath the nanoparticle. Figure is taken with permission from reference[200]. 50
Figure 4.13: Phase identification via determination of lattice spacings. Corresponding FFT images are shown in Figure 11.9. PdO (110) is highlighted in green, ZnO (002) and (102) in red, Pd (111) in blue. The lattice parameters are taken from reference[222,223]. Figure is taken with permission from reference[200]. 50
Figure 4.14: BF, SE and DF images of a pristine sample (top row) and the identical location after calcination at 500 °C in the E-STEM (bottom row). The illustrated reference locations were not exposed to the electron beam during the in situ calcination experiment and were imaged only before and after the reaction in vacuum at room temperature. The green arrows indicate locations where ZnO nanorods formed. Figure is taken with permission from reference[200]. 51
Figure 4.15: SE and corresponding DF image series of PdO/ZnO decomposition between 600 and 690 °C. The red arrow indicates faceting of the ZnO support, while the green arrows point out the agglomeration of PdO particles. The dotted blue line illustrates the shrinking of the ZnO support. Figure is taken with permission from reference[200]. 52
Figure 4.16: The DF image series illustrates the high-temperature properties of PdO/ZnO between 700 and 790°C. The dotted blue line highlights the shrinking of the ZnO support, while the red circles indicate the faceting of the PdO particle. Figure is taken with permission from reference[200]. 53
Figure 4.17: Schematic summary which shows the effects of different calcination temperatures at 1.5 Pa oxygen pressure. An increase in calcination temperature leads to a particle growth. Particles and their chemical composition are highlighted. Figure is taken with permission from reference[200]. 58
Figure 5.1: BF, DF and SE image showing a SiN membrane, which is sputtered with single crystalline Zn particles. 60

Figure 5.2: BF and DF image series of hexagonal Zn crystals coated with a ZnO passivation layer. Time stamps indicate the time of hydrogen exposure. BF images show particles with Moiré fringes, indicating a complete coverage by zinc oxide. Oxide layers were not decomposed during the reduction treatment. Insets show interfaces between Zn and ZnO at a higher magnification. 61
Figure 5.3: BF and SE images of Zn nanoplates, which are irritated by the electron beam. Red arrows indicate identical sample locations at different magnifications imaged in immediate succession. 62
Figure 6.1: Left: Series of SE images of PdO nanoparticles supported on ZnO prepared with different Pd loadings after calcination. Right: Corresponding XRD measurements (top) and particle size distributions (bottom) of the sample with different Pd loadings. XRD reflections of ZnO, PdO and Pd are given as reference. The XRD data of the 5 wt% sample shows a small hump around 34°, corresponding to PdO. The strong peaks correspond well to the reference ZnO peaks, identifying the support. 67
Figure 6.2: A DF STEM image of a pristine PdO nanoparticle on ZnO is shown. The PdO nanoparticle is aligned along [110] as shown in the model[241]. The ZnO crystal is aligned along [110] as exemplified in the model[242]. Pd, Zn and O are represented yellow, blue and red, respectively. 68
Figure 6.3: DF and BF image series of the evolving nanoparticle-support structure during the first 11 min of reduction in hydrogen atmosphere. Structural changes are highlighted by arrows. Red arrows indicate change in morphology of the existing ZnO support. Yellow arrows indicate formation of new ZnO features. Green circles highlight atomic positions and the change in crystal structure from distorted ZnO to the mixed phase at the interface. The blue arrows and outline illustrate the interaction between nanoparticle and support. Orange arrows indicate the formation of an amorphous, hydrocarbon coverage, which is most likely triggered by the electron beam. White rectangle indicates ROI, which is shown in Figure 6.4. 69
Figure 6.4: Clipped DF image of supported PdO after 11 min of hydrogen exposure. Original image is displayed in Figure 6.3. Interatomic spacings are measured along the row of atoms in the arrow's direction. Atom rows are numbered from left to right as displayed. 71
Figure 6.5: Series of DF and BF images during reduction. The time stamp indicates the time the specimen was exposed to a hydrogen atmosphere at room temperature. Images were acquired under identical conditions as those displayed in Figure 6.3. Orange arrows indicate the ZnO enrichment development on the surface of the support. Red arrows highlight surface migration of ZnO on the nanoparticle. Its progress can be tracked by following the features circled in red. 72
Figure 6.6: Series of DF images during reduction. The time stamp shows the time of reduction in a hydrogen atmosphere at room temperature. Lower row shows the magnified nanoparticles. Red arrows indicate the increase in ZnO coverage. Blue arrows highlight detachment of the nanoparticle from the support. Region marked in green show the nucleation and growth of a new phase. 73
Figure 6.7: The growth of phase is quantified by measurements of area (blue squares), circumference (red triangle) and Feret's diameter (orange triangle). The area

is given in nm² on the left axis. The length is given in nm on the right axis. An example of the phase measurement is represented in Figure 11.13. 74

Figure 6.8: Series of DF images during reduction. The time stamp indicates the time of reduction in a hydrogen atmosphere at room temperature. First minutes of reduction at the identical location are displayed in Figure 6.5. Red arrows highlight nucleation and particle growth. Green arrows indicate unchanged particle region. Lattice spacings measured are in good agreement with ZnPd crystal structured displayed from reference.[46] 75

Figure 6.9: Series of DF images during reduction. The time stamp indicates time of reduction in a hydrogen atmosphere at room temperature. First minutes of reduction at the identical location are displayed in Figure 6.3 and Figure 6.6. Red arrows indicate growth of new phase indicating a core-shell structure. Green arrows highlight unchanged region with darker contrast that is encapsulated by formed phase. Blue arrows mark separation of the nanoparticle from the support. 76

Figure 6.10: Supported nanoparticle before and after reduction in a hydrogen atmosphere at room temperature. The location was not exposed to the electron beam in presence of a hydrogen atmosphere. While the pristine nanoparticle matches with the lattice of PdO along [2 0 -1], the nanoparticle after reaction corresponds well to ZnPd along [0 1 0]. Zn is coloured in blue, Pd in yellow, O in red. The structure models are taken from reference.[46,243] 78

Figure 6.11: Series of BF images shown during the reduction of supported PdO at 200 °C. Time stamp indicates time of hydrogen injection. Region marked in red highlights the nanoparticle, region marked in green the encapsulation by ZnO. Neck formation and ZnO dissolution is marked in blue. The orange arrows indicate phase transformation. 79

Figure 6.12: Top: BF image of a nanoparticle shown after 16 min of reduction. The structural evolution during reduction is illustrated in Figure 6.11. The crystal structure of the nanoparticle may correspond to Pd along [1 1 0] or ZnPd along [1 1 1], since the interatomic spacing and angles match well to the models taken from references.[46,223] Bottom: The measured interatomic spacings along a (black square), b (red circle) and c (blue triangle) direction displayed over the past reduction time. The spacings show no considerable change. 80

Figure 6.13: Series of BF images during the reduction of supported PdO at 200 °C. Time stamp indicates time of hydrogen injection. Red ROI marks location shown in Figure 6.11. The support is activated and encapsulates the nanoparticles. Red arrows show morphological evolution of ZnO. 81

Figure 6.14: Comparison between sample locations before (top) and after (bottom) reduction at 200 °C. Left: Pd nanoparticle exhibit the same crystal structure along [1 1 0] before and after the reaction. Middle and Right: Identical sample location imaged in DF and BF. The red arrows show the formation of regions with darker DF contrast, indicating a mass loss. The green arrows indicate the nanoparticle decoration by the oxide. 82

Figure 6.15: Energy diagrams of different heterojunctions illustrating different ZnO interfaces. PdO and Pd lead to an upbend of the ZnO energy band at the interface. Figure is taken from reference with permission.[84] 84

Figure 6.16: Schematic illustration of the surface activation mechanism during reduction. Zn is green, H blue and O red. Hydrogen is activated on PdO and spilt over to

the support. In ZnO, hydrogen diffuses to lattice oxygen (I) and bonds, forming water (II). Water desorbs from the surface and generates an oxygen vacancy V_O (III). Unsaturated Zn species donate delocalized electrons to the system, which transfer to the nanoparticle (IV). Positive Zn species form a positive net space charge in ZnO (V). Positive net space charge is reduced due to Zn migration to the surface (VI). Subsequently, migration of negative oxygen species is activated and oxygen-deficient ZnO_{1-x} cluster form on the surface. The nanoparticle is encapsulated by Zn_xO to minimize the surface energy of the system. 85

Figure 7.1: Left: SE image series of ZnPd nanoparticles supported on ZnO with different Pd loadings. Right top: Corresponding XRD measurements of the identical sample batch. XRD reflexes of pure ZnO, ZnPd and Pd are given as reference. Right bottom: A particle size analysis which shows the size distribution of ZnPd nanoparticles according to the total Pd loading. 95

Figure 7.2: Series of BF, DF and SE images of ZnPd nanoparticles supported on ZnO with different Pd loadings (1 – 10 wt.%). Images in one column represent the same nanoparticle. Some ZnPd nanoparticles are coated with a thin surface layer. 96

Figure 7.3: *In situ* BF images series of supported ZnPd nanoparticles, which are reduced at 200 °C in hydrogen atmosphere. The E-STEM was operating at 60 kV. Time stamps indicate time of reduction. The system shows no significant change in structure. ZnO decomposes slightly in the perimeter of the nanoparticle. 97

Figure 7.4: BF and DF images of two ZnPd nanoparticles imaged before (top row) and after (bottom row) reduction. Locations were not exposed to the electron beam during hydrogen injection. Red arrows indicate faceting. ROI highlights ZnPd crystal along [1 0 0] direction. Crystal model is adapted from reference.[46] 98

Figure 7.5: Series of BF images of ZnPd nanoparticle exposed to water steam at 320 °C. Time stamps indicate the time of water steam injection. The graph shows the corresponding column pressure. The red arrows indicate the detachment of a surface feature. 99

Figure 7.6: Series of images of different reference locations acquired before (top) and after (bottom) water steam exposure. Locations were not exposed to the electron beam during water steam injection. 99

Figure 7.7: Series of BF images of a ZnPd nanoparticle exposed to methanol steam at 320 °C. Time stamp indicate time of methanol injection. DF and SE images of the same *in situ* experiment are displayed in Figure 11.17. 101

Figure 7.8: Properties of ZnPd nanoparticle studied *in situ*, as shown in Figure 7.7: a) Logarithmic illustration of the change in column pressure as function of time with a constant injection rate. b) Change in area (blue), Feret diameter (red) and perimeter (black) of the nanoparticle considered over time. c) Corresponding roundness (black) and circularity (red) of the nanoparticle calculated using eq. 7.1 and 7.2. Circularity and roundness have the same axis scale. 101

Figure 7.9: Series of DF images acquired at lower magnifications during methanol steam injection. The red arrows indicate temporary faceting of nanoparticles. White ROI highlights the region, which was observed at higher magnification in Figure 7.7. 102

Figure 7.10: Series of BF images of randomly selected locations before (top) and after (bottom) methanol injection. Images in one pillar were acquired at the same magnification. 103

Figure 7.11: Schematic illustration of ZnO decomposition process. The system is exposed to methanol steam. Methanol is adsorbed on the ZnPd and activated (I). Methanol is decomposed, splits off hydrogen and spills over to the ZnO support (II). The residual CO binds to lattice oxygen, forms CO_2, which desorbs and generates an oxygen vacancy (III). ZnO is partially reduced and decomposes. A nanocolumn, as illustrated in bright green, underneath the nanoparticle is stabilized temporarily. 105

Figure 7.12: Series of DF (top) and BF (bottom) images of a nanoparticle compositionally evolving during MSR at 320 °C. Time stamp gives time of MSR. Blue arrows show initial locations of contrast deviations. The red arrows indicate formation of dark contrast regions. The green arrows highlight the presence of twin boundaries throughout the observation. 107

Figure 7.13: High resolution DF images of a ZnPd nanoparticle studied during MSR. Red arrows highlight regions of heterogenous composition in the nanoparticle, indicating deviations in Pd content. Left inset illustrates the SE image of the same region, indicating surficial features. Right inset shows twin boundary of the nanoparticle at a higher magnification. The tilt angle between the lattice planes is ~ 8°. Both ZnPd crystals are aligned along [0 1 0], as illustrated by the crystal model. 108

Figure 7.14: DF images of ZnPd nanoparticles acquired after exposure to MSR conditions. Images of pristine nanoparticles are shown in Figure 11.18. Inlays illustrate crystal structure and orientation of ZnPd nanoparticles. The nanoparticle in the left DF image is aligned along [1 1 1], the nanoparticle in the right DF image along [1 0 0]. 109

Figure 7.15: Surface damage activated by the electron beam shown by a series of SE images. ZnO continuously degrades due to combination of the present MSR conditions and electron beam exposure. The time of electron beam exposure is indicated by the time stamps. 110

Figure 7.16: SE image of electron beam-activated ZnO degradation. White square indicates scan region. Only the imaged ZnO region is subject to decomposition. 110

Figure 7.17: Series of SE and DF images of *in situ* ZnO decomposition activated by the exposure to electron beam and MSR conditions. The red arrows indicate hole formation. The green arrows show faceted growth of holes. 111

Figure 7.18: Left: Quantification of ZnO decomposition, represented by the perimeter (blue circle) and the area (red triangle) of a hole as a function of time. Right: Example of a manually marked hole after 30 seconds of electron beam and MSR irradiation. 112

Figure 7.19: Series of DF images of a supported ZnPd nanoparticle exposed to methanol steam, water steam and hydrogen. Column pressure (black), partial pressure of water and methanol (red) and hydrogen partial pressure (green) are displayed as a function of injection time. Red arrows indicate increasing encapsulation of the nanoparticle. After 48 min of injection, measurements of the interatomic distances are shown along the marked directions. Corresponding BF images are shown in Figure 11.20. The structure of the encapsulation layer is identified as ZnO, as illustrated in Figure 7.20. 118

Figure 7.20: High resolution DF and BF image of a ZnPd nanoparticle exposed to methanol steam, water steam and hydrogen for 48 min, as shown in Figure 7.19. ZnO model identifies orientation and structure of the surface layer. Layer crystal is aligned along ZnO [1 0 0]. Model is created from reference[286]. 119
Figure 7.21: Series of DF images of a supported ZnPd nanoparticle exposed to methanol steam, water steam and hydrogen. The red arrows indicate ZnO patch formation on the ZnPd surface. 119
Figure 7.22: DF and BF images of the identical sample location acquired before (left), after treatment with hydrogen saturated by methanol and water (middle) and after treatment with methanol and water (right). Two rows of DF images show different brightness levels. The arrows indicate formation of superficial patches. The blue arrow shows a surface patch. The red arrow highlights surface layer. The white square represents an area, which was investigated at higher magnification, as shown in Figure 7.24. 120
Figure 7.23: DF and BF images of an identical sample location before (left) and after treatment in hydrogen enriched with methanol and water. The ZnPd crystal is aligned along [1 1 0]. Atom rows with bright DF signal correspond to Pd, darker atom rows to Zn, as illustrated in yellow and blue by the model. ZnO_2 patch aligned along [1 0 0] forms during MSR. Reference location was not exposed to the electron beam. 121
Figure 7.24: BF, DF and SE images of a surface patch formed during *in situ* treatment with hydrogen enriched with methanol and water. The ZnPd nanoparticle is aligned along [1 1 0]. The crystal structure of the patch corresponds best with ZnO_2 aligned along [1 0 0]. The red arrow indicates a crystalline surface and the absence of amorphous covering layers. 122
Figure 7.25: DF images of randomly selected ZnPd nanoparticles acquired after treatment with hydrogen enriched with methanol and water. No patches were formed on the surface of the nanoparticles. Nanoparticles were only exposed to the electron beam in vacuum. Zn is displayed in blue, Pd in yellow. 122
Figure 7.26: DF and BF image, FFT and corresponding inverse FFTs showing different phases of the system. Different colours assign FFT spots to inverse FFTs. 3 different phases are present: The bulk of the nanoparticle, intermediate phase at the edge of the nanoparticle and patch. The white box represents the ROI of the DF image. The graph indicates the DF intensity, where peaks identify the location of an atom column. The red arrow indicates the position of the respective peak in the DF image. The orange arrow indicates the distance shown in the graph. 123
Figure 7.27: SE and DF images of ZnPd nanoparticles taken before (left), after treatment with hydrogen saturated with methanol and water at 200 °C (middle) and after treatment with sole water and methanol steam at 320 °C (right). The reference location was only exposed to the electron beam in vacuum. Red arrows indicate formation and decomposition of a patch. 124
Figure 7.28: EDX measurement of a ZnPd nanoparticle taken after treatment with methanol and water steam at 320 °C. Line scan (left graph) was acquired along the dotted line illustrated in the DF image. Elemental maps (right) were recorded for oxygen (green), palladium (blue) and zinc (red). 125
Figure 7.29: Schematic sketch of dynamical, structural changes in composition and morphology of the ZnPd/ZnO system during varying, reactive conditions.

Formation of facets and Zn-rich surface are activated by MSR. Under the right redox conditions and in the presence of hydrogen, ZnO_2 surface features are formed on ZnPd. 127
Figure 7.30: Series of HR-TEM images showing the ZnPd/ZnO system during reduction in a hydrogen atmosphere at 200 °C. Time stamps indicate time of reduction. 130
Figure 7.31: HR-TEM of ZnPd nanoparticles before (top row) and after reduction (bottom row) in a hydrogen atmosphere at 200 °C. The system is largely unaffected by the hydrogen treatment. 131
Figure 7.32: Series of HR-TEM images illustrating the formation process of a crystalline feature on a ZnPd nanoparticle. 132
Figure 7.33: Series of HR-TEM images illustrating the dynamic contrast changes of ZnPd nanoparticles. The TEM signal of particles of interest, which are indicated by the red arrows, varied as a function of catalysis time. 132
Figure 7.34: Series of HR-TEM images demonstrating an electron beam effect on the system during methanol steam reforming. The ZnO support degrades due to electron beam exposure. Time stamp indicates time of electron beam exposure. 133
Figure 7.35: HR-TEM images showing reference locations before (top row) and after MSR (bottom row). The green arrows indicate change in contrast of the nanoparticles. The red arrows highlight the change in morphology. Some nanoparticles appear to form facets. 134
Figure 11.1: Laboratory closed cell setup enabling *in situ* gas experiments. A schematic illustration of the setup is given in Figure 3.6. 160
Figure 11.2: Optical microscopical image of MEMS heating chips. Left: SiN membranes centred in heating spiral (5x magnification). Right: SiN-windows loaded with $Pd(NO_3)_2$ supported on ZnO, which is visible as dark particles (50x magnification). Figure is taken with permission from reference[200]. 160
Figure 11.3: XRD results of different Pd-loading on ZnO (1%, 3% and 5%); calculated ZnO reflections are given for reference[300]. Missing PdO reflections are due to small crystallite size and/or bad crystallinity. Diffraction patterns of anhydrous and water containing palladium nitrate are added for reference.[220,221] Figure is taken with permission from reference[200]. 161
Figure 11.4: E-STEM series of BF images and the corresponding FFTs of an *in situ* calcination experiment demonstrate the structural transformation of $Pd(NO_3)_2$/ZnO to PdO/ZnO in oxygen. Figure is taken with permission from reference[200]. 162
Figure 11.5: Measurements of interatomic spacings in two directions labelled h and g on the same nanoparticle at 120°C and 190°C. Figure is taken with permission from reference[200]. 163
Figure 11.6: Histograms of *ex situ* calcinated PdO on ZnO with different loadings (left to right: 1%, 3%, 5%) performed under identical, ambient lab conditions (500°C, 180 min dwell time, ambient air pressure). Figure is taken with permission from reference[200]. 163
Figure 11.7: High resolution BF image series of single particle evolution during a calcination treatment between 400 and 500 °C. Formation of nanorods are visible. Figure is taken with permission from reference[200]. 164

Figure 11.8: BF images series of particle evolution during a calcination treatment between 400 and 500 °C. Figure is taken with permission from reference[200]. 164
Figure 11.9: Series of FFTs based on images, which are shown in Figure 4.13. Figure is taken with permission from reference[200]. 164
Figure 11.10: SE E-STEM overview image illustrating the distribution of nanorods anchored to nanoparticles. Red ROI marks the region that is displayed in Figure 4.12 and Figure 4.13. Blue ROI highlights the region that is represented in Figure 11.7. Green arrows mark ZnO nanorods, which have not been imaged *in situ*. Figure is taken with permission from reference[200]. 165
Figure 11.11: Illustration of heating ramp between 500 and 800 °C during imaging of high temperature behaviour of PdO/ZnO system. 165
Figure 11.12: Series of SE images that show formation of contamination over time during reduction in a hydrogen atmosphere at room temperature. Specimen structures cannot be resolved after 22 min. 166
Figure 11.13: Series of DF images illustrating the phase growth during reduction. The time stamps identify time of reduction. The corresponding measurements are displayed in Figure 6.7. 166
Figure 11.14: The change in thickness of the coverage layer is shown as a function of reduction time. The coverage layer converges to a thickness of ~1.5 nm, after it is formed. The corresponding covered nanoparticle is displayed in Figure 6.11. At each reduction time, the layer thickness was measured at 9 different locations and averaged. 167
Figure 11.15: Series of DF images during reduction of PdO at room temperature after a pre-treatment at 200 °C. Time stamp indicates reduction time. ZnO is activated within the first 5 min. After interaction between nanoparticle and support, structural changes in the nanoparticle are observed. 168
Figure 11.16: BF images series of ZnPd nanoparticles imaged after prereduction at 200 °C. 169
Figure 11.17: Series of SE (top) and DF (bottom) images of a supported ZnPd nanoparticle exposed to methanol steam. The corresponding *in situ* experiment is discussed in chapter 7.4.2. 170
Figure 11.18: DF and BF images of pristine ZnPd nanoparticles acquired before exposure to MSR conditions and discussed in chapter 7.5. DF images represent reference locations. Post MSR states are shown in Figure 7.14. 171
Figure 11.19: High resolution DF images of ZnPd nanoparticles acquired after MSR exposure. Crystal structure is identified and shown in Figure 7.14. Different species can be distinguished in the right image. Atom columns with high DF signal correspond to Pd and with low to Zn. 171
Figure 11.20: Series of BF images of ZnPd nanoparticle exposed to methanol steam, water steam and hydrogen at 200 °C. Column pressure (black), partial pressure of methanol and water (red) and hydrogen partial pressure (green) are illustrated as a function of injection time. 172

Abbreviations

BF	Bright field
DF	Dark field
E-TEM	Environmental transmission electron microscopy
E-STEM	Environmental scanning transmission electron microscopy
EDX	Energy-dispersive X-ray spectroscopy
EELS	Electron energy loss spectroscopy
HRTEM	High resolution transmission electron microscopy
ICP/OES	Inductively-coupled plasma/optical emission spectroscopy
DTA/TG	Differential thermal analysis/thermogravimetry
MEMS	Micro-electromechanical system
MS	Mass spectroscopy
MSR	Methanol steam reforming
RMSI	Reactive metal-support interaction
ROI	Region of interest
SE	Secondary electron
SNR	Signal-to-noise ratio
SMSI	Strong metal-support interaction
STEM	Scanning transmission electron microscopy
TEM	Transmission electron microscopy
XRD	X-ray diffractometry

‘Just look at the thing.’

- **Richard Feynman**

1 Motivation

One of the biggest challenges, which society faces nowadays, is the climate crisis. The imperative to abandon the dependency on fossil fuels in order to stop the global warming is vivid in many research areas such as biology[1], bio economy[2] or medicine[3] but lately even left its footprints in a rather unscientific area: the judicature. The German Federal Constitutional Court stated at its decision on the 29th of April 2021 that "future obligations to reduce emissions have an impact on practically every type of freedom"[4]. The policies proposed by the government were too minor to reduce emissions sufficiently by 2030 and beyond, leaving future generations with "drastic restrictions" to meet the Paris target by then. This decision highlights the urgency and extent to act.

Still, many sections in our daily life like electricity, industry or transportation rely heavily on fossil resources and emit greenhouse gases. For instance, in 2023, 39,7 % of the electricity fed into Germany's grid, equivalent to 178,4 TWh, were obtained from fossil fuels such as coal and gas.[5] An expansion of the renewable energy sources is therefore essential to meet the Paris target. However, most renewable energy sources are inherent to external factors such as weather conditions, making them a volatile source of energy. Therefore, the development of a storage technology to bridge the outages of renewable energy sources is just as critical for a renewable energy economy as the initial energy production.

Due to its high energy density, carbon-free combustion, green generation and non-toxicity, hydrogen has emerged as a powerful energy carrier in a renewable energy economy.[6] For instance, Germany is implementing a national hydrogen strategy, which aims to increase the hydrogen production capacity to at least 10 GW and build a hydrogen pipeline network, thereby promoting the national use of hydrogen.[7] In addition, hydrogen is needed in large quantities in industry, for instance as a chemical in the Haber-Bosch process[8] or as reducing agent in steel making[9].

Despite its potential, the storage of hydrogen represents a major challenge. One of the main obstacles is its low volumetric density. At room temperature and atmospheric pressure, 1 kg of hydrogen gas occupies a volume of 11000 l, compared to 1 kg of liquid gasoline occupying around 1 l under similar conditions. [10,11] Thus, the density of hydrogen must be increased significantly in order to achieve an economic viability.

The **storage of hydrogen** and its research can be divided into three different types: physical storage, adsorption and chemical storage. An overview of the different storage types with examples of each technique is illustrated in Figure 1.1. Physical storage types contain pure hydrogen by compression and liquefaction.[12] Adsorption stores hydrogen in a porous, solid material through physisorption.[13] Although these methods hold great promise, energy is required to enable and maintain the storage at high pressures or low temperatures to minimise the hydrogen loss. These storage types are not covered in this work.

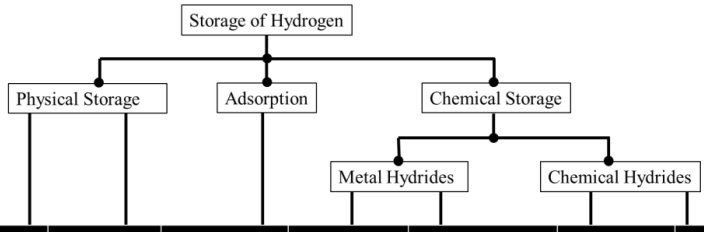

Storage medium	Compression [H_2(g)]	Liquefaction [H_2(l)]	Metal- organic Frameworks	Alanates [NaAlH4]	Borohydrides [LiBH4 + MgH2]	Methanol [CH_3OH]	Ammonia [NH_3]
Density [kg/m³]	7,8	70	40 - 50	54	68	99	123
Gravimetric storage capacity [wt.-%]	/	/	8 - 10	3,5 - 4	7 – 9,1	12,5	17,7

Figure 1.1: Storage types of Hydrogen can be classified in physical storage, adsorption and chemical storage. Examples of the specific storage types are illustrated with their respective densities and gravimetric storage capacities. Values are taken from reference. [14]

In chemical storage, hydrogen is incorporated into a metal or a chemical hydride, e.g. a molecule, as a result of a reaction with a hydrogen-deficient molecule or a metal.[15] The use of such hydrides is advantageous due to their high gravimetric storage capacity, ease of handling and flexible storage options, which reduce the risk of handling and loss of hydrogen during storage. A number of different chemical compounds for hydrogen storage have been suggested in the past, including ammonia[16], methylcyclohexane[17] and methanol[18–20].

Methanol Steam Reforming

Methanol is a promising storage medium as it has a high hydrogen-to-carbon ratio, is a liquid which is easy to handle and can be sustainably produced from carbon dioxide and hydrogen[21]. In particular, its liquid state under standard temperature and pressure differentiates it from other potential molecules such as ammonia and methane, as compression and decompression treatments are not required.[20] An economy based on methanol was also proposed by Olah *et al*.[22] In their book, they set out a scenario in which methanol can be used as an energy carrier, a transport and storage medium, and a recycling agent for carbon dioxide.

In order to make use of methanol in the most efficient way, it is reasonable to reform it together with water steam (eq. 1.1). This reaction is also coined as **methanol steam reforming** (MSR). The reformed gas mixture has a hydrogen portion of 75 vol.-% and can be employed by a Proton Exchange Membrane Fuel Cell (PEMFC) directly.[23,24] In PEMFC environments, the suppression of CO formation by methanol decomposition (eq. 1.2) or reversed water gas shift reaction (eq. 1.3) is crucial, since the Pt catalysts of fuel cells only tolerate very low CO concentrations up to 50 ppm.[25]

$$CH_3OH \rightleftharpoons 2 \cdot H_2 + CO \quad 1.1$$

$$CH_3OH + H_2O \rightleftharpoons 3 \cdot H_2 + CO_2 \quad 1.2$$

$$H_2 + CO_2 \rightleftharpoons H_2O + CO \quad 1.3$$

In this regard, catalytically active, intermetallic **ZnPd nanoparticles supported on ZnO** are really promising due to their high stability and selectivity compared to conventional Cu-based catalysts.[26,27] In order to accomplish high CO_2 selectivity, both ZnPd and ZnO compounds have to be present in the catalyst material.[28–34]

The characterization of single compounds, namely the unsupported intermetallic compound ZnPd[35] and the metal oxide ZnO[36], have shown that a bi-functional synergy between both species exist[37]. Figure 1.2a shows the Zn-Pd phase diagram, which comprises several intermetallic compounds. The intermetallic compound ZnPd has a wide compositional existing range and forms a homogenous phase at 900 °C from 37.5 to 53 at. -% Zn. Its catalytic properties during MSR depend sensitively on the composition.[38] Highly active and selective ZnPd catalyst materials exhibit a Zn-rich composition and a high ZnPd-ZnO interface area. Here, the bulk composition of the ZnPd compound determines the surface composition and thus the Zn oxidisability at the surface.[35] Further evidence for the existence of a synergy between ZnO and ZnPd can be drawn from studies of inverse catalyst models, namely ZnO on surface-near intermetallic compounds. Here, a presence of oxidized Zn in surface-near regions could be directly linked to high CO_2 selectivity.[39–41] These works on ZnPd model and real systems improved the comprehension of its working mechanism during MSR massively.

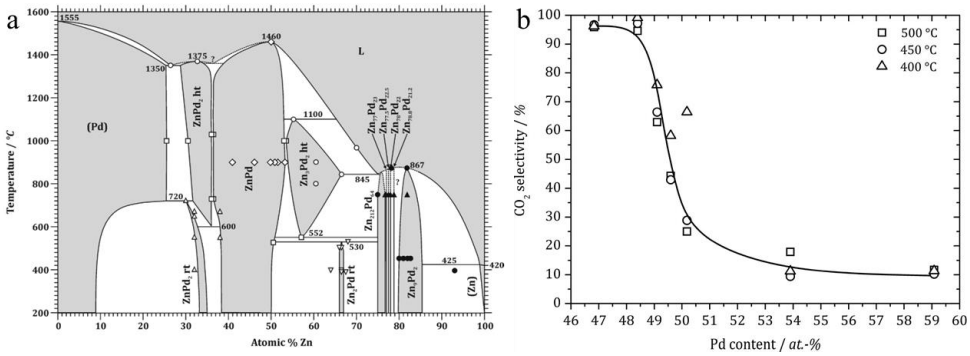

Figure 1.2: a) Pd-Zn phase diagram indicating the existence of the ZnPd intermetallic compound. b) CO_2 selectivity plotted as a function of composition of unsupported ZnPd under MSR conditions. The graphs presented have been taken with the permission of the references[42,43].

The sudden drop in CO_2 selectivity under MSR conditions at around 51 at. - % Zn is illustrated in Figure 1.2b. Performing operando photo electron spectroscopy, it was shown that selective, Zn-rich materials are partially oxidized during MSR conditions[43].

Next to unsupported ZnPd, recent research had a detailed look on the high selectivity of ZnPd nanoparticles supported on ZnO.[37,38] Supported ZnPd particles were studied before and after MSR applying high resolution transmission electron microscopy. Previously reduced ZnPd/ZnO featured only 40% CO_2 selectivity initially which increased above 95% after 4 hours in MSR conditions (Figure 1.3a). This improvement in CO_2 selectivity was closely linked to the formation of nm-sized ZnO patches on the surface of the ZnPd nanoparticles, which enhanced the ZnPd-ZnO interface density. The ZnO patches can be clearly identified by their lattice plane spacings of 2.8 Å in (100) direction, as shown in Figure 1.3b. This change in structure is of great importance for the synergy of both compounds. The described behaviour is reversible by reduction of the catalyst.

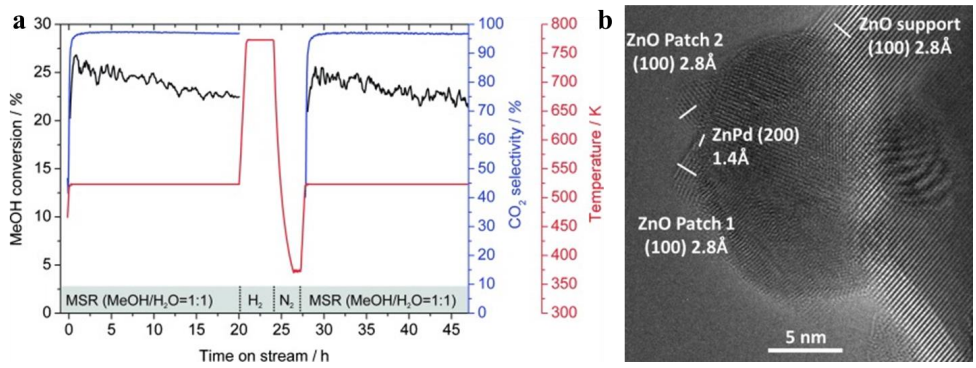

Figure 1.3: a) Temporal development of the catalytic performance of freshly reduced ZnPd/ZnO under isothermal MSR conditions at 523 K. b) HRTEM image of a single ZnPd nanoparticle after MSR, with indications of the corresponding lattice spacings for ZnO patches. Figures are taken with permission from reference[37].

Another significant aspect of supported ZnPd nanoparticles is their spatially heterogenous composition, which was investigated using high resolution STEM.[25] STEM studies after MSR indicated Pd-depleted regions with high O and Zn contents, as illustrated by the dark contrast in Figure 1.4c at positions 1, 2 and 6. Positions 3,4 and 5 show bright contrast ascribing to Pd-richer phases. These findings suggest that the supported ZnPd particles were structurally and compositionally heterogenous after MSR. While ZnO patches were preferably formed at Zn-rich phases, the Pd-rich phases were not covered by these.

Up to now, research on the ZnPd system has focused on pre- and post-catalysis TEM characterisations, i.e. ex-situ investigations, of arbitrary sample positions.[37,38] The active state of a catalyst cannot be unambiguously determined from *ex situ* investigations and their

intermediate states and dynamic behaviour remain unclear. However, such determination is essential to enhance the understanding of the working mechanisms of catalysts and requires the utilisation of *in situ* TEM. Structural changes caused by the reactive environment may include the structural distribution of ZnPd and ZnO phases, their composition, particle shape, size, agglomerations, phase transitions and also occur during synthesis.[44] Given that such changes in material alternate their catalytic properties, an elucidation of the present, dynamic evolution of the ZnPd/ZnO system during synthesis and catalysis is highly desirable.

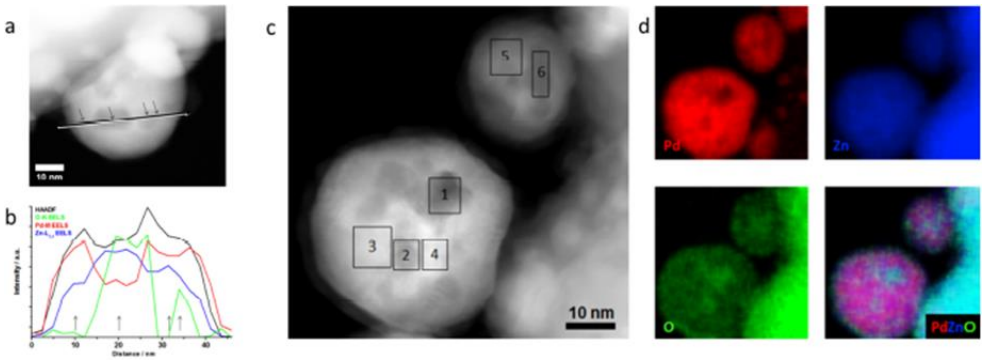

Figure 1.4: a) DF-STEM image of a ZnPd particle and b) a related EELS line scan for Pd, Zn and O as well as HAADF intensity profile, dark regions in the figure correspond to Pd-depleted and Zn- and O-rich phases (Z-contrast); c) DF-STEM image of two ZnPd particles and d) related EDX maps showing the elemental distribution of Pd (red), Zn (blue) and O (green). Graphics are taken and modified with permission from reference.[45]

1.1 Research Goals

This study aims to investigate the preparation of ZnPd nanoparticles supported on ZnO and their applications as a catalyst in MSR applying *in situ* TEM. **Chapter 2** provides an overview of the fundamentals of the ZnPd system, metal-support interactions, Ellingham diagrams and TEM operation modes. **Chapter 3** introduces the relevant materials and methods employed in this thesis. Given that many properties of catalysts such as composition, morphology and size are determined during preparation and these properties are fundamental for their catalytic performance, an investigation of the preparation is crucial to understand the behaviour of the system during catalysis. Two essential preparation steps are investigated in detail: the calcination of supported palladium nitrate and the reduction of supported palladium oxide. **Chapter 4** addresses the calcination of supported palladium nitrate. Here, supported palladium nitrate is heated from 110 to 500 °C at a 1.5 Pa oxygen pressure employing *in situ* STEM. The experiment targets to examine the decomposition temperature of palladium nitrate. Additional

analysis using differential thermal analysis is conducted to verify the findings. A calcination window is determined, in which the system remains stable. The onset temperature for particle growth and the underlying mechanisms are resolved as function of temperature. The high temperature behaviour and resistance of the system is explored by heating to a temperature of 800 °C in vacuum. *Ex situ* experiments under conventional calcination conditions allow an examination of the pressure gap. In **chapter 5**, the reducibility of ZnO is investigated by using an E-STEM. The investigation of the reduction aims to identify the dominant hydrogen species present during E-STEM experiments. In **chapter 6**, the reduction and transformation of supported PdO is investigated. During reduction, PdO nanoparticles supported on ZnO are exposed to a 1.5 Pa hydrogen pressure at room temperature and at 200 °C applying E-STEM. The reduction experiments aim to investigate the effect of the reducing atmosphere on the nanoparticle and the support. It is investigated if and how ZnPd is formed and whether the transformation process can be divided into distinct mechanisms. An *in situ* experiment at 200 °C permits an examination of the reaction kinetics. The impact of experimental conditions, which are inherent to *in situ* STEM such as electron beam effects, is investigated and a potential activation of the observed changes in material is estimated.

Supported ZnPd nanoparticles exhibit a high selectivity for CO_2 during methanol steam reforming. Given that this high CO_2 selectivity is only activated by the catalytic conditions, the *in situ* investigation, which is presented in **chapter 7**, aims to unravel the dynamic changes of the catalyst that facilitate the increase in catalytic properties. To enable MSR experiments, a custom gas supply system is designed. This setup allows for a flexible control of the methanol and water content, which are injected into the column. Since different species are present in the environment during MSR, the effect of the individual species on the pristine ZnPd nanoparticles is investigated at a temperature of 200 and 320 °C and pressures < 10 Pa in **chapter 7.4**. Subsequently, the effect of simultaneous injection of methanol and water steam is explored in **chapter 7.5**. Here, special attention is paid on the potential changes in composition and morphology of the nanoparticles. In order to increase the partial pressure of hydrogen, in **chapter 7.6**, hydrogen enriched with methanol and water is injected. Here, different redox potentials in the column are produced to investigate their effect on the system. In order to estimate the effect of the pressure, **chapter 7.7** addresses experiments with a closed cell TEM configuration. Here, MSR experiments are conducted at a pressure of up to 1 bar. In this experimental *in situ* set up, a carrier gas is saturated by methanol and water. The sample is exposed to this steam and simultaneously studied using TEM.

2 Fundamentals

2.1 Zinc Palladium Supported on Zinc Oxide and Methanol Steam Reforming

The intermetallic compound ZnPd has a wide existence range in the ZnPd phase diagram, as illustrated in Figure 1.2. Intermetallic compounds consist of two or more metals. In contrast to alloys, i.e. solid solutions, they exhibit crystal structures, which are different from those of the component metals. ZnPd with a Zn content between 37,5 and 53 at.-% crystallises in a tetragonal, CuTi-type bulk structure (space group P4/*mmm*), which is different from cubic Pd and hexagonal Zn. Equimolar ZnPd exhibits lattice parameters of a = 2.895 Å and c = 3.327 Å and corresponds to a c/a-ratio of 1.15.[46] Figure 2.1 shows the crystal structure of ZnPd.

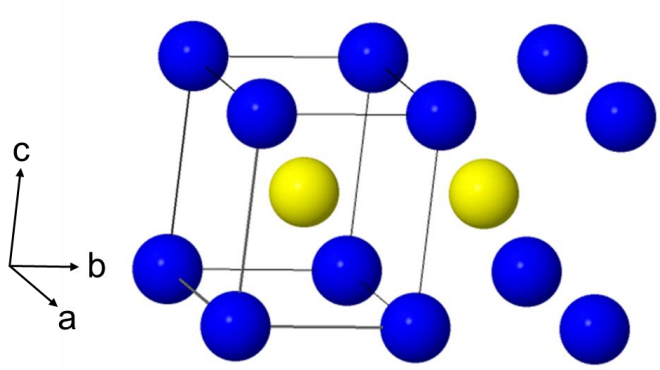

Figure 2.1: Sketch illustrating the tetragonal crystal structure of ZnPd. Pd is highlighted in yellow, Zn in blue. The unit cell is marked. Structure is adapted from reference.[46]

The lattice parameters sensitively depend on the ZnPd composition, such that parameter a increases and parameter c decreases with a rising Pd content, adapting to the cubic crystal structure of elemental Pd.[42] A determination of the melting point of ZnPd is challenging due to the high vapor pressure of Zn, but was reported to be at ~1458 °C.[47]

Supported ZnPd nanoparticles are typically synthesised through the application of reactive metal support interaction (RMSI), transforming Pd/ZnO composites by partial reduction of the metal oxide. The formation mechanism is described in detail in chapter 2.3. Wang *et al.* report that such a reduction treatment in a 5% hydrogen atmosphere at a temperature between 250 and 300 °C form supported ZnPd nanoparticles with a size between 5 and 14 nm.[48] Karim et al. investigated different deposition approaches for Pd on ZnO and their effect on MSR.[29] The Pd/ZnO system is typically obtained by impregnation of a pre-formed ZnO support with a palladium precursor. In general, it is highly desirable that the preparation result is homogenous

and all nanoparticles are uniform in size, composition and morphology, thereby obtaining the same reactivity at all interfaces. For instance, small deviations in composition due to residual elemental palladium nanoparticles may change the catalytic properties of the entire system.[32] Large Pd nanoparticles may undergo partial transformation to ZnPd during a mild reduction, whereas smaller Pd nanoparticles are fully transformed.[42] The residual elemental Pd then facilitates methanol decomposition, yielding carbon monoxide instead of carbon dioxide. To avoid such inhomogeneities, close attention needs to be paid during selection of the palladium precursor, pH of deposition and drying and calcination parameters.[42] Other preparation routines include co-precipitation and -impregnation of Pd- and Zn-precursor.

The electronic structure of surfaces is a crucial property in heterogenous catalysis. Reactions with chemical elements may introduce deviations to the electronic structure of the catalyst that can be beneficial. In particular, the valence band region at the Fermi edge is decisive. However, its characterisation is challenging, let alone under reactive conditions. Tsai et al. reported in their UHV XPS study that the Pd4d level of ZnPd is shifted away from the Fermi edge compared to pure Pd, reducing the band width as a function of Zn content.[49] This result was confirmed by XPS experiments under MSR conditions[43], in which higher binding energies were found with increasing Zn content. Zn introduces more valence electrons, thereby decreasing the density of states around the Fermi edge. These electronic properties seem to be beneficial for good catalytic properties in methanol steam reforming.

In terms of relative energy, band width and density of states, the valence band of ZnPd is similar to that of Cu(111)[49]. The use of Cu as a catalyst is well established in methanol production and has been employed industrially for many years. [50] Additionally, in methanol steam reforming it exhibits a high activity and a good selectivity towards the formation of CO_2[51]; however, its usage as catalyst is limited due to deactivation. Deactivation can occur in a number of ways, including thermal sintering, poisoning, carbon deposition, or physical damage. [52] Thermal sintering represents a pivotal factor, which contributes to a decrease in activity of catalysis performed at a temperature higher than 300 °C. In comparison to other metallic catalysts, such as Pt, Pd or Fe, which are commonly employed in hydrogen and dehydrogenation reactions, Cu exhibits low thermal stability. Thus, Cu-based catalysts are predominantly operated at a low temperature < 300 °C. Since oxides reduce the thermal sintering of Cu-based catalysts, most of such catalytic systems incorporate oxides such as ZnO, CuO or Al_2O_3.[52] An additional concern in the usage of Cu is that nanocrystalline Cu is pyrophoric. The introduction of Cu-based catalysts to air results in a notable increase in temperature, which displays a safety concern in some applications.[53] It can be concluded that Cu is not an appropriate catalyst for methanol steam reforming, despite its favourable electronic structure. In comparison, ZnPd exhibits an electronic structure that is catalytically active in MSR and is resistant to deactivation.

Despite many efforts, the precise reaction mechanisms of supported ZnPd as a catalyst during MSR remain unclear.[54] Various reaction pathways have been discussed in literature, including

the formation of intermediates such as methoxyls, formaldehydes and hydroxyls on the ZnPd surface.[55,56] Köwitsch and co-workers focused in their recent work on the role of the supporting metal oxide in the In_3Pt_2/In_2O_3 system during MSR.[57] The application of oxygen isotopes revealed that oxygen required for the oxidation of reducing agents such as carbon monoxide was supplied by In_2O_3 in the close proximity to In_3Pt_2. This resulted in the formation of temporary oxygen vacancies at the metal oxide. The replenishment of these oxygen vacancies by the present water indicates the presence of a Mars-Van Krevelen mechanism. This mechanism, which was initially proposed by Mars and Van Krevelen[58], describes the oxidation reactions that occur during catalysis involving metal oxides. A reducing agent is oxidised by a lattice oxygen, generating an oxygen vacancy. The oxygen-deficient lattice is reoxidised by an oxidising agent such as molecular oxygen or water, thereby restoring the original state. Köwitsch et al.[57] suggested that the Mars-van Krevelen mechanism is a universal concept in intermetallic MSR catalysts and may be responsible for the good catalytic performance. Accordingly, the excellent catalytic performance of the ZnPd/ZnO system may be based on the Mars-van Krevelen mechanism. However, a proof for this is still lacking

2.2 Evaporation of Liquids

Methanol steam reforming requires the evaporation of the reactants, namely methanol and water, prior to the reaction. The evaporation of a liquid is dependent on a number of factors, including temperature, surface area, humidity and pressure.

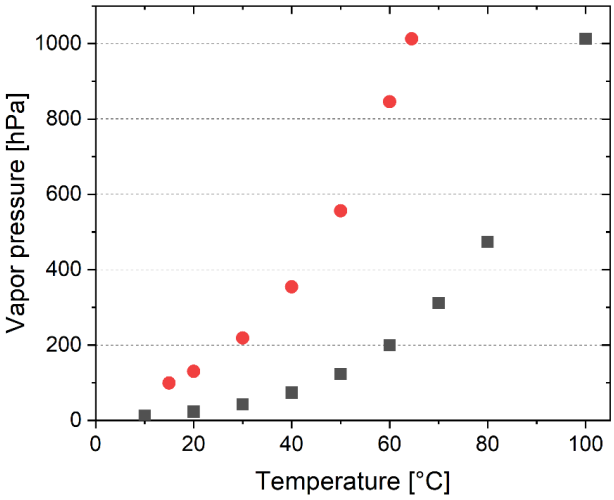

Figure 2.2: Vapour pressures of methanol (red circles) and water (black squares) plotted as a function of temperature. Values are taken from reference[59,60].

The vapour pressure of a liquid determines its probability for evaporation and changes with temperature, as illustrated for water and methanol in Figure 2.2. The phenomenon of boiling occurs when the vapor pressure of a substance exceeds the pressure of the surrounding atmosphere.[61] This boiling point can be surpassed by heating the liquid or lowering the pressure of the present atmosphere.

$$\rho = \rho_a \cdot x_a + \rho_b \cdot x_b \qquad 2.1$$

The vapour pressures of mixtures ρ can be estimated using Raoult's law (eq. 2.1), with ρ_i indicating the respective vapour pressures of the components and x_i denoting the respective mole fractions[62]. Raoult assumed an ideal behaviour between unlike molecules with similar intermolecular forces to those of identical molecules. A comparison between the results of experimental measurements and the predictions of this simplified model also allows for an approximation of the actual intermolecular forces. For instance, a negative deviation from Raoult's law indicates that the intermolecular forces between unlike molecules are stronger than predicted.

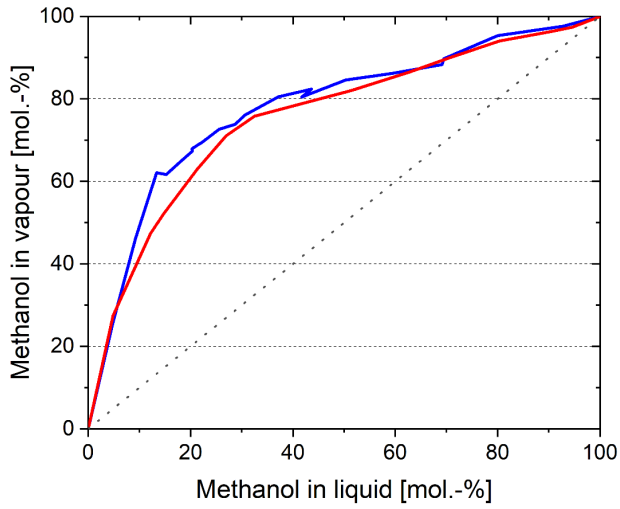

Figure 2.3: Composition of different water and methanol mixtures in liquid and vapour at 40 °C (blue) and 50 °C (red). Data is taken from reference[63].

In such binary mixture, the components evaporate unequally, such that the mole fractions in liquid do not correspond to those in gas. The saturation quantity of a single component ρ_γ can be calculated in kg/m³ using Sonntag's equation (eq. 2.2)[64]. $E_\gamma(T)$ is the temperature-dependent vapour pressure for the specific component γ, T is the temperature and R_γ is the gas constant for the specific component.

$$\rho_\gamma(T) = \frac{E_\gamma(T)}{R_\gamma \cdot T} \qquad 2.2$$

Bredig and co-workers studied the evaporation behaviour of methanol and water mixtures.[63] They showed experimentally how the mole fractions of the components change from liquid to vapour. Figure 2.3 shows the mole fractions of methanol as a liquid and as a vapour in a mixture with water. In this thesis, the methanol content in the vapour is estimated using the experimental data at 40 °C from Bredig *et al*.

2.3 Metal-Support Interactions

Many metallic nanoparticles employed in catalytic reactions are typically supported on metal oxides such as Al_2O_3[65], TiO_2[66], ZnO[67] and CeO_2[68]. Classically, oxide supports are applied to enhance the utilization efficiency and longevity of catalysts by slowing down deactivation mechanisms and thus maintaining their fine distribution and size. For instance, a systematic study by Kong *et al.*[69] reports the conversion of toluene over Ni nanoparticles, which are supported on different oxides. Smaller Ni nanoparticles are less likely to be deactivated by coking and therefore show the highest catalytic activity. Kong's study illustrates the importance of stabilizing nanoparticles with oxide supports in catalysis. However, supports should not be considered as inert and decoupled from catalysis, since oxide supports interacting with metallic nanoparticles can improve the selectivity and activity of a catalytic system.[70–72] Such a phenomenon is referred to as metal-support interaction and is often the cause for the catalytic properties. Consequently, the selection of the support material and a controlled preparation in which the design of the catalyst can be variably tuned are of high interest.

Different types of metal-support interactions have been proposed such as interfacial perimeter, spillover, chemical composition as well as reactive and strong metal-support interactions.[73] Those interactions interfere frequently and occur concomitantly.

Interfacial Perimeter

The **interfacial perimeter** of a nanoparticle has special properties, as it forms the interface between nanoparticle, support and reactive atmosphere and thus the only environment on the catalysts allowing an interaction of those phases. In addition, the interfacial perimeter is prone to compositional evolution and lattice defects due to strain caused by lattice mismatches and atomic diffusion between support and nanoparticle. These defects increase the energy of the lattice forming non-equilibrium states. Since such energetic excited states are favourable to host catalytic reactions, active species are frequently found at the interfacial perimeter.[73]

Spillover

Another mechanism reported at the interfacial perimeter is the migration of surface adsorbed reactant to an adjacent surface, which is coined as **spillover**.[74] During spillover, the reactant is initially adsorbed exothermally by the original surface and may dissociate. Given that the activation energy required for surface diffusion is provided, the reactant is then transported to the neighbouring surface and bound there. Spillover is characterized by the fact that the accepting surface cannot activate the reactant itself under identical conditions and requires an adsorbing parent surface for activation.[75] The reducibility of the accepting material determines reaction speed and extend of the spillover. The spillover on reducible materials occurs faster and at larger distances compared to non-reducible materials.[76] Depending on desorption rate and surface mobility of the relevant species, the spillover distance on oxide supports can be up to 600 µm.[77] Spillover is originally and prominently known for the surface adsorption and transportation of hydrogen from a metal nanoparticle to an oxide support.[78] The phenomenon was found first by Khoobiar during hydrogen migration from platinum-alumina catalysts to neighbouring tungsten trioxide particles.[79] However, spillover has also been reported from metal to metal[80], oxide to oxide[81] and oxide to metal[82] in the past. Due to adsorption and activation, especially of hydrogen, the spillover effect is found in many applications such as preparation of nanoparticles[42], catalysis[74], energy storage[83] and hydrogen detection[84]. In preparation of catalytic systems, hydrogen spillover is frequently used for reduction of metal oxides. Transition metals such as Pt, Pd or Ni lower the reduction temperature of oxide supports via spillover.[85,86]

Chemical Composition

Such solid-state reactions may trigger a change in **chemical composition** and in catalytic properties of the metal-support tandem. The way the catalytic properties are changed depends on the present type of redox reaction. Exchange of species between particle and support may lead to oxidation of the metal phase and to the formation of a mixed metal oxide phase, which is typically inactive and a known cause for deactivation.[87] For instance, van Deelen *et al.* found cobalt atoms migrating from their original nanocrystals to the titanium dioxide support during reduction, which passivated the catalytic system.[88] However, an incorporation of the metallic support species into the metal particle can also be beneficial. Given that the incorporation is triggered by reductive reaction conditions and a high temperature, it may lead to the formation of catalytically active intermetallic compounds and alloys.

Reactive Metal-Support Interaction

Such an interaction, which is only reversible under extremely oxidizing conditions, is known as **reactive metal-support interaction (RMSI)**.[55] Regardless of the material system, the formation of an intermetallic compound or alloy by RMSI typically consists of three formation steps.[89] First, hydrogen is chemisorbed on the supported nanoparticle and spiltover to the metal

oxide support, which is (partially) reduced in the vicinity of the nanoparticle. Secondly, the reduced metal species migrate into the nanoparticle. Thirdly, the reduced metallic species are incorporated into the noble metal lattice and the respective intermetallic compound is formed. Such a mechanism can be explained using the reduction of PdO nanoparticles supported on ZnO as an example system, that is a prominent reaction in the formation of intermetallic ZnPd[90–94]. Martin *et al* found that PdO already adsorbed and dissociated hydrogen at a low temperature of 110 K, but was only completely reduced at room temperature.[95] As-reduced Pd forms palladium hydrate and hydrogen is spiltover onto the ZnO support. Iwasa et al. identified this hydrogen spillover by temperature-programmed reduction.[92] They showed excessive hydrogen consumption during the reduction of PdO and remaining hydrogen on the particle-support tandem after decomposition of palladium hydrate during heating, which indicates a spillover onto the ZnO. In addition, on systems such as Pd/SiO_2 and Pd/Al_2O_3, where no spillover is expected, hydrogen was completely desorbed. Activated hydrogen (partially) reduces ZnO and combines with the present oxygen to form water, which is desorbed from the surface. The amount of metallic Zn reduced is proportional to the Pd loading.[92] Given that the formation energy required is provided by the present temperature, metallic Zn diffuses to the nanoparticle and is incorporated in the palladium lattice, resulting in the formation of intermetallic ZnPd nanoparticles. XRD and XPS measurements by Iwasa *et al* provides evidence for different palladium states.[92] Direct experimental proof of this formation mechanism for supported ZnPd nanoparticles, which elucidates the structural evolution between particle and support during reactive conditions, is, however, still lacking. As-formed ZnPd has excellent, catalytic properties in numerous reactions such as methanol steam reforming[92], formic acid decomposition[94], methanol synthesis[96] and selective hydrogenation reactions[97–99].

RMSI is the fundamental reaction in the preparation of many supported intermetallic nanoparticles. The large majority of the reported nanoparticle systems are based on noble metals such as Pt, Pd and Rh, less studied are Ni, Cu and Ru. The preparation pathway of intermetallic compounds by RMSI is affected by their thermodynamic stability and diffusion kinetics and is therefore dependent on temperature, time and particle size.[89] As a consequence, the resulting system often consists of a mixture of different intermetallic compounds. Such multiphase formation is facilitated by, for example, larger particle sizes[100] and formation during catalytic reactions[101–103], and occurs for $Rh_3Ti/RhTi$[104], Pd_3Si/Pd_5Si[105,106] and Ga_5Pd/Ga_5Pd_2[107]. Single-phase formation of an intermetallic compound is best achieved if a well-defined temperature region exists that favours the formation of a single intermetallic compound. For instance, preparation protocols stabilizing a single-phase have been established for ZnPd[108], Pt_3Al[109] and Rh_2Si[110]. Therefore, understanding the effect of reaction conditions on the formation mechanism of supported nanoparticles plays a pivotable role in the tuneable preparation of catalytically active intermetallic compounds. In most cases, RMSI promotes the catalytic properties by forming intermetallic compounds. Prominent examples are gas phase hydrogenation of crotonaldehyde over $Pt/\alpha\text{-}GeO_2$[102], methanol steam reforming over Pd-

In_2O_3[111] and isomerization of neopentane over Pd-Al[112]. Few systems are known in which RMSI has a detrimental effect on catalytic activity. For example, Moss *et al.* report a loss of specific activity in the dehydrogenation of benzene over Pd-Si catalysts due to interactions between support and particle at a reduction temperature of 600 °C.[113] Yamaguchi *et al.* found a lower activity in CO oxidation due to the formation of an intermetallic compound between Sn and Pt and reduced CO absorption.[114]

Strong Metal-Support Interaction

A phenomenon similar to RMSI and therefore often mixed up is the **strong metal-support interaction (SMSI)**, which also typically emerges on supported nanoparticles during preparation and heterogeneous catalysis. Tauster *et al.* were the first to coin the term SMSI for the loss of chemisorption abilities of finely dispersed group VIII metals supported on TiO_2 towards H_2 and CO after reduction at a temperature over 500 °C.[115] They suggested that chemical perturbations due to Pt-Ti bonding caused disappearance of chemisorption rather than loss of surface area due to encapsulation of the noble nanoparticle. Metal-metal bonding between Rh-Ti activated by reduction was identified by Sakellson *et al.*[116], supporting the original interpretation of SMSI. Nowadays, SMSI is classified by the change in physiochemical and electrical properties of catalysts, typically manifested by coverage of nanoparticles by a reducible metal oxide support and loss of chemisorption capacities, due to reduction at an elevated temperature.[117] However, it must be recoverable to the pristine state of the catalysts with identical catalytic properties by a mild oxidative treatment. Fully reversibility of the phenomenon distinguishes SMSI from RMSI.[89] In addition, metal-support interactions can only classified as „strong", if the catalysts has conventional chemical properties at a low reduction temperature. These catalytic properties in combination with their chemisorption abilities must change when the reduction temperature is increased.[89]

The SMSI-characteristic decoration of nanoparticles by suboxides follows a specific formation process that can be explained by supported Pd on TiO_2.[118–125] Spiltover hydrogen from the noble metal nanoparticle or low oxygen partial pressures in a high vacuum reduce the metal oxide support TiO_2 and oxygen vacancies are generated by water formation and oxygen desorption. The present oxygen deficiency leads to unsaturated titanium states around the defect, which act as electron donor and introduce delocalized electrons to the system.[126] Thus, TiO_2 becomes a n-type doped semiconductor. This leads to an increase in the Fermi-level of the partially reduced support (E_F(oxide) > E_F(metal)), which promotes the transfer of delocalized electrons from the support to the nanoparticle and restores the equilibrium at the interfaces. The as-formed positive net space charge in TiO_2 facilitates outward diffusion of the positively charged titanium species.[125] This transport phenomenon favours a metal cluster (nanoparticle) with a larger work function than the support exhibits.[125] As the positive net space charge declines due to enrichment of titanium on the surface, negatively charged oxygen diffuses to the surface, recombines with the metal species and forms an oxygen-deficient titanium oxide TiO_{2-x} ($x < 2$).

Since oxygen diffusion is thermally activated, a higher temperature favours stoichiometric metal oxide formation and leads to compositionally different coverage layers.[125] Migration of partially reduced metal oxides MeO_y ($y < 1$) onto the surface of the nanoparticle is driven by different surface energies.[127] Coverage of the metal surface by metal oxides minimizes the total surface energy of the system and occurs preferentially if the surface energy of the metal oxide MeO_y is lower than the one of the respective metal.[125] Thus, metals with either small work functions or low surface energies, for example alkali and transition metals, are known to resist coverage and rather sinter or oxidize.[128] However, Tang et al. found encapsulation of metals with relatively low work functions and surface energies (Au, Ag, Cu), which indicates that other parameter such as reduction conditions and structure factors must also be considered.[129] For instance, Du *et al.* studied the effect of particle size on SMSI.[130] In the systematic work, larger Au particles are encapsulated by TiO_2 to a greater degree and at a lower reduction temperature. Since electron transfer and surface energy correlate positively with an increase in particle size in their work, such properties are likely to play pivotal role in the size-dependent occurrence of SMSI. The investigation of SMSI on small metal species such as single atoms and nanoclusters is hampered by their increased surface mobility and tendency for agglomeration at a higher temperature[131], which is required to activate encapsulation of small structures. In addition to conventional SMSI, encapsulation by reducible metal oxides in a reductive hydrogen atmosphere, other types of SMSI have been reported. For example, the decoration of nanoparticles by non-reducible oxides such as SiO_2[132] and Al_2O_3[133] as well as by non-oxide supports[134,135] was found. A high formation temperature for non-reducible oxides and minimization of surface energies for non-oxides are expected to be an important factor in the formation mechanism. It should be noted that SMSI does not exclusively occur in a hydrogen atmosphere. Different types of environments are reported: Liu *et al.*[136] found SMSI for Au supported on ZnO under high-temperature oxidation conditions. Matsubu *et al*[137] identified SMSI for Rh/TiO_2 in a CO_2-H_2 atmosphere forming a coverage of HCO_x adsorbates. Zhang *et al.*[138] showed SMSI by a redox interaction between Au and Ti precursors in aqueous solution. Such phenomena are denoted as oxidative (O-SMSI), adsorbate-induced (A-SMSI) and wet chemistry SMSI (wcSMSI) and demonstrate the range of formation mechanisms and the versatility of SMSI. In many of the reported systems, generation of lattice defects, especially oxygen vacancies[118,120,137–140], is a key mechanism and decisive for the mobility of the oxide support.

Structural and electronical evolution caused by SMSI may alter the catalytic properties of catalysts. Encapsulation increases the interface between particle and support. Bimetallic, interfacial sites are formed, which are covered by a reduced metal oxid layer.[117] Such a construction leads to a loss of adsorption capacity, since the active, metal centres for chemisorption are blocked.[89] The modulated surface leads to a change in the reaction pathway, as the activation of the reactants on the surface is changed. For instance, Zhang *et al.* tuned the selectivity in CO_2 hydrogenation from CH_4 to CO by encapsulating Ir nanoparticles with a TiO_x

layer, which increased the activation energy for CH_4 production.[135] Iwasa *et al.* found an increase in CO_2 selectivity in methanol steam reforming over ZnPd nanoparticles supported on ZnO.[141] While the exact formation mechanism is unclear, ZnO patches on the ZnPd presumably caused by SMSI are expected to play a pivotal role in the enhanced, catalytic properties.[37] Another catalytically beneficial characteristic of SMSI is boosted electron density at active metal species. The partial reduction of the metal support creates oxygen vacancies that lead to the formation of donor states and an upward bending in the oxide support. The equilibration of the Fermi levels is achieved by electron transfer to the nanoparticle, which leads to electron-rich active sites. Xu *et al.* demonstrated that an increase in particle coverage and in electron density of interfacial Ni caused by SMSI enhances the activity of the present water gas shift reaction.[142] *In situ* extended x-ray absorption fine structure spectroscopy (EXAFS) revealed the enrichment of electrons on Ni atoms at a reduction temperature above 450 °C. In addition to pure catalytic improvements, SMSI may enhance the resistance of catalysts to thermal deactivation. The encapsulation of nanoparticles limits their migration and stabilizes the system against agglomeration effects at a high temperature. The reactive conditions must be selected in such a way that the coverage of the particle restrains their mobility, but the layer thickness still allows the adsorption of reactants. The design and control of such stabilizing conditions is challenging.[117] A material, which is catalytically active but vulnerable to sinter, is copper.[143] As Cu exhibits great potential in many catalytic reactions, but is restricted to a low operation temperature, an increase in resistance against thermal degradation is highly desirable. Li *et al.* introduced a concept to improve the activity and stability of Cu catalysts supported on ZnO/Al_2O_3 in methanol steam reforming.[144] A treatment in $H_2/H_2O/CH_3OH/N_2$ activates the migration of oxygen-deficient ZnO onto the Cu surface and leads to an increase in interfacial Cu-ZnO sites. The pre-treated catalyst preserved 90 % of its original activity, three times more than the untreated catalyst, indicating an improved thermal stability. The peculiar properties of SMSI described above can be utilized in the design of catalysts to steer the catalytic properties in the desired direction. Utilization of SMSI is desirable in chemical reactions where a high selectivity to only one product is beneficial. For instance, in hydrogen supply for fuel cell applications by methanol steam reforming, high CO_2 selectivity is required to prevent CO poisoning of the Pt catalyst.[145]

Solid-Solid Wetting

Surface migration of mobile, solid species is an important transport mechanism in the propagation of reaction zones. Such solid-state reactions, in which the surface of one solid is covered with another solid in order to lower the surface tension of the system, are also known as **solid-solid wetting**.[146,147] Solid-solid wetting is driven by the specific surface free energies (γ) between the mobile solid (m), gas phase (g) and support (s). Wetting of the support by a mobile solid occurs, when the condition specified in equation 2.3 is fulfilled and free energy is obtained.[148]

$$\gamma_{mg} + \gamma_{ms} < \gamma_{gs} \quad 2.3$$

Thus, the free energy required for the formation of an interface between mobile solid and gas phase and support must be lower than the free energy of the interface between support and gas phase. However, specific surface free energies are temperature-dependent and typically determined close to the melting point. Thus, a quantitative determination, if and how much energy is gained, is challenging. In addition, solid-solid wetting requires sufficient surface mobility of the active species, which is controlled by diffusion and is therefore activated by temperature. Appropriate temperatures benchmarks are the Tamman[149] and Hüttig[150] temperatures, which represent the temperatures required to achieve significant diffusion of bulk atoms and surface atoms of solids. The Tamman temperature T_T is approximately the half of the absolute temperature of the melting point T_M (equation 2.4) and the Hüttig temperature T_H is a third of the absolute temperature of the melting point (equation 2.5). At a temperature above the Hüttig temperature, significant atomic surface diffusion is expected. As solid-solid wetting is diffusion controlled, only single atom species are transported at a time.

$$T_T = \frac{1}{2} \cdot T_M \quad 2.4$$

$$T_H = \frac{1}{3} \cdot T_M \quad 2.5$$

Intriguingly, solid-solid wetting takes place in a reducing atmosphere, as it is the case during SMSI, but can also occur during calcination at an elevated temperature. Taglauer *et al.* demonstrated solid-solid wetting of MoO_3 on TiO_2 during calcination in a dry and H_2O-saturated oxygen stream at 720 K.[148] MoO_3 spread over TiO_2 and formed a surface layer. WO_3 was also found to cover TiO_2. At a temperature below the Tamman temperature, a different mechanism of surface migration is reported, in which the surface layer moves as agglomerate of multiple atoms in a liquid-like manner.[150] The migration of such crystallites is slower than the diffusion of single atoms and is activated by relatively weak metal-substrate interaction. An increase in atomic mobility can also be activated by a high density of lattice defects. In heterogenous catalysis, the lattice defects can be formed by present, reactive conditions that the material is exposed to. For instance, a reductive atmosphere may reduce metal oxides and generate oxygen vacancies.[151] Local oxygen vacancies may introduce a difference in the electrochemical potential in semiconducting materials.[125] Thus, atoms or ions may move from regions of higher potential to lower potential to balance the difference. All named phenomena may contribute to formation of solid-solid wetting.

2.4 Reduction of Metal Oxides – Ellingham Diagram

The energy elements consume to form one mole of compound at atmospheric pressure, is defined as standard Gibbs energy change of formation ΔG_f^0 and can be determined applying equations 2.6 and 2.7.[152]

$$\Delta G_f^0 = \Delta H_f^0 + T \cdot \Delta S_f^0 \qquad 2.6$$

$$\Delta G_f^0 = \left[\Delta H_{298}^0 + \int_{298}^{T} \Delta C_p dT\right] + T \cdot \left[\Delta S_{298}^0 + \int_{298}^{T} \frac{\Delta C_p}{T} dT\right] \qquad 2.7$$

ΔH_f^0 and ΔH_{298}^0 are the change in standard enthalpy of fusion and at 298 K, ΔS_f^0 and ΔS_{298}^0 the change in standard entropy of formation and at 298 K, T the temperature and ΔC_p the change in heat capacity. The feasibility of reactions depends on their ΔG_f^0. Reactions are only exergonic under standard conditions if $\Delta G_f^0 < 0$.[153]

Ellingham plotted experimentally determined ΔG_f^0 of different metal oxides over temperature and found a linear relationship, which allows a prediction of ΔG_f^0 of binary material systems.[154] The enthalpy represents the y-intercept, whereas the entropy is the slope, which undergoes a change when any of the materials undergo a change in their aggregate. Ellingham diagrams provide a thermodynamic estimation, which indicate how a chemical equilibrium is affected by reactive conditions. As a result, Ellingham diagrams are employed to assess occurrence of chemical reactions. Figure 2.4 illustrates an Ellingham diagram comprising a selection of reactions.

Metal oxides are reduced if the ΔG_f^0 of a competing reaction is lower, i.e. it has a lower value in the Ellingham diagram. Reducing capacities of materials, in particular of gases, are therefore determined by the ΔG_f^0 of their oxidation under the same reactive conditions. For instance, PdO has a relatively high ΔG_f^0 of ~ -30 kcal/mol at 500 °C and can easily be reduced by hydrogen and carbon monoxide with respective oxidation values of -100 and -130 kcal/mol. As shown in Figure 2.4, energetically excited states of a species may have a substantially lower ΔG_f^0, as it is the case with atomic and ionic hydrogen, which have superior reducing capacities to molecular hydrogen. Such excited states are applied in plasma chemistry, in order to facilitate the reduction of metal oxides.[153] It is important to emphasise that Ellingham diagrams are based only on thermodynamic laws and do not consider kinetics. Therefore, the predictive power of Ellingham diagrams is limited in environments with low kinetics, e.g. low pressure atmospheres. In addition, properties such as different diffusion and nucleation rates of surface alloys may impede oxidation of the bulk material, leading to a discrepancy between prediction and observation. [155]

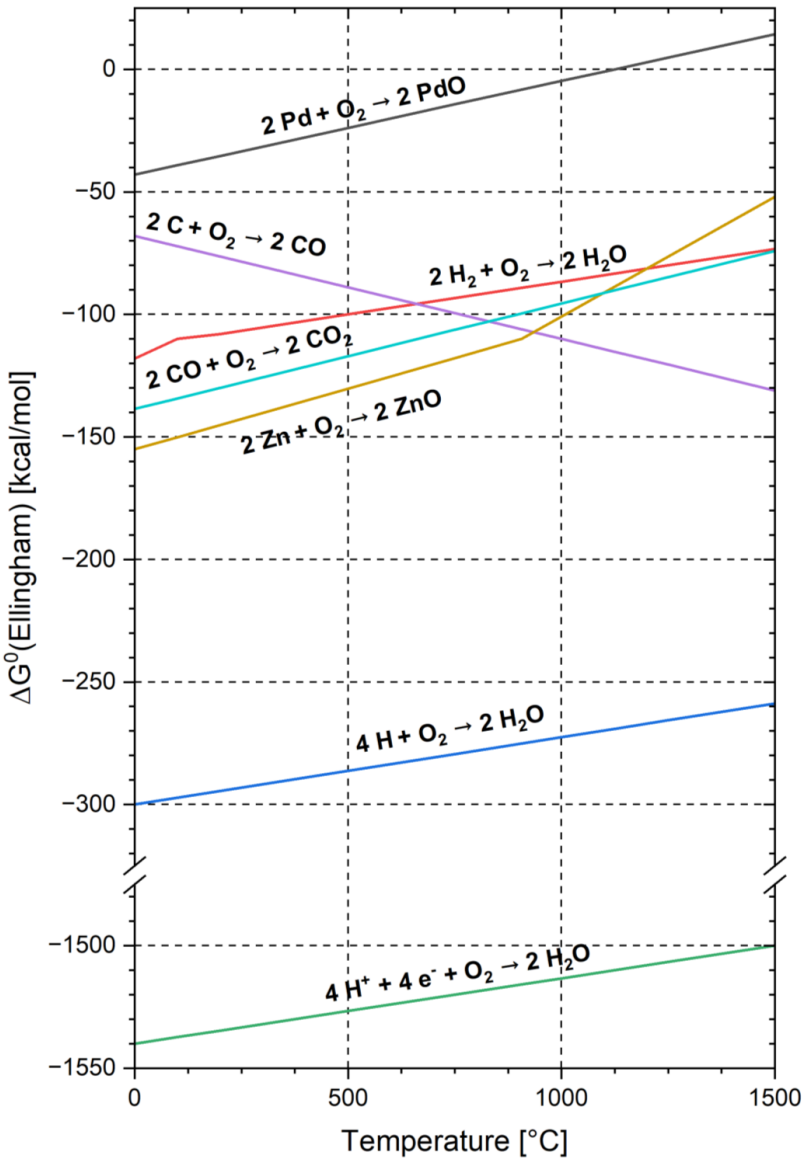

Figure 2.4: Standard Gibbs energy change of formation for various compounds as a function of temperature displayed in an Ellingham diagram. Figure is adapted from reference.[152–154,156]

Ellingham diagrams can also be employed to estimate the equilibrium partial pressure of oxygen. An oxygen partial pressure above the equilibrium will oxidize the metal at a given temperature. An oxygen pressure below the equilibrium will reduce the corresponding oxide. The equilibrium can be calculated using Ellingham diagrams, as referenced[157].

2.5 Transmission Electron Microscopy

Transmission electron microscopy (TEM) is an advanced characterisation technique that employs a high-energy electron beam to study materials down to the sub-Ångstrom level.[158] In TEM, the structures of a material are magnified on the image plane by the use of electromagnetic lenses. During transmission through the sample, the electrons interact with the sample atoms in an elastic or inelastic manner. Such deviations in energy and trajectory, and their associated secondary signals are detected and provide information about the structure, morphology, and chemistry of the sample.[159] Secondary signals may be characteristic X-rays and secondary electrons, the detection of which is discussed in detail below. Given that electrons only transmit through thin samples with a thickness less than ~ 100 nm and most of the imaging signal in TEM is detected below the sample, a careful sample preparation is crucial. The column of the microscope is evacuated due to the strong interaction of electrons with matter, which otherwise result in a significant number of scattering events. This process is employed to maintain an intense, directed beam of electrons.

The investigation of samples is typically conducted through the application of two distinct operational modes: transmission electron microscopy (TEM) and scanning transmission electron microscopy (STEM). In TEM mode, the sample is uniformly illuminated by a parallel electron beam, which generates a coherent image on a screen. In contrast, the STEM mode involves the use of a convergent electron beam, which is focused on the sample to form a fine probe. The probe scans the sample and the image is reconstructed by mapping the signal acquired at each scan location.

2.5.1 Transmission Electron Microscopy Mode

A transmission electron microscope typically consists of electromagnetic lenses, apertures and deflectors, which determine the trajectory of the electrons. The microscope can be divided into different sections, including an electron-emitting gun, a condenser system, the sample holder, an objective lens, intermediate lenses and a detector system, as shown in Figure 2.5. In the electron emitter system, electrons are extracted from a fine tip and accelerated by an acceleration voltage, which typically varies from 60 to 300 kV. Higher acceleration voltages reduce the wavelength of the electrons and thus improve the spatial resolution. In modern TEM, electrons are emitted from a field emission gun (FEG) via quantum tunnelling. The applied electric field lowers the potential barrier, which confines the electron to the tip, and thus increases the probability of a tunnelling event.[160] This technique is employed due to its high brightness, small virtual source size and small energy dispersion, which are superior to those of conventional thermal emitters such as LaB_6.[159] Cold FEGs possesses better properties such as current density, crossover size and energy spread than thermal field emitters (FE) such as Schottky FE.[159] However, the aforementioned properties are accompanied by the necessity for regular flashing cycles to remove contamination, which accumulates at cold FEGs. The

interplay between flashing and continuous contamination results in a volatile beam current, which may impede quantitative characterisation measurements such as EELS and EDX.[161]

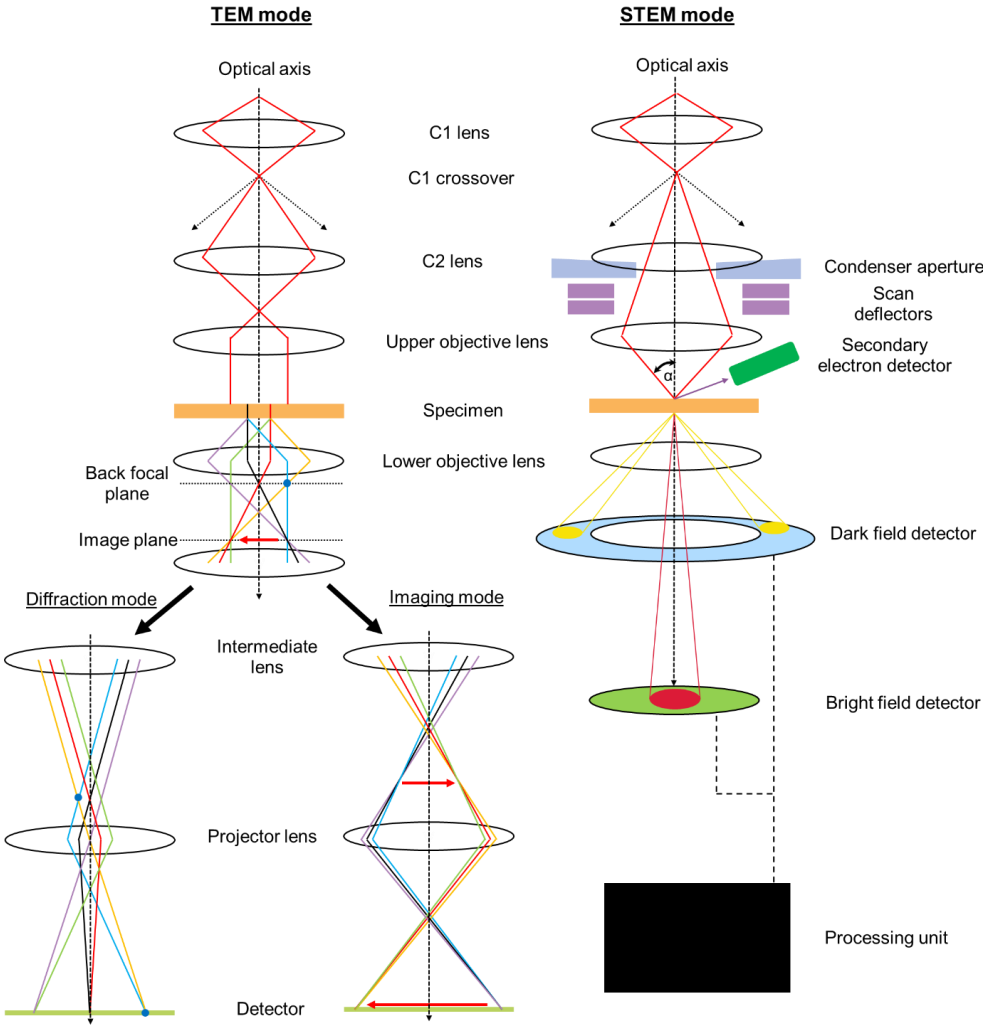

Figure 2.5: Schematic representation of the electron beam trajectory comparing TEM (left) and STEM mode (right). Individual lenses, apertures and detectors are omitted for simplicity. Diffraction and imaging modes have the same lens settings up to the intermediate lens and are shown separately below. The processing unit digitally recombines the individual signals from the scan into a coherent image.

The condenser system controls the illumination of the sample. The first condenser lens determines the minimum spot size on the sample by imaging the electron source at its crossover. Depending on the TEM configuration, the second condenser lens or the upper objective lens regulate the convergence angle of the incident beam and forms a disk of parallel illumination.

A condenser aperture cuts of the edge of the electron beam and reduces the signal on the sample, thus controlling the signal-to-noise ratio and the lens aberrations introduced by the condenser lenses.[159]

When electrons have passed through the sample, they are dispersed by the objective lens, resulting in the formation of a diffraction pattern at the back focal plane of the objective lens and an image at the image plane. The objective lens creates the initial and most important magnification of the sample image due to its short focal length. The subsequent intermediate lens system modifies the trajectory of the beam depending on the selected imaging mode.[159] In diffraction mode, the back focal plane serves as the object for the intermediate lenses and a diffraction pattern is projected onto the detector. In imaging mode, the intermediate lenses are adjusted such that the imaging plane of the objective lens act as their object plane, resulting in the production of a magnified image on the detector. Additional apertures incorporated into the trajectory facilitates the investigation of selected areas or diffraction spots. The electrons are typically detected by a fluorescent screen, a direct detection camera and a pixelated charge-coupled device (CCD) camera, which is paired with a scintillator, converting the electrons into photons.[162]

2.5.2 Scanning Transmission Electron Microscopy Mode

A STEM probe is formed by exciting either the condenser lens 2 or the upper objective lens in such a way that the electron beam is focused on the eucentric height, as shown in Figure 2.5. The electron beam converges under a convergence angle α, resulting in the generation of a probe with a sub-Ångstrom size in the case of aberration-corrected STEM.[163] Given that the probe can only illuminate a small fraction of the sample, it is moved in a raster-like manner by scanning coils.

At each location, interaction between the sample and the electron beam generates signals, which are then collected spatially resolved by the respective detectors. In STEM, the most commonly employed detection modes are bright field (BF), dark field (DF), and secondary electron (SE) imaging. The BF detector is placed on the optical axis and collects only low-angle scattered electrons within a few mrad. The collection angle of the BF disk should be equal to the convergence angle α of the BF probe in order to enhance the SNR.[163] The resulting phase contrast is similar to that observed in TEM imaging and is therefore suited to the investigation of light elements.[164]

In contrast to the BF imaging, DF imaging detects high-angle scattered electrons. The designation of DF imaging is dependent on the collection angle of the detector in use. For collection angles between 10 and 50 mrad, the term 'annular dark field' (ADF) is typically employed, while for collection angles exceeding 50 mrad, the designation 'high-angle annular dark field' (HAADF) is used. As DF images are obtained from electrons that are scattered in

accordance with Rutherford's model for scattering, the DF contrast is dependent on the scatter properties of the sample. The degree of scattering scales with the atomic number and the thickness of the sample, which is why DF contrast is also referred to as Z-contrast. For a sample with different elements, atomic columns that appear brighter are likely to be heavier than those with less signal, given that the contrast depends approximately on the square of the atomic number.[165]

A signal emitted as a secondary effect is the secondary electron (SE) signal. SEs are generated by inelastic interaction of the high-energy electron beam with the sample. Due to the interaction, energy is transferred to electrons of the atoms, providing them with sufficient energy to become excited and eventually overcome their binding energy. SEs are emitted with a kinetic energy < 50 eV. [166] The low energy of SEs restricts their detectable emission to the surface with an emission depth of ~ 5 nm. As a consequence, SEs are surface-sensitive and are predominantly used to image the morphology of a material. The SE detector typically sits above the sample and attracts the electrons with a positive bias following the design of Everhart-Thornely[166].

2.5.3 Imaging Theory

In order to comprehend the process of image formation in a transmission electron microscope, it is essential to focus on the interaction between the electron beam and both the sample and the objective lens. In case of thin samples and small scattering angles, where absorption can be disregarded, electron optics behave analogously to light optics. The propagation of an electron through a crystal results in an increase in its potential energy due to the interaction with the periodic potential of the lattice. Consequently, the total energy of the electron is increased, which results in a decrease in wavelength and a phase modulation. Given that the phase change is dependent on the atomic potential, the sample can be treated as a phase object.[159] Consequently, an incident electron beam with a wavefunction $\Psi_I(\vec{r})$, which enters an object at its entrance surface, will exit the object with a wavefunction $\Psi_{obj}(\vec{r})$. In order to obtain the exit wavefunction, it is necessary to solve the Schrödinger equation for the electron, which describes the interaction with the object. This can be achieved using either the Bethe-Bloch approximation[167,168] or the multislice algorithm[169]. The first approach describes the electron wave function as superposition of Bloch waves, which are states of the crystal potential, solving the Schrödinger equation for periodic boundaries. This approach is well suited for periodic materials, but it has inherent limitations when applied to aperiodic materials, as the number of necessary Bloch waves increases rapidly. The multislice approach divides the material into thin layers in the z-direction, with the diffraction at each slice and the propagation between slices determined in successive order. The atomic potentials are projected onto the slices and the interaction of the electron wave with each projected potential is calculated. This approach is also applicable for non-periodic materials. Both approaches converge to equivalent values for

infinitely thin slices and a high number of Bloch waves. A comprehensive and quantitative deduction of the approaches is given by De Graef[170].

The exit wavefunction of the object $\Psi_{obj}(\vec{r})$ is transferred with high magnification by the microscope optics from the sample to the final image, where the modulus squared of the image wavefunction $\Psi_{Ima}(\vec{r})$ is detected. The transfer of $\Psi_{obj}(\vec{r})$ can be described in two stages. First, the object wavefunction is dispersed by the objective lens on its the back focal plane, which is described by the Fraunhofer diffraction. The propagation can be considered to be a Fourier transformation of the object wavefunction, which is referred to as complex diffraction spectrum. This depends on the spatial frequency $\Psi_{obj}(\vec{g}) = \mathcal{F}[\Psi_{obj}(\vec{r})]$[171]. In the second stage, the complex diffraction spectrum propagates to the image plane, undergoing an inverse Fourier transformation to form the image wavefunction $\Psi_{Ima}(\vec{r})$. In an ideal microscope, the wavefunction of the object and the image would be equal $\Psi_{obj}(\vec{r}) = \Psi_{Ima}(\vec{r})$. However, this does not reflect the actual conditions observed in a microscope, as electron lenses are not perfect and are subject to lens aberrations. When considering thin samples and small scattering angles, the impact of the lens aberrations on the object wavefunction can be incorporated through the coherent transfer function $T(\vec{g})$, which is a reciprocal factor and multiplied with the object spectrum to form the image spectrum $\Psi_{Ima}(\vec{g})$ $(eq.\,2.8)$.

$$\Psi_{Ima}(\vec{g}) = \Psi_{obj}(\vec{g}) \cdot T(\vec{g}) = \Psi_{obj}(\vec{g}) \cdot 2\sin\chi(\vec{g}) \qquad 2.8$$

$$\chi(\vec{g}) = \pi\Delta z\lambda g^2 + \frac{\pi}{2}C_s\lambda^3 g^4 \qquad 2.9$$

Where $\chi(\vec{g})$ is the aberration function and represents the phase shift for waves, which are affected by aberrations, including spherical aberration (C_S), defocus (Δz) and astigmatism (C_a). Given that the astigmatism is small and neglectable, $\chi(\vec{g})$ is the sum of C_S– and Δz-terms (eq. 2.9) and $T(\vec{g})$ exhibits an oscillatory nature with values between -1 and 1. $T(\vec{g})$ is comprised of regions of spatial frequencies of good transmission, which are divided by spatial frequencies of no transmission. No contrast is transferred for values $\chi(\vec{g}) = \pm n\pi$.[159] Figure 2.6 shows a schematic graph of a transfer function with an envelope damping function.

The inverse Fourier transformation of $T(\vec{g})$ represents the point spread function in real space. This function results in the smearing of a point in the object plane into a disk in the image plane due to the presence of aberrations. The delocalization of object information thus defines the spatial resolution of an electron microscope. The instrumental point resolution g_1, which permits a direct interpretation of image details, is defined by the first crossover with the x-axis. Image-simulation is required to obtain information from spatial frequencies > g_1.

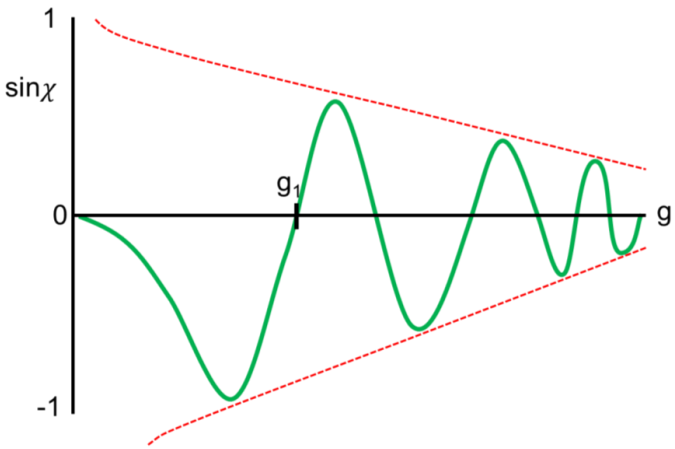

Figure 2.6: Schematic illustration of a transfer function with an envelope damping function (red). The spatial frequency g_1 represents the point information limit of the microscope under the given aberrations.

As with microscopes with a given C_S, Scherzer postulated an ideal defocus condition, which pushes g_1 to the highest achievable spatial frequency and thus increases the spatial resolution. The so-called Scherzer defocus[172] is derived by flatting $T(\vec{g})$ at $-\frac{2\pi}{3}$ and is given by eq. 2.10.

$$\Delta z_{sch} = -1.2\sqrt{\lambda C_s} \qquad 2.10$$

The transfer of the object wavefunction is also impeded by incoherent effects, including partial incoherence of the electron beam, image spread by the operation environment and detector modulation function,[171] resulting in the incapability to image the finest features. The partial incoherence of the beam includes the chromatic effects introduced by the objective lens and the energy dispersion of the electron beam and spatial coherence of the electron source. The latter describes the extent to which well the phases of electron waves emitted from different regions of the electron gun are correlated. These effects are considered by imposing an envelope damping function on the transfer function, as shown by the red dotted curve in Figure 2.6. Consequently, higher spatial frequencies are damped out, serving as a virtual aperture at the back focal plane. Given that high spatial frequencies are not accessible, the damp-out is referred to as the information limit.

For many years, the resolution of an electron microscope was constrained by its aberration, particularly spherical aberration, which could not be corrected for electron optical systems using rotational symmetric magnifying lenses. A lens, which suffers from spherical aberration, deflects a ray propagating through its outer part more strongly than one closer to the optical axis, thereby failing to converge the beam at a single focal point. As Scherzer postulated, spherical aberration are inherent to axially symmetric, electric and magnetic fields that are free

from sources and vortices in the neighbourhood of the optic axis and do not vary with time.[172] Haider and co-workers were the first to successfully correct the spherical aberration in an electron microscope by applying two hexapole units and four additional lenses.[173] In their solution, the two hexapoles are excited in such a way that they mutually compensate for their primary second-order aberration, thereby inducing an additional spherical aberration that compensates for that introduced by the objective lens. This technique allows for the tunability of the spherical aberration of the objective lens. Following the initial experiments, which aimed to employ a C_s value close to zero, imaging conditions were derived that significantly enhanced the phase contrast and minimised delocalisation.[174] The application of a low negative value of the spherical aberration in overfocus conditions further enhanced the image contrast.[175,176] This negative C_s imaging (NCSI) mode images atomic columns with a bright contrast and dark background, yielding a negative phase contrast of atomic objects and enabling atomic enhanced contrast for imaging light atoms and even single atoms at sub-Ångstrom resolution.

2.5.4 In Situ Gas Transmission Electron Microscopy

In situ experiments facilitate the investigation of material changes that are activated through the present reactive conditions. *In situ* experiments are essential to study catalysts in their active state, as the active state of a catalyst may only form under catalytic conditions.[177] Such conditions typically involve the presence of a liquid or gaseous medium and the application of an external stimulus, such as heating or biasing. An important class of catalytic reactions, frequently studied using *in situ* TEM, are thermo-activated gas reactions. This class of *in situ* TEM experiments will be discussed in this chapter. There are two different approaches to conduct *in situ* TEM experiments: closed and open cell experiments.[178]

Closed cell configurations for *in situ* gas experiments occupy a TEM holder with a sealed nanoreactor. This decouples the sample from the surrounding column atmosphere.[178] The confined gas is situated between two electron-transparent windows and flows over the sample, which is positioned on a heating spiral. The closed cell setup permits the application of high specimen pressures, thereby enabling the replication of catalysis under realistic, reactive conditions. For instance, for the Dens Climate System, the closed cell configuration enables specimen pressures up to 2 bar.[179] The commercially available closed cell systems are typically based on *in situ* holders, which allow them to be applied in different microscopes, taking advantage of the requisite specifications. Connection of the gas outlet of the holder with a mass spectrometer enables the examination of the residual gas, allow for the conduction of *operando* experiments and for instance, the evaluation of the catalytic performance. Micro-electromechanical systems (MEMS)-based nanoreactors have major drawbacks in terms of chemical and surface analysis. Since the sample is encapsulated inside a nanoreactor using electron transparent windows, imaging and spectroscopy is limited by the background signal of the nanoreactor windows and the major part of secondary electrons, X-rays (EDX) or inelastic

scattered electron (EELS) might be absorbed. Thus, the collection of reliable data containing information about the surface or the chemical distribution conducting in situ experiments using MEMS-based nanoreactor systems is hampered. Xin and co-workers reported that the membrane has larger detrimental effect than the high gas pressure.[180] Due to the optimized design of MEMS-based nanoreactors, the membranes are a few nanometres thin and careful assembly is required to perform successful experiments. Therefore, experiments with closed cell configurations and their preparation are error-prone.

At open cell configuration, the column is differentially pumped and gas is injected in the specimen chamber directly. Such open cell configurations require special microscopy equipment. A mass flow controller with a nozzle introduces the gas at the specimen position, allowing for specimen pressures of < 2000 Pa.[181] Additional column apertures with small holes contain the gas to the specimen part of the column and thus protects the gun and the post-column. Additional vacuum pumps remove the injected gas from the column, maintaining stable pressure conditions for the remaining high vacuum part of the column.[178] The employment of an open cell configuration allows for high spatial and spectroscopic resolution. The geometry of the setup facilitates the acquisition of the emitted signal with minimal distortion by the detector, as the signal is not shielded by a sealed holder, in contrast to the configuration of a closed cell. This configuration also enables surface analysis by the detection of secondary electrons with a comparable low energy.[182] Nevertheless, the open cell configuration is constrained by the limitations of low gas pressure. Furthermore, the low pressure restricts the utilisation of a residual gas analyser, thereby impeding the examination of the composition of the residual gas. This is due to the fact that the gas is removed by multiple vacuum pumps, resulting in a dilution effect. Furthermore, *in situ* gas experiments introduce gases, whose residues remain present to some degree in the base vacuum even after baking the column.[183] Consequently, TEMs with an open cell configuration may suffer more frequently from contamination. Finally, as a specific setup is required for open cell *in situ* TEM, the operation is restricted to microscopes with the necessary capabilities.

Identical location experiments partially represent an alternative to real in situ experiments, as they permit the examination of the effect of real catalytic conditions on the same sample location before and after the reaction. However, dynamic changes and intermediate state that are activated during catalysis remain unresolved. Therefore, they are not appropriate for experiments that aim to investigate the active species of a material.

3 Materials and Methods

3.1 Preparation of Palladium Nitrate Supported on Zinc Oxide

3.1.1 Synthesis Protocol

Samples with a targeted palladium loading of 0.1, 1, 3, 5 and 10 wt.-% were prepared by incipient wetness impregnation following a protocol reported by Iwasa et al. [184] This involved the dissolution of $Pd(NO_3)_2 \cdot x\ H_2O$ (Sigma-Aldrich) in the appropriate amount in water. The palladium-containing solution was added to ZnO (Thermo Scientific, 99.99%). As palladium nitrate contains an undefined amount of water, the Pd content was determined by thermogravimetry (NETSCH STA 449F3) from the mass loss during reduction in 20% H_2/He at 40 mL/min. This resulted in a residue of 42.71 wt.-%, corresponding to $Pd(NO_3)_2 \cdot 1.04\ H_2O$. After impregnation, samples were dried at 110 °C for five days. The samples investigated in this thesis were prepared by the TU Chemnitz, Germany.

3.1.2 Differential Thermal Analysis and Thermogravimetry

In differential thermal analysis (DTA), the temperature difference between a sample and an inert reference is measured as a function of time during an identical, predefined heating programme. Features of such a thermogram plot indicate the presence of a heat transfer from or to the sample, which can be attributed to the occurrence of an endothermic or exothermic reaction.[185,186] Endothermic reactions involve dehydration, nitrate decomposition and melting.[187,188] In contrast, crystallisation represents an exothermic reaction.

In thermogravimetry (TG), the mass of a given sample is monitored over time during a heat treatment. A change in mass may indicate phenomena such as evaporation, decomposition and oxidation of a system.[189]

DTA combined with TG (NETSCH STA 449F3) was conducted in 20% O_2/He with a mass flow of 40 mL/min and a heating/cooling rate of 2 K/min. This was done to record temperatures of ongoing processes and mass-loss during calcination of dried samples up to 500 °C. Samples of ~100 mg were placed in Al_2O_3 crucibles, an empty Al_2O_3 crucible was used as reference. The data was corrected by subtracting the results of blind measurements conducted with the crucibles that were to be used under identical conditions before loading the samples.

3.1.3 Inductively-Coupled Plasma/Optical Emission Spectroscopy

Inductively-coupled plasma/optical emission spectroscopy (ICP/OES) is an analytical method used to examine the chemical composition of a sample. The sample is dissolved in a solution and then pumped into a nebuliser, which forms a fine aerosol. The aerosol is injected into a spray chamber, where the sample atoms are excited by a plasma. In order to reach a lower energy level, the excited atom emits photons that are characteristic for the specific element. Emitted photons with a wavelength in the optical spectrum are refracted by a prism and detected by a spectrometer. The spectrometer collects the signal photon-sensitively, whereby the intensity is proportional to the elemental content. Consequently, the accumulation of varying intensities enables the identification of the composition of the investigated sample.[190,191]

Elemental analysis of the samples was conducted in triplicate, by ICP/OES against a matrix-calibrated standard (Vista RL, Varian) as the reference. A fraction of each sample was dissolved in aqua regia, diluted with distilled deionized water, and acidified with HCl prior to analysis.

3.1.4 X-Ray Diffractometry

X-ray diffraction (XRD) is an analytical technique employed to examine the crystal structure of a given material. In the process of XRD, a crystalline sample is irradiated by X-rays with a specific wavelength. Typical X-ray targets are copper and molybdenum, employing their Kα1 radiation as X-rays.[192]

Due to the interaction of the incident beam with the electron shell of the lattice atoms, the x-rays are elastically scattered. Most scattered X-rays cancel each other out through destructive interference. However, in specific directions, X-rays interfere constructively, generating a diffraction pattern. The angles of constructive interference can be determined by applying Bragg's law (eq. 3.1) .[193]

$$n\lambda = 2d \sin \Theta \qquad 3.1$$

The diffraction condition is met, if incident X-rays with a wavelength λ hit parallel lattice planes with the distance d under an incident angle Θ. Under such conditions, the phase difference between the diffracted beams is such that the x-rays add constructively, resulting in the production of a reflected peak. Figure 3.1 illustrates the diffraction condition based on Bragg's law. In XRD, the angular signal is measured in order to determine the angle at which the diffraction condition is met. The application of Bragg's law allows for the calculation of the interatomic distance of the sample in different crystallographic directions, thus facilitating the identification the atomic structure of the sample.

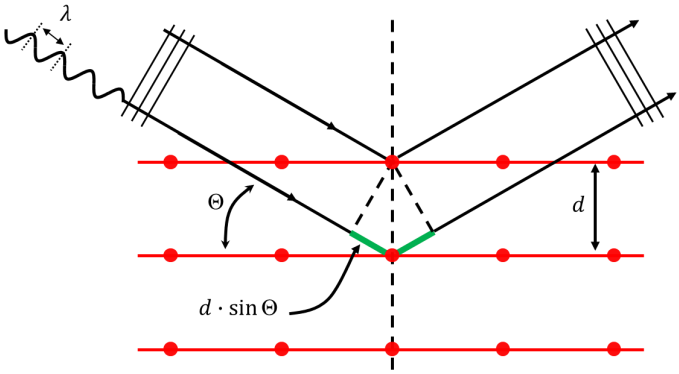

Figure 3.1: Schematic sketch illustrating Bragg's law and the diffraction conditions necessary for constructive interference. The lattice is highlighted in red. X-rays with a wavelength of λ are black. The phase difference that permits constructive interference is indicated in green.

A phase analysis of the crystalline phases was conducted for the as-prepared samples, employing XRD (STOE Stadi P, Cu Kα1 radiation λ = 1.54060 Å, Ge(111) monochromator).

3.2 Transmission Electron Microscopy

The *in situ* TEM gas and vapor experiments were performed employing two different experimental configurations: an open and closed cell configuration. Both systems have different properties, which were derived in chapter 2.5.4. The specifications and techniques used in this work are deduced in the upcoming chapter.

3.2.1 Environmental Scanning Transmission Electron Microscopy – Open Cell Configuration

Environmental *in situ* gas and vapor STEM experiments using an open cell configuration were performed on a HF5000 (Hitachi High-Tech, Krefeld, Germany). The scanning transmission electron microscopy has a probe corrector for spherical aberrations, a cold field emission gun (FEG), a nozzle for gas injection and several detectors for image acquisition and spectroscopy. An overview of the HF5000 specifications can be found in Table 3.1.

In situ gas experiments were performed using the open cell configuration of the HF5000. A schematic illustration is shown in Figure 3.2. The type and quantity of gas is controlled by a gas mixing station and a mass flow controller. The gas is injected into the column via a nozzle near the sample, increasing the pressure of the column locally.

Electron acceleration voltage [kV]	60, 80, 200
Beam current [pA]	4 - 135
STEM resolution @ 200 kV and 100 pA [pm]	< 78
Collection semi-angle BF and DF [mrad]	0 – 8.5; 60 - 300
Energy resolution cold FEG [eV]	< 0.4
EDX energy resolution [eV]	< 72
EDX Solid angle [sr]	2
Specimen pressure [Pa]	< 15 Pa
BF, DF, SE detector	Hitachi High-Tech
Spherical aberration corrector	Hitachi High-Tech
EDX - AztecEnergy with 2 Ultrim Max TLE detectors	Oxford Instruments
EELS - CEFID spectrometer	CEOS

Table 3.1: Specifications of the HF5000

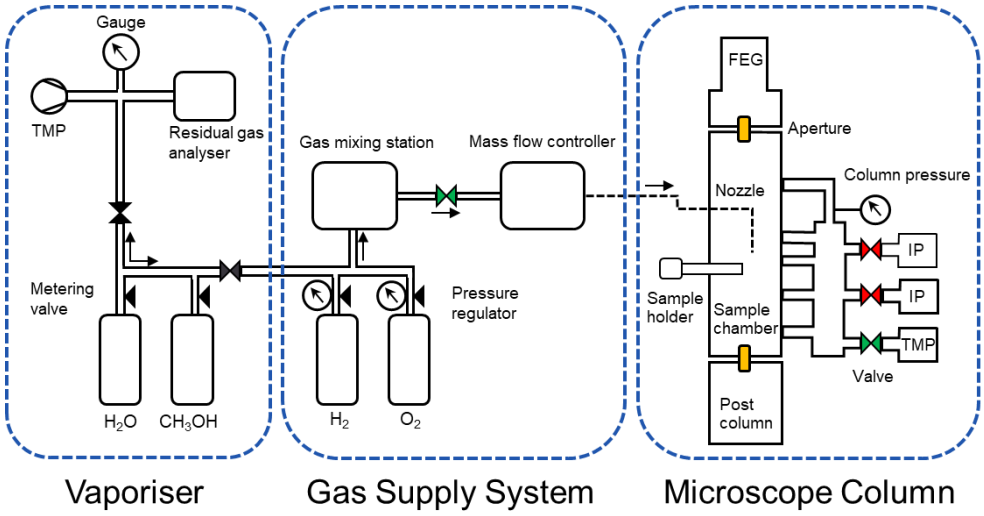

Figure 3.2: Schematic illustration of the environmental setup of the HF5000, consisting of a self-constructed vaporizer, a gas supply system and the open cell STEM system. Green colouring indicates an open valve.

During the '*in situ* mode' of the HF5000, the specimen chamber of the column is differentially pumped by an additional turbo molecular pump (TMP), while the ion getter pumps (IP) are protected. The gas is prevented from penetrating regions of high vacuum levels (e.g. FEG) by

additional, small apertures and thus confined to the sample chamber, as highlighted in yellow in Figure 3.2.

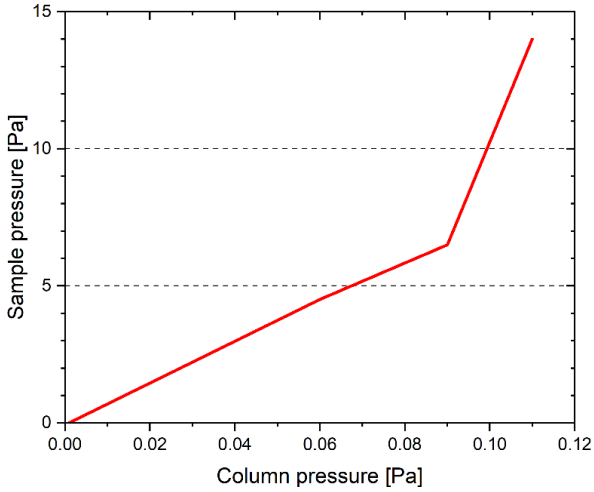

Figure 3.3: Calibration of the sample pressure assigned to the corresponding column pressure, which is measured at the side column, shown in Figure 3.2.

The pressure in the column is set by the pumping speed of the vacuum pumps and the mass flow and remains constant once equilibrium is reached. As the nozzle is close to the specimen, the actual sample pressure is higher than the measured column pressure. A calibration is given in Figure 3.3. A maximum oxygen mass flow of 5 sccm translates to a sample pressure of ~12 Pa.

The vaporizer system was custom-built and enables the evaporation of water and methanol in order to enable an injection into the microscope column in a gaseous form. For evaporation, the residual air in the liquid tanks is first pumped out. Freezing prevents the liquids from evaporating. When the tanks and tubing are under vacuum, the metering valves are closed and gas phases of the respective liquids are formed. The ratio between the gases is qualitatively controlled by adjusting the metering valves. A residual gas analyser, which is connected to the vaporizer system, allows a semiquantitative analysis of the gas contents. In addition, this setup allows the saturation of carrier gas such as hydrogen with methanol and water.

The sample is prepared on a MEMS heating chip with holey, electron transparent SiN membranes, allowing TEM imaging. A single tilt heating holder MHS-5000 (Hitachi High-Tech Canada, Toronto, Canada) is applied to contact and control the MEMS heating chip. The sample is located in the centre of a heating spiral, which is resistively heated by an electric current passaging through the wire, enabling a temperature of up to 1100 °C. Two additional contacts measure the temperature and regulate the heating current applied. The holder and the chip design are shown in Figure 3.4.

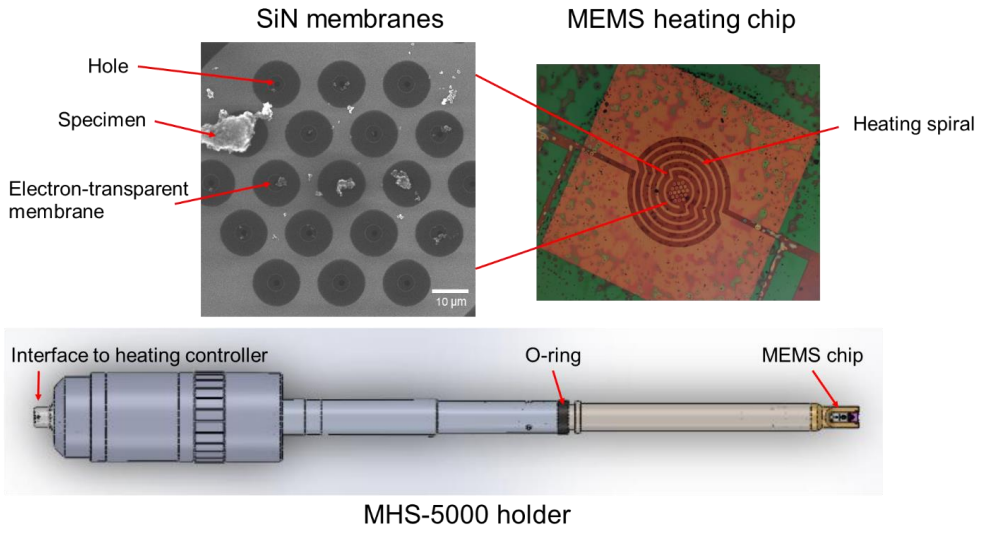

Figure 3.4: Schematic representation of the heater holder and the corresponding MEMS chip. The sample is prepared on the SiN membrane in the centre of the heating spiral. Holder sketch is taken and modified from reference.[194]

3.2.2 Micro-Electromechanical System Reactor – Closed Cell Configuration

Closed cell experiments were conducted on the Climate™ system (DENSsolutions B.V., Delft, Netherlands). The Climate™ *in situ* holder consists of a gas inlet and outlet, a MEMS heating chip pair with two electron transparent windows, as shown in Figure 3.5. The electron transparent windows form a nanoreactor for the sample and gas that is decoupled from the vacuum of the column. The sample is prepared on the heating element of a MEMS chip, which allows temperatures of up to 1000 °C. A four-point measurement is employed to determine the electrical resistance, which is then used to estimate the temperature of the sample. Reactive gas is supplied to the sample via the gas inlet and outlet. Tubes inside the holder enable gas transport from the back to the reactor. The reactor is encapsulated due to O-rings and electron transparent windows, protecting the vacuum of the microscope and enabling reactor pressures up to 2 bar. Similar to the open cell configuration, a gas mixing station sets the type of gas and its mass flow. The gas is directed from the gas mixing station to the vaporiser unit, as shown in Figure 3.6. The vaporiser consists of a dry and wet line. The dry line acts as by-pass. Thus gas, which is directed through the dry line, proceeds unaffected to the reactor. The wet line operates similar to a gas washing bottle: The carrier gas bubbles through the selected liquid, is saturated and carries vapor to the reactor. The wetness of the carrier gas can be adjusted by the amount of gas, which is led through the dry line. The ratio between gas proceeding through the wet and dry line is controlled by a needle valve. The wet line can be closed by a ball valve.

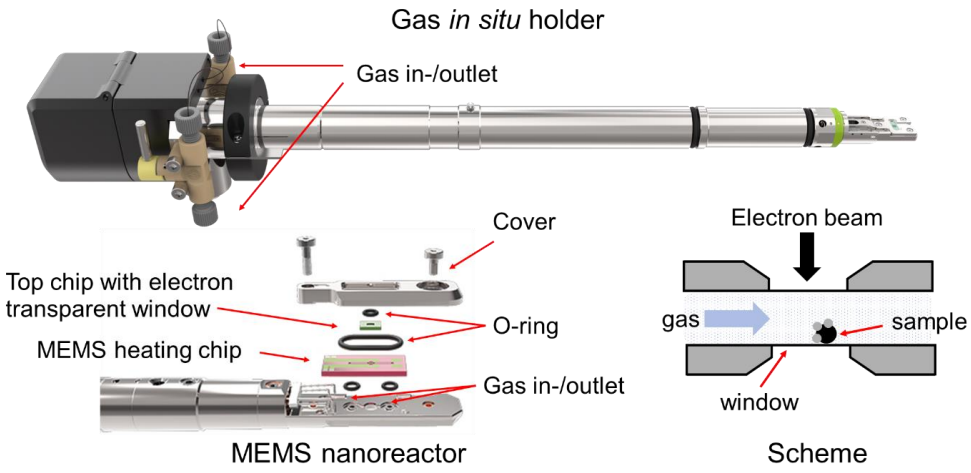

Figure 3.5: An overview image of the Climate™ *in situ* holder and an exploded view of its tip are shown. A working scheme of the tip illustrates the configuration of the components. Images are taken and modified from reference.[195]

The gas exiting the *in situ* holder is analysed using a mass spectrometer, which enables to measure the reaction products directly, thereby allowing an estimation of the performance of *operando* experiments. Figure 11.1 shows the experimental setup in the laboratory.

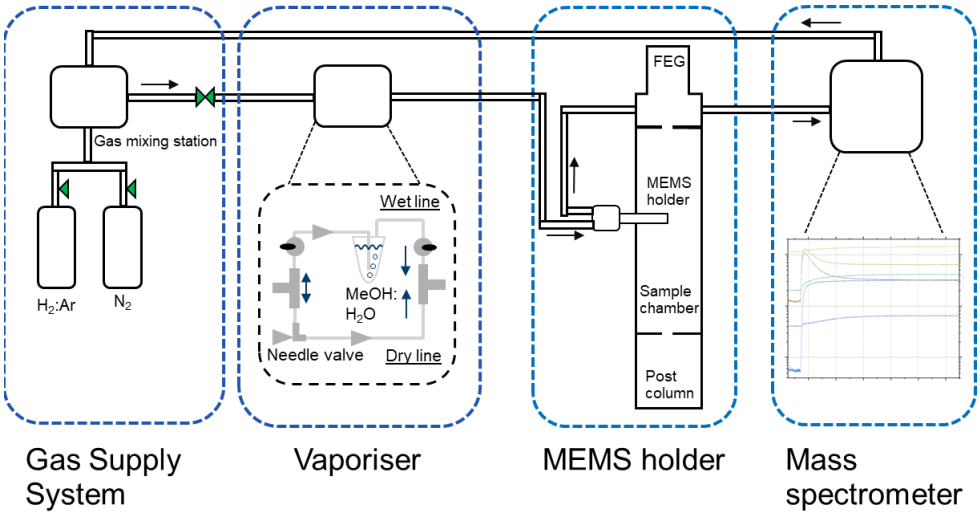

Figure 3.6: Schematic illustration of the *in situ* closed cell configuration consisting of a gas supply system, a vaporiser, a MEMS holder inside a TEM and a mass spectrometer.

Experiments that require the use of the Climate™ system can generally be conducted on any transmission electron microscope, as long as it has a suitable stage and pole piece gap. In this

work, all *in situ* gas experiments using the closed cell configuration were performed on a Titan 80-300 TEM (ThermoFisher Scientific, Waltham, MA, USA)[196]. The transmission electron microscope exhibits a field emission gun (FEG) and an image corrector for spherical aberrations. It was operated at 300 kV and has an information limit < 100 pm at 300 kV[196].

3.2.3 Energy-Dispersive X-ray Spectroscopy

Energy-dispersive X-ray spectroscopy (EDX) is an analytical method that employs electron microscopy to examine the chemical composition of a material.[197,198] In EDX, inelastic interaction of the electron beam with the electron shell of the investigated material triggers the emission of characteristic X-rays.

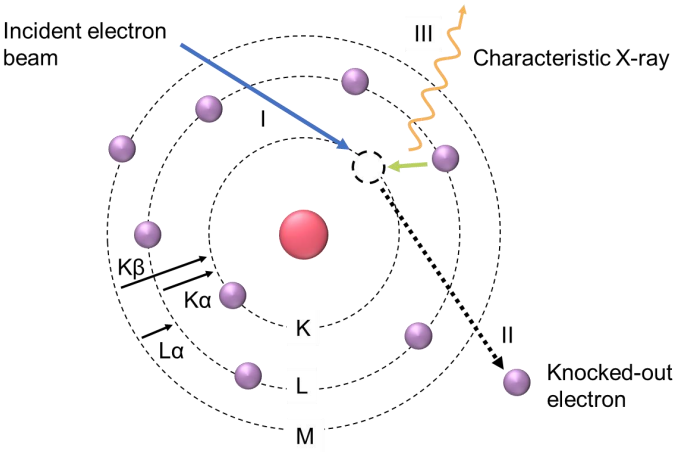

Figure 3.7: Schematic illustration of the inelastic interaction between an electron beam and an electron shell during EDX. The incident electron beam interacts with a shell electron (I), which is excited and subsequently knocked out of its ground state (II), generating an electron hole. An electron from an upper energy level replenishes the hole and emits a photon with an energy ΔE (III), which represents the energy difference between the levels. Such photons are detected during EDX and allocated to an element. Kα, Kβ and Lα transitions are displayed as illustration.

The incident electron beam excites and thus knocks out a shell electron from its ground state, thereby generating an electron hole on that energy state. In order to restore the energetically most favourable state, an electron from an upper energy state will replenish the generated hole. As a result, a photon is emitted with an energy ΔE, which is equivalent to the energy difference between the upper and lower state. The transitions are named after the shell in which the hole is generated and the shell the replenishing electron is from. For instance, the transition from the L to K shell emits Kα radiation with a discrete photon energy, which is characteristic for the specific element. EDX is primarily a qualitative analysis, although it can also provide

quantitative data on chemical compositions with an accuracy of a few weight percentages. The detection of light elements with an atomic number below 5 is typically not feasible with EDX. Figure 3.7 illustrates schematically the inelastic interaction between incident electron beam and electron shell. Given that X-ray emission is locally triggered by an electron probe, the scan of the probe over the sample, as it is conducted during STEM, allows for the acquisition of an elemental map. This is achieved by the probe scanning the sample and the subsequent reconstruction of the signal at each location. [197,198]

In the present experimental setup, an AztecEnergy EDX system (Oxford Instruments, Abingdon, United Kingdom) with 2 Ultim Max TLE detectors with a solid angle of ≤ 2 sr was applied.

3.3 Electron Beam Dosimetry

Many materials are highly sensitive to electron beam radiation, which is why it is crucial to quantify the electron dose to which the sample is exposed during STEM experiments. The electron dose per frame D_f in STEM experiments was determined according to Egerton[199] (eq. 3.2).

$$D_f = \left(\frac{I_b}{A}\right) \cdot t_f \qquad 3.2$$

Where t_f is the frame time, I_b the beam current and A the frame area on the sample. A frame time of 20 s was applied using the HF5000 and the frame area is set by the magnification. The beam current depends on the selected aperture and column operation mode, as illustrated in Table 3.2. As the HF5000 has a cold FEG, whose current decreases over time, the values should be considered a guideline only.

Column operation	Apt.1	Apt. 2	Apt. 3	Apt. 4	Apt. 5	Apt. 6
UHR	197.1	10.8	8.9	6.3	4.6	0.9
HR mapping	1421.8	70.6	60.8	42.4	28.1	5.4
HR	3056.6	158.4	133.9	84.6	56.5	11.8
Normal	13295.3	673.5	560.1	393.3	251.9	47.8

Table 3.2: Beam currents given for different column operation modes and apertures in pA. The diameter of the apertures decreases with number. HR mapping and HR modes with apt. 3 and 4 were used most frequently during STEM experiments. Beam currents were measured with a Faraday cup shortly after flashing the cold FEG.

Since HR mapping and HR mode were most frequently used with aperture 3 and 4, some exemplary dose values are calculated with these settings using eq. 3.2. Magnifications between

500k x and 1200k x will be termed “high” and between 50k x and 200k x are considered “medium” magnifications. Table 3.3 provides the upper and lower limits of beam doses for medium and high magnifications. Medium magnifications generate a dose per frame in the range of 10^5 - $10^7 e^-/Å^2$, while high magnifications have a frame dose range of 10^7 - $10^8 e^-/Å^2$.

Column operation	Aperture	High [$e^-/Å^2$]		Medium [$e^-/Å^2$]	
		500k	1200k	50k	200k
HR mapping	3	$3.7 \cdot 10^7$	$21.2 \cdot 10^7$	$3.7 \cdot 10^5$	$59.4 \cdot 10^5$
	4	$2.5 \cdot 10^7$	$14.8 \cdot 10^7$	$2.6 \cdot 10^5$	$41.4 \cdot 10^5$
HR	3	$8.1 \cdot 10^7$	$46.7 \cdot 10^7$	$8.2 \cdot 10^5$	$130.7 \cdot 10^5$
	4	$5.1 \cdot 10^7$	$29.5 \cdot 10^7$	$5.2 \cdot 10^5$	$82.6 \cdot 10^5$

Table 3.3: Overview of electron beam doses shown for different column operation settings and apertures.

4 Calcination of Palladium Nitrate Supported on Zinc Oxide Using In Situ Scanning Transmission Electron Microscopy

The contents of the forthcoming chapter were published on 16 May 2024 in the journal 'Small Science' under the title 'In Situ Scanning Transmission Electron Microscopy Calcination of Palladium Nitrate Supported on Zinc Oxide'[200]. The following contributions were made by the co-authors Marc Heggen, Rafal E. Dunin-Borkowski and Marc Armbrüster: M.H. contributed to the planning of the experimental work, participated in discussions and undertook proofreading of the manuscript; R.D.B. supported discussions and proofreading of the manuscript; M.A. prepared the samples under investigation, conducted the XRD and DTA/TG measurements and contributed to the planning of the experimental work, discussions and proofreading of the manuscript. All other contributions, e.g. reviewing the literature, planning and preparation of the experimental work, execution of the STEM experiments, data analysis, preparation of the manuscript and figures, and incorporation of the reviewers' comments, were made by the author of this thesis. All figures are reproduced with permission.

Calcination is the process of heating a chemical substance in an oxygen-containing atmosphere to remove volatile components and impurities such as carbonates or nitrates. Calcination treatments are critical in the preparation of many supported, metallic nanoparticles.[201–204] The selected calcination parameters have a strong effect on the properties of the nanoparticles. Composition, morphology, size and crystal structures can be affected by calcination. Since such metallic nanoparticles are often employed as catalysts and their properties are crucial for their catalytic performance, the calcination of nanoparticles plays a pivotal role for their catalytic performance. Consequently, calcination of nanoparticles has been the subject of several studies in the past.[205–209] The vast majority of the studies have investigated the post-reaction states after calcination. However, such *ex situ* studies do not resolve intermediate states and the dynamic behaviour of the system during calcination. Environmental scanning transmission electron microscopy (E-STEM) is well suited to investigate the *in situ* state of nanoparticles, as it combines the required spatial resolution with the reactive gas atmosphere and temperature. To date, only very few studies have utilized *in situ* STEM to study calcination phenomena.[210–217]

In a study conducted by Epicier *et al.*[211], the calcination and reduction of Pd nanoparticles on δ-alumina were examined at temperatures between 150 and 450 °C using E-STEM. The findings of their study indicated that particle mobility is limited at calcination temperatures below 450 °C, with the observed size increase mainly attributed to Ostwald ripening. Moreover, the authors demonstrate that E-STEM is an effective method for investigating the *in situ* evolution of nanoparticles. In an *in situ* TEM study, Zhang *et al.*[217] demonstrate the structural change in supported palladium-ceria core-shell nanoparticles at calcination temperatures between 500 and 800 °C. At 500 °C, the researchers report the separation of single Ce atoms from smaller nanoparticles, resulting in the formation of non-crystalline "clouds". At 650 °C,

such clouds underwent a restructuring process, forming clusters that were anchored to neighbouring nanoparticles. Fiordaliso *et al.*[216] employed environmental TEM to investigated the morphological changes of $GaPd_2$ nanoparticles supported on SiO_2 during calcination at 260 °C and reduction at 550 °C. The environmental TEM studies demonstrate that the size and distribution of the intermetallic nanoparticles, which are frequently used in CO_2 hydrogenation reactions, were determined upon calcination. During reduction and hydrogenation, no significant change was observed. All of aforementioned papers report features that can only be unravelled *in situ*. This emphasises the necessity for *in situ* TEM investigations to gain a comprehensive understanding of the dynamic changes of supported nanoparticles during calcination.

A highly interesting material system prepared by a preceding calcination step consists of the intermetallic compound ZnPd, which is supported on ZnO. This material system displays excellent catalytic properties in a number of heterogeneous catalysis reactions, including methanol steam reforming (MSR)[42], the reverse water-gas-shift reaction (RWGS)[218] and selective hydrogenation reactions[97–99]. It is anticipated that the calcination parameters will have an influence on the nanostructure of the supported particles, although this has not been examined in any great detail, nor under *in situ* conditions.

The present systematic study aims to gain a deeper understanding of the structural changes that occur in palladium nitrate supported on zinc oxide in a calcinating environment, and to elucidate the impact of these changes on particle morphology and chemical properties. Palladium nitrate is subjected to *in situ* heating from 100 to 500 °C at 1.5 Pa oxygen pressure using E-STEM. The material system is investigated simultaneously at the nanoscale level, with transformation processes such as agglomeration and decomposition studied as a function of the corresponding parameters during the calcination process. Furthermore, the high temperature behaviour of supported PdO/ZnO is studied by heating the sample in vacuum up to a temperature of 800 °C employing *in situ* STEM. The E-STEM capabilities employed facilitate the precise determination of material properties, including the decomposition temperature of palladium nitrate and zinc oxide. *Ex situ* experiments are conducted under identical calcination temperatures and dwell times but higher oxygen pressures to investigate the influence of the pressure difference and the predictive power of the E-STEM experiments. In light of these findings, the objective of this study is to provide guidance for the enhancement of control over the preparation of PdO nanoparticles and their size.

4.1 Experimentals

Palladium nitrate samples with varying loadings were prepared following the synthesis protocol outlined in chapter 3.1.1. TEM samples of $Pd(NO_3)_2$ supported on ZnO (3 and 5 wt.-% loading)

were prepared using two different methods. For the dry preparation method, the palladium nitrate powder was collected using a dropper tip and gently blown on a MEMS heating chip. The sample's proper placement on the chip, particularly on the SiN windows of the MEMS heating chip, was then confirmed using an optical microscope, as shown in Figure 11.2. If the catalyst powder was not properly positioned on the transparent windows or heating spiral, the process was repeated. The HTN-101H MEMS heating chips were supplied by Norcada Inc., Edmonton, Canada.

For the wet preparation method, the sample powder was mixed with ultra-pure water and suspended by shaking. A 10 µl tip on an Eppendorf pipette was used to transfer the suspension onto a MEMS chip using the drop-cast method. The sample was then dried under normal laboratory conditions. An optical microscope was used to inspect the sample, similar to the dry preparation process. Both casting methods yielded comparable sample distributions on the MEMS chip. The specimens were stored in a vacuum desiccator until needed. Prior to transitioning into the electron microscope, the specimens were treated under UV light at 10% air pressure for a period of 5 minutes and subsequently plasma cleaned for a duration of 10s in an Ar atmosphere. This process was conducted employing to instruments: a Hitachi ZONETEM II sample cleaner (Hitachi High-Technology, Krefeld), and a Fischione Instruments 1020 plasma cleaner (E.A. Fischione Instruments Inc., Export, USA)[219].

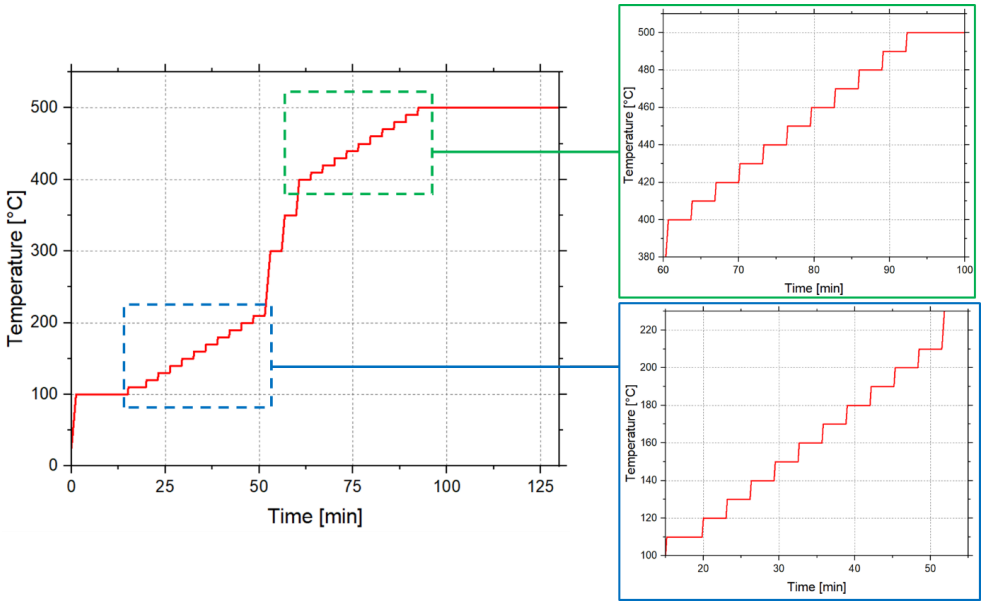

Figure 4.1: Heating profile of the *in situ* calcination E-STEM experiment, heating regions of interest and image times are enlarged.

The in situ calcination experiment was conducted using E-STEM on a Hitachi HF5000 operating at 200 kV. Detailed specifications of the instrument are given in chapter 3.2.1. The specimens were subjected to a specific heating profile which is shown in Figure 4.1. First, the temperature was increased from room temperature to 100 °C and held for 15 minutes. Subsequently, the temperature was risen by increments of $\Delta T = 10\,°C$ and maintained for a period of 3 minutes, until 210 °C was reached. Subsequently, the temperature was increased to 400 °C, maintained at 300 °C and 350 °C for a duration of 3 minutes between each increment. In the temperature range between 400 °C and 500 °C, the temperature profile was controlled in a manner analogous to that employed between 100 and 210 °C. Subsequently, the sample was heated at 500 °C for a period of 30 min. A heating rate of $r_{heating} = 1\,°C/s$ was applied for every heating step. Ultra-pure oxygen (99,99%) was introduced into the microscope column with a mass flow rate of $\dot{m} = 1\,sccm$ resulting in a column pressure of $p_{column} = 2{,}0 \cdot 10^{-2}\,Pa$ and a corresponding specimen pressure of $p_{specimen} = 1{,}5\,Pa$. The TEM in situ calcination was repeated three times. The decomposition of ZnO was studied under the following conditions: The sample was heated in vacuum continuously from 500 to 650 °C, with a dwell time of 3 min at 600 °C. The temperature was increased in 10 °C increments between 650 and 800 °C, with each increment held for 3 min. A heating rate $r_{heating} = 1\,°C\,s^{-1}$ was applied during every heating ramp. An illustration of the heating ramp is provided in Figure 11.11.

4.2 Results of In Situ Calcination of Supported Palladium Nitrate

Decomposition of Palladium Nitrate – Calcination Temperature between 100 and 200 °C

Figure 11.3 shows XRD measurements of sample with different palladium loadings. All reflexes can be assigned to ZnO, thereby identifying the support of the system. Accordingly, no XRD signal could be attributed to any particular Pd species. Figure 4.2 shows an E-STEM image series of a cluster of palladium nitrate nanoparticles supported on zinc oxide recorded during an *in situ* heating experiment from 110 to 210 °C in an oxygen atmosphere at 1.5 Pa. BF images, DF images and corresponding FFT are shown. Further results are displayed in Figure 11.4. This heating sequence was continued up to 500 °C at the identical sample location illustrated, as shown in Figure 4.7 and Figure 11.8. At 110 °C, the palladium nitrate nanoparticles are attached to the ZnO support. Palladium nitrate forms dense clusters of nanoparticles that strongly attach to both the ZnO support and neighbouring nanoparticles. Single nanoparticles within the cluster can still be identified. The cluster is coated by an amorphous surface layer. A comparison between dark DF and SE images, as shown in Figure 4.3, indicates that most particles can be located on the support surface.

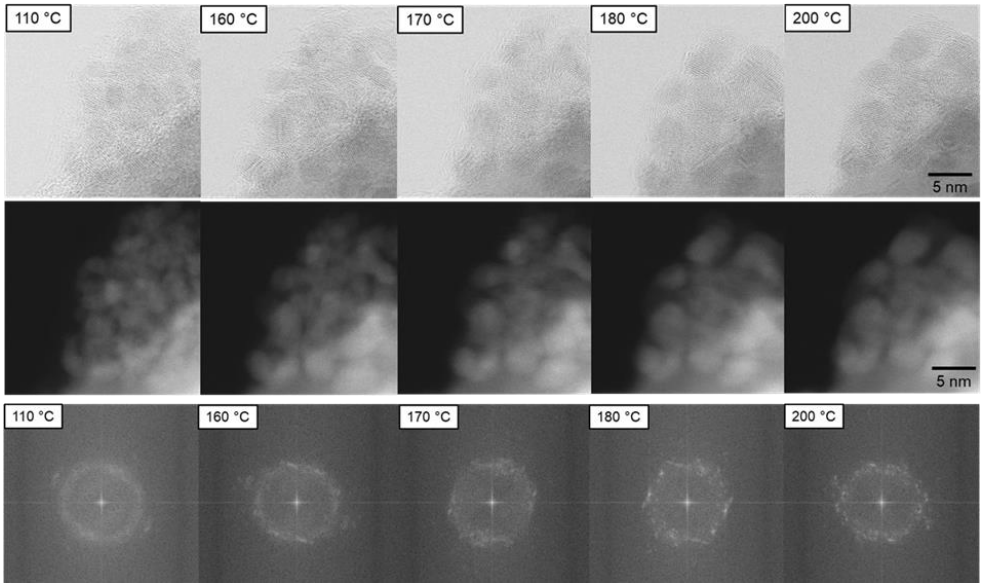

Figure 4.2: E-STEM image series of the *in situ* calcination of $Pd(NO_3)_2$/ZnO in oxygen. Upper row: BF image series; middle row: corresponding DF image series; lower row: FFT series of corresponding particle cluster. New reflections appear at temperatures > 170 °C. Figure is taken with permission from reference[200].

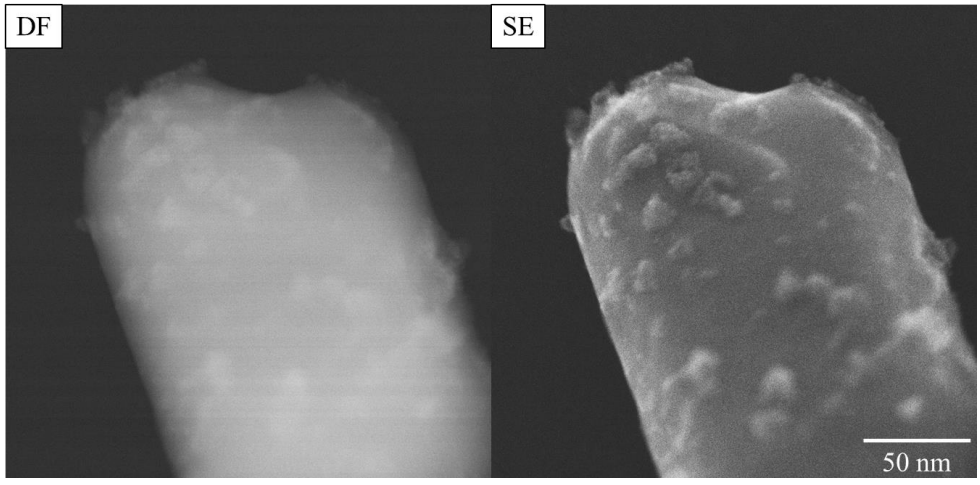

Figure 4.3: The DF and SE images of the support-particle structure between $Pd(NO_3)_2$ and ZnO at room temperature are in correspondence, indicating that the majority of the particles is located on the surface. Figure is taken with permission from reference[200].

The particle size is determined by measuring the diameter with two perpendicular lines. To ensure consistency in the analysis, only those structures that are clearly visible in the DF and crystalline in the BF are considered for comparison. The diameters are averaged and the standard deviation is calculated as the error. Figure 4.4a shows the mean diameter as a function of temperature. At 110 °C, the mean size is $d_{110} = 2{,}4 \pm 0{,}9\ nm$. The relatively high standard deviation is attributed to the fact that fewer than 30 particles are examined. The morphology of the particles and support material remains unchanged until ~160 °C.

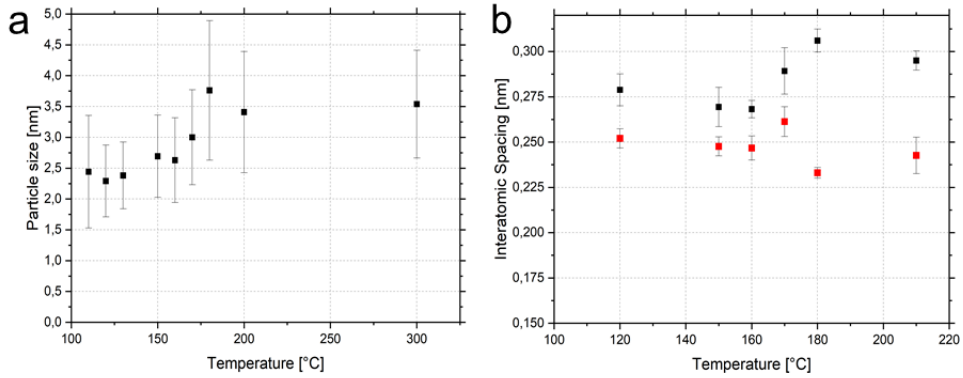

Figure 4.4: Particle size evolution versus temperature, particle diameter was measured along two perpendicular lines (left); b) Interatomic distances along two directions (right). Figure is taken with permission from reference[200].

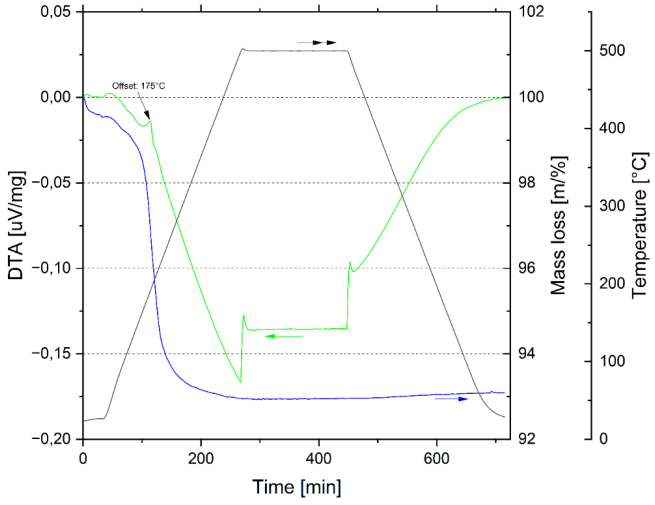

Figure 4.5: DTA signal (green), the mass loss (blue) and temperature (black) are plotted as a function of time. The endothermic offset is indicated at 175°C. Figure is taken with permission from reference[200].

At elevated temperatures, initial microstructural changes emerge: The aggregation of nanoparticles occurs at a slow rate, resulting in an increase in average particle size to 2.6 ± 0.7 nm at 160 °C and 3.4 ± 1 nm at 200 °C, as shown in Figure 4.4a. In the temperature range between 160 and 180 °C, a notable increase in particle size is observed. Interestingly, an additional increase in temperature up to 300 °C does not result in a further increase in particle size; the average particle size remains at 3.5 ± 0.9 nm. The temperature range of the size increase corresponds to the decomposition temperature of $Pd(NO_3)_2$ found in the DTA measurement, which is displayed in Figure 4.5. The DTA results show the presence of an endothermic signal at ~175 °C and an endothermic shoulder from 165 to 200 °C. These temperatures are in accordance with those measured in the *in situ* STEM experiment. An additional indicator of the phase transformation from $Pd(NO_3)_2$ to PdO is the alteration of the interatomic spacings of a particle, which is monitored in two directions while heating as illustrated in Figure 4.4b. The directions and labels are provided in Figure 11.5. A comparable behaviour is evident in this instance: The interatomic spacings remain unchanged at $g_{120\,°C} = 2{,}8\ \pm 0{,}1$ Å and $h_{120\,°C} = 2{,}5\ \pm 0{,}1$ Å below 170 °C.

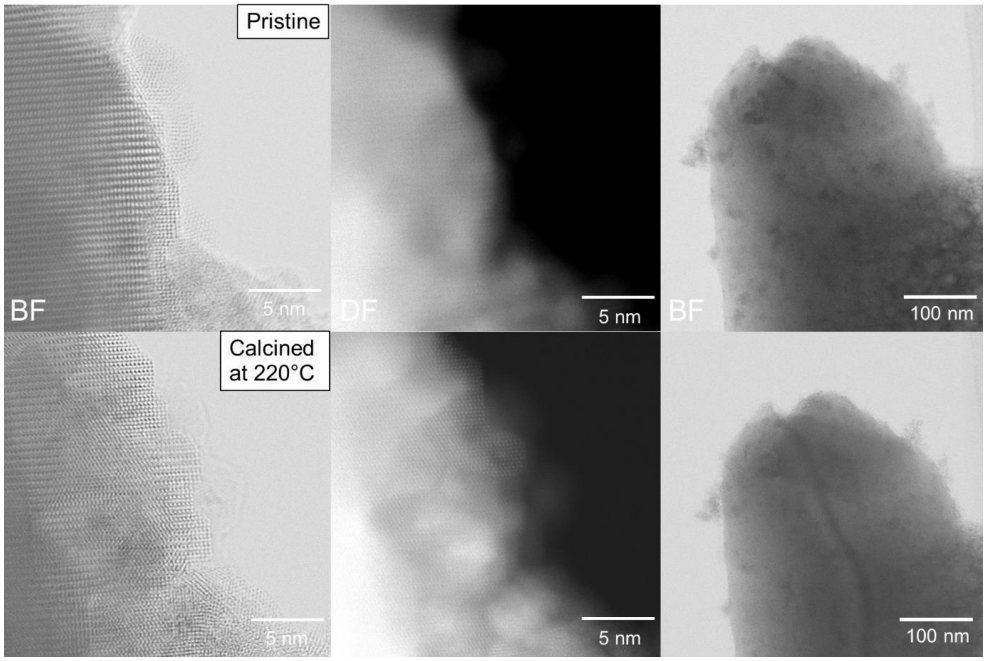

Figure 4.6: BF and DF images of pristine sample (top row) and the identical location after calcination at 220 °C in the E-STEM (bottom row). The locations were not exposed to the electron beam during the *in situ* calcination experiment and were imaged solely prior to and following the reaction in vacuum at 60 °C. Figure is taken with permission from reference[200].

The complex crystal structure of palladium nitrate and the uncertain quantity of water present pose significant challenges to the clear assignment of interatomic spacings. However, the lattice spacings may correspond to anhydrous $Pd(NO_3)_2$ (1 1 -3) lattice parameter of 2.39 Å, (1 -2 0) of 2.47 Å, (1 0 -3) of 2.56 Å and (0 2 1) of 2.77 Å.[220] For a hydrate crystallite, the $Pd(NO_3)_2 \cdot 2(H_2O)$ (1 3 1) lattice spacings of 2.80 Å, (0 4 1) of 2.58 Å, (0 2 4) of 2.56 Å, (1 0 4) of 2.52 Å, (2 0 0) of 2.50 Å, (1 1 4) of 2.46 Å and (0 4 2) of 2.41 Å are close to the measure lattice spacings.[221] At temperatures T > 170 °C, the spacings in direction g increase to $g_{210°C} = 3{,}0 \pm 0{,}1$ Å, while direction h shrink to $h_{210°C} = 2{,}3 \pm 0{,}1$ Å most likely corresponding to the PdO (100) lattice planes with 3,04 Å and (110) with 2,15 Å.[222]

The findings are corroborated by the corresponding Fast Fourier Transformation (FFT) images of the particle cluster shown in Figure 4.2. During the heating treatment, the initial continuous, diffuse FFT ring, indicative of the presence of an amorphous phase, changes into sharp spatial frequencies above the transformation temperature (T > 170 °C). This change indicates the formation of a new crystalline structure.

In order to evaluate the electron beam effect on the system during calcination, a reference location was only imaged before and after the introduction of reactive conditions. Figure 4.6 shows such reference locations following a calcination treatment at 220 °C. The observed changes in the structure of the reference locations are consistent with the results obtained through *in situ* observation. After the calcination treatment, nanoparticles exhibit a higher DF and BF signal and increase in size.

Stable Calcination - Calcination Temperature between 200 and 400 °C

Figure 4.7 provides an overview of the morphology of the PdO/ZnO system over the temperature range between 200 and 400 °C.

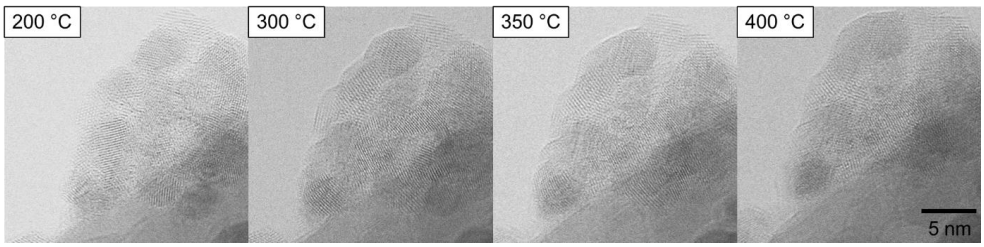

Figure 4.7: A series of BF E-STEM images were recorded over a temperature range of 200 to 400 °C. The morphology of the PdO/ZnO particles was found to be largely unaffected by the temperature rise. However, a small increase in size of individual nanoparticles was observed at higher temperatures. Figure is taken with permission from reference[200].

At this temperature range, most PdO nanoparticles demonstrate no notable increase in size. However, isolated cases of growth in size are observed. Measuring this slight growth is difficult because the nanoparticles are closely packed and lack clear boundaries. The ZnO support resists any decomposition or morphological changes. Figure 4.8 shows the surface evolution of the system during calcination between 300 and 400 °C at a lower magnification. As illustrated in Figure 4.8, remote nanoparticles exhibit no significant growth. The SE signal of the nanoparticles increase with temperature. To conclude, the structure and morphology of the PdO/ZnO system is largely unaffected by the temperature rise from 200 to 400 °C.

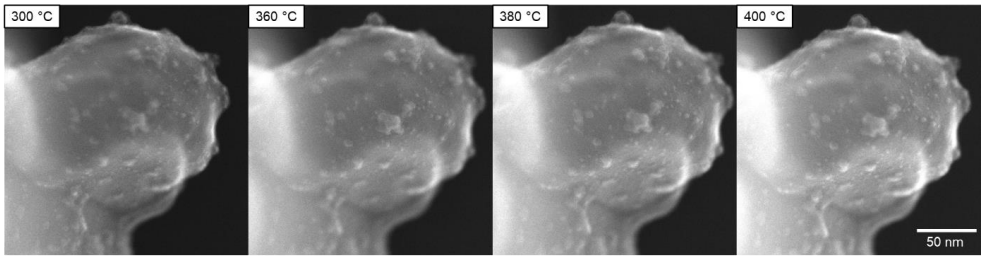

Figure 4.8: A series of SE images was captured at different heating steps between 300 °C and 400 °C. No particle movement or agglomeration was observed. Figure is taken with permission from reference[200].

Agglomeration of Nanoparticles and Nanorod Formation - Calcination Temperature between 400 and 500 °C

Figure 4.9 illustrates the E-STEM results obtained from an *in situ* calcination experiment performed at 1.5 Pa oxygen pressure between 300 and 500 °C. Three ROIs, indicated by green circles, demonstrate the evolution of PdO nanoparticles during the calcination treatment. Within this temperature range, structural changes in the PdO/ZnO system begin to occur. A detailed examination of the surface during heating first reveals particle movement, rounding, and agglomeration at temperatures between 450 and 460 °C. At 450 °C, the PdO nanoparticles depicted in Figure 4.9 exhibit a rough and irregular surface. Figure 4.10 illustrates the structural changes of a representative nanoparticle at 460 °C. Over 33 s, surrounding nanoparticles migrate across the surface in the direction of the highlighted particle. Over the next 30 s, the particles proceed to agglomerate, forming a larger particle that becomes increasingly rounder due to a relative reduction in the surface area (at 63 s). This agglomeration process changes the particle shape from irregular to a compact, rounded form. Notably, the alteration of the particles' morphology is almost complete within the initial 90 s of exposure at 460 °C. Following this rapid initial change, the particle morphology remains stable.

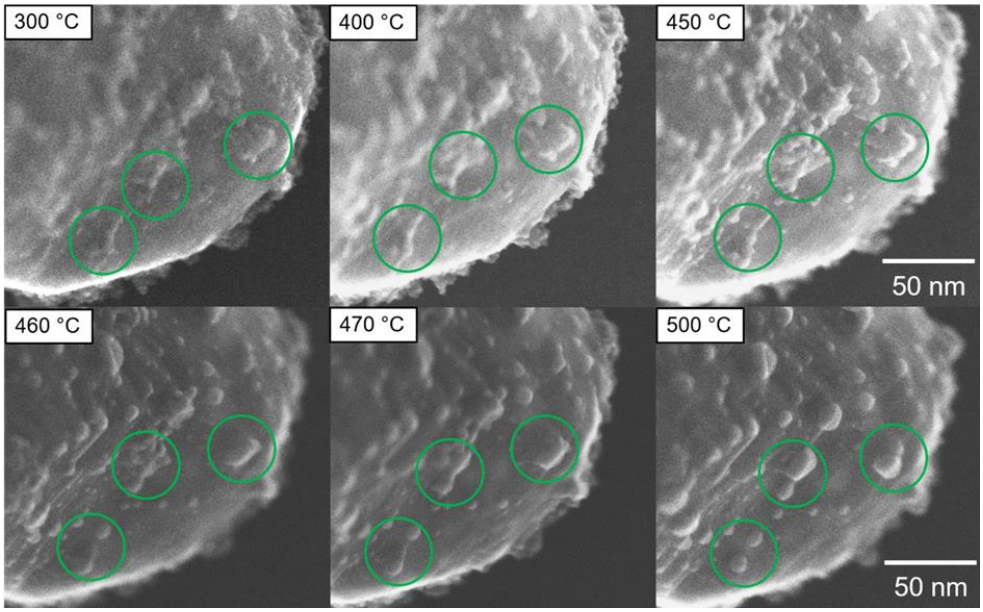

Figure 4.9: The SE E-STEM image series illustrates the structural changes that occur as a result of the temperature rise during the heating treatment between 300 and 500 °C. The areas of interest are indicated by green circles. Figure is taken with permission from reference[200].

It is observed that with each incremental increase in temperature, the aforementioned particle changes occur, resulting in a discontinuous and step-like evolution of the particle-support morphology. At 500 °C, the majority of the nanoparticles display a spherical morphology and have increased in size, which results in a reduction in specific surface area. In some cases, isolated nanoparticles of a smaller size are present. The analysis reveals that 35 nanoparticles measuring less than 5 nm exhibited an approximate distance to their closest neighbours of $d_{neigh} = 5.6 \pm 2.4\,nm$. This is distinctly larger than the mean approximate particle distance at 400 °C. In qualitative terms, this distance is dependent on the temperature and size of the particle, as well as on the sizes of the neighbouring nanoparticles and the support morphology. *Ex situ* calcination experiments were conducted at ambient air pressure at 500 °C with a 180 min dwell time. PdO loadings of 1, 3 and 5 wt.-% on ZnO were calcined under identical conditions. Representative SE images of these samples and their particle size distributions are shown in Figure 4.11. Particle size histograms for the corresponding loadings are present in Figure 11.6. At 500 °C and 3% loading, the mean particle size is $d_{3\%,500} = 8.3 \pm 4.2\,nm$. It

is noteworthy that the 1% and 5% loadings exhibit comparable mean particle sizes at 500 °C, with $d_{1\%,500} = 8.3 \pm 4.4\ nm$ and $d_{5\%,500} = 7.6 \pm 2.5\ nm$.

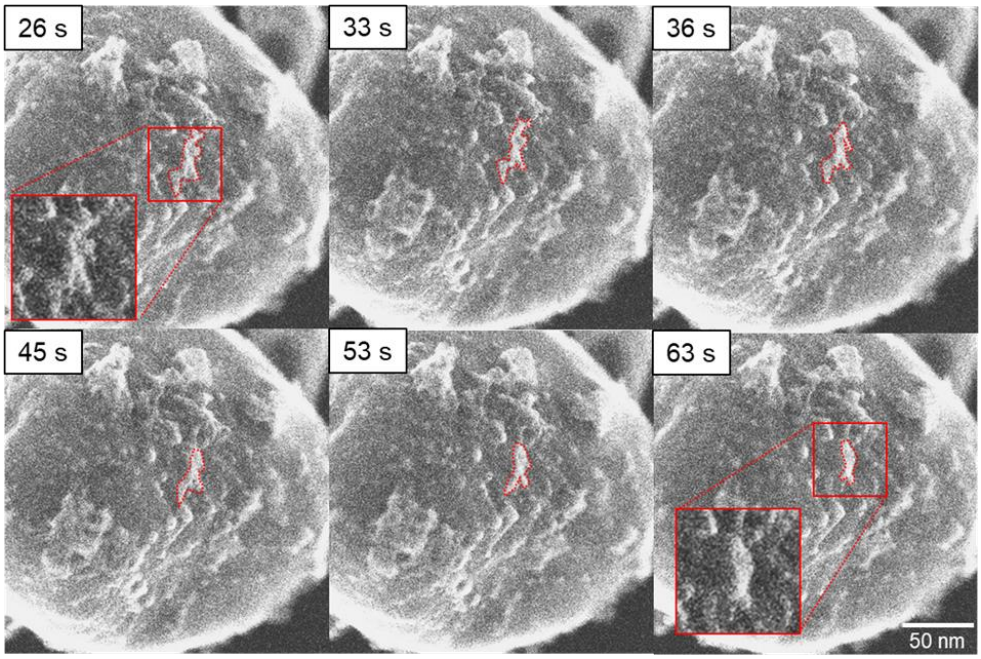

Figure 4.10: The SE E-STEM image series depicts the process of particle merging at 460 °C in an oxygen environment. The time stamps indicate the period after 460 °C was reached. The red dotted lines mark a group of selected particles, illustrating the dynamics of their movement and agglomeration of these particles over time. The insets provide a magnified view of selected regions of interest. Figure is taken with permission from reference[200].

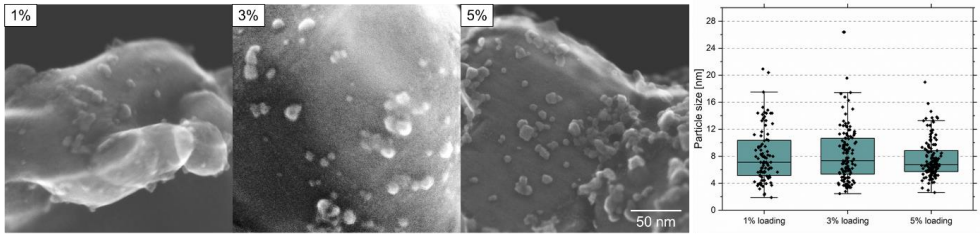

Figure 4.11: The SE images on the left illustrate the impact of varying PdO/ZnO loadings (1%, 3%, 5%) on calcined samples at 500 °C for 180 minutes under ambient conditions. The plot on the right illustrates the corresponding particle size distribution. Figure is taken with permission from reference[200].

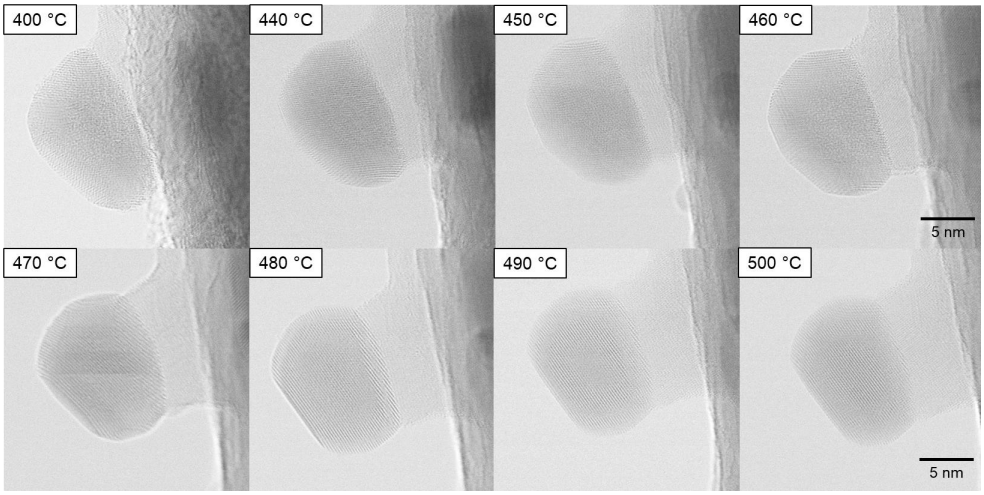

Figure 4.12: Series of high-resolution BF images of a single particle undergoing structural evolution as a result of heating from 400 to 500 °C. The formation of a nanorod occurs beneath the nanoparticle. Figure is taken with permission from reference[200].

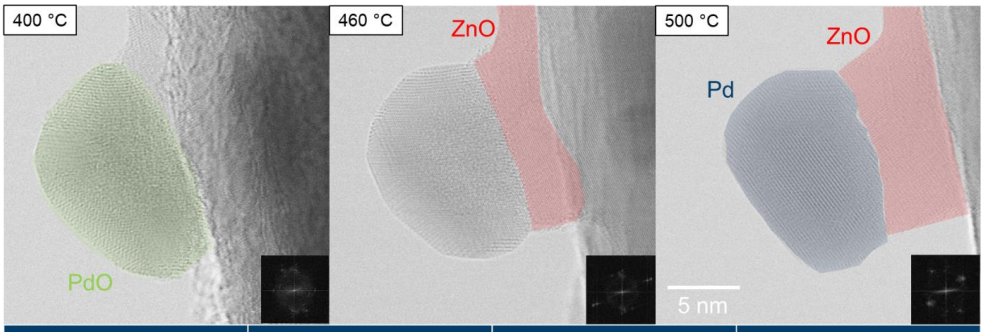

Position	400°C	460°C	500°C
Particle [Å]	2.2 ± 0.1	1.2 ± 0.1	2.2 ± 0.1
Neck [Å]	/	1.3 ± 0.1	1.9 ± 0.1
PdO (110) – 2.15 Å	Pd (111) – 2.25 Å	ZnO (002) – 2.61 Å	ZnO (102) – 1.91 Å

Figure 4.13: Phase identification via determination of lattice spacings. Corresponding FFT images are shown in Figure 11.9. PdO (110) is highlighted in green, ZnO (002) and (102) in red, Pd (111) in blue. The lattice parameters are taken from reference[222,223]. Figure is taken with permission from reference[200].

In addition to the agglomeration kinetics discussed above, the calcination process was examined at high magnification to show the structural evolution on the atomic scale between 400 and 500 °C at 1.5 Pa oxygen pressure. Figure 4.12, Figure 11.7 and Figure 11.8 illustrate the morphological evolution of the nanoparticles. As illustrated in Figure 3.12, the PdO

nanoparticle is polycrystalline and is attached to a flat ZnO support edge at 400 °C. During the heating treatment, the PdO nanoparticle undergoes a restructuring process, forming surface facets at 460 °C, and developing a single-crystalline structure. This is evidenced by a change in FFTs, as illustrated in Figure 11.9.

At 400 °C, the lattice spacing of the particle is $d_{particle,400} = 2.2 \pm 0.1$ Å, which corresponds to PdO (110) with $d_{PdO} = 2.15$ Å[222] highlighted in green in Figure 4.13. At 460 °C, the measured lattice spacing decreases to $d_{particle,460} = 1.2 \pm 0.1$ Å, which is indicative of a mixed phase during the transformation to metallic Pd. At 500 °C, the lattice spacing of the nanoparticle is $d_{particle,500} = 2.2 \pm 0.1$ Å, which is in close agreement with that of Pd (111), which has a lattice spacing of $d_{Pd} = 2.25$ Å[223], indicating that PdO is converted to fcc Pd.

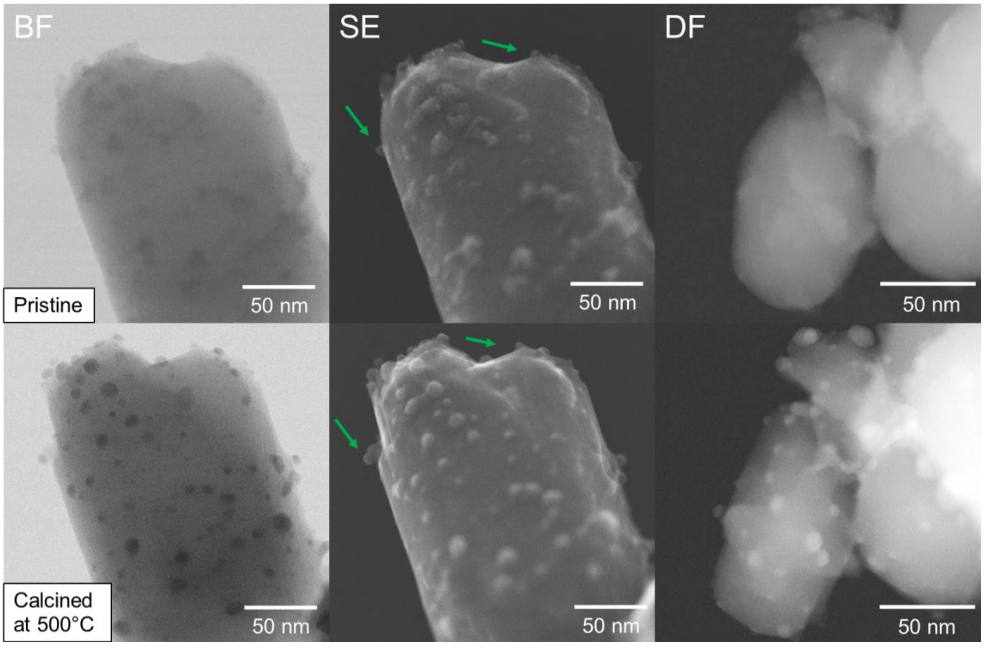

Figure 4.14: BF, SE and DF images of a pristine sample (top row) and the identical location after calcination at 500 °C in the E-STEM (bottom row). The illustrated reference locations were not exposed to the electron beam during the in situ calcination experiment and were imaged only before and after the reaction in vacuum at room temperature. The green arrows indicate locations where ZnO nanorods formed. Figure is taken with permission from reference[200].

In order to evaluate the effect of the electron beam, reference locations were imaged before and after calcination at 500 °C, allowing for a comparison of the pre- and post-calcination states. Figure 4.14 shows BF, SE and DF images of such reference locations. The nanoparticles exhibit

a more pronounced BF and DF contrast following calcination, indicating a change in composition and/or an increase in thickness. In general, a growth of the nanoparticles compared to the pristine ones can be observed. At specific locations, nanorods are formed during calcination, as indicated by the green arrows in Figure 4.14. A formation of nanorods is also shown in Figure 11.10.

Decomposition of Zinc Oxide - Calcination Temperature between 500 and 800 °C

After *in situ* calcination, the high temperature behaviour of supported PdO/ZnO was studied by using *in situ* STEM during heating in vacuum at a pressure of $< 10^{-4}$ Pa. The sample was heated continuously from 500 to 650 °C, with a dwell time of 3 min at 600 °C. Subsequently, the temperature was increased in 10 °C increments between 650 and 800 °C, with each increment maintained for a period of 3 minutes. A heating rate $r = 1\ °C/s$ was applied throughout each temperature change. An illustration of the heating ramp is given in Figure 11.11.

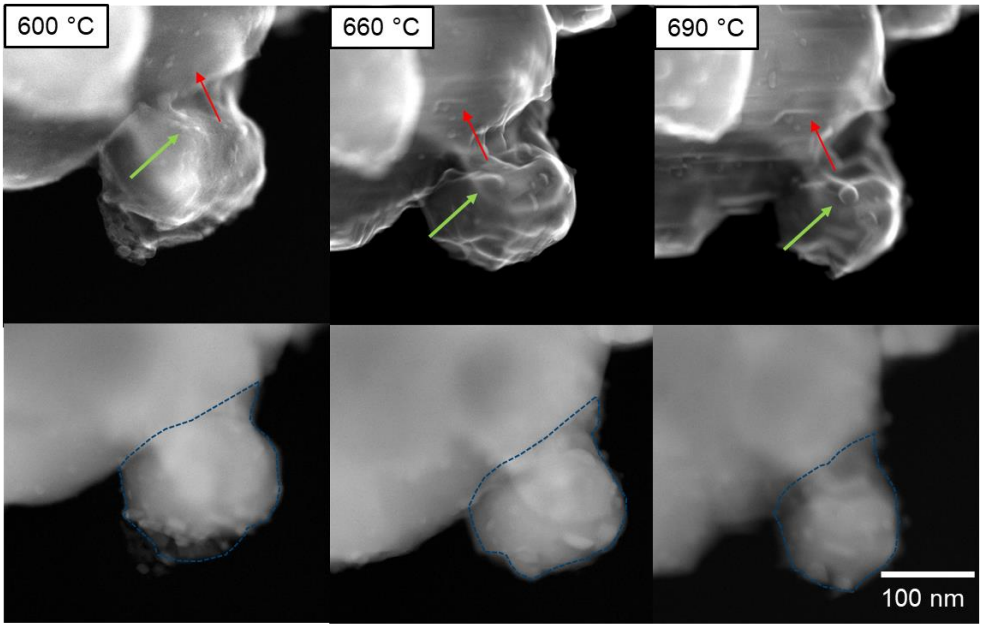

Figure 4.15: SE and corresponding DF image series of PdO/ZnO decomposition between 600 and 690 °C. The red arrow indicates faceting of the ZnO support, while the green arrows point out the agglomeration of PdO particles. The dotted blue line illustrates the shrinking of the ZnO support. Figure is taken with permission from reference[200].

Figure 4.15 provides the experimental data acquired in the temperature range between 600 to 690 °C. At 600 °C, the support-particle structure is similar to that found at 500 °C. Smaller Pd nanoparticles agglomerate to form particles with sizes of ~10 nm. The support undergoes no

decomposition and has a regular, unfaceted surface. At 660 °C, the ZnO surface starts to become faceted, as indicated by the red arrows in SE image in Figure 4.15. At a temperature of 690 °C, an increased number of facets is observed. At the same time, the ZnO support shrinks and decomposes, as marked by the dotted blue lines. As a consequence of the shrinkage of the support and an increase in temperature, the nanoparticles become more mobile and continue to agglomerate and grow in size, as illustrated by green arrows in Figure 4.15.

The morphological changes in the Pd/ZnO system that are triggered at temperatures between 700 and 790 °C are summarized in Figure 4.16. At temperatures over 700 °C, the system further destabilizes. Between 700 and 760 °C, the support decomposes, until the region of interest vanishes at around 770 °C. Smaller nanoparticles, which are more exposed to the atmosphere, disappear more rapidly. Thus, the decomposition speed of the ZnO appears to be affected by the surface, which exposed to the atmosphere. At the same temperature, Pd nanoparticles grow due to decrease in support volume. At 740 °C, Pd starts to form facets, as indicated by the red circles in Figure 4.16.

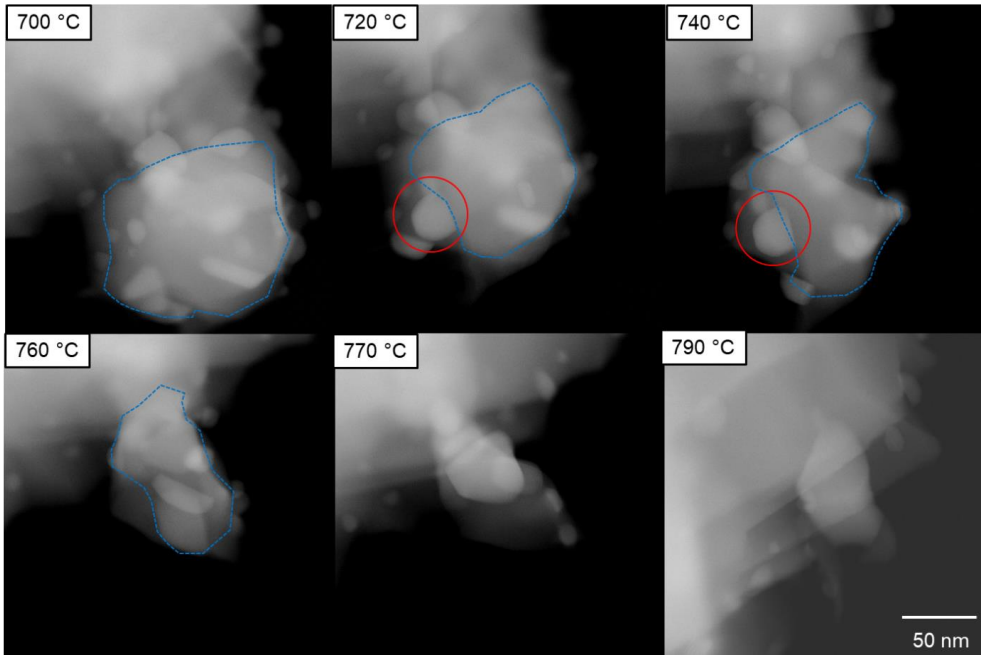

Figure 4.16: The DF image series illustrates the high-temperature properties of PdO/ZnO between 700 and 790°C. The dotted blue line highlights the shrinking of the ZnO support, while the red circles indicate the faceting of the PdO particle. Figure is taken with permission from reference[200].

4.3 Discussions

The calcination temperature has a pronounced effect on the structure and composition of supported palladium nitrate nanoparticles. Consequently, the calcination treatment can be classified into four distinct temperature ranges, each of which exhibits a particular influence on the nanoparticle system. These include the decomposition of palladium nitrate, stable calcination, the agglomeration of nanoparticles, and the decomposition of the ZnO support.

Decomposition of Palladium Nitrate

The first temperature range between 110 and 200 °C shows the decomposition of palladium nitrate. The absence of XRD peaks corresponding to any particular Pd species is based on the small crystallite size and low Pd loading of the investigated samples. The amorphous layer, observed on the surface of the pristine nanoparticles, is likely caused by contamination from residual hydrocarbons, which are adsorbed during sample preparation. Another possibility is that the layer may originate from the nitrate ligands of palladium nitrate, which is a coordination polymer. The weak DF signal of the surface layer in Figure 4.2 suggests the absence of Pd. As the amorphous layer decomposes with increasing temperature, it may be incorporated into the nanoparticle.

The initial growth in nanoparticle size can be attributed to the calcination reaction, where palladium nitrate is converted into palladium oxide. This size increase may also be driven by a reduction in surface area and hence minimisation of the free surface energy of the system. The temperature at which the size increase occurs aligns well with the DTA results. The endothermic signal found in DTA indicates the decomposition of palladium nitrate. The onset temperature of the endothermic signal (165 °C) matches the value reported by Bruns *et al.* [220] for anhydrous palladium nitrate. However, their maximum decomposition and final temperature are higher. The present thermal discrepancy likely arises from variations in morphology and heating rates. In the present *in situ* study, the crystallites are in the nm-size range, while Bruns' study involved palladium nitrate crystallites in the µm-size range. The nanoparticles possess a higher surface energy and are less stable, which promotes their decomposition and explains the lower temperatures. Moreover, Bruns *et al.* employed a heating rate of 10 K/min during the DTA measurement, which is higher than 2 K/min used in this study. Consequently, the DTA signal may be delayed and only detectable at elevated temperatures.

The combination of the results obtained from the employed characterisation methods, namely an increase in particle size, the results of the DTA measurements and FFT analysis, leads to the conclusion that palladium nitrate is decomposed at ~170 °C, accompanied by an increase in particle size and the formation of palladium oxide. A comparison between the STEM and DTA/TG results reveals only a small dependence on the O_2 pressure at which the experiments are conducted and hence a negligible pressure gap of the calcination reaction. The good

correlation between reference locations and those that were exposed to the electron beam during the calcination treatment suggests that the electron beam has a negligible effect.

Stable Calcination Window

In the temperature range between 200 and 400 °C, only those nanoparticles that were closely aggregated exhibited a slight increase in size. In the absence of particle mobility, it can be assumed that nanoparticle growth is initiated by surface diffusion and Ostwald ripening. The presence of this growth mechanism is consistent with the observation that no growth of remote nanoparticles was observed. The enhanced SE signal, which is observed for specific nanoparticles at a higher temperature, can be attributed to a facilitated emission of secondary electrons by thermal activation and thus a superior signal-to-noise ratio. The observation of only minor growth phenomena occurring at individual nanoparticles provides evidence of the stability of the system above 200 °C, and thereby supporting the assumption that the discrete increase in particle size at 170 °C is associated with the phase transformation of $Pd(NO_3)_2$ into PdO.

These findings align closely with the results of Li and co-workers[224,225]. They developed a 5 wt.-% ZnPd/ZnO(-3Al) catalyst via incipient wetness impregnation with an acetone solution of $Pd(C_2H_3O_2)_2$, for converting glycerol to 1,2-propanediol. The preparation involved a two-step calcination process: the support was first calcined at 350 °C for 5 h, followed by calcination of the impregnated material at 300 °C for 2 hours, and then reduction at 400 °C for 2 hours. The as-formed average particle size was found to be 1.4 nm for the ZnPd/ZnO(-3Al) particles and 4.5 nm for ZnPd/ZnO. These sizes are consistent with the *in situ* experimental data obtained here, despite using different precursors and conditions. The correspondence with the *ex situ* experiments conducted by Li *et al.* indicates that neither dwell times below 120 min nor temperatures below 400 °C exert a considerable effect on particle size. Furthermore, the results suggest that there is a wide stability range for the calcination process, which results in the formation of uniform, small particles. This enhances the robustness and reproducibility of the preparation process. Furthermore, these experiments demonstrate that the pressure gap of the present E-STEM calcination experiments is, if present at all, small. This is an interesting outcome, given the considerable pressure difference between the E-STEM experiments and laboratory calcination experiments. During the *in situ* TEM experiment, the O_2 pressure is around $p_{ESTEM} = 1.5\,\mathrm{Pa}$, whereas the O_2 partial pressure in ambient air is about $p_{air} = 20\,000\,Pa$. Despite the large difference between the O_2 pressure levels and thus the lower chemical potential of oxygen, the PdO nanoparticles display analogous behaviour and do not agglomerate. In light of these findings, it can be concluded that the O_2 partial pressure exerts a minor impact on the mobility of the nanoparticles.

Agglomeration of Nanoparticles and Formation of Nanorods

The results obtained from the calcination process at temperatures between 400 and 500 °C allow for the drawing of several conclusions. The nanoparticles, which were calcined *ex situ* and *in situ* at 500 °C, are significantly larger than those prepared by Li *et al.*, which were calcined and reduced at temperatures below 400 °C and exhibited an average particle size of below 4.5 nm.[224,225] Moreover, the mean particle size is only slightly affected by varying Pd loadings between 1 and 5 wt.-%. It can be concluded that a calcination temperature above 400 °C is the driving force for particle growth. The mobility of nanoparticles at the surface of the ZnO support at temperatures above 460 °C, as observed in the *in situ* TEM calcination experiments, suggests that agglomeration is most likely a main mechanism for nanoparticle growth. In the case of closely spaced and aggregating nanoparticles, where surface diffusion is energetically favourable, Ostwald ripening cannot be excluded as mechanism for particle growth. This hypothesis is supported by Epicier *et al.*[211], who observed Ostwald ripening as a mechanism for particle growth during the calcination of palladium nitrate on δ-alumina at temperatures of up to 450 °C. Given that 400 °C represents the onset temperature for the decomposition of PdO nanoparticles in an oxygen atmosphere[226,227], it can be concluded that the underlying reason for the observed change in morphology is the initiation of atomic mobility in PdO. The observed correspondence between *ex situ* and *in situ* experiments highlights the small "pressure gap". These findings suggest that calcination temperatures should not exceed 400 °C, when aiming at small particles. The resulting small and well-dispersed nanoparticles have a high active surface area, and are promising to have a good catalytic performance and high mass activity.

By combining the micro- and macroscale effects, it can be demonstrated that PdO decomposition is associated with enhanced particle mobility and agglomeration, which result in an increase in particle size. Following the decomposition of PdO nanoparticles, a neck forms between the nanoparticles and the support. At 460 and 500 °C, the crystal of the neck correspond to the interatomic spacings of ZnO (002) and ZnO (102), thereby confirming the identification of hexagonal wurtzite ZnO, which is the typical ZnO nanorod structure[228,229]. This phenomena is likely triggered by the O_2 atmosphere and elevated temperature and is known as catalytic formation of ZnO nanorods[230–234]. The observed formation process of ZnO nanorods under the present experimental conditions can be explained as follows[200]: In the presence of a low partial pressure of oxygen, ZnO may be partially reduced to form oxygen-deficient Zn_xO ($x > 1$). The mobility of $Zn^{\delta+}$ increases due to the generation of oxygen vacancies. At the same time, Pd activates oxygen from the atmosphere and functions as an oxygen donor, oxidising adjacent $Zn^{\delta+}$. The present conditions initiate the formation of an epitaxially growing nanorod, the length of which is determined by the temperature-dependent equilibrium. This proposed mechanism is corroborated by the fact that nanorods are exclusively found in the vicinity of Pd nanoparticles.

Decomposition of ZnO

The exposure of the ZnPd/ZnO system to temperatures between 500 and 800 °C and vacuum conditions activates growth of the nanoparticles and strong decomposition of the ZnO support. Smaller and more isolated regions are affected more strongly due to their higher surface area and surface to volume ratio. The strong decomposition of the ZnO support at temperatures of ≤ 800 °C may appear unanticipated, since ZnO is known to melt at ambient pressure at ~ 1975 °C[235]. However, ZnO is known to dissociate at the surface, forming elemental Zn and O_2 at temperatures above ~700 °C. [236] As a consequence of the dissociation and the high vapor pressure of Zn, metallic Zn evaporates and oxygen desorbs. The residual ZnO support restructures to the energetically most favorable shape and forms facets. The dissociation of ZnO might also be accelerated by the presence of the electron beam and the low pressure of the present vacuum.

Conclusions

The calcination of $Pd(NO_3)_2$ supported on ZnO was studied *in situ* using STEM. Decomposition of the $Pd(NO_3)_2$ was observed at approximately 170°C, accompanied by an increase in particle size. Figure 4.17 illustrates the results at different calcination temperatures. A stable calcination window was identified between 200 and 400 °C, within which no significant temperature dependency was detected. At temperatures exceeding 460°C, increased mobility of PdO nanoparticles on the ZnO surface and their agglomeration were noted. Atomic-scale analysis of the nanoparticles suggest a transition to metallic Pd. At 660°C, the ZnO support begins to decompose, exhibiting faceting and structural disintegration as it dissociates into metallic Zn and molecular O_2. These *in situ* STEM observations are corroborated by corresponding *ex situ* calcination experiments conducted under laboratory conditions at ambient pressure, demonstrating consistency across experimental methods. This synergy facilitates controlled synthesis of PdO nanoparticles and highlights the influence of calcination parameters, such as temperature and dwell time. In light of the present results, it can be concluded that *in situ* STEM experiments possess a strong predictive power with regard to the calcination of $Pd(NO_3)_2$. The present findings shed new light on the potential of *in situ* STEM experiments and their impact on the controlled preparation of ZnPd nanoparticles.

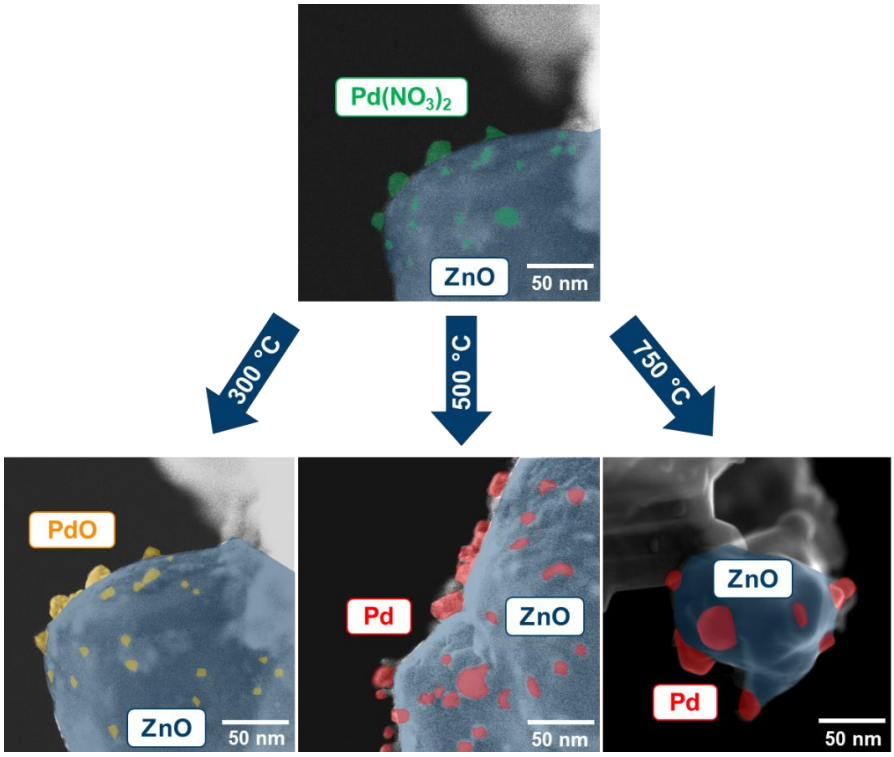

Figure 4.17: Schematic summary which shows the effects of different calcination temperatures at 1.5 Pa oxygen pressure. An increase in calcination temperature leads to a particle growth. Nanoparticles and their chemical composition are highlighted. Figure is taken with permission from reference[200].

5 Reduction of Zinc Oxide Using Environmental Scanning Transmission Electron Microscopy

The work in this chapter was performed in collaboration with the Massachusetts Institute of Technology, Cambridge, MA, USA. Hanglong Wu prepared the studied Zinc sample.

Isolating the effects of reactive conditions on a single component of a metal-support system is challenging due to interfering phenomena and interactions between the components. It is often challenging to judge whether an effect occurs because of or in spite of an interaction when supported systems are considered. Therefore, the components must be examined individually in order to evaluate possible metal-support interactions accurately. This is particularly important when the experimental conditions differ from typical laboratory conditions, e.g. *in situ* experiments using STEM. In such experiments, the electron beam can interact with the sample and the atmosphere.

During reduction, the interaction between molecular hydrogen and the electron beam may result in the formation of atomic, excited and ionic hydrogen, which is known to have a higher reducing potential. The reducibility of metal oxides can be assessed using Ellingham diagrams, as they show the temperature-dependent change in Gibbs free energy, as derived in chapter 2.4. A metal oxide is reduced if the Gibbs free energy of reduction is lower than that of oxidation. As shown in the Ellingham diagram in Figure 2.4, the Gibbs free energy of ionic hydrogen is 15 times lower than of molecular hydrogen. As illustrated in Figure 2.4, ZnO is not reduced by molecular hydrogen at 200 °C, but by atomic and ionic hydrogen. This makes ZnO an ideal reference to assess whether a sufficient amount of activated hydrogen species is formed by electron beam interaction during an *in situ* reduction experiment. Furthermore, a metal oxide can be reduced due the absence of oxygen, e.g. a low partial pressure of oxygen. The typical vacuum pressure applied during TEM experiments is less than 10^{-4} Pa. Given that the partial pressure of oxygen is in a similar range, the partial pressure is insufficiently low to reduce ZnO. However, the low oxygen pressure associated with a hydrogen atmosphere may have synergic effects, which facilitate the reduction of ZnO.

This chapter aims to investigate the reducibility of non-supporting zinc oxide using E-STEM. Zinc with an oxide passivation layer is exposed to a hydrogen atmosphere at 200 °C. The effects of electron beam exposure on the sample and the atmosphere will be investigated, evaluating if sufficient amounts of atomic and ionic hydrogen form. Moreover, it is investigated if the combination of a low oxygen partial pressure and the injection of hydrogen generate conditions that result in the reduction of ZnO. The *in situ* study is set out to provide a fundamental understanding of the reduction behaviour of sole ZnO during electron beam exposure and reduction. The results are essential for understanding the reduction of more complex and supported systems.

5.1 Experimentals

Zn nanoplates were directly deposited onto the MEMS *in situ* heating chips in a thermal evaporator integrated in a glovebox (Inert Eng Model PL-HE-4GB-1800). Zn pellets (99.99% pure) were first placed in a molybdenum (Mo) boat and subjected to heating by a current of 77.4 A at 2.9 V. Thermal evaporation was then performed at a chamber pressure of $1{,}6 \cdot 10^{-4}$ Pa, with a deposition rate of 1-2 Å/s until a final thickness of 50 nm was achieved. The thickness of the Zn layer was monitored by a quartz crystal microbalance (QCM) in the evaporation chamber. Single crystalline Zn nanoplates were formed on an electron transparent SiN membrane, as displayed in Figure 5.1. Due to exposure to ambient laboratory conditions, a thin ZnO passivation layer was formed, encapsulating the Zn nanoparticles. The *in situ* reduction experiment was performed on a HF5000 environmental STEM (Hitachi High-Technology), which was operating at 200 kV in HR and HR mapping STEM mode. The experimental setup is described in chapter 3.2.1. The evaporation unit was not used and was disconnected. The sample was heated to 200 °C, when pure hydrogen was injected with a mass flow of 2.0 sccm into the microscope column, resulting in a specimen pressure of ~1.5 Pa. The sample was exposed to hydrogen for ~ 50 min.

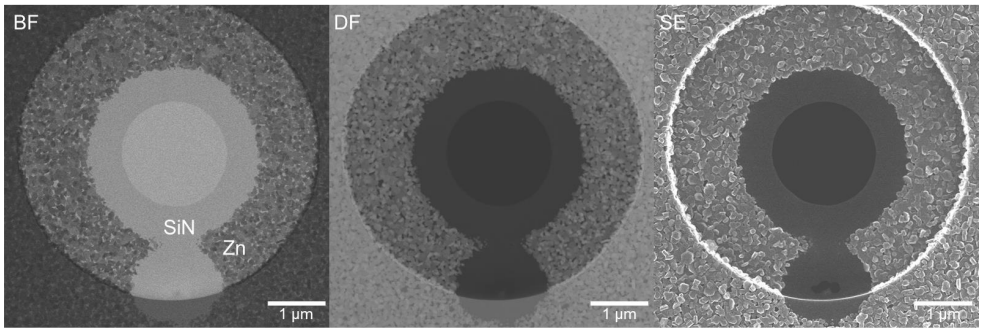

Figure 5.1: BF, DF and SE image showing a SiN membrane, which is sputtered with single crystalline Zn particles.

5.2 Results of Zinc Oxide Reduction Experiment

Pristine Zn nanoplates are encapsulated by a 1-2 nm thick ZnO passivation layer, as shown by the inset in Figure 5.2. Occasionally, ZnO passivation layers, which are continuously exposed to the electron beam for a long period (> 2 min) at high magnifications in vacuum, are subject to local structural changes, as illustrated in Figure 5.3. As a result, small features such as nanorods and islands are formed and disintegrated. Such features are limited to the passivation layer.

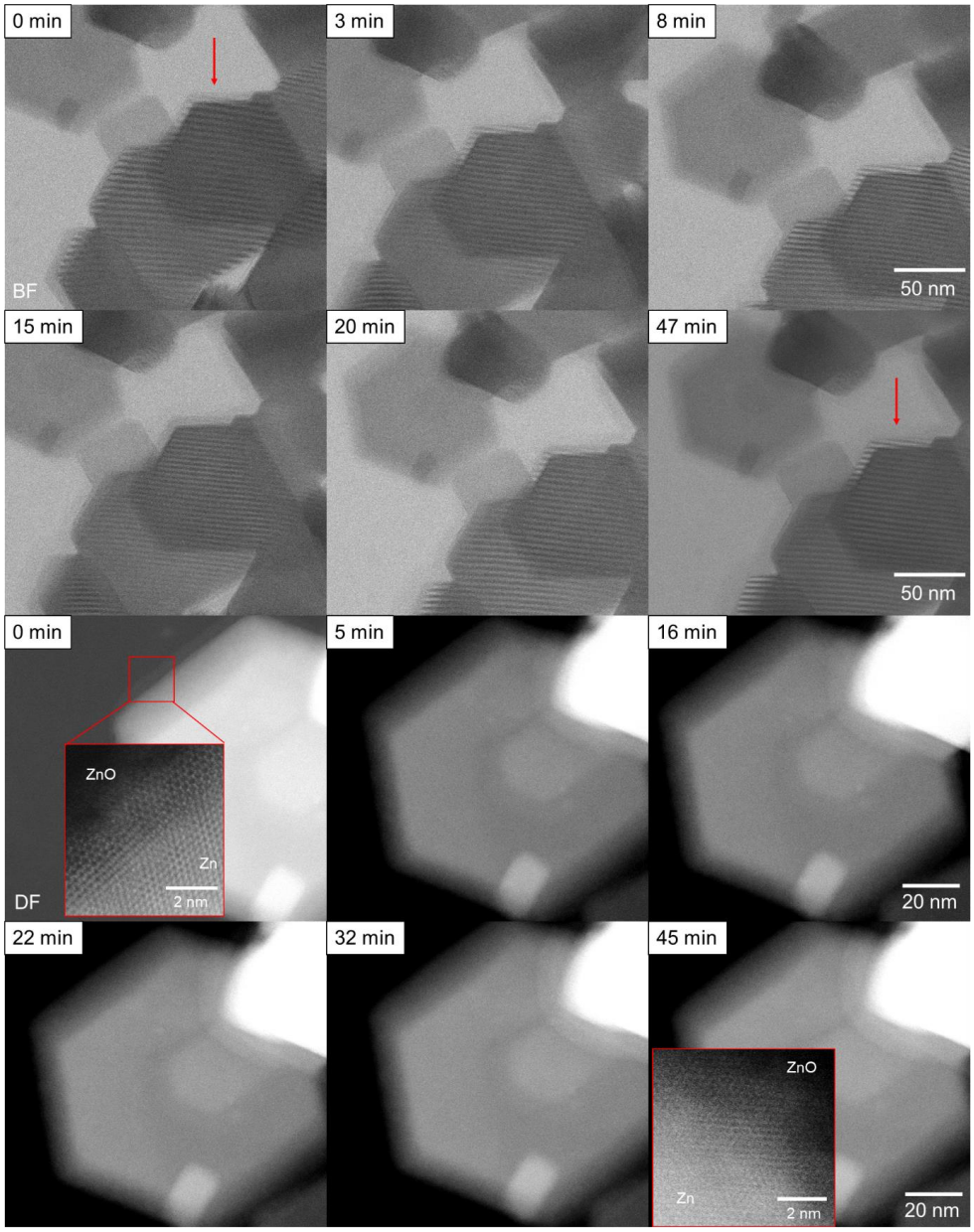

Figure 5.2: BF and DF image series of hexagonal Zn crystals coated with a ZnO passivation layer. Time stamps indicate the time of hydrogen exposure. BF images show particles with Moiré fringes, indicating a complete coverage by zinc oxide. Oxide layers were not decomposed during the reduction treatment. Insets show interfaces between Zn and ZnO at a higher magnification.

The Zn nanoplates remain unchanged. Such changes in structure only occur after imaging at high magnifications > 1000k x and this investigation is predominantly performed at lower magnification < 200k x, where beam effects are not observed. After hydrogen injection, the nanoplates do not undergo any structural changes. The intact structure is highlighted by the largely unchanged Moiré pattern as shown in Figure 5.2. Only slight contrast differences are apparent in the Moiré pattern. Correspondingly, the Zn nanoplates are still coated by the ZnO passivation layer, as shown by DF images.

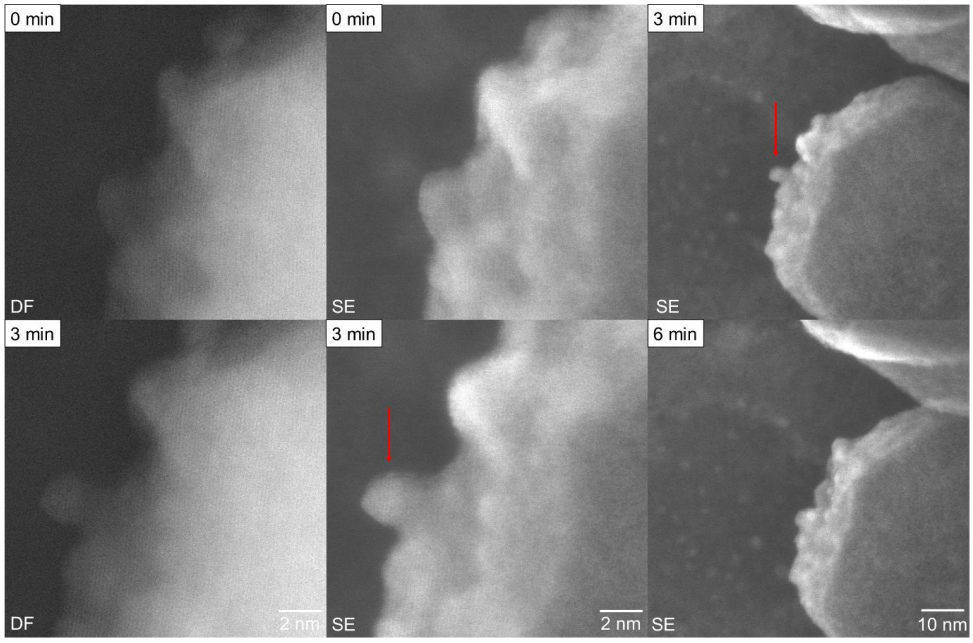

Figure 5.3: BF and SE images of Zn nanoplates, which are irritated by the electron beam. Red arrows indicate identical sample locations at different magnifications imaged in immediate succession.

5.3 Discussions

The present Moiré pattern is constructed through the interference of the overlapping ZnO and Zn lattice. The unit cells of Zn (a=b=2.66 Å, c=4.86 Å)[237] and of ZnO (a=b=3.25 Å, c=5.21 Å)[238] have a mismatch, which result in the generation of Moiré pattern. As shown in Figure 5.2, the periodicity of the present Moiré pattern is 4.2 ± 0.1 nm. The complete coverage of the Zn nanoplates by the Moiré pattern indicates the encapsulation of the entire nanoplate by the metal oxide. Since the Moiré pattern remains unchanged throughout reduction, it can be concluded that ZnO is stable and is not decomposed by the hydrogen atmosphere present. Given that ZnO is decomposed by atomic and ionic hydrogen, as suggested by the Ellingham diagram

(Figure 2.4), the quantity of these hydrogen species formed is only small and insufficient for reduction of the ZnO passivation layer. Activation of hydrogen by the electron beam is therefore neglectable. Given the stability of the ZnO passivation layer, it can be concluded that the synergic effect of the low oxygen partial pressure and injected hydrogen on the reduction of ZnO is also negligible.

Since Ellingham diagrams and the change in Gibbs free energy are only obtained from thermodynamic laws, reduction of the passivation layer may be kinetically limited. The activation energy for reduction is lower for active hydrogen species than for hot molecular hydrogen, so lower temperatures are required for reduction.[153] In addition, low-pressure hydrogen plasma is used to partially reduce native oxide layers and semiconducting oxides at moderate temperature between 150 to 300 °C.[239,240] Inhibition of reduction in the present experiment is therefore unlikely due to kinetic limitation.

Conclusions of Zinc Oxide Reduction Experiment

In summary, the *in situ* experiment confirms that no or only a neglectable quantity of atomic and ionic hydrogen is formed, as the passivation layer is not decomposed by the reduction treatment. It can therefore be concluded that ZnO is stable during *in situ* STEM experiments in a hydrogen atmosphere at 200 °C. These results contribute to the understanding of the interaction between the atmosphere and the electron beam and suggest that the electron beam hardly excites the hydrogen present. Thus, molecular hydrogen is dominant hydrogen species during the *in situ* STEM reduction experiments.

6 Reduction of Palladium Oxide Supported on Zinc Oxide Applying Environmental Scanning Transmission Electron Microscopy

The work in this chapter was performed in collaboration with the TU Chemnitz, Germany. Oytun Tiryaki and Marc Armbrüster prepared the studied PdO/ZnO sample and conducted the XRD measurement.

Reduction treatments are important reaction steps in the preparation of supported nanoparticles. During reduction, metal oxides are exposed to a reducing atmosphere and an elevated temperature. Chemically bound oxygen reacts with the reducing gas present, e.g. carbon monoxide and hydrogen, and is removed from the oxide lattice. The remaining metal may stay in its elementally pure form or interact with the support. Such interaction is referred to as strong- and reactive-metal support interaction and is described in more detail in chapter 2.3. As a result, nanoparticles can alloy and form intermetallic compounds during reduction. Preparation of supported, intermetallic ZnPd nanoparticles also includes a reduction treatment. As-prepared PdO supported on ZnO is reduced in a hydrogen atmosphere. It is expected that PdO is reduced to elemental Pd. Subsequently, hydrogen is activated on Pd and spills over to the ZnO support, which is partially reduced. As-reduced Zn is incorporated into the Pd lattice and ZnPd is formed. Literature on the topic is reviewed in chapter 2.3. Pd-containing nanoparticles supported on ZnO are employed due to their excellent catalytic performance in various heterogenous catalytic reactions. Although their frequent use as a catalyst, no standardized preparation protocol has been established and various reduction routines have been proposed in the past, using different reduction temperature, atmosphere, time and pressures. While hydrogen spillover is widely accepted to play a pivotal role in the transformation from PdO to ZnPd, research about the precise structural evolution of the metal-support system during reduction is still rare. However, an insight in the formation process is crucial to develop a complete picture of the prominent material system that would allow a purposive catalyst design with desired catalytic properties. Although the work of Penner *et al.*[108] provides valuable information about different reduction temperatures at ambient pressure, its significance is limited to explain dynamic changes, which are triggered during reduction. An *in situ* study, which elucidates the ZnPd formation mechanism time resolved, is therefore highly desirable. Niu et al. investigated the formation of ZnO-supported ZnPd nanoparticles *in situ* and paid special attention on the role of the intermediate phase palladium hydrate.[241] The authors show that Pd transforms to β-PdH at 50 °C and to α-PdH with increasing temperature. A complete transformation into ZnPd is reported for a 20 wt.-% Pd-loading at 340 °C. In addition, they demonstrated that the intermetallic ZnPd phase favours a growth along PdH_x ⟨111⟩ due to preferential Zn diffusion. Inspired by the work of Niu et al., the mechanics of RMSI should be

further investigated. Complementing their work, which elucidates the temperature dependence of the particle evolution during RMSI illustratively, this study aims to unravel RMSI-triggered support activation with high temporal resolution.

This chapter aims to unravel the formation mechanism of intermetallic ZnPd nanoparticles during reduction, using E-STEM. Activation of ZnO and transformation of PdO to ZnPd is studied *in situ*. The effect of different reaction parameters such as the electron beam, temperature and hydrogen pressure on the material system is discussed with available *ex situ* data.

6.1 Experimentals

Palladium nitrate supported on ZnO with a 5 wt.-% Pd loading was prepared as described in Chapter 3.1.1. Subsequently, the sample was calcined at 500 °C for 3 h in O_2:N_2 (20:80). The as-prepared palladium oxide supported on zinc oxide was transferred to a MEMS heating chip fabricated by NORCADA (Edmonton, Canada) and cleaned following the procedure given in Chapter 4.1. *In situ* reduction experiments were conducted, employing E-STEM on a Hitachi High-Technology HF5000, which was operating at 200 kV. The equipment used is illustrated in chapter 3.2.1. As the vaporizer system was disconnected, only the gas supply system and open cell setup of the microscope were used. Hydrogen was injected with a mass flow of 2.5 sccm resulting in a column pressure of $1.5 \cdot 10^{-2}$ Pa, which corresponds to a specimen pressure of ~1.5 Pa. The reduction was performed at room temperature and 200 °C for 100 min with a freshly prepared sample of supported palladium oxide. The regions of interest were only exposed to the electron beam during image acquisition and focus alignment to reduce electron beam effects to a minimum. The imaged regions were therefore not observed in between image acquisition. In addition, some locations were only imaged before and after the reduction, to evaluate the effect of the electron beam. The dose per frame D_f is given in chapter 3.3.

6.2 Characterisation of Pristine Palladium Oxide Nanoparticles

After calcination, supported PdO nanoparticles with different Pd loadings were pre-characterised using STEM and XRD. Acquired SE images, XRD measurements and particle size distributions (PSDs) are shown in Figure 6.1.

The SE images indicate a homogenous distribution of nanoparticles on the ZnO surface. Some nanoparticles aggregate to form dense clusters. Next to single, bigger nanoparticles (> 10 nm), many small nanoparticles are present. The density of nanoparticles tends to decrease for lower Pd loadings. Over 100 nanoparticles were measured in two perpendicular directions to determine the PSD of each Pd loading. All PSDs demonstrate that most nanoparticles are

smaller than 10 nm with a mean of ~7 nm. With the exception of minor deviations observed in the 5 wt.% loading sample, which exhibits the most compact PSD, the PSDs show a roughly similar trend, indicating that a Pd loading between 1 and 5 wt.% has a minor effect on the particle size.

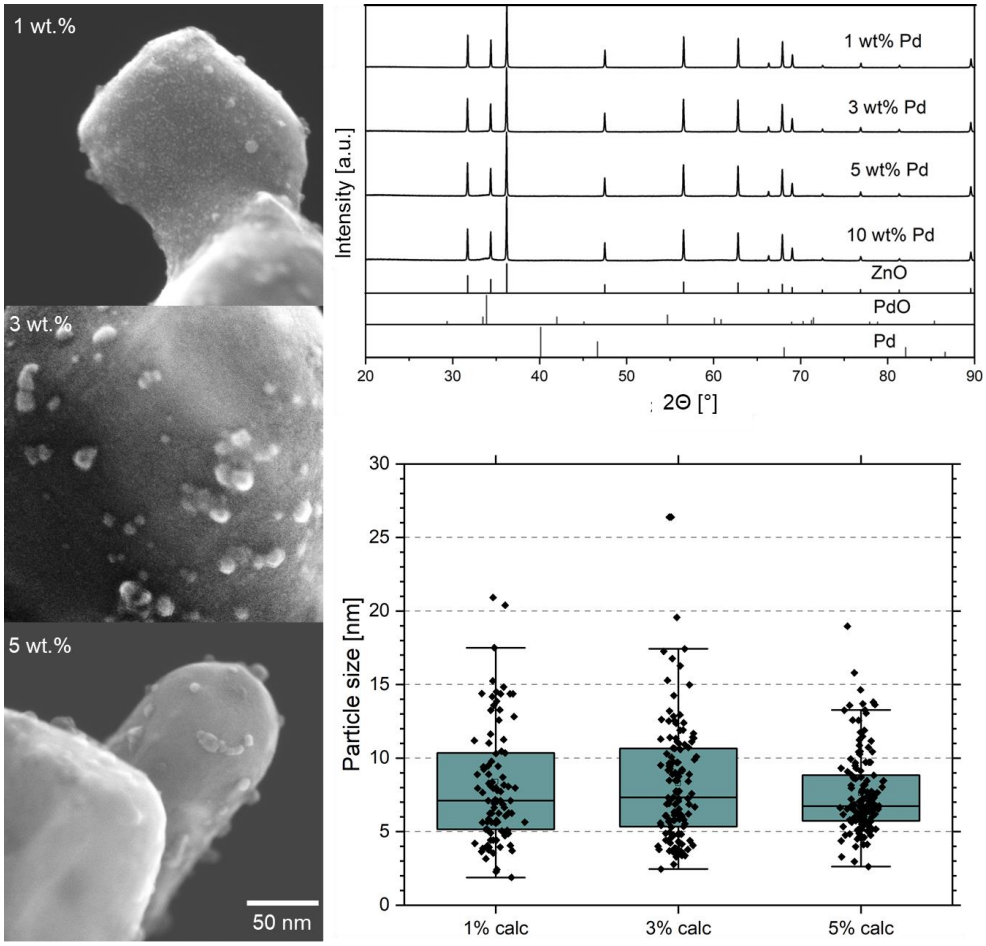

Figure 6.1: Left: Series of SE images of PdO nanoparticles supported on ZnO prepared with different Pd loadings after calcination. Right: Corresponding XRD measurements (top) and particle size distributions (bottom) of the sample with different Pd loadings. XRD reflections of ZnO, PdO and Pd are given as reference. The XRD data of the 5 wt.-% sample shows a small hump around 34°, corresponding to PdO. The strong peaks correspond well to the reference ZnO peaks, identifying the support.

The XRD measurements show similar results for different Pd loadings. For instance, the sample with 5 wt.% Pd loading, which is investigated during reduction, has many characteristic reflections, which can be assigned to ZnO and represent the support. None of the intense peaks correspond to a palladium species. There is a small increase in intensity around 34°, which can potentially be allocated to PdO. The intensity of this hump increases with loading. The 10 wt.% loaded sample was only investigated by XRD not by STEM.

6.3 Reduction of Palladium Oxide at Room Temperature

In this chapter, two distinct sample locations are studied during reduction in a hydrogen atmosphere at room temperature. To facilitate temporal comparison, observation periods of equivalent duration have been selected at each location and are analysed in succession.

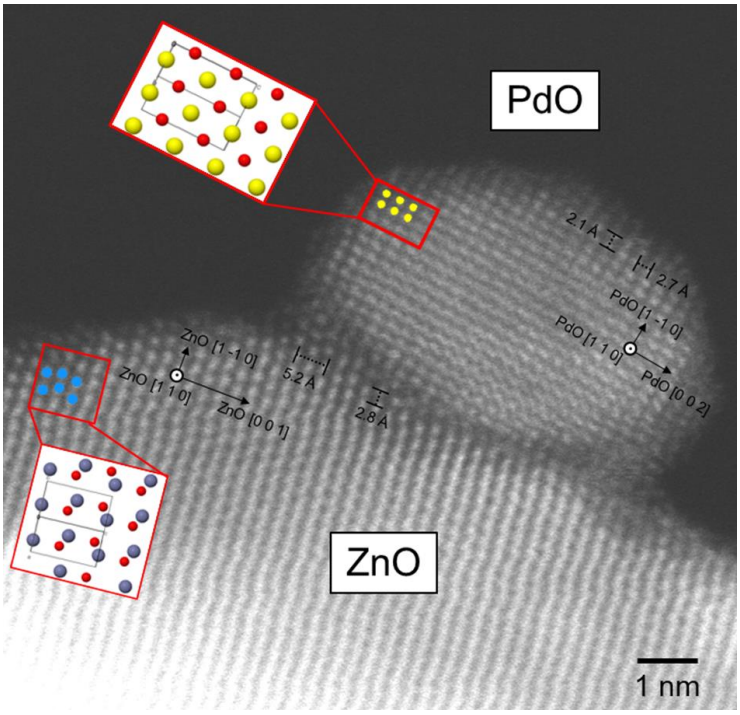

Figure 6.2: A DF STEM image of a pristine PdO nanoparticle on ZnO is shown. The PdO nanoparticle is aligned along [110] as shown in the model[242]. The ZnO crystal is aligned along [110] as exemplified in the model[243]. Pd, Zn and O are represented yellow, blue and red, respectively.

Figure 6.2 shows a DF image of the pristine nanoparticle-support structure. The interatomic spacings are measured by averaging several particle distances along two perpendicular

directions. The number of atom rows analysed varies between 3 to 8 depending on the degree of separation. The measured directions $g_{part,0min} = 2.1$ Å and $h_{part,0min} = 2.7$ Å are in good agreement with PdO [1 -1 0] $g_{PdO} = 2.15$ Å and [0 0 2] $h_{PdO} = 2.68$ Å.[242] The nanoparticle can accordingly be identified as PdO and is aligned along [1 1 0]. In Figure 6.2, the Pd atoms are highlighted in yellow to indicate their location within the tetragonal PdO structure model[242]. The structure of the support is analysed in the same way. The measured directions $g_{sup,0min} = 2.8$ Å and $h_{sup,0min} = 5.2$ Å correspond to ZnO [1 -1 0] $g_{ZnO} = 2.82$ Å and [0 0 1] $h_{ZnO} = 5.2$ Å.[243] A ZnO unit cell aligned along [1 1 0] is illustrated by the blue Zn atoms in the ROI in Figure 6.2. The oxygen atoms represented in red in the structure models for PdO and ZnO are not visible in the DF image. During imaging in vacuum, exposure by the electron beam introduces no changes to the particle-support system.

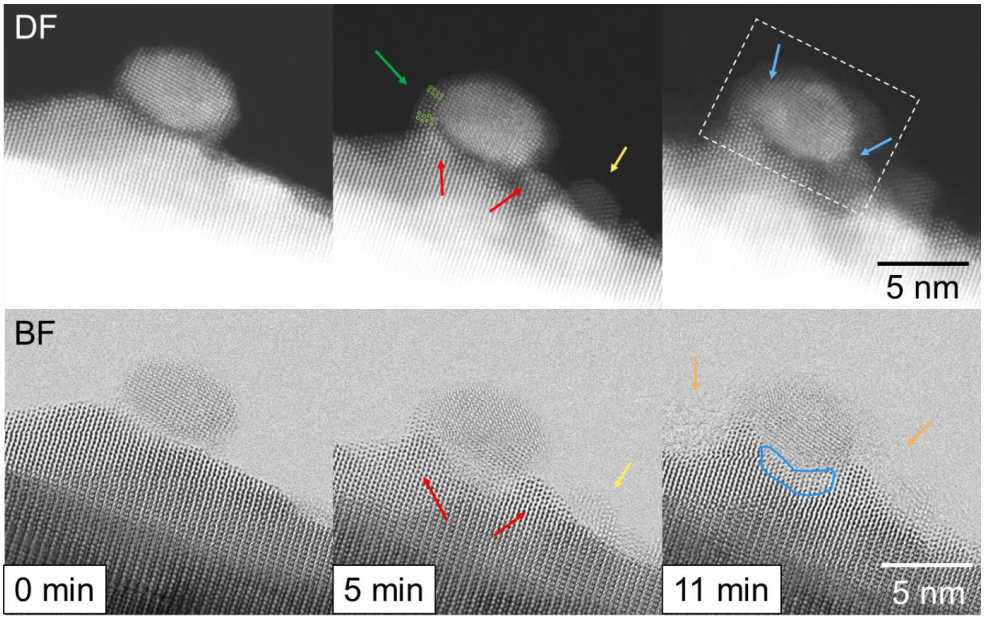

Figure 6.3: DF and BF image series of the evolving nanoparticle-support structure during the first 11 min of reduction in hydrogen atmosphere. Structural changes are highlighted by arrows. Red arrows indicate change in morphology of the existing ZnO support. Yellow arrows indicate formation of new ZnO features. Green circles highlight atomic positions and the change in crystal structure from distorted ZnO to the mixed phase at the interface. The blue arrows and outline illustrate the interaction between nanoparticle and support. Orange arrows indicate the formation of an amorphous, hydrocarbon coverage, which is most likely triggered by the electron beam. White rectangle indicates ROI, which is shown in Figure 6.4.

Figure 6.3 shows a series of BF and DF images of the evolution of a nanoparticle-support structure during an *in situ* experiment conducted in a hydrogen atmosphere. The corresponding SE images are shown in Figure 11.12. After 5 min, the support changes considerably and develops a coarse surface. Changes of the support can be divided into two populations: As highlighted by the red arrows in Figure 6.3, ZnO is stacking up and partially envelopes the nanoparticle. Here, the BF and DF contrast of the ZnO support is similar to the original state, indicating a migration of ZnO to the nanoparticle or the subsidence of the nanoparticle into the support. On the other side, shown by the yellow arrows in Figure 6.3., other support features have the same crystal structures but weaker contrast particularly in SE and BF suggesting thinner thickness or compositional differences. The present changes in surface morphology occur preferably in the perimeter of the nanoparticle. Migrated ZnO covers the left side of the PdO nanoparticle. A transformation of the crystal structure can be seen here. At the areas highlighted by red arrows, lattice spacing and crystal structure match those measured in Figure 6.2. In the area close to the nanoparticle, where selected atoms are highlighted by green circles in Figure 6.3, the [0 0 1] lattice spacing increases by 3.5 % from 5.2 Å to 5.5 Å, and the [1 -1 0] spacings decreases by 3% from 2.8 Å to 2.7 Å, indicating a distortion of the hexagonal ZnO structure.

The area, which is highlighted by the green arrow, represents an interface between phases with stronger and weaker contrast in BF and DF in Figure 6.3. In the area of weaker contrast, a change in the hexagonal crystal is found. The interatomic spacings measured between the atom rows marked in green are 2.3 Å and 2.4 Å and are rectangularly arranged, which indicates a tetragonal crystal structure. The values at the interfaces to the particle match those at the gas atmosphere. The tetragonal phase is however not part of the nanoparticle, as it is clearly evident in all detected images. Within the first 5 min of hydrogen exposure, the crystal structure of the nanoparticle begins to transform exclusively at the supported interface, as illustrated by the increase in contrast in the DF in Figure 6.3.

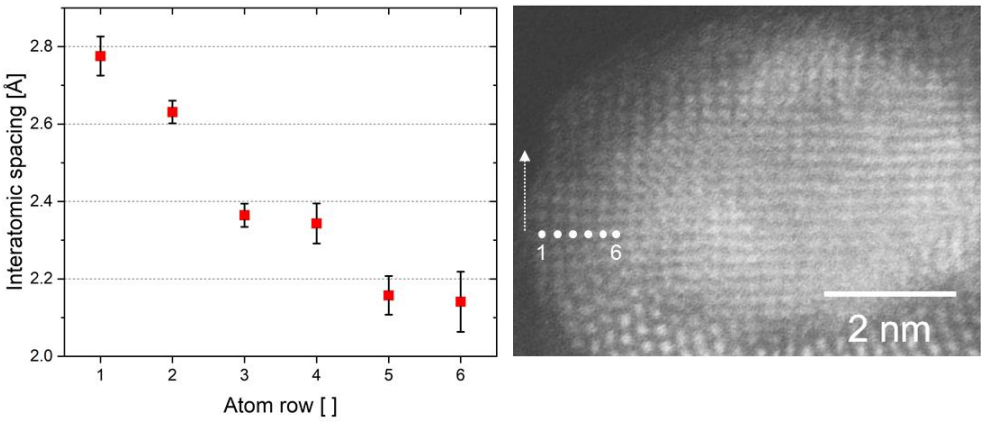

Figure 6.4: Clipped DF image of supported PdO after 11 min of hydrogen exposure. Original image is displayed in Figure 6.3. Interatomic spacings are measured along the row of atoms in the arrow's direction. Atom rows are numbered from left to right as displayed.

After 11 min, an interaction between nanoparticle and support is activated, as displayed by the blue arrows in Figure 6.3. At the interface of the nanoparticle, the crystal structure of adjacent support changes such that it matches the interatomic spacings of the nanoparticle. To estimate the change in interatomic spacing, 6 rows of atoms are labelled and measured along the direction of the arrow from the position marked, as shown in the sectioned DF image in Figure 6.4. Interatomic spacings of 4 to 5 atoms are measured three times and are averaged. The error is given by the standard deviation. The interatomic spacings shrink from ~2.8 Å at the edge to ~2.1 Å at the interface between support and nanoparticle. While the interatomic spacings of the outer perimeter match well with ZnO and the inner perimeter with PdO, there is a transition zone with ~2.4 Å in between. A change in support can be seen below the nanoparticle, as highlighted by the area marked in blue in the BF image in Figure 6.3.

In addition, formation of surface contamination is observed after 11 min, as indicated by the orange arrows BF imaging in Figure 6.4. Since the detection of SE is surface sensitive, SE imaging is particularly affected by an increase in contamination over time. Sample areas, which are imaged with SE longer than 11 minutes after the start of reduction, are largely covered by contamination. Figure 11.12 demonstrates the degree of contamination.

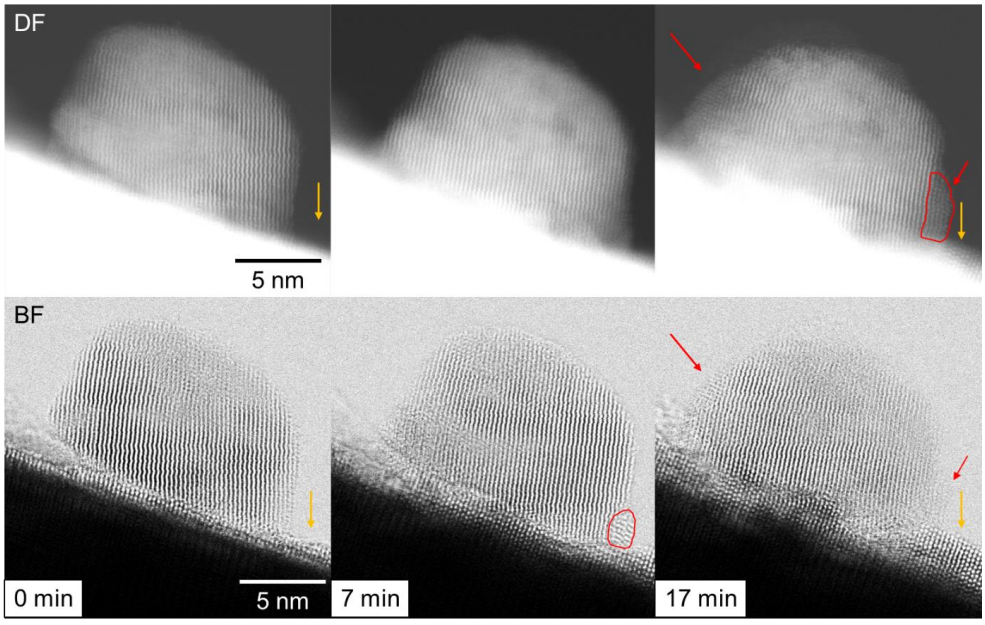

Figure 6.5: Series of DF and BF images during reduction. The time stamp indicates the time the specimen was exposed to a hydrogen atmosphere at room temperature. Images were acquired under identical conditions as those displayed in Figure 6.3. Orange arrows indicate the ZnO enrichment development on the surface of the support. Red arrows highlight surface migration of ZnO on the nanoparticle. Its progress can be tracked by following the features circled in red.

Figure 6.5 shows series of DF and BF images of a different location of the specimen in the identical *in situ* reduction experiment already shown in Figure 6.3. Similar to the results described above, the ZnO support evolves over time during reduction. As indicated by orange arrows in Figure 6.5, migrating ZnO forms clusters on the surface of the support. The ZnO cluster grows along [1 -1 0] and partially envelopes the nanoparticle. Such changes in support also occur at other locations along the interface of the particle, but in a less pronounced form. In addition, ZnO migrates steadily onto the PdO nanoparticle. The progress of surface migration can be tracked by following the areas marked in red in the BF images. After 17 min, the surface of the nanoparticle is partially decorated by crystalline ZnO island, as highlighted by red arrows in Figure 6.5.

Figure 6.6 shows that the PdO nanoparticle is largely encapsulated by ZnO after 16 min. As indicated by red arrows in Figure 6.6, the coverage layer once formed has a constant thickness that hardly changes over time. For instance, the thickness of the coverage layer at the indicated location is ~1,48 ± 0,1 nm after 16 min and after 32 min ~1.58 ± 0.1 nm. The lattice spacing on the nanoparticle, as indicated by the black bar after 26 min, corresponds to that of ZnO, corroborating the assumption of complete coverage. Intriguingly, the nanoparticle partly detaches from the support after 22 min and forms a gap, as indicated by blue arrows in Figure 6.6. Given that the nanoparticle is immobile, ZnO is the disintegrating species.

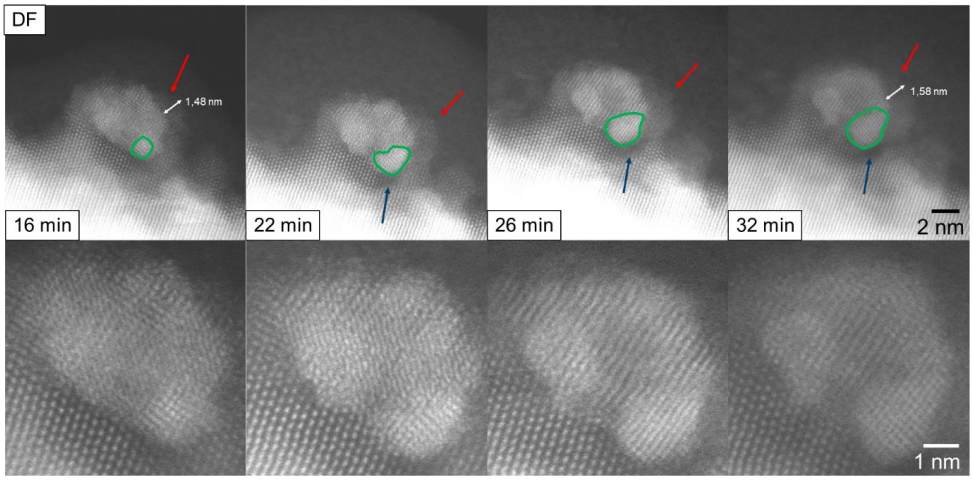

Figure 6.6: Series of DF images during reduction. The time stamp shows the time of reduction in a hydrogen atmosphere at room temperature. Lower row shows the magnified nanoparticles. Red arrows indicate the increase in ZnO coverage. Blue arrows highlight detachment of the nanoparticle from the support. Region marked in green show the nucleation and growth of a new phase.

While in the first minutes of reduction the support is mainly affected by the reducing atmosphere, subsequently nanoparticles start to evolve. At the locations, where nanoparticle and support first interact (Figure 6.3), nucleation of a new phase occurs, as highlighted in green in Figure 6.6. Given that the phase is represented by an area of brighter contrast, it grows continuously over time. To estimate the growth of the phase formed, its perimeter is manually determined three times per image and average values for area, circumference and Feret's diameter are determined with the respective standard deviations as errors. For a better understanding of the measurement procedure applied, examples of shapes are marked in Figure 11.13 and the corresponding values are displayed in Figure 6.7. Values measured suggest a linear growth in diameter of ~0.1 nm/min. In addition to the size of the phase under consideration, interatomic spacings were measured after 32 minutes. The almost perpendicular lattice spacings (~86 °) are 2.3 ± 0.1 Å and 1.9 ± 0.1 Å.

Compound	Interplanar Distance	Interplanar Distance
PdO[244]	(1 1 0) - 2.15 Å	(1 0 2) - 2.00 Å
Pd[223]	(1 1 1) - 2.25 Å	(2 0 0) - 1.95 Å
ZnPd[46]	(1 0 1) - 2.18 Å	(1 1 0) - 2.05 Å

Table 6.1: The interplanar distance of PdO, Pd and ZnPd that correspond most closely with the measured interatomic spacings are presented.

The lattice parameter of elemental Pd matches best with the present interatomic spacings (Table 6.1). Interestingly, the growth of the phase of interest is accompanied by dissolution of adjacent ZnO, described above. At the left hand side in Figure 6.6, a second bright feature, which evolves on the nanoparticle, indicates the growth of another phase.

Time [min]	Area [nm²] ■	Circumference [nm] ▲	Feret's diameter [nm] ▼
16	1.5 ± 0.3	4.7 ± 0.5	1.6 ± 0.1
22	2.6 ± 0.3	6.6 ± 0.4	2.5 ± 0.1
26	4.0 ± 0.1	7.6 ± 0.1	2.7 ± 0.1
32	5.5 ± 0.3	9.2 ± 0.1	3.3 ± 0.1
38	6.4 ± 0.3	10.4 ± 0.3	3.9 ± 0.3

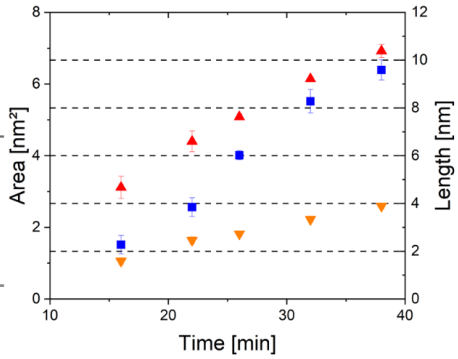

Figure 6.7: The growth of phase is quantified by measurements of area (blue squares), circumference (red triangle) and Feret's diameter (orange triangle). The area is given in nm² on the left axis. The length is given in nm on the right axis. An example of the phase measurement is represented in Figure 11.13.

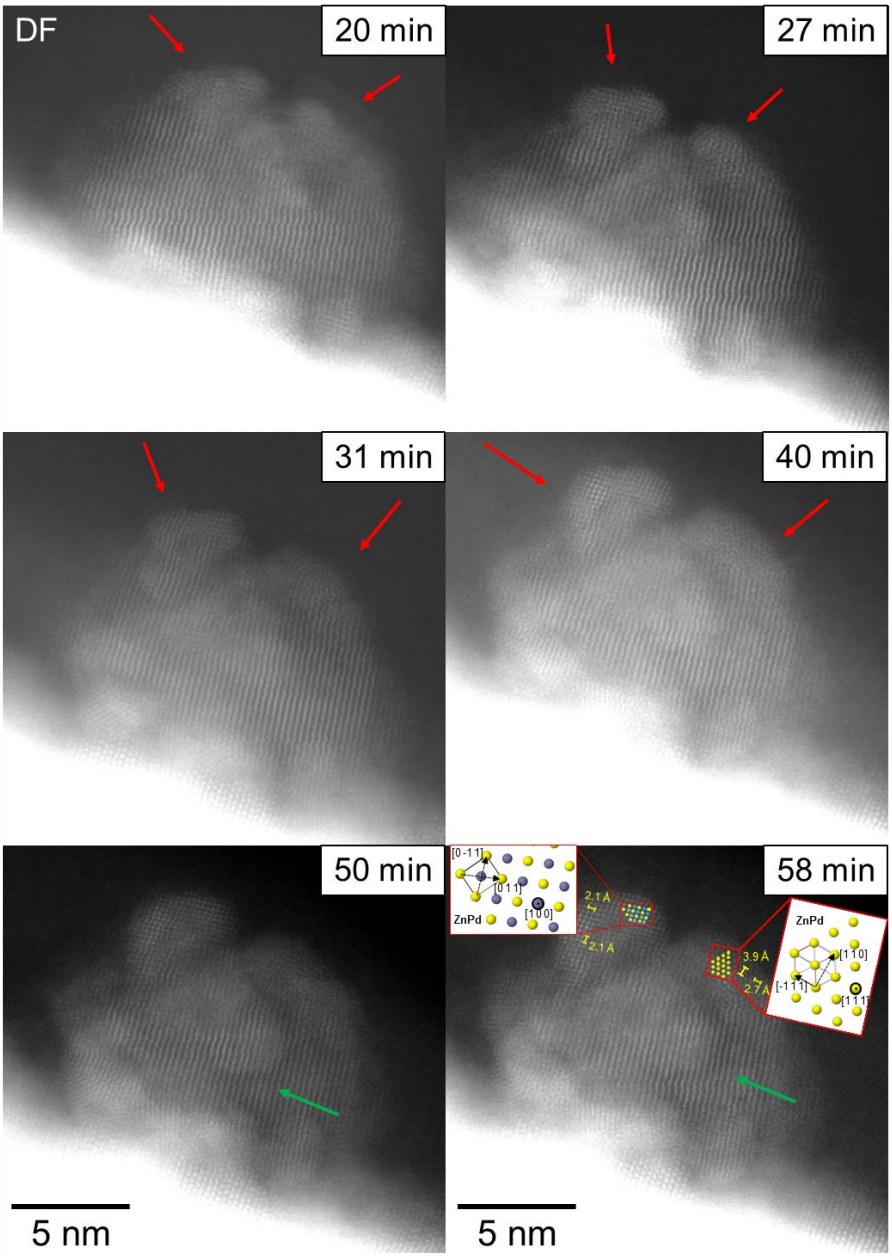

Figure 6.8: Series of DF images during reduction. The time stamp indicates the time of reduction in a hydrogen atmosphere at room temperature. First minutes of reduction at the identical location are displayed in Figure 6.5. Red arrows highlight nucleation and particle growth. Green arrows indicate unchanged particle region. Lattice spacings measured are in good agreement with ZnPd crystal structured displayed from reference.[46]

Figure 6.8 shows the same sample region, which is displayed in Figure 6.5, during reduction between 20 and 58 min. Similar to the results discussed above, nucleation and growth of new phases can also be observed here. Locations, where nuclei form, are decorated with ZnO layers or are in their vicinity. After 20 min, the single crystalline structure of the observed nanoparticle is distorted by the emergence of phases with a different crystal structure, which are visible at the locations indicated by red arrows in Figure 6.8. The novel phases continue to grow over time and slowly transform most of the nanoparticle. After 58 min, the novel phases are the dominant feature on the top of the nanoparticle. The crystal structure of the left phase agrees well with ZnPd aligned along [1 0 0], as demonstrated by the model in Figure 6.8. The lattice spacings measured are 2.1 ± 0.1 Å and 2.2 ± 0.1 Å, corresponding to ZnPd (0 1 1) of 2.18 Å. The orientation of the right phase is different and corresponds to ZnPd aligned along [1 1 1]. Here, the lattice spacings are 4.0 ± 0.1 Å and 2.7 ± 0.1 Å and matches with transmitted ZnPd (1 1 1) of 2.64 Å and (1 1 0) of 4.09 Å. Analysis of the crystal structures suggests that ZnPd is formed during reduction. Parts of the nanoparticle still show the pristine crystal structure, as marked by the green arrows, indicating only a partial transformation. In addition, the nanoparticle is increasingly buried due to the formation of surface contaminations.

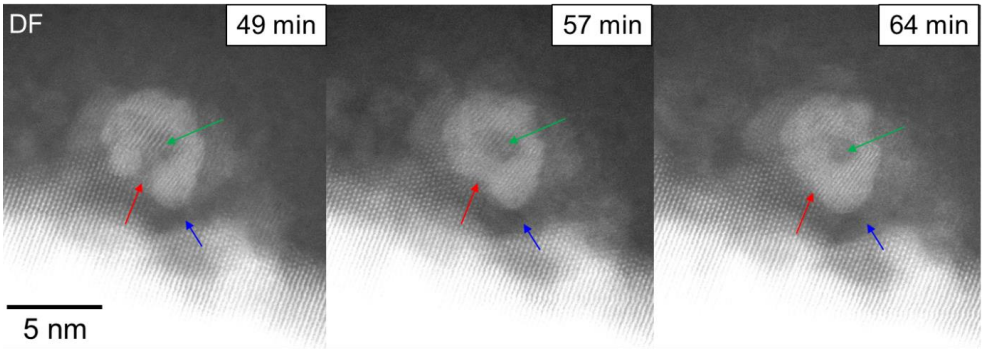

Figure 6.9: Series of DF images during reduction. The time stamp indicates time of reduction in a hydrogen atmosphere at room temperature. First minutes of reduction at the identical location are displayed in Figure 6.3 and Figure 6.6. Red arrows indicate growth of new phase indicating a core-shell structure. Green arrows highlight unchanged region with darker contrast that is encapsulated by formed phase. Blue arrows mark separation of the nanoparticle from the support.

Figure 6.9 demonstrates the final changes that are triggered by reduction. The blue arrows show that the nanoparticle continues to detach from the support, indicating ongoing ZnO dissolution. Growth of individually formed phases leads to their assembly and formation of a core-inner shell-outer shell structure, as highlighted by the red arrows. The centre of the nanoparticle still shows the pristine crystal structure, as indicated by green arrows, and is coated with

presumably-formed ZnPd. Both Pd-rich phases are capsulated by ZnO. Prolonged exposure to a reducing atmosphere does not trigger any further structural changes.

In another experiment, PdO supported on ZnO was annealed in vacuum at 200 °C for 60 min prior to reduction to remove residual hydrocarbons from the sample. The sample was then reduced under the same conditions as described above. Figure 11.15 shows the sample during reduction at room temperature after a preheating treatment. Here, ZnO is activated first as during the previously described experiment. Small clusters are formed on the ZnO surface, which preferentially migrate to the nanoparticle. When the nanoparticle is decorated by a ZnO layer, the nanoparticle is transformed by a solid state reaction. Intriguingly, the transformation is activated at the interface first and proceeds through the crystal. During reduction, the nanoparticle tends to grow in size. Quantification of the particle growth is difficult due to a lack of segmentation. In contrast to the experiment with no preheating, no contamination is formed during beam exposure.

6.3.1 Evaluation of Electron Beam Effects During Reduction

Nanoscale structures are vulnerable to high energetic electron beam exposure. The nature of such beam effects might differ strongly depending on the energy and intensity of the electron beam and on the properties of the exposed material. In particular, during *in situ* experiments, where structural changes activated by the imposed conditions are anticipated, it is important to assess the effect of the electron beam on the material under investigation. In addition, the electron beam could also interact with the present atmosphere, forming a plasma and change the reaction conditions. Such catalytic reactions, in which a plasma is intentionally used to steer the catalytic properties, are referred to as plasma catalysis.[245] As a possible consequence of beam effects, plasma catalysis is treated here only phenomenologically. Thus, it is important to compare the results of *in situ* experiments with those of *ex situ* experiments or reference sample positions, which were not exposed to the electron beam during the *in situ* experiment. Such images, which are acquired under identical conditions to the *in situ* experiment presented in chapter 6.3, are displayed in this chapter and in Figure 6.10.

The crystal structure of the nanoparticle before reduction can be identified as PdO. The lattice spacings measured of 3.1 ± 0.1 Å and 2.2 ± 0.1 Å are in good agreement with PdO (0 1 0) of 3.03 Å and (1 0 3) of 2.14 Å. After reduction, the crystal structure of the nanoparticle has changed. The measured lattice spacings of 2.2 ± 0.1 Å in each direction match best with ZnPd (0 1 1) of 2.18 Å, indicating the formation of an intermetallic compound. Although the structure of the nanoparticle after reduction is largely single-crystalline, some regions, e.g. the left edge, have an irregular morphology. In addition, the activation of the support is weaker than that of the support, which was exposed to the electron beam *in situ*. Less encapsulation by the metal oxide is visible.

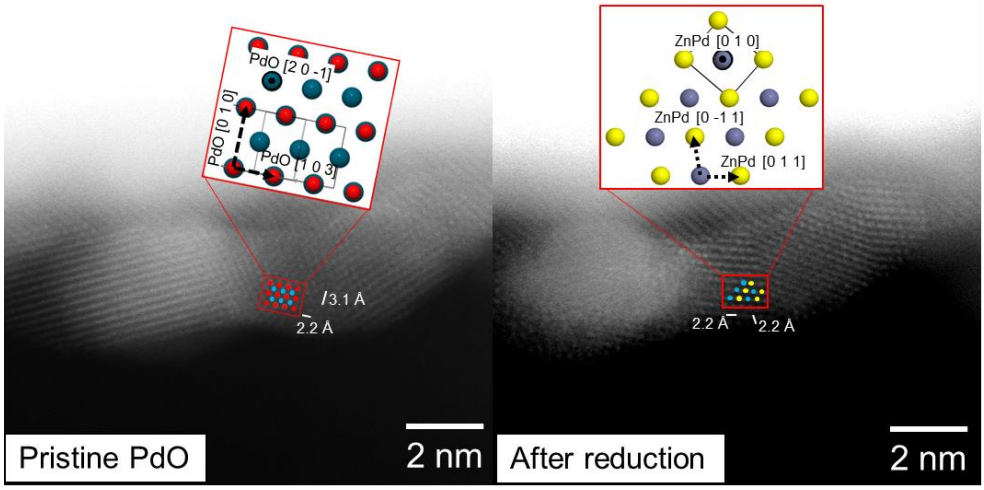

Figure 6.10: Supported nanoparticle before and after reduction in a hydrogen atmosphere at room temperature. The location was not exposed to the electron beam in presence of a hydrogen atmosphere. While the pristine nanoparticle matches with the lattice of PdO along [2 0 -1], the nanoparticle after reaction corresponds well to ZnPd along [0 1 0]. Zn is coloured in blue, Pd in yellow, O in red. The structure models are taken from reference.[46,244]

6.4 Reduction of Palladium Oxide at 200 °C

In addition to the reduction experiments performed at room temperature, supported PdO was reduced *in situ* at 200 °C. The sample was tempered at 200 °C for 20 min, before hydrogen was injected. Sample preparation was conducted accordingly to the protocol described in chapter 6.1.

Figure 6.11 and Figure 6.13 show the structural evolution of the system during reduction at two different magnifications. The pristine crystal structure of the support and nanoparticle with 2.4 ± 0.1 Å and 2.1 ± 0.1 Å matches well with ZnO (0 1 1)[243] of 2.48 Å and PdO (1 1 0)[242] of 2.15 Å. ZnO has an undistorted morphology and is only in contact with the nanoparticles on the supporting side. After 3 min of reduction, the support evolves and forms small ZnO cluster on the support surface. The nanoparticles are encapsulated by a continuous ZnO layer, as shown by the green shape in Figure 6.11. The perimeter of the nanoparticle is marked in red as guide to the eye. The thickness of the coverage layer is ~1.5 nm, as shown in Figure 11.14. After the initial encapsulation, the support undergoes further morphological changes, as displayed by the red arrows in Figure 6.13. The evolution includes the formation of spherical ZnO enrichments, which grow with time in contrast to the encapsulation layer. Near the interface of the nanoparticle and the support, ZnO is removed and forms a small neck underneath the

nanoparticle, as highlighted by the blue dotted lines. Given that other features of the ROI in Figure 6.11 are immobile, it can be concluded that the neck does not grow outwards, but that ZnO dissolves around the interface. The phenomenon occurs simultaneously with the encapsulation of the nanoparticle.

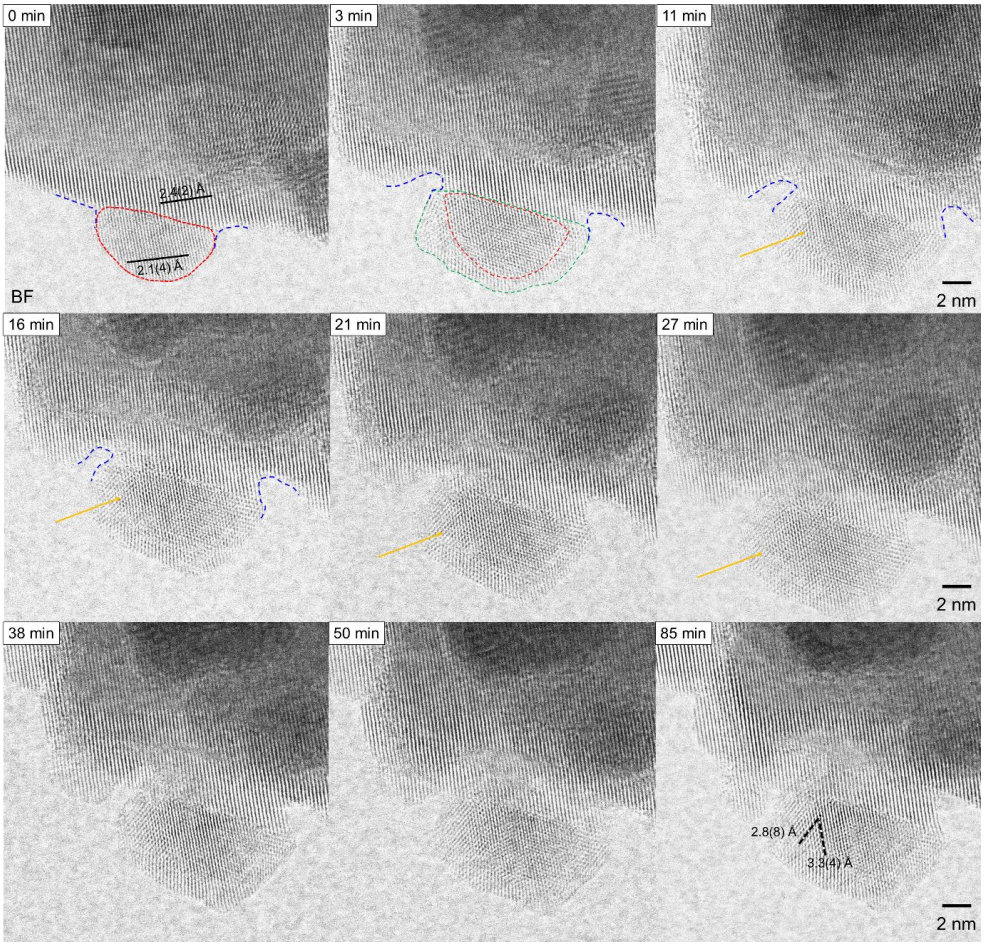

Figure 6.11: Series of BF images shown during the reduction of supported PdO at 200 °C. Time stamp indicates time of hydrogen injection. Region marked in red highlights the nanoparticle, region marked in green the encapsulation by ZnO. Neck formation and ZnO dissolution is marked in blue. The orange arrows indicate phase transformation.

The encapsulation has no influence on the size of the nanoparticles. However, a change in the crystal structure can be recognised. The crystal structure is single-crystalline throughout the nanoparticle. The lattice parameters in three different directions (a, b, c) are measured during reduction, as shown in Figure 6.12. Since these lattice parameters are the same on the right side

of the nanoparticle within the measurement accuracy, it can be concluded that the same crystal structure is present between 3 and 85 minutes of reduction.

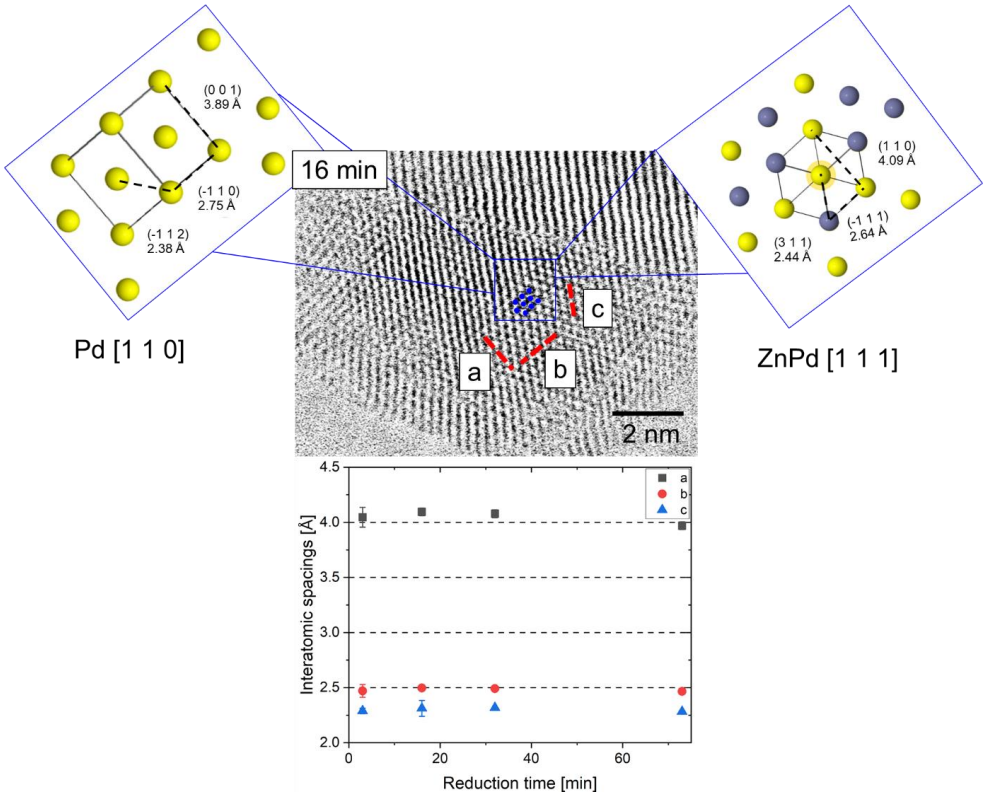

Figure 6.12: Top: BF image of a nanoparticle shown after 16 min of reduction. The structural evolution during reduction is illustrated in Figure 6.11. The crystal structure of the nanoparticle may correspond to Pd along [1 1 0] or ZnPd along [1 1 1], since the interatomic spacing and angles match well to the models taken from references.[46,223] Bottom: The measured interatomic spacings along a (black square), b (red circle) and c (blue triangle) direction displayed over the past reduction time. The spacings show no considerable change.

Assuming no change in crystal structure after 3 min of reduction, a representative identification of the crystal structure is performed after 16 minutes. As defined in Figure 6.12, the interatomic spacings measured along a, b and c are 4.1 ± 0.1 Å, 2.5 ± 0.1 Å and 2.3 ± 0.1 Å. These values are in good agreement to Pd[223] along [1 1 0] and ZnPd[46] along [1 1 1]. Thus, a may correspond to Pd (0 0 1) of 3.89 Å or ZnPd (1 1 0) of 4.09 Å, b to Pd (-1 1 0) of 2.75 Å or ZnPd (-1 1 1) of 2.64 Å and c to Pd (-1 1 2) of 2.38 Å or ZnPd (3 1 1) of 2.44 Å. The measured angles of 63.5 ± 0.8° and 58.9 ± 2.0° are in between the theoretical values for Pd of 54.7° and 65.3° and for ZnPd of 60°. In addition, the large standard deviation underlines that manual angle

measurement is error-prone. A distinct allocation for the crystal structure of the right side of the nanoparticle to ZnPd or Pd is therefore not feasible. In contrast to the right side, on the left side of the particle, as indicated by the orange arrows in Figure 6.11, the phase transforms with time. After 85 min, the measured lattice spacings of 2.9 ± 0.1 Å and 3.3 ± 0.1 Å match to ZnPd (0 0 1) of 3.27 Å and (1 0 0) of 2.89 Å, allowing an allocation to ZnPd.

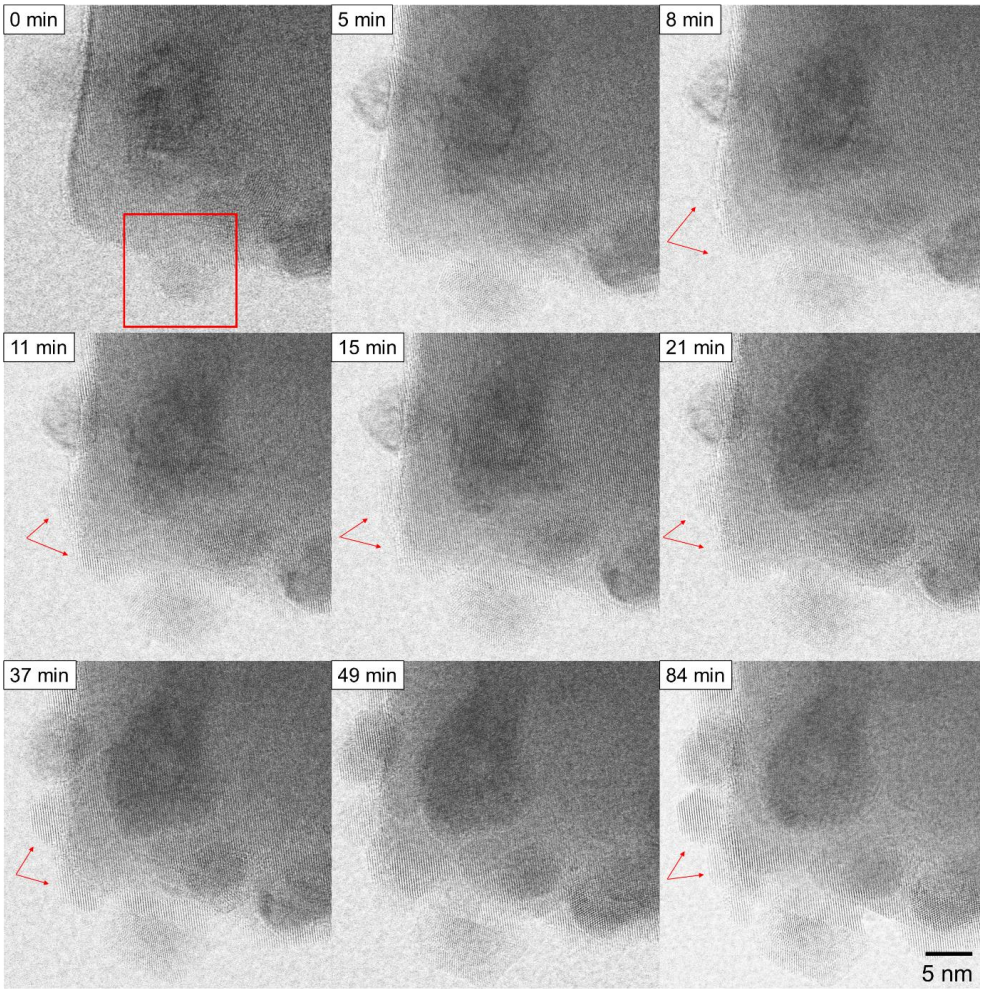

Figure 6.13: Series of BF images during the reduction of supported PdO at 200 °C. Time stamp indicates time of hydrogen injection. Red ROI marks location shown in Figure 6.11. The support is activated and encapsulates the nanoparticles. Red arrows show morphological evolution of ZnO.

6.4.1 Evaluation of Beam Effects During Reduction at 200 °C

Figure 6.14 shows sample locations, which have been imaged before and after, but not during, reduction at 200 °C to evaluate the effect of the electron beam. The crystal structure of the nanoparticle displayed in the left images can be identified as Pd along [1 1 0]. Intriguingly, the Pd phase is already present at 200 °C in vacuum before hydrogen is injected. After reduction, the lattice shows mild distortions, but can still be assigned to Pd.

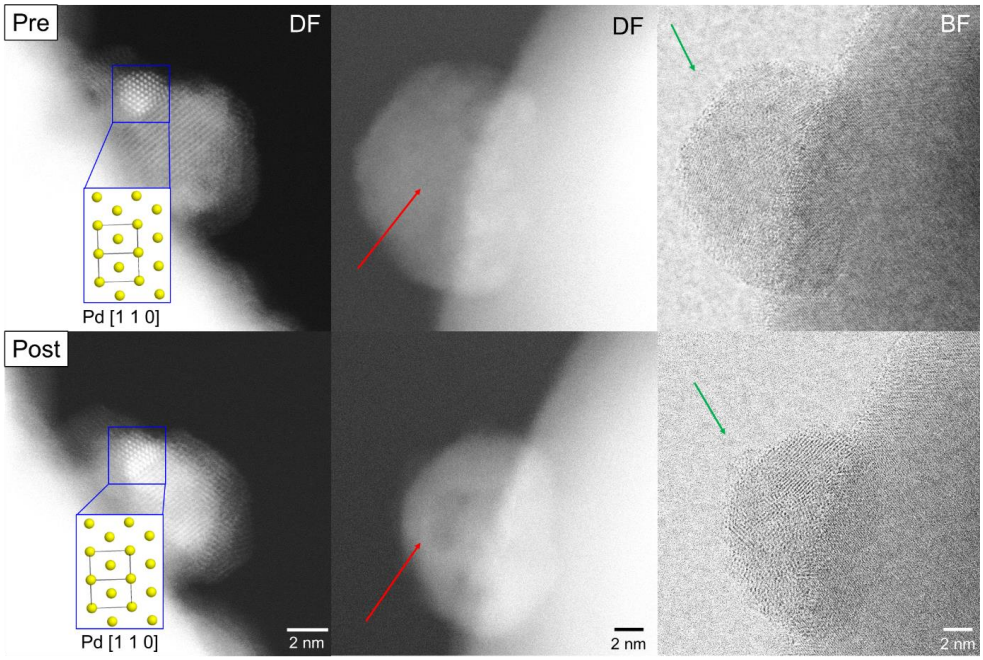

Figure 6.14: Comparison between sample locations before (top) and after (bottom) reduction at 200 °C. Left: Pd nanoparticle exhibit the same crystal structure along [1 1 0] before and after the reaction. Middle and Right: Identical sample location imaged in DF and BF. The red arrows show the formation of regions with darker DF contrast, indicating a mass loss. The green arrows indicate the nanoparticle decoration by the oxide.

In vicinity of the nanoparticle, the support is activated and has formed a cluster at the surface. Additional support activity can be seen on the nanoparticle, which is displayed in DF and BF images in Figure 6.14. Here, the BF image reveals formation of ZnO decorations on the nanoparticle, as marked by the green arrows. In the DF image, the nanoparticle is equally bright before reduction, indicating a homogenous thickness and mass distribution. After reduction, the edge appears brighter than the core, forming a core-shell structure, as highlighted by the red arrows.

6.5 Discussions

The *in situ* STEM experiments reveal a complex evolution of the support-nanoparticle system during reduction. Despite the occurrence of numerous simultaneous structural changes, the reaction can be divided into two distinct mechanisms: the activation of the ZnO support and the transformation of the nanoparticle. Potential effects, which arise due to the *in situ* conditions such as beam effects and low partial pressure, are discussed separately.

Activation of ZnO support

The STEM images and XRD measurements confirm that the pristine material system consists of PdO nanoparticles supported on ZnO. The absence of XRD peaks identifying palladium species can be explained by the small crystallite size and low loading. Potential PdO peaks are weak and broad, thus making them hardly distinguishable, as shown at ~34°. Thus, the occurrence of other Pd species such as Pd, PdH and ZnPd cannot be excluded and minor quantities might be present.

At room temperature, the ZnO support changes strongly during the initial 5 min of reduction. This is rather surprising, given that pure ZnO is known to resist reduction at such low temperatures, as derived in chapter 5 and shown in the Ellingham diagram in Figure 2.4. Thus, a direct activation of hydrogen by ZnO is unlikely and an interaction between the nanoparticle and support must be considered. In contrast to ZnO, PdO is known to absorb and dissociate hydrogen at a temperature of 110 K.[95] Activation of hydrogen on the surface of the nanoparticles is therefore more probable than on ZnO directly. The activation mechanism is schematically illustrated in Figure 6.16 and is similar to the SMSI model introduced by Fu et al. for the encapsulation of Pd by TiO_2.[125] Hydrogen species activated on the PdO surface migrate due to spillover from the nanoparticle to the ZnO surface. The existence of such hydrogen spillover effects from a noble metal to ZnO has long been known in methanol synthesis with Cu catalysts and is also expected here.[246] ZnO is partially reduced by spilt over hydrogen. Hydrogen combines with oxygen to water, which is desorbed from the ZnO surface and oxygen vacancies are generated. Due to the missing oxygen, Zinc states around the vacancy are unsaturated and donate delocalized electrons to the system. Such electron excess around the oxygen vacancies increases the Fermi-level and leads to an n-type doping of ZnO. The electronic structure of semiconducting ZnO is also determined by the composition and electronic nature of the supported nanoparticle.

The work function of materials W depends strongly on their Fermi-level E_F (eq. 6.1), where e is the charge of an electron and ϕ is the electrostatic potential in the vacuum.

$$W = e\phi - E_F \qquad 6.1$$

Since Pd and PdO with 4.8-5.6 eV and 6.04 eV have a higher work function than ZnO with 4.6 eV[84], their Fermi-level is lower. Consequently, the equilibrium at the interface between support

and nanoparticle is distorted. The present interface is similar in structure to a Schottky diode, where a metal and a n-type semiconductor form a junction. The equilibrium at the junction is restored by an electron transfer to the nanoparticle. As a result, the nanoparticle becomes negatively charged and the bands of ZnO are upbent, as illustrated in Figure 6.15. An electron depletion zone is formed.

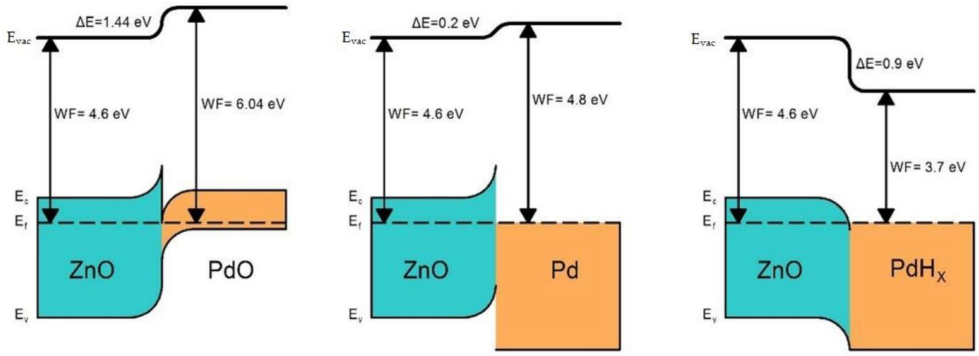

Figure 6.15: Energy diagrams of different heterojunctions illustrating different ZnO interfaces. PdO and Pd lead to an upbend of the ZnO energy band at the interface. Figure is taken from reference with permission.[84]

Due to oxygen vacancies, ZnO is defect rich and has a positive net space charge. The electrostatic attraction by the negatively charged nanoparticle promotes outward diffusion of positive Zn species and inhibit the transport of negative oxygen species to the surface at low temperature. The mass transport at room temperature is therefore activated by a combination of the present electrostatic force and the defect rich structure. Zn enrichment on the surface lowers the positive net space charge in bulk ZnO and oxygen starts to migrate to the surface and recombines to ZnO on the surface. Since sufficient oxygen diffusion, which is a prerequisite for stochiometric formation, is only achieved at higher temperatures, only oxygen-deficient ZnO_{1-x} ($x < 1$) enriches at room temperature. Such cluster are present in Figure 6.3. Their lower contrast can be also explained by a lower thickness. Nanoparticles are likely encapsulated by solid-solid wetting. Such mass transport in a single atomic or liquid-like movement is activated by a difference in surface energy and charge between nanoparticle and ZnO. Pd and PdO have a higher surface energy than ZnO.[247–249] In order to minimize the total surface energy of the system, oxygen-deficient and stochiometric ZnO cover the nanoparticle, as illustrated in Figure 6.3 and Figure 6.5. Oxygen-deficient ZnO appear to have a higher mobility, as it migrates to the side of the nanoparticle far from the support, forming a few atom-thick layer, which wets the nanoparticle. In contrast, stochiometric ZnO is less mobile and covers the lower part of the nanoparticle, reshaping its surface only. The bulk atoms tend to move collectively, indicating a 'liquid-like', slow mass transport as first described by Michaelson et al.[150] The difference in surface mobility can be caused by the negative charge of the nanoparticle. As oxygen-deficient

ZnO_{1-x} has a positive net charge, there is an attractive force for particle encapsulation. Stochiometric ZnO is neutrally charged, so there is no driving force for particle migration, which is reflected in lower mobility. As a result, the surface of the nanoparticle is decorated by different types of ZnO.

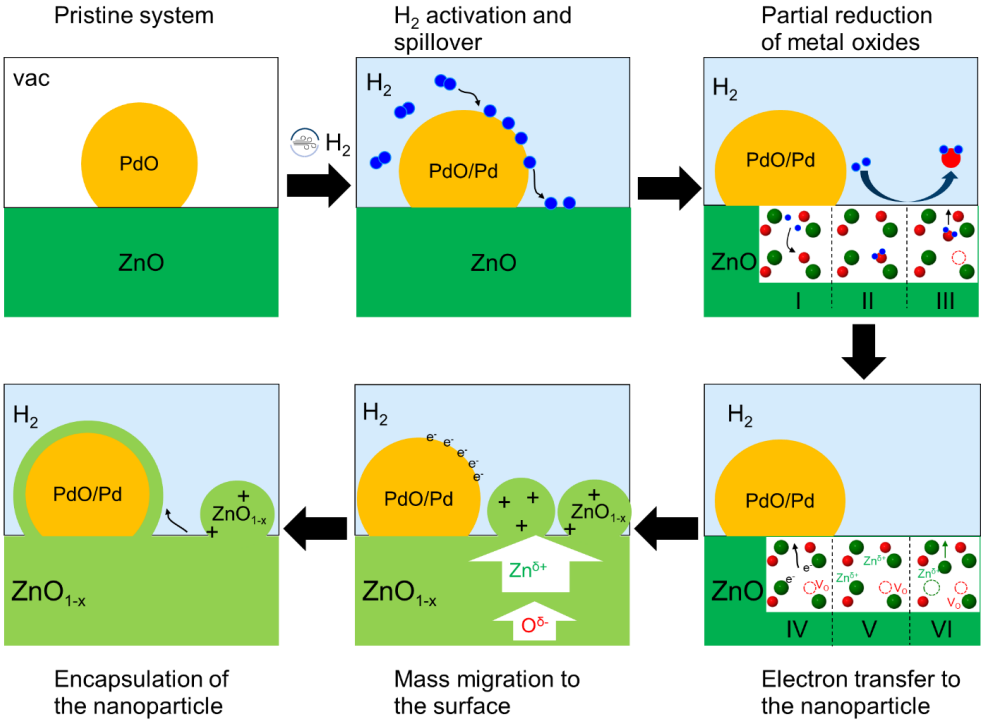

Figure 6.16: Schematic illustration of the surface activation mechanism during reduction. Zn is green, H blue and O red. Hydrogen is activated on PdO and spilt over to the support. In ZnO, hydrogen diffuses to lattice oxygen (I) and bonds, forming water (II). Water desorbs from the surface and generates an oxygen vacancy V_O (III). Unsaturated Zn species donate delocalized electrons to the system, which transfer to the nanoparticle (IV). Positive Zn species form a positive net space charge in ZnO (V). Positive net space charge is reduced due to Zn migration to the surface (VI). Subsequently, migration of negative oxygen species is activated and oxygen-deficient ZnO_{1-x} cluster form on the surface. The nanoparticle is encapsulated by Zn_xO to minimize the surface energy of the system.

After ~20 min, ZnO shows no further activity, indicating an equilibrium. This is in good agreement with the model derived above. The nanoparticle is now covered by ZnO, which reduces the surface energy and neutralizes the charge. Thus, the system is in an energetically favourable state with no apparent driving force for ZnO migration. This is reinforced by the coverage layer of the nanoparticle, which stops to grow after being a few atoms thick. As

illustrated by Figure 6.4, a coherent interface is formed between the nanoparticle and the covering layer, which determines the thickness of the covering layer. If there would be an additional driving force, a continuous grow of the layer is anticipated. However, this is not the case.

The interface between nanoparticle and coverage layer is presumably formed by a Zn-Pd bond. Given that the undistorted crystal structures of the interfacial regions are Pd and ZnO, the transition phase reduces the stress induced by the difference in lattice parameters and is bound by a metal-metal bond. Interfacial metal-metal bonds might act as a nucleus for the formation and growth of intermetallic compounds in RMSI. The existence of such intermetallic interfaces was already proposed by Tauster et al, who assigned the SMSI-related loss in chemisorption to the formation of metal-metal bonds at the interface during reduction.[115]

At 200 °C, the activation of the support is accelerated. As the encapsulation of the nanoparticles is completed within the first 3 minutes of reduction, the temporal resolution of image acquisition was too poor to dissect the individual steps of the activation mechanism. Due to rapid and complete encapsulation, it can be concluded that surface diffusion is significantly enhanced by an increase in temperature. Simultaneously, the temperature effect on bulk diffusion is lower, as the rate of ZnO cluster formation at the surface is similar to that of room temperature, which indicates a similar diffusion rate for outward migration of positive Zn species. In addition, encapsulation may have a detrimental effect on outward diffusion as it covers the negatively charged nanoparticle and thus reduces the electrostatic attraction for positive Zn species. The correspondence between the thickness of the coverage layers supports the assumption derived above that minimization of surface energy is the driving force for encapsulation. In general, the activation mechanism of the support at room temperature and 200 °C are in good agreement. The different kinetics of the reactions can be well explained by the temperature difference.

Although the pristine structure of the nanoparticle corresponds to PdO, the nature of the nanoparticle, e.g. if it is PdO or Pd, remains uncertain until ZnPd forms. The *in situ* images acquired do not allow a clear assignment of the structure to a Pd compound. However, the increase in Z-contrast during reduction indicates a compositional change, suggesting a gradual reduction of PdO to elemental Pd. The occurrence of a transformation is supported by the fact that PdO can be reduced at room temperature.[95] In addition, the PdO nanoparticles were observed to undergo rapid reduction at 200 °C. Consequently, the formation of elemental Pd is a probable outcome of the reduction process, despite the absence of a definitive structural evidence.

The distinct effect of hydrogen on the electric conductivity of Pd-supporting ZnO is also used for hydrogen detection.[84] The work by Platonov et al. demonstrates that a low hydrogen content of 40 ppm already leads to significant formation of PdH_x ($x \leq 0.6$) in oxygen-free atmosphere at 350 °C. In the present *in situ* experiment, activation of PdH_x formation might be hampered

kinetically by a low temperature or compositionally by a residual oxygen level in the microscope column. Furthermore, Tew and co-workers[250] reported a size-dependency on the formation of PdH_x. Smaller nanoparticles provide fewer interstitial places for the formation of hydrides and therefore incorporate less hydrogen in their lattice. In contrast, due to their higher surface to bulk ratio, smaller Pd nanoparticles have a higher relative surface absorption. In case of palladium hydrate formation, a reversed electron transfer is expected. As PdH_x with 3.7 eV has a lower working function than ZnO, the conduction band of ZnO is bent downward and electrons are transferred to ZnO bulk, which results in an increase in electric conductivity. As a consequence, diffusion of positive Zn species would be directed to the bulk and an enrichment of Zn on the surface is hindered. However, such structural behaviour could not be observed, since the surface showed distinct structural evolution with ZnO enrichment on the surface and the crystal structure of the nanoparticles did not correspond to PdH_x. In the study of Niu et al.[241], such pronounced support activation, including ZnO enrichments and particle encapsulation, was not reported. Potential explanations for this discrepancy may be found in the absence of palladium hydrate formation, as discussed previously, and variations in the preparation protocols. Niu et al. use polyvinylpyrrolidone during preparation, which could still be present during the in situ experiment and modify the surface properties, thereby limiting the mobility of ZnO and its surface migration.

In addition to crystalline ZnO coverage, surface contaminations are formed in the vicinity of the nanoparticles during reduction. The present contamination could be water and formed by recombination of activated hydrogen with oxygen provided by the oxides. However, as contamination could not be found homogenously over the specimen and at the sample which were annealed prior to the reaction, the sample is more likely to be contaminated by residual hydrocarbons, which are absorbed during preparation and are activated by the electron beam.

Transformation of the Nanoparticle

While the ZnO support was subject to strong structural evolution during the first part of the reaction (< 20 min) at room temperature, the individual nanoparticles were largely unaffected by the reactive atmosphere. However, after the encapsulation of the nanoparticle, new phases nucleate at the Zn-Pd interface, which have a considerable brighter DF contrast than the pristine particle phase, which indicates a gain in elemental mass and a compositional change. The higher Z contrast can be attributed to an incorporation of Zn into the Pd lattice. An increase in thickness as an explanation can be excluded as the nanoparticle is buried by surface contamination and there is no apparent driving force for an entropically unfavourable, strong change in local thickness. Furthermore, the novel phase can be distinguished due to a different crystal structure, which cannot clearly be identified after formation. Intriguingly, all nuclei are formed in direct contact with the interface between the nanoparticle and ZnO, indicating that the interface favours heterogenous nucleation. The intermetallic compound ZnPd has a wide, compositional existence range in the Zn-Pd phase diagram and its lattice parameters exhibit only small

mismatches to cubic Pd.[108] Chen *et al.* showed via density functional theory (DFT) measurements that Pd-Zn heteronuclear bonds are stronger than homonuclear Zn-Zn and Pd-Pd bonds.[251] Thereby, substitution of 50% of the Pd atoms in the Pd (111) surface by Zn forms the most stable ZnPd configuration. Given that ZnPd has a large enthalpy of formation[252], ZnPd formation is thermodynamically favourable. However, formation might be kinetically hampered due to low diffusion at room temperature.

The observed phase grows with an average rate of $3.7 \cdot 10^{-3}\ nm^2/s$ and $3.7 \cdot 10^{-17}\ cm^2/s$ respectively between 16 and 38 min. In order to determine if growth is controlled by diffusion, the interdiffusion rate of Zn in CuZn is used as reference. Since there is no literature available for the diffusion of Zn in Pd respectively in PdZn and CuZn has the same crystal structure and a similarly large unit cell (Cu a = 3.62 Å[253]; Pd a = 3.89 Å[254]), CuZn is used as an alternative. Kuper et al. reported a diffusion coefficient of $2.87 \cdot 10^{-13}\ cm^2/s$ for Zn in ordered and disordered copper-zinc at 264 °C.[255] Eastman et al. found similar values for interdiffusion coefficients for the same system in the range of $10^{-12}\ cm^2/s$ at 100 °C.[256] Assuming that the given Arrhenius plots are correct at room temperature, the growth rate has about the same order of magnitude as the anticipated diffusion coefficient at room temperature. Since the diffusion coefficients depend on composition and temperature, the approach should be considered a guideline only that semi-quantitively supports the assumption that growth is controlled by diffusion.

Incorporation of Zn into the Pd lattice is also supported by dissolution of ZnO at the interface. As shown in Figure 6.6, continuous loss of ZnO image contrast indicates a decrease in thickness. Such behaviour is predominately found in the vicinity of a growing phase. Remote ZnO regions do not demonstrate such behaviour. After ~ 60 min, a stable multicrystalline system is formed. The observed structure features of the novel phases correspond well to ZnPd. In particular, the good agreement along two crystallographic directions allow an identification, as illustrated in Figure 6.8. Little deviations in size and angle from the structure model can be explained by the accuracy of measurement, broad compositional existence range of ZnPd, small particle size leading to a high surface to volume ratio, strain induced by contact to different crystal structures and potential imaging artefacts such as de-scan, calibration inaccuracy and residual lens aberrations. Intriguingly, residual parts of the nanoparticle have still the pristine crystal structure and contrast. Such pristine crystals are predominately found in the centre of the nanoparticle, while the 'skin' is transformed to ZnPd, which leads to a core-shell structure. The present formation can be explained by kinetic limitations at room temperature and compositional changes. Given that most Zn is provided from the interface directly, Zn penetrates into Pd, diffuses through the Pd lattice and forms ZnPd. As the diffusion coefficient of Zn in ZnPd is smaller than in Pd, assuming a similar diffusion coefficient for Zn as in CuZn, the already small diffusion at room temperature is further reduced and now hampers any substantial Zn transport to the centre. This explanation is supported by similarities in size

between different ZnPd phases. A restriction due to consumption of all available Zn and Pd in the system is unlikely, as Zn and Pd could be supplied by covering layer and the centre of the nanoparticle.

Interestingly, formation of ZnPd was only observed in the former Pd nanoparticle, but not in the encapsulating ZnO layer. Given that Cu in ZnO has similar diffusion properties to Pd, its diffusion rate in ZnO is significantly lower than that of Zn in the Pd lattice ($10^{-12}\ cm^2s^{-1}$ compared to $10^{-6}\ cm^2s^{-1}$ at 1000 °C)[255,257], suggesting that inward diffusion of Zn species is dominant over outward diffusion by Pd species. Such behaviour, in which the diffusion rate of a semiconducting species at an interface is faster than that of its metallic counterpart, is known as reversed 'Kirkendall' effect[258] and also applies here. In addition, the segregation of Zn to Pd is energetically more favourable.[251]

At 200 °C, the structure of the nanoparticle transforms rapidly from PdO to Pd. The advanced kinetics can be explained by the higher temperature. Reduction of PdO in certain morphologies, e.g. small particles, can already be activated by pure heating in vacuum already, as the Pd crystal structure is found in some nanoparticles before hydrogen was injected. Such behaviour emphasises the energetically favourable reduction of PdO at 200 °C. Accordingly, it is likely that the sample site studied *in situ* at 200 °C formed a monocrystalline Pd structure even before the hydrogen was first injected. While the right side of the nanoparticle remains unchanged during reduction, the left side transforms to ZnPd (Figure 6.11). Dissolution of neighbouring ZnO may be an indicator for Zn incorporation into the Pd lattice. Reference regions support the model of partial reduction, as the darker core in DF indicates a lower elemental mass and heterogenous element distribution in the nanoparticle (Figure 6.14). Such partial transformation, which was also found during reduction at room temperature, is in correspondence with the work by Penner *et al.*[108] Penner *et al.* studied the reduction of supported Pd nanoparticles *ex situ* at 1 bar hydrogen pressure. They demonstrated that Pd nanoparticles at a temperature of 250 °C predominantly occurred in a partially alloyed state, forming a ZnPd skin but retaining the elemental Pd core. At a temperature above 323 °C, a complete transformation of Pd into ZnPd was achieved. Formation of ZnPd could also be found at the lowest tested temperature of ~200 °C, which is consistent with the work by Iwasa *et al.*[107,259] The correspondence between the in the present *in situ* work and the absence of ZnPd peaks in the XRD and XPS data obtained by Iwasa *et al.*[259] after reduction at room temperature can be explained by closely neighbouring peaks and small thickness of ZnPd of 1 - 2 nm, which broadens the XRD signal. In addition, the XPS signal might be superimposed by the Pd and PdO phases present, which confine the ZnPd peak, and by a sample with higher catalysts loading, favouring bigger particles and thus the core species. Furthermore, the relatively strong ZnPd formation at room temperature can partially be explained by the experimental conditions.

Effects Induced by Experimental Conditions

There are three major differences between the present *in situ* E-STEM experiment and a conventional reduction under ambient laboratory conditions: The presence of an electron beam, lower chemical potential due to low partial pressure and lower temperature. The listed parameters will be discussed below.

An electron beam introduces kinetic energy and charge to the observed system. In case of a *in situ* gas experiment, the properties affect the sample and environment. Since the electron beam probe is in the nm-range, a beam effect will only be anticipated in imaged regions. Interaction between the electron beam and hydrogen may form hydrogen plasma. Due to the presence of atomic, ionic and excited hydrogen species, hydrogen plasma is recognised to exhibit a high reduction capacity for many metal oxides even at low temperature, typically superior to that of molecular hydrogen.[153] A quantification of the reduction potential of different hydrogen species for metal oxides is shown in Ellingham diagrams, as illustrated in Figure 2.4. Such diagrams show that the Gibbs free energy change for atomic and ionic hydrogen is 3 and 15 times less than that of molecular hydrogen, respectively, confirming that activated hydrogen is capable of directly reducing ZnO if present.[153,260] As demonstrated in chapter 5, pure ZnO is hardly reduced at 200 °C at a hydrogen atmosphere. As same imaging and environmental conditions were applied during the reduction of supported PdO, it can be concluded that the amount of hydrogen plasma generated by the electron beam is only small and its potential effect can be neglected for *in situ* experiments.

Direct interaction between the electron beam and the specimen must be considered, as nanoparticles can suffer from beam effects such as structural and electronic changes as well as local heating effects. Kim et al. demonstrated in their work that strong electron beam irradiation with beam energies of 1 MeV induces structural defects to Pd-supporting ZnO.[261] Typical structural defects, which can be generated[262], are oxygen vacancies and Zn interstitial defects (Frenkel defects[263]). These Zn interstitial defects may donate additional delocalized electrons to the system that may lower the work function of ZnO and increasing the electron depletion zone in ZnO. In addition, donor defects in semiconductors can act as active sites in the chemisorption process[264–266], thereby amplifying the process itself. It is likely that such phenomena also apply during support activation of the present *in situ* reduction experiments, so that electron transfer to the nanoparticle is increased and the above-mentioned mechanism of ZnO migration is facilitated. Sample regions, which were exposed to the electron beam during reduction, exhibit more pronounced support activity than reference regions. The amplified support activity is reflected in the enhanced encapsulation and the formation of ZnO clusters on the surface. An enhancement in chemisorption capabilities is likely to participate in the support activation, since the support was not activated by pure beam exposure but in combination with hydrogen during *in situ* experiments. However, the imaging conditions during the reduction experiment result in a lower beam dose to the system than the intentional electron beam treatment by Kim *et al.*[261] with lower exposure times (20 s instead of 54 s), lower beam

energy (200 kV instead of 1000 kV) and lower beam current (10 µA instead of 1000 µA), so that a lower beam effect on the present *in situ* experiment can be expected. Since both mechanisms were also found at reference locations with no beam exposure during reduction, the mechanisms were facilitated but not triggered by the electron beam. At the same time, these findings underline that SMSI and RMSI can be facilitated and potentially activated by an electron beam. This activation mechanism is interesting for the catalyst design of supported nanoparticles, where metal-support interactions enhance catalytic properties and therefore are deliberately triggered.

In addition to the energy of the electron beam, charges may accumulate on the support due to low electric conductivity of ZnO, manipulating the electric properties of ZnO and thus migration of the Zn/O atoms. So far, the debates on the nature of the charge induced by the electron beam in TEM have not yet been resolved[267,268], so that no assessment of the effects of the potential charge on the reduction will be made at this point.

Interaction with the electron beam can deposit energy to the specimen, generating heat and increasing the temperature of the system. The extent to which the local temperature is changed by the electron beam depends on numerous parameters such as the heat capacity and conduction and size of the materials, the electron beam dose and energy, the proportion of elastic and inelastic interaction between the sample and the beam, so that precise quantification is difficult and depends sensitively on the material and imaging system used.[269,270] As a detailed quantification of these processes would exceed the scope of this work, the temperature will be estimated at this point using literature values. The temperature gain of materials in the nanometre range is normally in the two-digit Kelvin range and increases with increasing particle size and beam current and decreasing with higher accelerating voltages.[271] Therefore, an increase in temperature (< 50 °C) is expected in the present *in situ* experiment, which introduces minor changes only. For the room temperature experiments, the temperature increase caused by the electron beam may facilitate the observed structural changes due to higher diffusion.

Gas *in situ* experiments in an open cell are limited to relatively low pressure. In the present E-STEM experiment the hydrogen pressure applied was around 1.5 Pa, which is significantly lower than the partial pressure of 100 kPa in the reduction by Penner *et al*[108] and the *ex situ* investigation of the sample. The reaction kinetics of chemical reactions are directly determined by the present chemical potential and thus the partial pressure.[272,273] A low partial pressure can therefore change the kinetics and the outcome of a reaction and also applies during synthesis. Such a pressure-related discrepancy in reaction kinetics is referred to as a ‘pressure gap’ and must be considered here. The partial pressure of hydrogen in an atmosphere therefore determines its reducing properties. A higher hydrogen content increases the reducing properties. However, the reducing properties of an atmosphere also depend on the residual amount of oxygen, as oxygen may re-oxidize metals and the reducing gas component. Platonov *et al.* demonstrated the influence of residual oxygen on Pd/ZnO and its ability for hydrogen detection

during reduction in a hydrogen atmosphere.[84] The absence of oxygen, as is the case in the UHV, can have similar properties and trigger similar reactions as a reduction in hydrogen, as shown by the work of Penner *et al.* in which ZnPd was formed on ZnO at elevated temperature in the UHV.[274] As a result, the present *in situ* experimental conditions may produce similar reducing properties as the *ex situ* experiment at 100 kPa hydrogen pressure due to the absence of oxygen resulting from the former high vacuum and the injected hydrogen. For instance, elemental Pd was found after pre-treating the sample at 200 °C in vacuum. In addition, there are similar results between *in* and *ex situ* experiments, e.g. ZnPd phases were found despite the low partial pressure. These findings provide support for a small pressure gap.

To sum up the effects induced by the experimental conditions, all of the derived beam effects may affect the present *in situ* reduction experiment. However, activation and transformation of reference regions, which were only imaged before and after reduction, indicate that the mechanisms derived may be facilitated and but not triggered by the electron beam. In addition, similar results between *ex* and *in situ* experiments indicate a small pressure a gap.

Conclusions of PdO Reduction

In summary, the reduction of PdO and formation of ZnPd is divided into two mechanisms. The first mechanism comprises the activation of the ZnO support by hydrogen spillover, ZnO migration to the surface, and an encapsulation of the nanoparticle. The second mechanism includes nucleation of the ZnPd phase, its diffusion-controlled growth and the formation of a core-shell structure due to kinetic limitation that are in good agreement with similar *ex situ* experiments. As a result, ZnPd nanoparticles with a thin ZnO shell are formed. The electron beam may enhance the effects of the reduction but not trigger them as shown by reference regions and the stability under pure electron beam exposure. Other potential effects induced by the experimental conditions such as formation of hydrogen plasma, temperature differences and pressure gap have a minor impact and can largely be neglected. The RMSI mechanism has many similarities with SMSI but is different in the interaction between nanoparticle and coverage layer, where an intermetallic phase is formed at RMSI. These results are interesting for many scientific communities such as heterogenous catalysis, reaction kinetics and hydrogen detection as it demonstrates the present formation in small steps.

7 Methanol Steam Reforming on Zinc Palladium Nanoparticles Supported on Zinc Oxide

The work in this chapter was performed in collaboration with the TU Chemnitz, Germany. Oytun Tiryaki and Marc Armbrüster prepared the studied ZnPd/ZnO sample and conducted the XRD measurement.

It is well-known that ZnPd nanoparticles on ZnO support exhibit excellent catalytic properties in methanol steam reforming.[37] However, as-prepared catalysts show poor CO_2 selectivity and high selectivity is only formed during methanol steam reforming, indicating a structural evolution of the catalytic system. Heggen and co-workers reported the presence of ZnO patches on ZnPd nanoparticles after methanol steam reforming.[45] The formation of ZnO patches appear to play a pivotal role in the change in selectivity. Given that the ZnO patches increase the selectivity of the ZnPd system, an *in situ* study about the conditions required for their formation and the formation process itself may elucidate the working mechanism of ZnPd catalysts during MRS. *In situ* TEM is required to enable imaging of the change in the catalytic system, since the anticipated changes take place on a nanoscale and are only active under reaction conditions. The reproduction of methanol steam reforming conditions inside an electron microscope is challenging, as it requires the injection of a steam mixture. *In situ* TEM configuration are typically designed for the injection of a gas or a liquid, while a steam configuration needs a high sophisticated control of the reaction parameters, for instance condensation effects. Effects such as pressure, temperature and the impact of the individual components need to be considered.

This chapter addresses the structural evolution of ZnPd nanoparticles supported on ZnO, which are triggered by methanol steam reforming. Two experimental *in situ* configurations are employed, namely open cell and closed cell configuration, in order to satisfy the varying pressure ranges and resolution requirements. The injection of individual components, as well as methanol steam and water mixtures, elucidates the effect of the components and the chemical potential required for ZnO patch formation that are triggered by methanol steam reforming.

7.1 Experimentals

Palladium nitrate nanoparticles supported on zinc oxide were prepared with different Pd loadings between 1 and 10 wt.%, as described in chapter Figure 4.1. The samples were calcined at 500 °C for 3 h in O_2:N_2 (20:80) and subsequently reduced at 500 °C for 2 hours in H_2:Ar (5:95), adapting the preparation protocol for catalytically active ZnPd nanoparticles introduced by Iwasa *et al*.[92,259] The sample was dispersed in ultra-pure water and deposited via drop-cast method on a SiN membrane of a respective MEMS heating chip (chapter 3.2).

Open Cell Configuration

The open cell setup used for the *in situ* methanol steam reforming experiment is introduced in chapter 3.2.1. ~20 ml of methanol (Sigma Aldrich, anhydrous, 99,8%) and deionised water were filled in the respective containment bottles, which were connected to the closed metering valves and sealed with a copper sealing ring. The bottles were dipped in a bath of liquid nitrogen for ~5 min to freeze the liquids inside. The metering valves were then opened and the residual gas was evacuated by a TMP, creating a vacuum < 10^{-4} mbar in the vaporiser system. The metering valves were closed and the methanol and water ice were heated to room temperature, thus restoring the initial state.

The loaded heating chip was mounted on a single tilt heating holder (Hitachi High-Tech Canada, Toronto, Canada) and the holder was inserted into the HF5000 (specifications are given in chapter 3.2.1), operating in HR and HR mapping STEM mode mostly at 200 kV. Only the experiments in chapter 7.3 and 7.4.2 were conducted at 60 kV. The ZnPd nanoparticles were reduced at 200 °C for 1 hour in a hydrogen atmosphere with a mass flow of 2.5 sccm, which translates in a specimen pressure of ~2 Pa. In some experiments, the hydrogen was moisturised with an uncertain amount of water and/or methanol, as derived in chapter 7.6. After reduction, the entire *in situ* configuration, including the microscope column, mass flow controller, gas supply system, tubing and vaporiser system, excluding the liquid bottles, were evacuated for ~15 min at a vacuum pressure < 10^{-4} mbar. Methanol steam reforming conditions were initiated by opening the metering valves. ~ 15 min after opening the metering valves, the steam mixture was injected with a mass flow of 1 sccm in the microscope column, creating a specimen pressure of ~4 Pa. MSR experiments were conducted at 200 °C and 320 °C. After each MSR experiment, the system was evacuated and the microscope was baked.

The regions of interest were only exposed to the electron beam during image acquisition and focus alignment. Reference regions were only image before and after the reaction, to evaluate the electron beam effect. Only after reaching a pressure of 10^{-5} Pa, reference images were acquired, such that the electron beam could not interact with the atmosphere.

Closed Cell Configuration

Methanol steam reforming experiments were performed by using the closed cell configuration, which is introduced in chapter 3.2.2. The sample was reduced for 1 hour at 200 °C at a pressure of 700 mbar in a hydrogen: argon mixture (4:96) with a mass flow of 1 ml/min. Subsequently to reduction, the piping was flushed using pure argon (99,9 %) for 10 min. A 1:7 liquid methanol: water mixture was weighted in and added to the wet line. Argon was employed as a carrier gas and completely directed through the wet line of the vaporizer, bubbling through the methanol-water mixture. The saturated argon was streamed over the sample for 45 min with a pressure of ~800 mbar with a mass flow of 0.4 ml/min at a sample temperature of 320 °C. Images were captured with an exposure time of 0,33 s/frame during the *in situ* experiment.

7.2 Characterisation of Pristine Zinc Palladium Nanoparticles

Pristine ZnPd nanoparticles supported on ZnO are investigated using STEM and XRD. Corresponding SE images, XRD measurements and PSDs are shown in Figure 7.1.

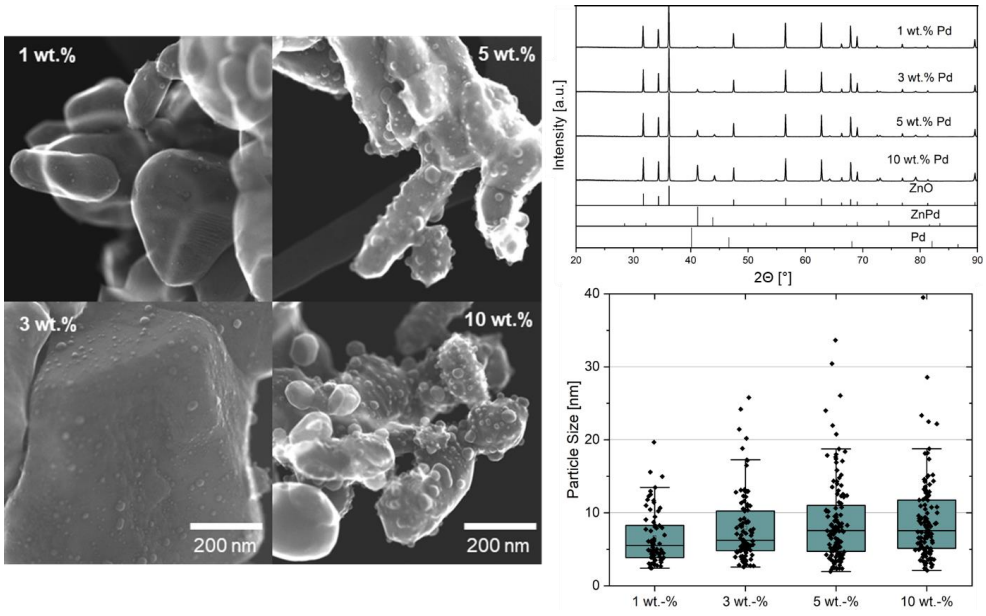

Figure 7.1: Left: SE image series of ZnPd nanoparticles supported on ZnO with different Pd loadings. Right top: Corresponding XRD measurements of the identical sample batch. XRD reflexes of pure ZnO, ZnPd and Pd are given as reference. Right bottom: A particle size analysis which shows the size distribution of ZnPd nanoparticles according to the total Pd loading.

SE images show that ZnPd is homogenously distributed on ZnO regardless of the loading. Only a few nanoparticles aggregate to clusters. Higher loadings cause higher particle densities on the ZnO surface. Over 50 nanoparticles are measured in two perpendicular directions to determine each PSD. PSDs demonstrate an increase in size with loading. For instance, the sample with 1 wt.% Pd loading has an average particle size of 6.6 ± 3.8 nm, 10 wt.% Pd loading of 9.0 ± 5.8 nm. In addition, the distribution broadens with loading, indicating accumulation of single bigger nanoparticles for higher loadings. The XRD measurements show characteristic reflections for ZnO and ZnPd. The ZnO reflections exhibit similar intensities for all loadings, as the same ZnO batch is used as support. In contrast, the ZnPd reflections scale with Pd loading. For instance, the reflexes at ~41 and 43° are most pronounced for a loading of 10 wt.%. At 3 wt.% and 5 wt.%, these peaks are relatively weak. Minor ZnPd peaks are not detectable at the present loadings.

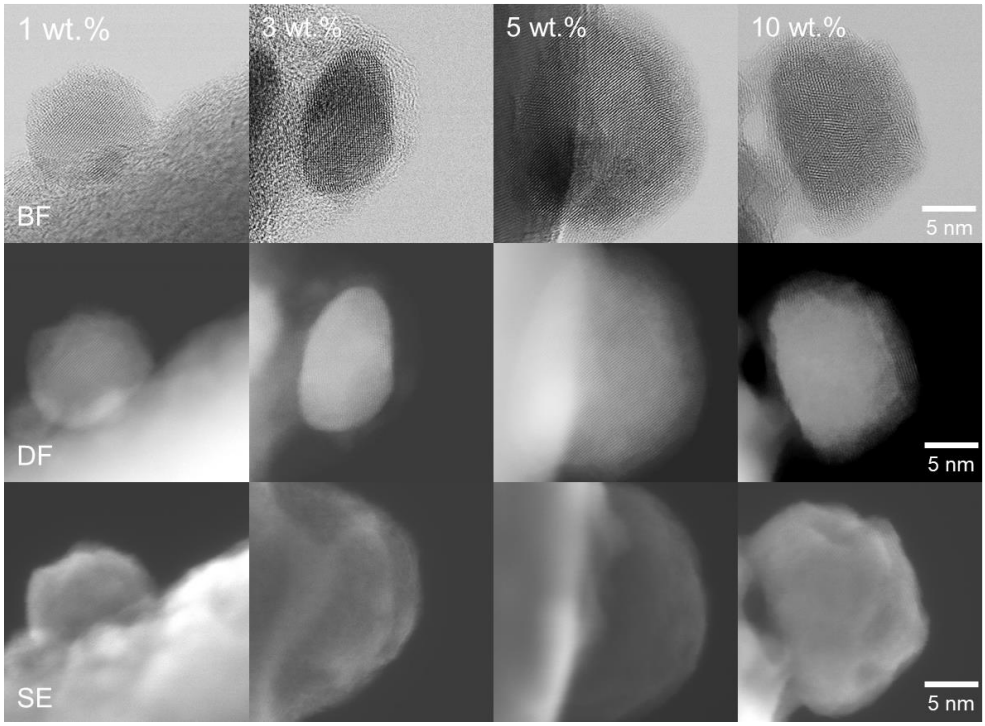

Figure 7.2: Series of BF, DF and SE images of ZnPd nanoparticles supported on ZnO with different Pd loadings (1 – 10 wt.%). Images in one column represent the same nanoparticle. Some ZnPd nanoparticles are coated with a thin surface layer.

Figure 7.2 shows a selection of high magnification images of ZnPd nanoparticles from sample batches with different Pd loadings. Representative nanoparticles have a polycrystalline structure, which are homogenous in composition, examined by the constant brightness of the DF images. Some nanoparticles, e.g. samples with 5 and 10 wt.%, are coated by a thin surface layer with lower contrast, as shown in the DF images in Figure 7.2. ZnPd is located on flat ZnO and ZnO nanorods, similar to that described in chapter 0. Occasionally, contamination forms around the nanoparticles during image acquisition at high magnification.

In summary, samples with different Pd loadings exhibit ZnPd nanoparticles that are largely similar in size and structure. The increase in mean particle size at higher loadings is due to single, larger nanoparticles that are more likely to form. It is therefore assumed that isolated ZnPd nanoparticles are approximately identical and that the structural changes to a single nanoparticle are independent of the Pd loading. Consequently, results obtained from experiment with different loadings are analysed equally.

7.3 Reduction in a Pure Hydrogen Atmosphere

ZnPd nanoparticles supported on ZnO were reduced at 200 °C in hydrogen before exposing them to methanol steam reforming conditions. Figure 7.3 shows a ZnPd nanoparticle during reduction. The E-STEM images were acquired at 60 kV.

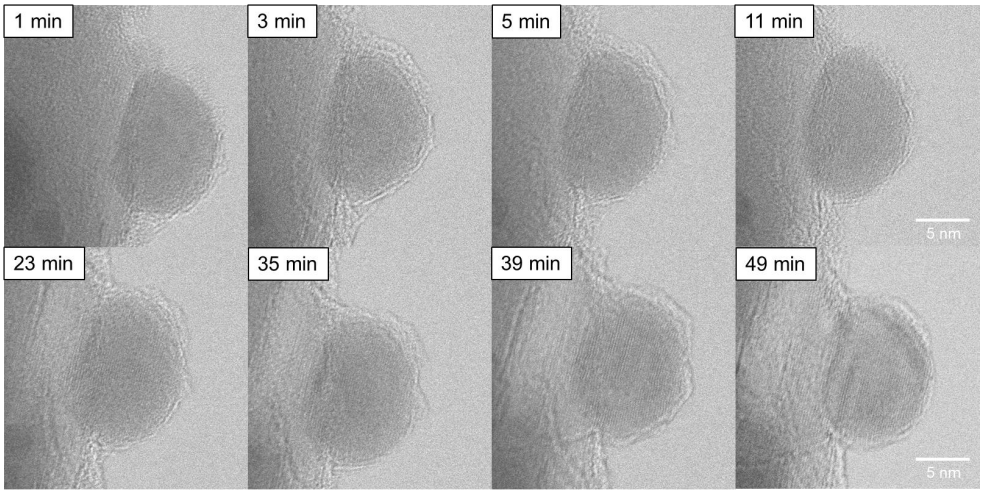

Figure 7.3: *In situ* BF images series of supported ZnPd nanoparticles, which are reduced at 200 °C in hydrogen atmosphere. The E-STEM was operating at 60 kV. Time stamps indicate time of reduction. The system shows no significant change in structure. ZnO decomposes slightly in the perimeter of the nanoparticle.

Nanoparticle and support are covered by a thin amorphous layer, which is preserved throughout reduction. The structure of the nanoparticle is largely unaffected by the reductive treatment and irradiation of the electron beam. ZnO begins to decompose slightly at the perimeter of the nanoparticle after ~ 35 min of reduction.

In addition, selected ZnPd nanoparticles were imaged solely before and after the hydrogen experiment in order to evaluate electron beam effects. BF and DF images of such reference locations are shown in Figure 7.4. In agreement with the *in situ* data, the nanoparticles show no significant change in structure. Perimetric ZnO exhibit slight traces of decomposition. The morphology of ZnPd nanoparticles evolves during reduction, which is indicated by formation of facets, as highlighted by the red arrows in Figure 7.4. The marked ZnPd crystal matches well to an alignment along [1 0 0], as the measured lattice spacings of 2.9 ± 0.1 Å and 3.5 ± 0.1 Å are in good agreement to ZnPd (0 1 0) with 2.89 Å and (0 0 1) with 3.33 Å.[46] Given that the crystal is orientated as derived, the present facets are ZnPd (0 0 1) and (0 1 1).

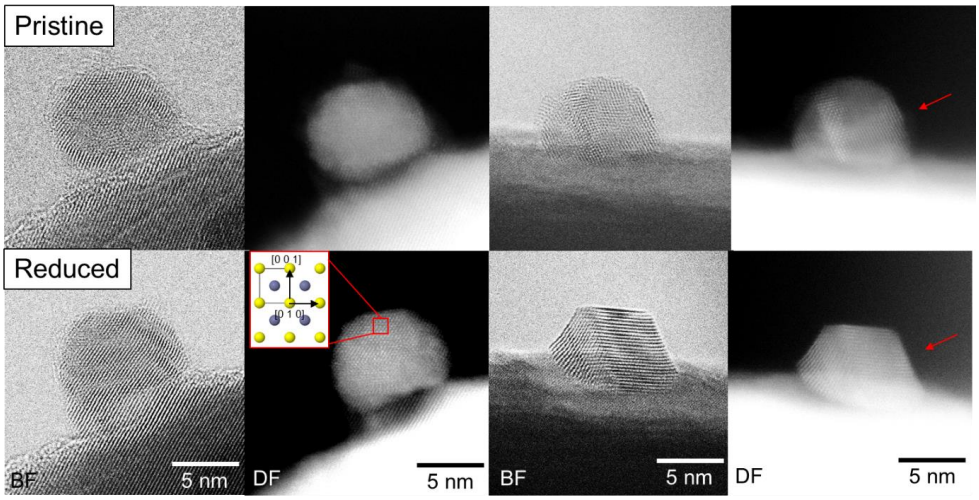

Figure 7.4: BF and DF images of two ZnPd nanoparticles imaged before (top row) and after (bottom row) reduction. Locations were not exposed to the electron beam during hydrogen injection. Red arrows indicate faceting. ROI highlights ZnPd crystal along [1 0 0] direction. Crystal model is adapted from reference.[46]

Further images, which are acquired after reduction, are shown in Figure 11.16. Faceting only occurs with some nanoparticles. In particular, larger nanoparticles maintain their round, isotropic shape. In addition, decomposition of ZnO close to the nanoparticles is frequently observed, especially with higher exposure times. Some nanoparticles are covered by thicker surface layers and decorations. It could not be determined whether such phenomena are formed during reduction or are already present at the pristine nanoparticle.

7.4 Effects of Individual Components

During the methanol steam reforming, water and methanol are converted into hydrogen and carbon dioxide. Since the interaction of the components is expected to trigger a structural evolution of the catalyst under the right reaction parameters, it is crucial to derive the effect of the individual components. In this chapter, the effect of pure water, and methanol steam on ZnPd nanoparticles supported on ZnO is studied using E-STEM.

7.4.1 Exposure to Water Steam

After reduction in a hydrogen atmosphere, supported ZnPd nanoparticles are exposed to a pure water steam at 320 °C. Figure 7.5 shows the evolution of a selected ZnPd nanoparticle during exposure to water steam. The experiment was conducted at an acceleration voltage of 200 kV.

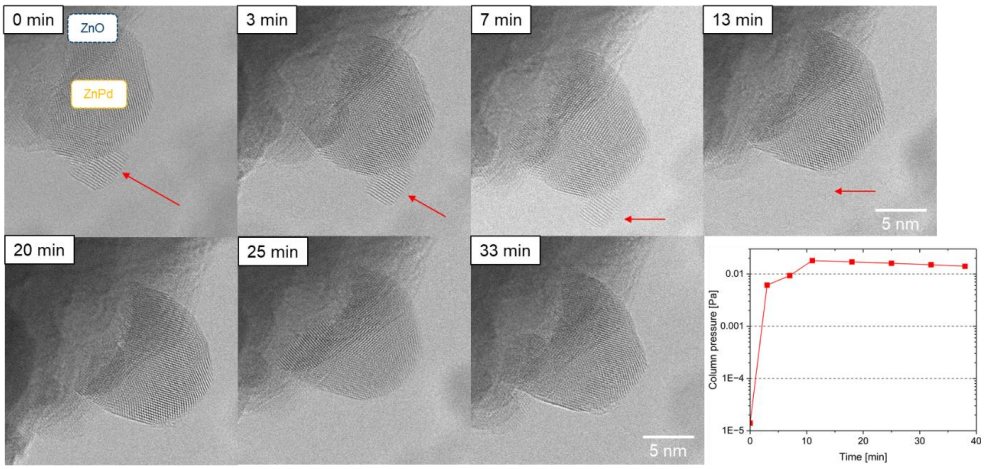

Figure 7.5: Series of BF images of ZnPd nanoparticle exposed to water steam at 320 °C. Time stamps indicate the time of water steam injection. The graph shows the corresponding column pressure. The red arrows indicate the detachment of a surface feature.

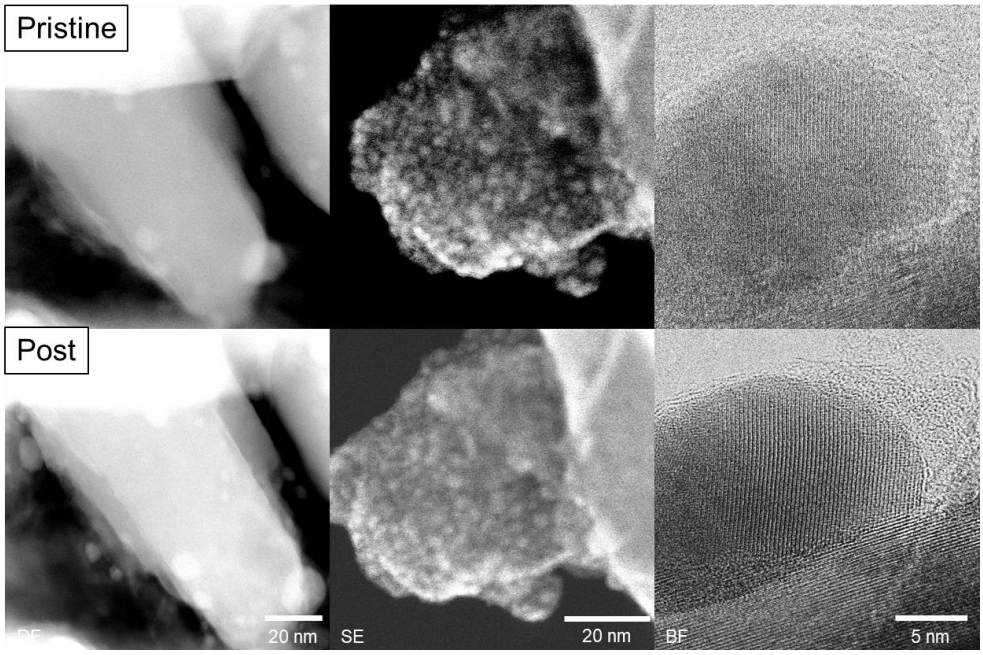

Figure 7.6: Series of images of different reference locations acquired before (top) and after (bottom) water steam exposure. Locations were not exposed to the electron beam during water steam injection.

The column pressure remains approximately constant after 10 min of equilibration, so stable reaction conditions are anticipated. The nanoparticle is stable throughout the exposure to water steam, as its crystal structure does not change. The nanoparticle shows only minor temporary elongation between 13 and 33 min. As indicated by the red arrows, a surface feature, which is present at the pristine nanoparticle, is dispatched after 13 min of water steam injection. In addition, the ZnO support maintains its morphology.

The results of the *in situ* experiment are in good agreement with those of the reference locations, which were not exposed to the electron beam during water steam injection. Figure 7.6 shows the reference locations before and after water steam injection. There are no apparent changes in structure between the two states. The difference in contrast is due to different imaging conditions.

7.4.2 Exposure to Methanol Steam

After reduction in a hydrogen atmosphere, supported ZnPd nanoparticles were exposed to pure methanol steam at a pressure of ~ 3 Pa at 320 °C for 60 min. The metering valve sealing the methanol bottle was opened when the mass flow into the microscope column was activated. The change in column pressure is shown in Figure 7.8a. When the mass flow was activated, the column pressure increased to a constant level of ~ $5 \cdot 10^{-3}$ Pa. After 25 min of injection, the column pressure increased rapidly to a maximum value of ~ $2 \cdot 10^{-2}$ Pa. The *in situ* experiment was conducted, employing an acceleration voltage of 60 kV.

Figure 7.7 shows the *in situ* evolution of a ZnPd nanoparticle during the methanol steam experiment. Further SE and DF images are shown in Figure 11.17. In the first 10 min of injection, the nanoparticle is stable, maintains its shape and is coated by a thin amorphous surface layer. The nanoparticle then starts to develop a more spherical shape. In order to quantify the change in shape of the nanoparticle, roundness and circularity are calculated using eq. 7.1 and 7.2.[275]

$$Roundness = \frac{4 \cdot Area}{Perimeter \cdot Diameter} \quad 7.1$$

$$Circularity = \frac{4 \cdot Area \cdot \pi}{Perimeter^2} \quad 7.2$$

Values for area, perimeter and Feret diameter are obtained and are shown in Figure 7.8b. Three measurements per time are averaged, with the standard deviation given as the error. Calculated values for roundness and circularity are illustrated in Figure 7.8c. Both parameters increase in the first 30 minutes, with the circularity increasing more steadily than the roundness. Both parameters reach their maximum at ~ 30 min with 95% of circularity and 92% of roundness, minimizing the surface area of the nanoparticle. At the same time, the contrast of the support

close to the nanoparticle weakens, indicating decomposition of ZnO. The amorphous surface layer also decomposes and becomes thinner.

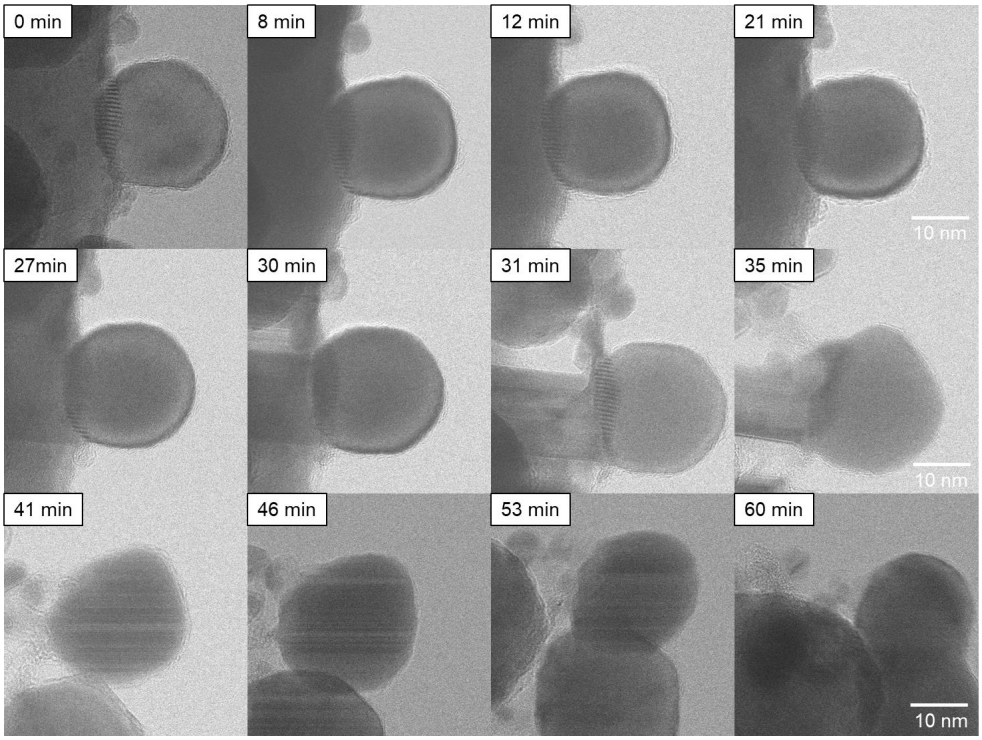

Figure 7.7: Series of BF images of a ZnPd nanoparticle exposed to methanol steam at 320 °C. Time stamp indicate time of methanol injection. DF and SE images of the same *in situ* experiment are displayed in Figure 11.17.

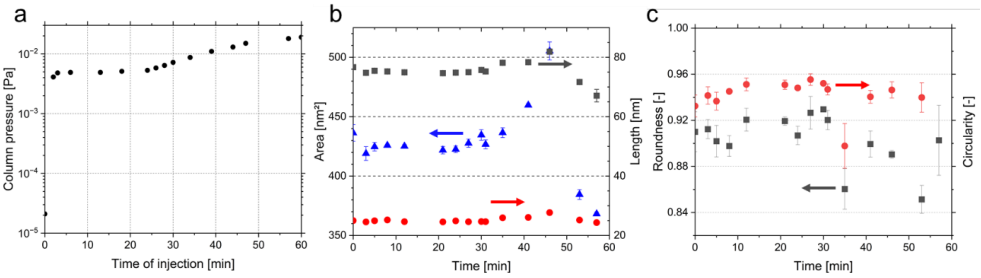

Figure 7.8: Properties of ZnPd nanoparticle studied *in situ*, as shown in Figure 7.7: a) Logarithmic illustration of the change in column pressure as function of time with a constant injection rate. b) Change in area (blue), Feret diameter (red) and perimeter (black) of the nanoparticle considered over time. c) Corresponding roundness (black) and circularity (red) of the nanoparticle calculated using eq. 7.1 and 7.2. Circularity and roundness have the same axis scale.

After 30 min of methanol steam injection, the support decomposes strongly. Intriguingly, decomposition around the nanoparticle removes ZnO, such that a residual nanocolumn is formed that supports the nanoparticle, as illustrated after 31 min in Figure 7.7. The nanocolumn appears to form along a crystallographic plane. At the interface between nanoparticle and column a Moiré pattern is present, indicating the presence of different crystal structures and partial encapsulation.

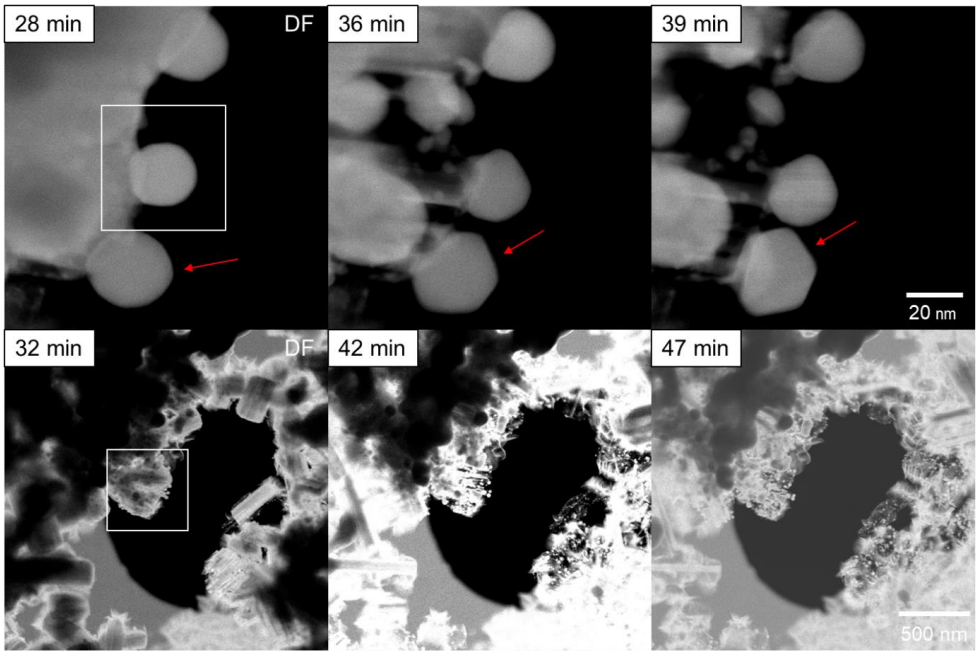

Figure 7.9: Series of DF images acquired at lower magnifications during methanol steam injection. The red arrows indicate temporary faceting of nanoparticles. White ROI highlights the region, which was observed at higher magnification in Figure 7.7.

The ZnPd nanoparticles are not affected by decomposition. The supporting nanocolumn becomes more pronounced before it is completely decomposed and the nanoparticle detaches. The separation process leads to a loss in circularity and roundness, forcing the nanoparticle to restructure into a faceted shape. After separation, the spherical shape is partially restored, as indicated by 94% of circularity after 46 min. In the last 15 min of the *in situ* experiment, ZnPd nanoparticles aggregates in a self-supporting manner, which reduces the interface between support and nanoparticles. In addition, less changes in structure suggests a decrease in decomposition speed.

Figure 7.9 shows sections of the above described *in situ* methanol steam experiment at lower magnifications. The white ROI highlights the region imaged in Figure 7.7. In agreement to the results obtained above, other ZnPd nanoparticles also stabilize nanocolumns and form facets

before separation, as illustrated by the red arrows. The lower row of DF images in Figure 7.9 demonstrates that ZnO decomposes globally throughout the entire sample at the same time, indicated by the loss in DF signal.

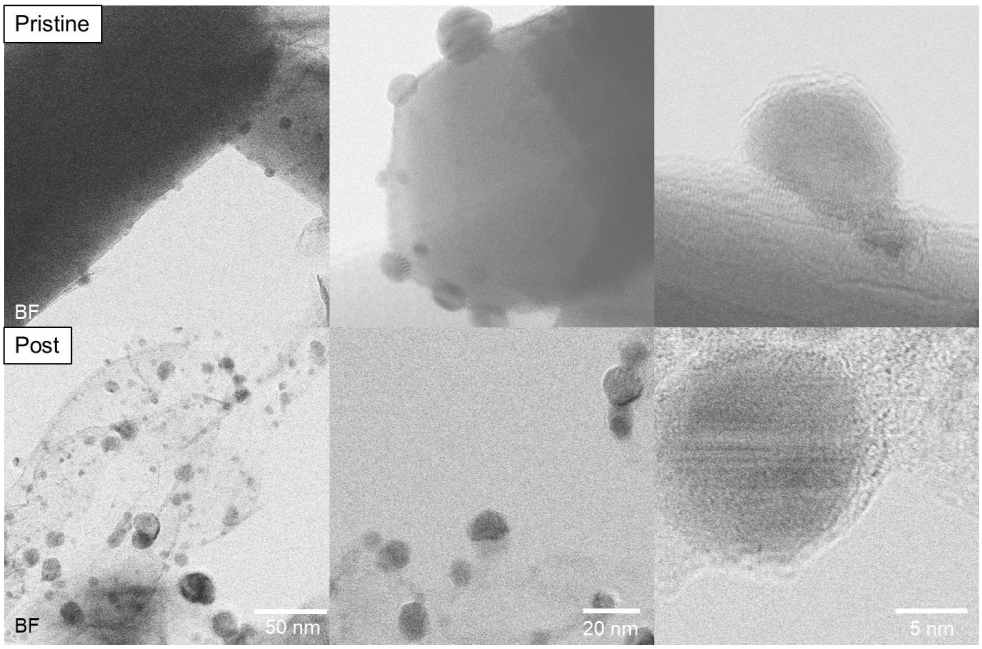

Figure 7.10: Series of BF images of randomly selected locations before (top) and after (bottom) methanol injection. Images in one pillar were acquired at the same magnification.

Reference locations are only imaged before and after methanol injection, as shown in Figure 7.10. Due to strong structural changes, it is not feasible to image identical locations, so randomly selected locations are imaged at the same magnification. In addition, high resolution imaging is hampered by strong mechanical vibrations, which occur after methanol injection. In comparison, the contrast of the support before injection is stronger than after, indicating a thicker initial sample. While the nanoparticles are initially anchored and homogeneously distributed on flat ZnO, they aggregate and occasionally are located on a nanocolumn after injection.

7.4.3 Discussions of Individual Components

The results suggest that water and methanol steam have different effects on ZnPd nanoparticles supported on ZnO. While water steam has a stabilising effect on the material system, strong ZnO decomposition is activated by methanol steam. The individual effects are discussed in this chapter.

Stabilisation by Water Steam

Exposure of water steam at an elevated temperature does not trigger any structural changes in ZnPd nanoparticles nor its support. Good agreement with the reference locations suggest the absence of an electron beam effect, which is typically present after long electron beam exposures. Consequently, water steam appears to stabilise the structure of the catalytic system.

Water is known to act as an oxygen donor to oxygen-deficient systems. In such systems, anion defects such as oxygen and nitrogen vacancies are predominantly found at the surface. Surface-absorbed water is capable of healing such defects by donating oxygen and splitting off hydrogen.[276] Oxygen vacancies in ZnO may be generated by electron beam exposure. As discussed in chapter 6.5, the present electron beam may assist in the generation of lattice defects to activate structural changes in ZnO. The absence of any ZnO activation indicates that electron beam-induced defects are healed by water steam, providing an explanation for its stabilising properties. The healing properties for electron-beam induced defects can also be interpreted as Mars-van Krevelen[58] mechanism, which predominantly occurs in heterogenous catalysis. In this mechanism, lattice oxygen from a metal oxide is abstracted to oxidise an absorbed reactant. The oxygen-deficient metal oxide is re-oxidised by dissociative absorption by an oxygen donor. The present results indicate that water acts as such an oxygen donor, which replenishes the oxygen abstracted from ZnO. Therefore, water is crucial for the stability of ZnO and its catalytic properties and thus for the longevity of the catalyst. This result helps to comprehend the role and capabilities of water steam in catalysis, especially, in methanol steam reforming.

Decomposition by Methanol Steam

The injection of methanol steam into the microscope column is delayed by opening the methanol metering valve and simultaneously activating the mass flow. The delay is characterised by two separate increases in column pressure. The initial increase corresponds to the activation of the mass flow controller, where gas residues from the supply line are injected. The second increase in column pressure after ~27 min is caused by methanol steam arriving at the mass flow controller, indicating that the transport of a sufficient quantity of methanol steam into the microscope column takes ~27 min. Thus, the present *in situ* experiment exhibits a temporal gradient in methanol partial pressure, such that early structural changes in the catalytic system are triggered by low methanol contents, while later changes are activated by higher methanol contents. Consequently, the first part of the experiment is referred to as the ‘low pressure’ phase and the second part as the ‘high pressure’ phase.

During the low pressure phase, ZnPd nanoparticles form a spherical shape, while the amorphous surface layer is partially removed. As derived in chapter 6.5, encapsulation by a reducible oxide minimises the surface energy of the nanoparticle. Due to deconstruction of the surface layer, the surface energy of the total system increases. As a result, the system restructures to reduce the surface area by formation of rounder nanoparticles, which is indicated by an increase in

circularity and roundness. After formation of a spherical shape, the high pressure phase is initiated. In this phase, the nanoparticles lose their spherical shape temporarily and form facets, which is probably triggered by the increase in methanol content.

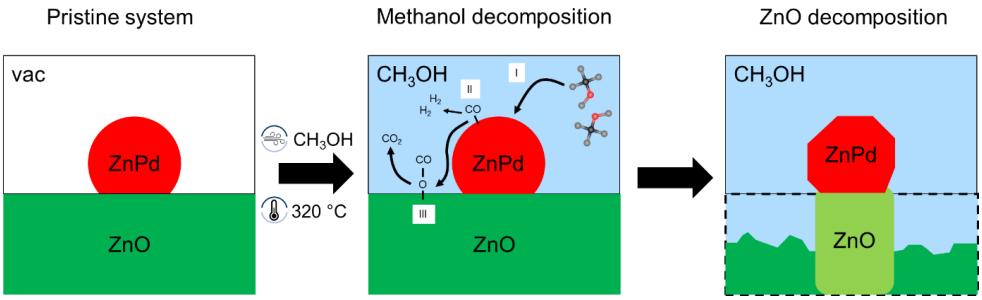

Figure 7.11: Schematic illustration of ZnO decomposition process. The system is exposed to methanol steam. Methanol is adsorbed on the ZnPd and activated (I). Methanol is decomposed, splits off hydrogen and spills over to the ZnO support (II). The residual CO binds to lattice oxygen, forms CO_2, which desorbs and generates an oxygen vacancy (III). ZnO is partially reduced and decomposes. A nanocolumn, as illustrated in bright green, underneath the nanoparticle is stabilized temporarily.

ZnPd nanoparticles supported on ZnO are highly CO_2-selective catalysts in the presence of methanol and water steam.[37] In the absence of water, the system promotes methanol decomposition. Methanol decomposition has high CO yield. Carbon monoxide is a potent reducing agent that has a higher reducing capacity than molecular hydrogen, as shown in Figure 2.4. Interaction between carbon monoxide and the ZnO support appear to cause the formation of CO_2, whereby the oxygen required for CO oxidation is removed from the ZnO lattice. The constant flow of produced carbon monoxide leads to continuous dissociation of oxygen from the lattice and to the formation of oxygen-deficient ZnO. Such material transport from ZnO to the gas phase is enhanced due to the low partial pressure during the *in situ* experiment. According to the Ellingham diagram, ZnO reduction and CO oxidation are not thermodynamically favourable under the selected conditions. Thus, it is expected that ZnPd nanoparticles play a pivotal role in the decomposition mechanism and activate CO by spillover to ZnO. This explanation is supported by the observation that the surface layer of the nanoparticles is first removed, followed by its direct vicinity. Interestingly, there is also an opposing effect: ZnO in direct contact to ZnPd is more resistant to decomposition, which is illustrated by the nanocolumn underneath the nanoparticles. This finding suggests that ZnPd nanoparticles stabilise ZnO by a certain extent. While it is well known that nanoparticles are stabilised by their support, e.g., against deactivation mechanisms, it is somewhat surprising that this mechanism acts in both directions here. The interface between the nanoparticle and -column appears to have a direct effect on the properties of the column, which has a similar width and

degrades after the nanoparticle is detached. The variation in decomposition resistances of formerly identical ZnO proves a structural or compositional change due to the supporting role and interaction with ZnPd nanoparticles. The formation of nanorods suggests that these changes are anisotropic in nature. In addition, the nanorod-supported nanoparticle is faceted, suggesting that the energy of the metal-support system is collectively affected. The fact that the nanoparticle loses its facets after detachment is an indicator for an intermediate and metastable state, which is only energetically favourable when supported on the nanocolumn. The phenomenon may only occur under low pressure conditions, which are present during the E-STEM experiment and indicate a pressure gap. As under low pressure condition, the mass transport is accelerated, the nanoparticle may also act as 'shielding', minimizing the interaction area between atmosphere and support and thus stabilizing the ZnO below. The common behaviour, in which the properties of the nanoparticle and support change, indicates the presence of a special kind of SMSI.

After ~53 min of methanol injection, the system reaches an equilibrium, when ZnO decomposition is stopped. There are presumably two reasons for equilibration. Firstly, it is known that oxygen is bound more strongly in oxygen-deficient oxides than in stochiometric oxides, which leads to higher binding energies in the defective structure. For instance, such phenomena have been reported for oxygen-deficient perovskites[277] and cobalt oxides[278] and are also likely to apply to the present system, which impedes the oxidation of CO. Secondly, the ZnPd nanoparticles are less homogeneously distributed on the support due to the initial decomposition of ZnO, but are more frequently aggregated, which leads to a reduction in the interface between nanoparticles and the support. Given that decomposition is activated by CO spillover from the nanoparticles onto the support, the probability of a spillover decreases due to a smaller interface and longer diffusion paths for CO.

An electron beam-induced decomposition is unlikely as decomposition occurred simultaneously and globally throughout the sample. In addition, the same decomposition behaviour is present independent of the applied dose.

Conclusions

The effects of methanol and water steam on ZnPd nanoparticles supported on ZnO are opposing and thus complementary. Due to methanol decomposition and the high CO yield, pure methanol leads to ZnO decomposition, which removes oxygen from the lattice. Here, decomposition may be facilitated by the low experimental pressure. In contrast, water steam acts as oxygen donor in a Mars-van Krevelen-like mechanisms, as it replenishes oxygen vacancies and stabilizes the defective ZnO structure, which is demonstrated by the absence of electron beam-induced defect generation. Thus, the catalytic system should be maintained if both components are applied in the correct ratio. Structural stabilisation of ZnO anchoring ZnPd nanoparticles proves that such tandems undergo changes in structure or composition induced by metal-support interaction that affect their properties. Such intermediate states often represent active sites and can only be

unravelled by *in situ* STEM. This finding raises the question of what other structural changes in ZnPd and ZnO are triggered by methanol and water, what effects they may have in catalytic reactions and whether they operate as active sites.

7.5 Structural Evolution During Methanol Steam Reforming

This chapter deals with the structural evolution of supported ZnPd nanoparticles during exposure to methanol and water steam at 320 °C. Different MSR experiments with an expected excess in methanol content were conducted. For a quantitative discussion on the steam composition, see chapter 7.8. Before MSR, the sample was reduced *in situ* at 200 °C for ~1 h in a hydrogen atmosphere, as shown in chapter 7.3. Different locations were investigated during reduction and MSR in order to reduce the electron beam dose. Reactions triggered by *in situ* MSR include changes in morphology of ZnPd nanoparticles and electron beam-assisted ZnO decomposition.

7.5.1 Changes in Morphology of Zinc Palladium Nanoparticles

The composition of pristine ZnPd nanoparticles is predominantly homogenous, as derived in chapter 7.2. Effects of MSR conditions on the local composition of ZnPd nanoparticles are studied *in situ*. Figure 7.12 and Figure 7.13 show the system during MSR conditions at 320 °C.

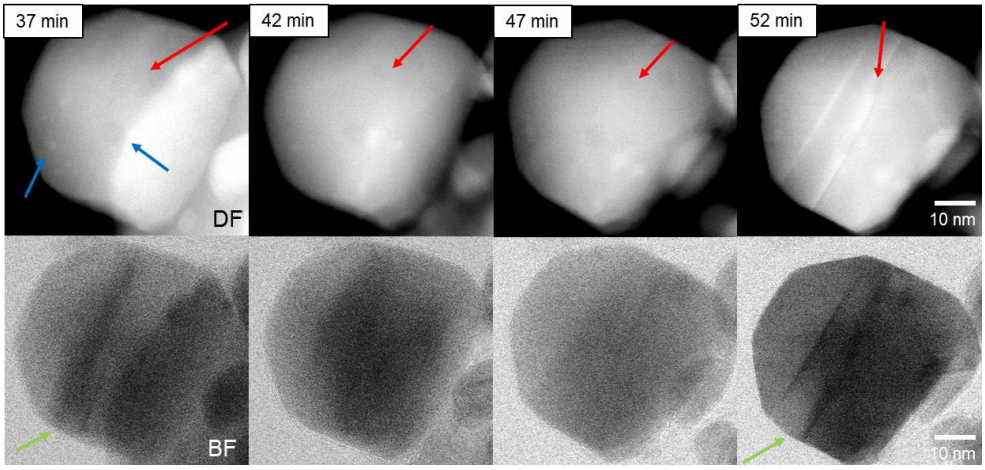

Figure 7.12: Series of DF (top) and BF (bottom) images of a nanoparticle compositionally evolving during MSR at 320 °C. Time stamp gives time of MSR. Blue arrows show initial locations of contrast deviations. The red arrows indicate formation of dark contrast regions. The green arrows highlight the presence of twin boundaries throughout the observation.

This region was continuously exposed to the electron beam. The nanoparticle is first investigated after 37 min of MSR. Few circular regions with darker and brighter contrast are already present, as indicated by the blue arrows in Figure 7.12. During imaging, ZnO degrades isotopically around the nanoparticle that increases the mobility and rotational freedom of the ZnPd nanoparticles and may lead to their tilt. Between 37 and 52 min, a further region with darker contrast is locally formed, as marked by red arrows. After 42 min, the first weak dark contrast variation is present, which intensifies as a function of time. The observed ZnPd also exhibits grain boundaries, which extends throughout the nanoparticles. As shown by the green arrows, the twin boundaries feature the nanoparticle from the point of observation.

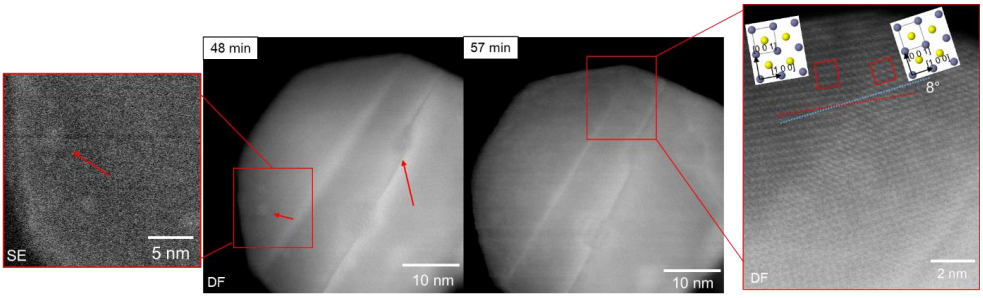

Figure 7.13: High resolution DF images of a ZnPd nanoparticle studied during MSR. Red arrows highlight regions of heterogenous composition in the nanoparticle, indicating deviations in Pd content. Left inset illustrates the SE image of the same region, indicating surficial features. Right inset shows twin boundary of the nanoparticle at a higher magnification. The tilt angle between the lattice planes is ~ 8°. Both ZnPd crystals are aligned along [0 1 0], as illustrated by the crystal model.

After 48 min of MSR, DF and SE images at a higher magnification reveal the nature of the features with brighter contrast, as shown by the red arrows in Figure 7.13. As demonstrated by the SE inlay, the bright feature in DF corresponds to a feature on the surface. The areas with dark contrast are patterned in a crystal structure that differs from the surrounding nanoparticle, indicating a Moiré pattern and the presence of a crystal deviation. The grain boundaries are highlighted in the inlay in Figure 7.13. The left grain boundary represents a twin boundary with bright contrast, where the two crystals are aligned along [0 1 0] and tilted by ~ 8°. Accordingly, the twin boundary runs through a (1 0 1) plane. A second grain boundary with darker contrast is present on the right. The ZnPd nanoparticle also exhibits a faceted surface and maintains it throughout the observation. As there is no image acquired of the *in situ* location before MSR, no comment about formation of facets can be made.

Reference locations, which are not exposed to the electron beam during MSR, are shown in Figure 7.14. DF images of reference locations before MSR are displayed in Figure 11.18. Such reference ZnPd nanoparticles are found to have formed facets during MSR. Comparing the

nanoparticle in the left DF image in Figure 7.14 with its pristine shape demonstrates an evolution from a roundish shape to a faceted one. The crystal is aligned along [1 1 1], assigning the facets to (1 1 0) planes. The crystal of the nanoparticle in the right DF image is aligned along [1 0 0]. Consequently, the facets formed represent (0 1 0) and (0 1 1) planes. High resolution images of the identified facets are shown in Figure 11.19. Here, differences in contrast allow an elemental identification of Pd and Zn. The heavier Pd appears brighter in DF imaging. The nanoparticle in the centred DF image in Figure 7.14 maintains its round, anisotropic shape, indicating that some nanoparticles do not form facets.

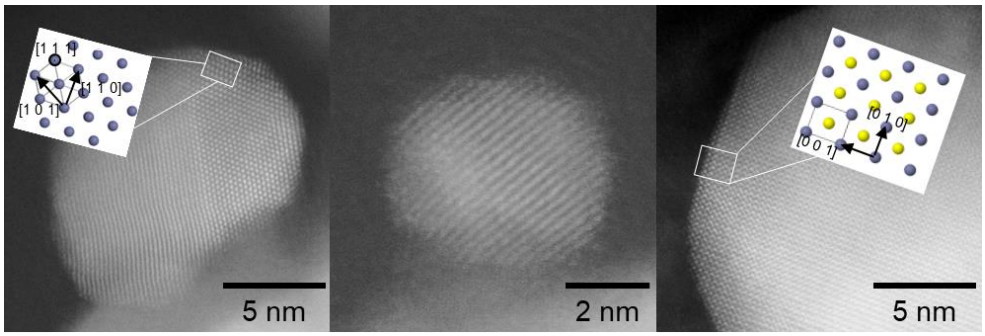

Figure 7.14: DF images of ZnPd nanoparticles acquired after exposure to MSR conditions. Images of pristine nanoparticles are shown in Figure 11.18. Inlays illustrate crystal structure and orientation of ZnPd nanoparticles. The nanoparticle in the left DF image is aligned along [1 1 1], the nanoparticle in the right DF image along [1 0 0].

7.5.2 Electron Beam-Assisted Decomposition of Zinc Oxide

The electron beam affects the catalytic system strongly during MSR. Figure 7.15 shows a series of SE images and, consequently, the impact of electron beam exposure on the surface of ZnO, as a function of exposure time. The sample was continuously exposed to the electron beam and MSR conditions. In vacuum, the system is stable under the electron beam, resisting any degradation. After 1 min of exposure, few-nanometre-sized holes form uniformly on the ZnO surface, indicating first ZnO degradation. These holes grow constantly over the next minutes of beam exposure to a size of 10-20 nm. After 4 min of exposure, ZnO at the edges are completely degraded. The state of degradation is maintained and is limited to the observed region. Figure 7.16 shows the region at a lower magnification, indicating that only ZnO exposed to the electron beam degrades. The ZnPd nanoparticles resist electron beam irradiations and retain their morphology.

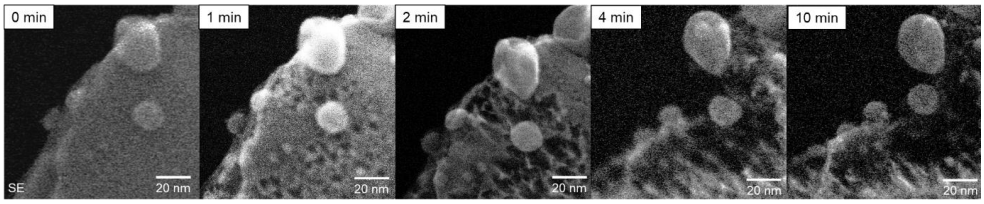

Figure 7.15: Surface damage activated by the electron beam shown by a series of SE images. ZnO continuously degrades due to combination of the present MSR conditions and electron beam exposure. The time of electron beam exposure is indicated by the time stamps.

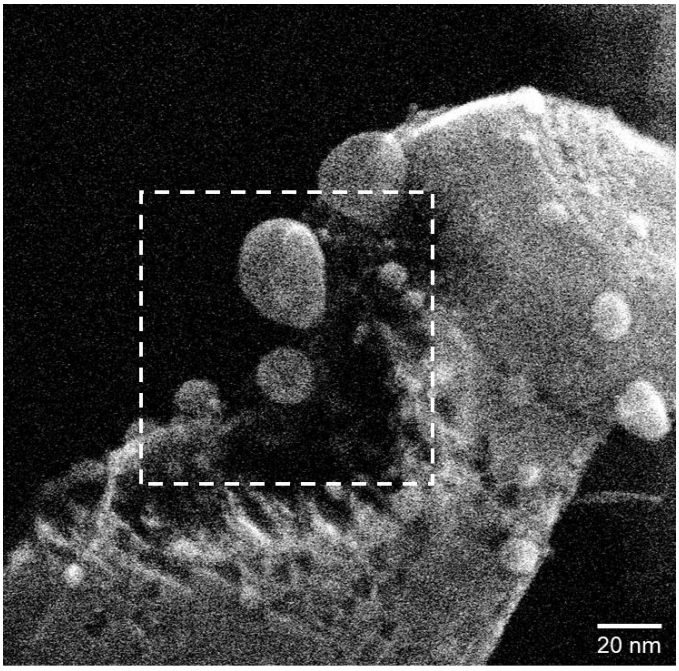

Figure 7.16: SE image of electron beam-activated ZnO degradation. White square indicates scan region. Only the imaged ZnO region is subject to decomposition.

Figure 7.17 shows the *in situ* ZnO decomposition activated by electron beam irradiation and MSR with higher temporal resolution. The first hole is formed on the ZnO surface after 21 s, as indicated by the red arrow in the SE image. After 30 s, a second hole is generated at a different location. The second hole has no corresponding feature in SE imaging, indicating a formation on the detector-far side or formation of a void. Both hole locations seem arbitrary with no obvious preference and relation to the nanoparticle. The holes grow continuously as a function of time, as highlighted by the green arrows in Figure 7.17. Straight boundaries suggest hole growth along crystallographic planes. After 70 s of exposure, the SE image acquired at a lower

magnification reveals that only the region exposed to the electron beam is damaged. The ZnPd nanoparticles are not affected by the present conditions.

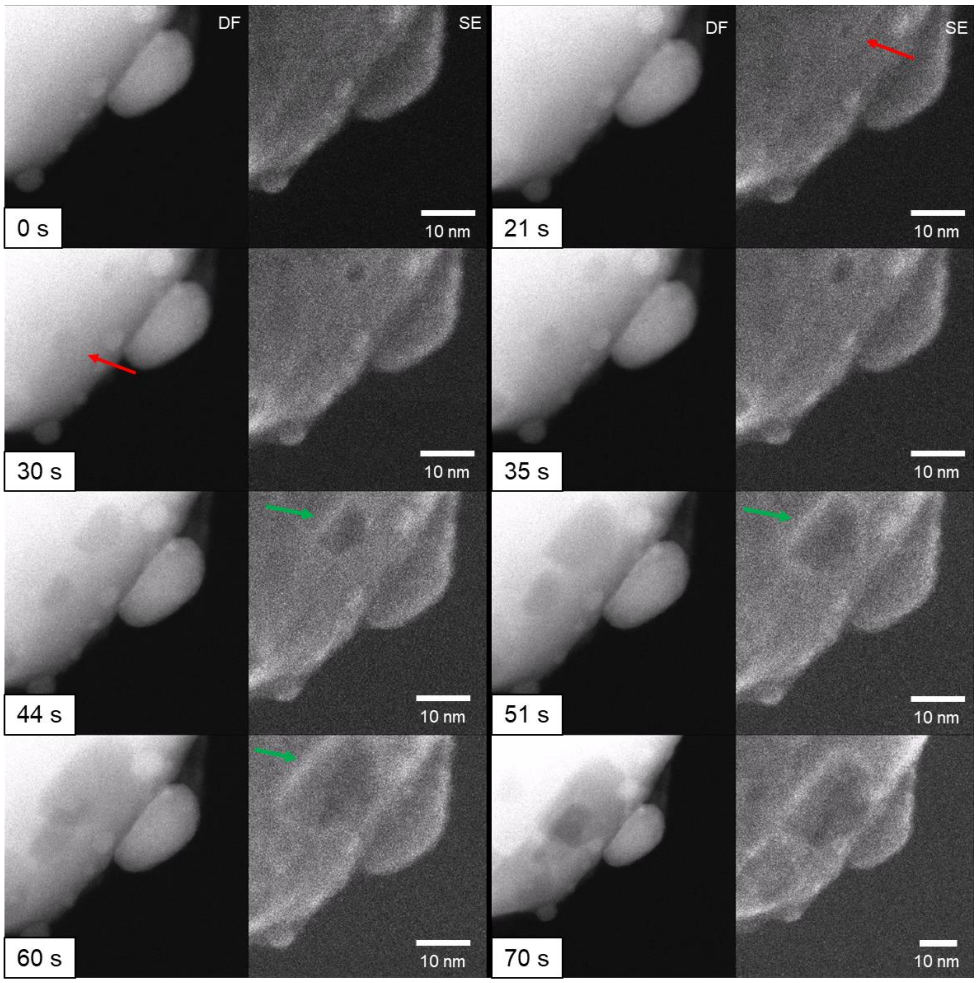

Figure 7.17: Series of SE and DF images of *in situ* ZnO decomposition activated by the exposure to electron beam and MSR conditions. The red arrows indicate hole formation. The green arrows show faceted growth of holes.

In order to quantify electron beam-assisted ZnO decomposition, the growth speed of a hole is measured by manually marking the perimeter of the upper right hole in SE images, as shown in Figure 7.18. Measurements of the perimeter and area of the hole are plotted as a function of time in Figure 7.18. Three measurements are averaged and the standard deviation is given as the error. The relationship between hole parameters and time signals a steady growth of the hole between 0 and 60 s. The linear approximated growth of the hole area between 21 and 60 s is ~ 4.5 nm^2/s.

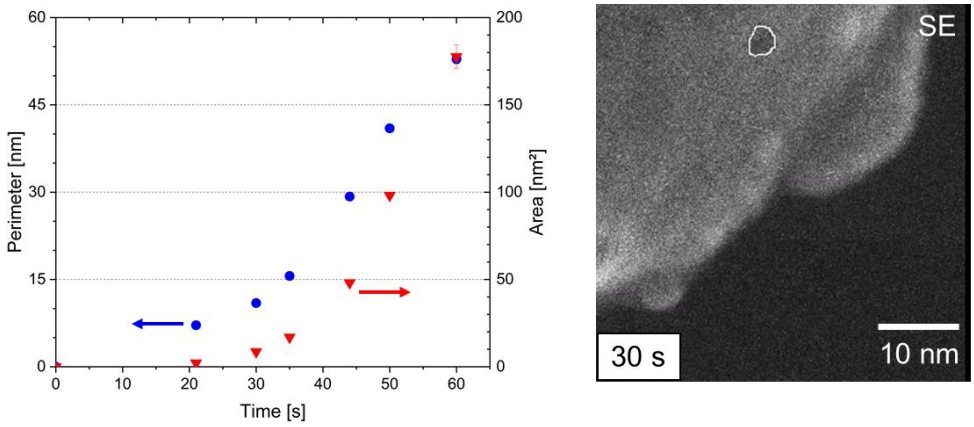

Figure 7.18: Left: Quantification of ZnO decomposition, represented by the perimeter (blue circle) and the area (red triangle) of a hole as a function of time. Right: Example of a manually marked hole after 30 seconds of electron beam and MSR irradiation.

7.5.3 Discussions of Structural Evolution During Methanol Steam Reforming

The ZnPd/ZnO system is subject to many concomitantly occurring, nanostructural mechanisms during MSR conditions at 320 °C The present mechanisms involve segregation, faceting and decomposition effects, which are discussed in this chapter.

Nanostructural Evolution of Zinc Palladium Nanoparticles

The darker DF contrast observed to be formed in some locations of the ZnPd nanoparticle during MSR may be attributed to either imaging artefacts or material changes. The dynamic contrast changes might be an imaging artefact, which may be triggered by the tilt of the nanoparticle due to the decomposition of the ZnO support. The presence of this phenomenon is supported by the areal contrast change observed in the BF images depicted in Figure 7.12.

Potential material effects that lead to the observed dynamic behaviour are a thinner sample thickness and lower elemental mass. A change in local thickness due to superficial changes is unlikely, as the no region with darker DF contrast correspond to any feature imaged by the SE detector. It is possible that all features are located on the SE detector-far surface, but rather unlikely. In contrast, regions with brighter DF contrast can be assigned to a superficial feature, as highlighted in Figure 7.13. Voids forming inside the ZnPd nanoparticles also reduce the pathway through material and thus the scatter probability, leading to lower DF signal. However, regions with lower DF contrast form Moiré pattern, which are based on overlaying and small deviations between crystals. Such Moiré pattern indicate the presence of a crystal, which is different in orientation or unit cell size from its surrounding and contradicts the presence of a void.

ZnPd has a wide, compositional existence range. The interatomic distances of the tetragonal ZnPd crystal in a and c direction are sensitive to the Pd/Zn ratio, as shown by Armbrüster and coworkers[42]. A lower elemental mass, e.g. a higher Zn content, increases the c/a-ratio. Such deviations in interatomic distances due to different Zn contents may form the present Moiré pattern with the predominately homogenous ZnPd nanoparticle. Thus, presence of the Moiré pattern and the weak DF signal suggest that regions with dark DF contrast in ZnPd nanoparticles exhibit lower elemental mass and are Zn enriched. Regions with weak DF signal are now referred to as 'Zn enriched'.

The possibility of Zn enriched regions indicates local deviations of chemical composition. Such regions with weak DF signal are predominantly found at the grain boundary that suggests a preferential Zn enrichment there. Such preferential enrichment of a certain species at grain boundaries is also coined as grain boundary segregation.[279] While some Zn enriched regions were present at the beginning of the *in situ* observation, other appear to form during MSR, as observed by *in situ* experiments. A preferred Zn enrichment at grain boundaries is likely as grain boundaries unlike a bulk lattice exhibit sites with different energy levels, which facilitates occupation by solute species, that is known as equilibrium segregation.[280] An occupation of such grain boundary states reduces the overall free energy of the system and thus is the thermodynamic driving force for enrichment. Zn enriched regions next to the grain boundary represent a non-equilibrium like segregation, which is typically activated by a flux of vacancies.[281] The present *in situ* formation of Zn enriched regions suggest that such vacancies are generated by the applied conditions, e.g. MSR, electron beam and low partial pressure, which change the chemical environment of the ZnPd nanoparticle and thus facilitate Zn enrichment.

It is unlikely that sole Zn is segregated in the present mechanism. The wide, compositional existence range of the intermetallic ZnPd phase indicates that formation of Zn rich or Pd depleted ZnPd is much more likely. This is in good agreement with Heggen and co-workers, who reported the formation of such locally Pd depleted areas in ZnPd nanoparticles during vacuum heating.[45] However, in their work the presence of grain boundaries was not reported.

Properties such as the mirror-image stacking of the phases on both sides of the grain boundary identify the present boundary as a twin boundary. Twin boundaries are a known defect in ZnPd bulk crystals that releases stress from the system[282], but have not been reported for supported ZnPd nanoparticles yet. The measured tilt between the crystallographic directions of the phases in the ZnPd nanoparticle of ~ 8° is in good agreement with the tilts reported by Ivarsson *et al.*[282] for ZnPd bulk.

In addition to compositional inhomogeneity and defects found in ZnPd, formation of facets indicates morphological evolution. Due to the MSR, the initially round shape of ZnPd nanoparticles changes into a low index-faceted surface, consisting of (1 0 0) and (1 0 1) ZnPd planes. At the (1 0 0) facets, Zn represents the surface atoms, as shown by the lower DF signal.

This behaviour indicates that low index facets are energetically more favourable under MSR conditions and the energetic minima are different for inert and reactive conditions. Faceting appear to predominantly occur for larger nanoparticles, suggesting a size effect. A quantification of a critical particle size for faceting is challenging due to the small number of observed nanoparticles. However, faceting was not found for ZnPd nanoparticles ≤ 5 nm. As facet formation was also found at reference locations in the absence of the electron beam, an electron beam-activated faceting can be excluded. However, an effect of the low partial pressure and thus a pressure gap is possible.

Compositional segregation[283], twin boundaries[284] and faceting[285] are all features, which are known to act as active sites and thus trigger a change in catalytic properties of a catalyst. As segregation and faceting were activated in ZnPd by the present catalytic reactions, they may change the catalytic properties of the system during catalysis. Such change in catalytic properties was reported for ZnPd nanoparticles supported on ZnO during MSR.[37,92] Here, the CO_2 selectivity of ZnPd/ZnO-catalysts increased with time of catalysis. As external conditions, e.g. temperature and feed, remained constant, it can be concluded that the catalyst changes. The dynamic changes of ZnPd observed here prove that the catalytic system evolves during MSR. These findings also support the idea that catalytically activated segregation and faceting may be part of the mechanism, which enhances the CO_2 selectivity. However, as the catalytic performance was not measured during the *in situ* experiment and the structural changes cannot be linked to its changes during MSR, further research is required to evaluate the impact of segregation and faceting of ZnPd nanoparticles and to explore the mechanisms behind the increase in CO_2 selectivity.

Electron Beam-Activated ZnO Decomposition

In addition to changes in structure and composition of the nanoparticle, ZnO is subject to strong decomposition during *in situ* STEM MSR experiments. Intriguingly, only ZnO areas exposed to the electron beam are decomposed during MSR. ZnO resists sole exposure to MSR, and the electron beam in vacuum. Thus, it can be concluded that the ZnO decomposition is electron beam-activated. In order to elucidate the beam effect on ZnO decomposition, the present experiment is compared to other *in situ* STEM experiments, derived above. ZnO as support and passivation layer resisted decomposition during electron beam exposure in hydrogen (chapter 5 and 7.3). Supporting ZnO was also stable during imaging in water steam (chapter 7.4.1). Thus, an effect of these environments can be excluded. However, *in situ* methanol decomposition triggered pronounced ZnO decomposition, also in the absence of an electron beam, as derived in chapter 7.4.2. The present ZnO degradation is therefore likely a result of methanol decomposition. Supported ZnPd catalysts in MSR conditions typically exhibit high CO_2 selectivity and thus supress methanol decomposition. Given that the ZnO decomposition is triggered by methanol decomposition, the electron beam changes the selectivity of the catalyst and shifts the equilibrium to methanol decomposition. As a result, more CO is produced that

reduces ZnO, as described in chapter 7.4.3. There are several possible explanations for this result:

Water steam provides the required oxygen for CO_2 production in MSR. A theory for the hydrous oxygen supply includes that water is part of a Mars-van Krevelen mechanism and indirectly supplies oxygen by replenishing the metal oxide lattice during MSR, as reported by Köwitsch and co-workers for InPt species supported on In_2O_3.[57] Electron beam-activated ZnO decomposition due to partial reduction indicates that the water absorption on ZnO is hindered by the electron beam and thus oxygen vacancies in the ZnO lattice are not healed. Following mechanism is proposed: Oxygen vacancies may be stabilized due to a change in oxidation state of the Zn species. Under standard conditions, Zn^{2+} is present in ZnO. Due to electron beam, reducing conditions are present, which contribute additional electrons to ZnO and form negatively charged ZnO^-. Subsequent generation of oxygen vacancies favour the formation of Zn species with a lower oxidation state, such as metallic Zn^0 and Zn^{1+}. Oxygen vacancies surrounded by such Zn species are less likely to be replenished due to the neutral charge. Residual, metallic Zn exhibits a relatively low melting point of ~419 °C under standard conditions[286] and vapour pressure of around 1 Pa at 320 °C[282]. Consequently, the sublimation of Zn is likely due to the present temperature and low partial pressure. Other explanations for the beam-assisted decomposition include that the electron beam may also selectively change the kinetics of sub-reactions and may accelerate the speed of methanol decomposition, producing CO faster than water is activated. Here, methanol steam may be excited by the electron beam, increasing its activity. ZnO might also be affected directly by the electron beam. The electron beam generates lattice defects, e.g. oxygen vacancies, which act as active sites for methanol absorption increasing chemisorption of ZnO for methanol. In addition to the activation on ZnPd, methanol may be now activated on defective ZnO, accelerating the overall activation of methanol compared to normal MSR conditions.

Regardless of the cause of ZnO decomposition, the electron beam-induced degradation hinders the *in situ* investigation of dynamic, nanostructural changes of the support. Thus, growth of the proposed ZnO patches on ZnPd cannot be detected *in situ* with TEM under the given conditions. Nanoparticle-related changes can be studied, as ZnPd resists the effect of the electron beam. Given that the effect is primarily caused by a selective change in reaction kinetics that accelerates methanol decomposition, a higher water ratio in the MSR feed should mitigate the electron beam effect.

Conclusions

In situ STEM studies of supported ZnPd nanoparticles reveal nanostructural phenomena that alter the composition and morphology of ZnPd and decompose ZnO. Nanostructural evolution of ZnPd involves the formation of presumably Zn-rich areas and low index facets. In contrast, ZnO suffers from electron beam-activated decomposition, which impedes the observation of any MSR-related ZnO changes.

7.6 Structural Evolution of Supported Zinc Palladium Nanoparticles in a Hydrogen Environment Enriched with Methanol and Water

During MSR, ZnPd is not only exposed to methanol and water but also to the products carbon dioxide and hydrogen. Due to the low partial pressure, limited catalytic activity and volatile hydrogen, the hydrogen partial pressure is comparable low at the sample. However, hydrogen may still play a pivotal role in the structural evolution of ZnPd catalysts during MSR, such that an investigation in a hydrogen containing MSR atmosphere is highly desirable. In this chapter, hydrogen is enriched with methanol and water to evaluate its structural effect on ZnPd nanoparticles supported on ZnO.

7.6.1 Experimentals – Hydrogen Enrichment with Water and Methanol

Supported ZnPd nanoparticles with different loadings were prepared on MEMS heating chips, as derived in chapter 7.1. For *in situ* MSR experiments, the open cell setup was used, as described in chapter 3.2.1. In order to supply water, methanol and hydrogen simultaneously, a different supply mechanism than the one used in chapter 7.5 was applied. Before injecting the mixture, the needle valves of water and methanol were opened equally for ~60 min, such that the components condensate on the supply tubes. The needle valves were then closed and a vacuum of $< 10^{-4}$ mbar was applied to the supply system, removing the water and methanol steam and leaving only the condensate. Subsequently, hydrogen with a pressure of 1 bar was injected into the supply tubes, where it is enriched with methanol and water that were adsorbed by the supply tubes. Saturated hydrogen was then injected into the microscope column with a mass flow of 2 sccm. The ZnPd/ZnO catalyst was heated to 200 °C. After 1 hour of injection, the hydrogen flow was stopped. MSR conditions identical to the those described in chapter 7.1 were then applied.

7.6.2 Discussions of Experimental Feasibility

After the MSR and the evacuation of the system, methanol and water residues were found in the supply line, which became apparent through an increased sample pressure that decreased with injection time at a constant hydrogen mass flow rate. Such decreasing partial pressures of water and methanol in a constant hydrogen flow exhibits ideal, experimental prerequisites to evaluate the effect between variable ratios of hydrogen and water/methanol. In contrast to the conventional MSR experiments, in which methanol was dominant, a higher water content is estimated in such a setup. The cause for a higher water content is its lower vapor pressure at room temperature, increasing its probability to condensate and be adsorbed by the supply lines. Given that the hydrogen partial pressure $\bar{p}_{H_2}$ remains constant, continuous column pressure p_{spec} measurements allow an estimation of the methanol and water content p_{MSR} in the atmosphere, following eq. 7.3.

$$p_{MSR} = p_{spec} - \bar{p}_{H_2} \quad 7.3$$

The hydrogen partial pressure $\bar{p}_{H_2}$ is determined as the average of the specimen pressure between 50 and 60 min of injection when the column pressure remains constant. At this point, it is assumed that all methanol and water residues are removed from the line and that the column environment consists mainly of hydrogen. In addition, when hydrogen is injected through clean tubes with the same mass flow, corresponding column pressures can be measured. Other residual gases, which may be present in the column due to previous *in situ* experiments, are neglected.

7.6.3 Results of In Situ Experiment in a Hydrogen Environment Saturated with Methanol and Water

Supported ZnPd nanoparticles were exposed to a hydrogen atmosphere enriched with methanol and water at 200 °C, as shown in Figure 7.19, Figure 7.21 and Figure 11.20. The corresponding column pressure as a function of the injection time is illustrated in Figure 7.19. The sum of the water and methanol partial pressures is calculated using eq. 7.3 and shown in red. Shortly after injection, the maximum column pressure is reached and decreases continuously for 50 min. After 50 min of injection, a pressure equilibrium is established that represents the partial pressure of hydrogen. At the beginning of the injection, the nanoparticles are locally supported on ZnO and partially embedded in an amorphous phase, which has relatively weak and inhomogeneous DF contrast. During the first 30 min of injection, nanoparticles and support remain largely unchanged. The irregular shape of the nanoparticle undergoes small morphological changes to a more faceted shape. After 40 min of injection, when methanol and water are largely removed, a crystalline surface decoration forms, as indicated by the red arrow in Figure 7.19. The surface decoration evolves during reduction, extending to the support-far side of the nanoparticle. A reduction in the water and methanol contents results in an acceleration of the encapsulation process, with the nanoparticle becoming completely covered by a crystalline surface layer with a thickness of 1-3 nm after 60 minutes. Figure 7.20 shows DF and BF images at a higher magnification, which reveal that the surface layer consists of crystalline ZnO aligned along [1 0 0]. The measured interatomic spacings of 3.1 ± 0.1 Å and 4.6 ± 0.1 Å are in good agreement with values for ZnO (1 1 1) of 3.21 Å and ZnO (1 4 1) of 4.57 Å.

Figure 7.21 shows a different sample location that is subjected to identical experimental conditions as the sample shown in Figure 7.19. Following the removal of methanol and water after 51 minutes, first surface decorations on ZnPd nanoparticles are observed, as indicated by the red arrows. Intriguingly, these ZnPd nanoparticles are only partially covered by a crystalline layer and are not completely encapsulated. The ZnO support remains stable throughout the

entire exposure period, and no apparent electron beam-assisted effect is observed. The ZnPd nanoparticle does not undergo changes in composition during the applied treatment.

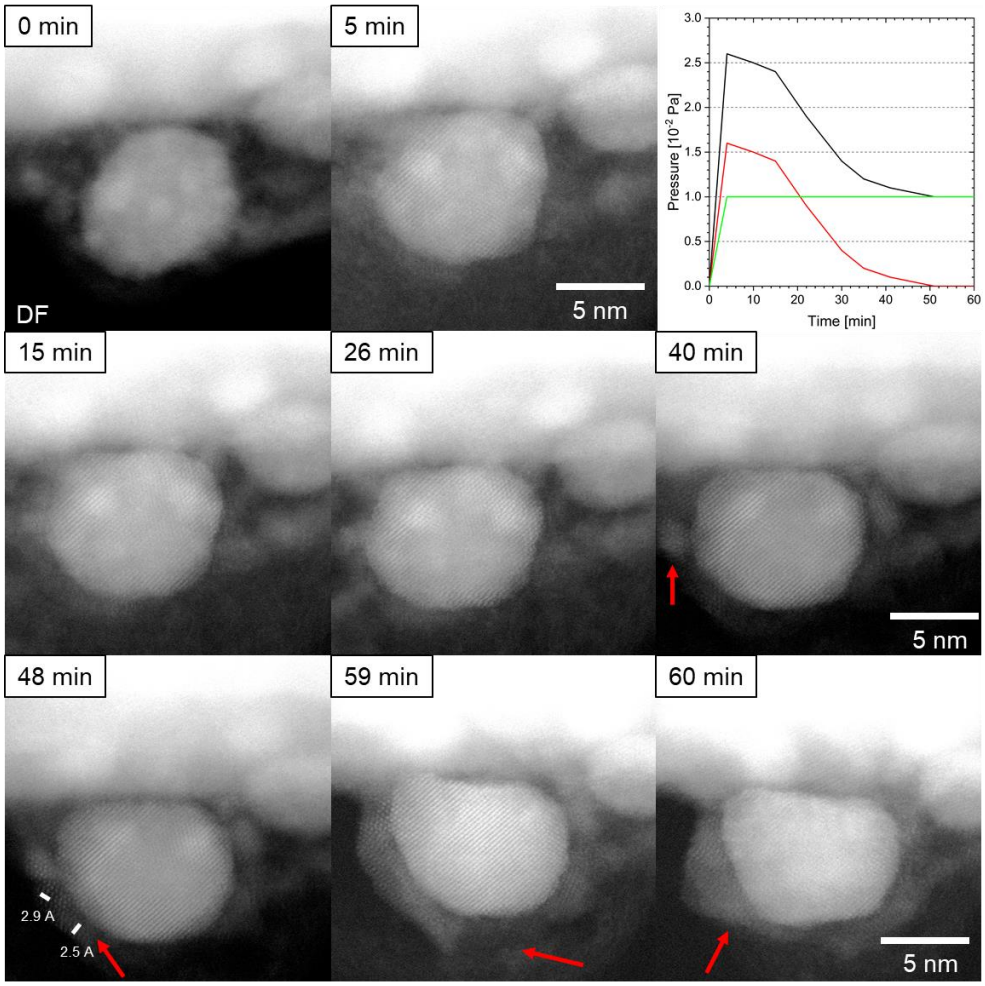

Figure 7.19: Series of DF images of a supported ZnPd nanoparticle exposed to methanol steam, water steam and hydrogen. Column pressure (black), partial pressure of water and methanol (red) and hydrogen partial pressure (green) are displayed as a function of injection time. Red arrows indicate increasing encapsulation of the nanoparticle. After 48 min of injection, measurements of the interatomic distances are shown along the marked directions. Corresponding BF images are shown in Figure 11.20. The structure of the encapsulation layer is identified as ZnO, as illustrated in Figure 7.20.

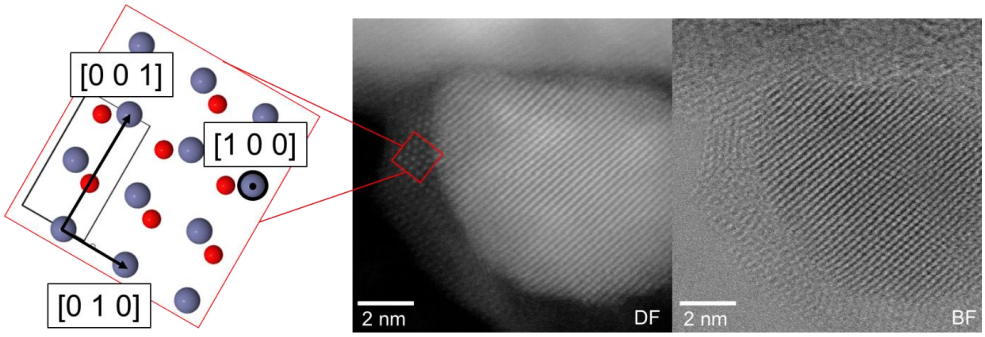

Figure 7.20: High resolution DF and BF image of a ZnPd nanoparticle exposed to methanol steam, water steam and hydrogen for 48 min, as shown in Figure 7.19. ZnO model identifies orientation and structure of the surface layer. Layer crystal is aligned along ZnO [1 0 0]. Model is created from reference[287].

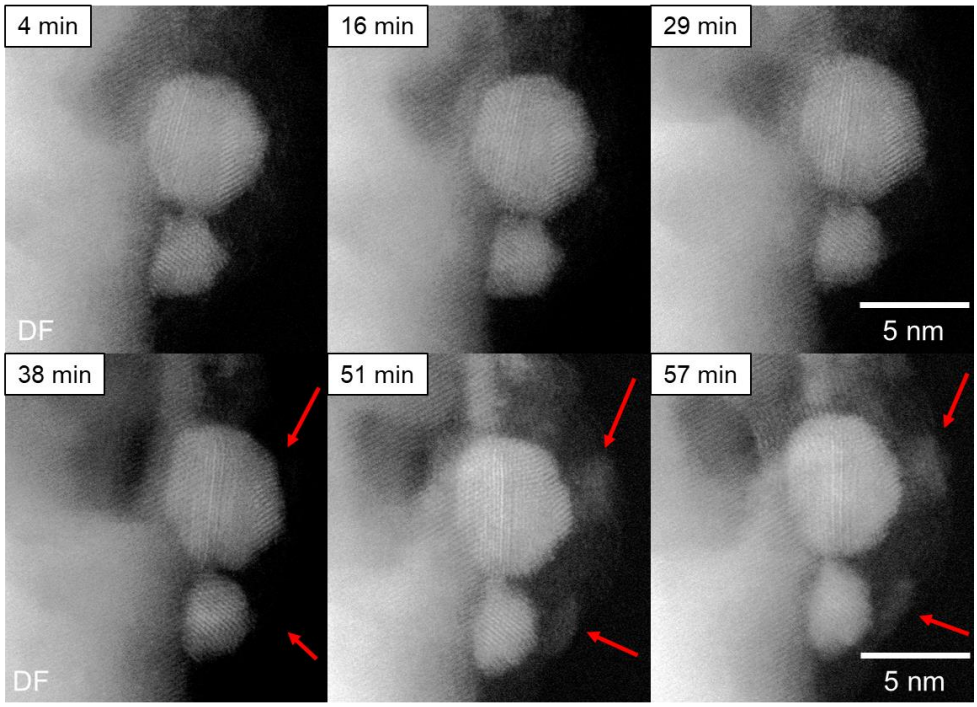

Figure 7.21: Series of DF images of a supported ZnPd nanoparticle exposed to methanol steam, water steam and hydrogen. The red arrows indicate ZnO patch formation on the ZnPd surface.

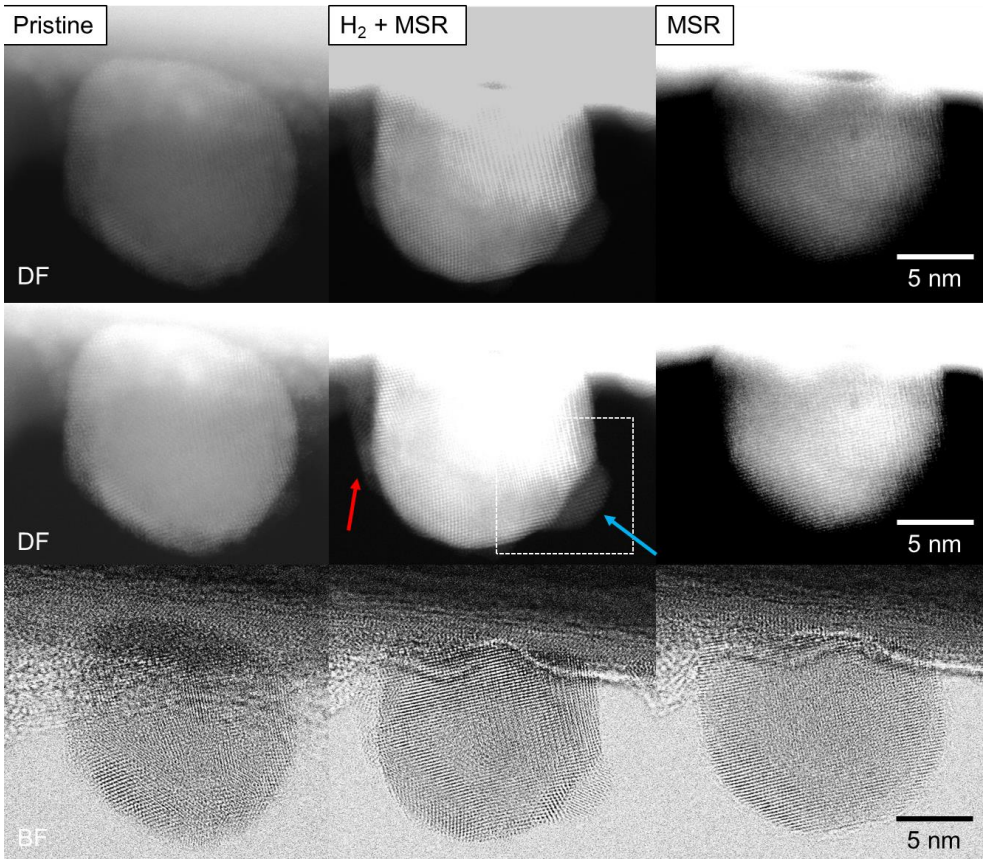

Figure 7.22: DF and BF images of the identical sample location acquired before (left), after treatment with hydrogen saturated by methanol and water (middle) and after treatment with methanol and water (right). Two rows of DF images show different brightness levels. The arrows indicate formation of superficial patches. The blue arrow shows a surface patch. The red arrow highlights surface layer. The white square represents an area, which was investigated at higher magnification, as shown in Figure 7.24.

In the absence of a reactive atmosphere, reference locations are examined to evaluate the effect of the electron beam. Such reference locations are shown in Figure 7.22 and Figure 7.23. A comparison of the morphology of the pristine and the spent catalysts reveals that the treatment in hydrogen saturated with methanol and water results in the formation of superficial decorations on ZnPd. The formed decorations differ in size and morphology. Some decorations are surface layers with a large lateral extension in comparison to a relatively thin thickness, e.g. 8.8 nm to 1.7 nm, as indicated by the red arrow in Figure 7.22. It is likely that the surface layer originates from the ZnO support, as evidenced by its growth path along the nanoparticle. A

similar coverage layer has also formed on the nanoparticle investigated in Figure 7.23. In this instance, the nanoparticle is smaller in size with a mean diameter of ~ 5.7 nm compared to ~13.9 nm in Figure 7.22 and the coverage layer occupies most of its surface area.

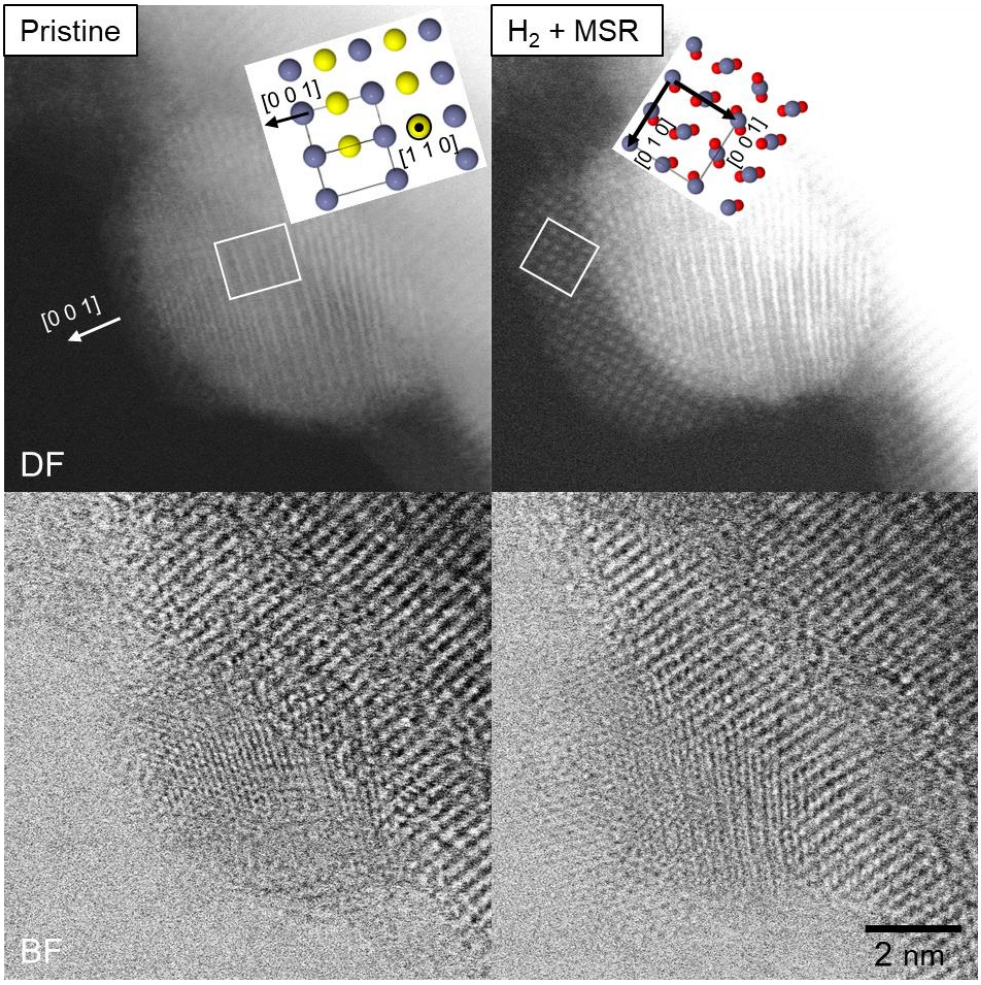

Figure 7.23: DF and BF images of an identical sample location before (left) and after treatment in hydrogen enriched with methanol and water. The ZnPd crystal is aligned along [1 1 0]. Atom rows with bright DF signal correspond to Pd, darker atom rows to Zn, as illustrated in yellow and blue by the model. ZnO_2 patch aligned along [1 0 0] forms during MSR. Reference location was not exposed to the electron beam.

Other surface decorations have a hemispherical shape, as shown by the blue arrow in Figure 7.22. Such patches exhibit a lateral extension, which is found to be similar in size to their thickness. For instance, the patch highlighted in Figure 7.22 has a thickness of ~2.0 nm and width of ~4.4 nm. Given that the nanoparticle is aligned along [1 1 0], the patch grows on a

ZnPd (1 1 1) facet, as shown in Figure 7.24. The superficial crystal structures present in the corresponding SE image indicate that ZnPd is not obstructed by a surface layer, thus allowing for direct contact with the formed patch. ZnPd also exhibits (0 0 1) facets. The patch structure matches best with ZnO_2 along [1 0 0] with measured interatomic spacings of 2.6 ± 0.1 Å and 2.5 ± 0.1 Å and its cubic structure. These values align well with ZnO_2 (2 0 0) with 2.45 Å.[288]

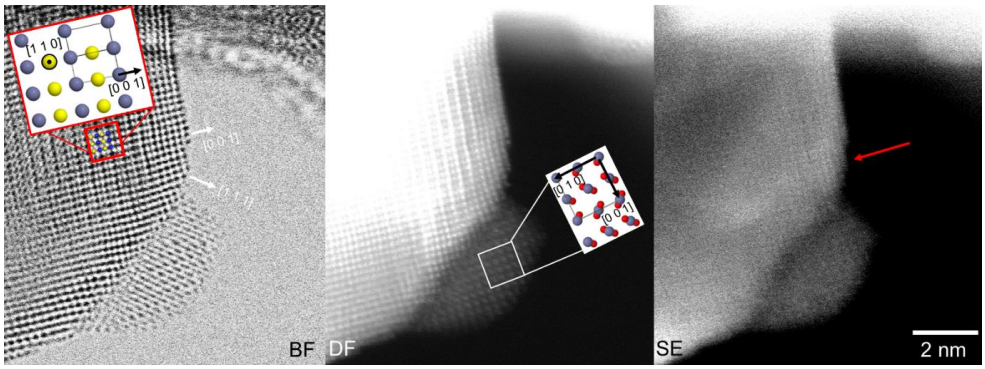

Figure 7.24: BF, DF and SE images of a surface patch formed during *in situ* treatment with hydrogen enriched with methanol and water. The ZnPd nanoparticle is aligned along [1 1 0]. The crystal structure of the patch corresponds best with ZnO_2 aligned along [1 0 0]. The red arrow indicates a crystalline surface and the absence of amorphous covering layers.

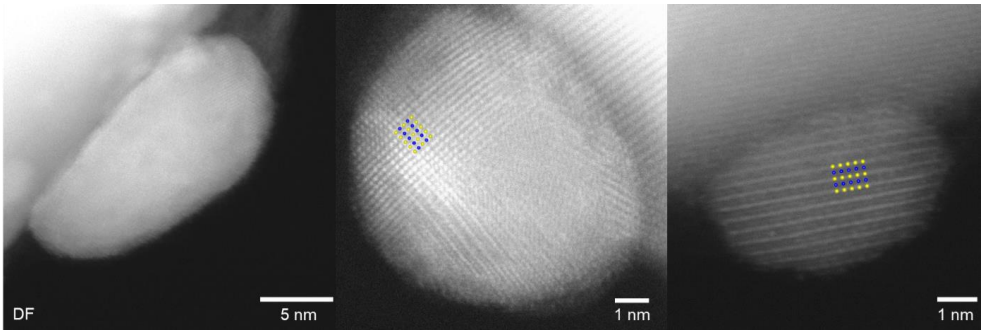

Figure 7.25: DF images of randomly selected ZnPd nanoparticles acquired after treatment with hydrogen enriched with methanol and water. No patches were formed on the surface of the nanoparticles. Nanoparticles were only exposed to the electron beam in vacuum. Zn is displayed in blue, Pd in yellow.

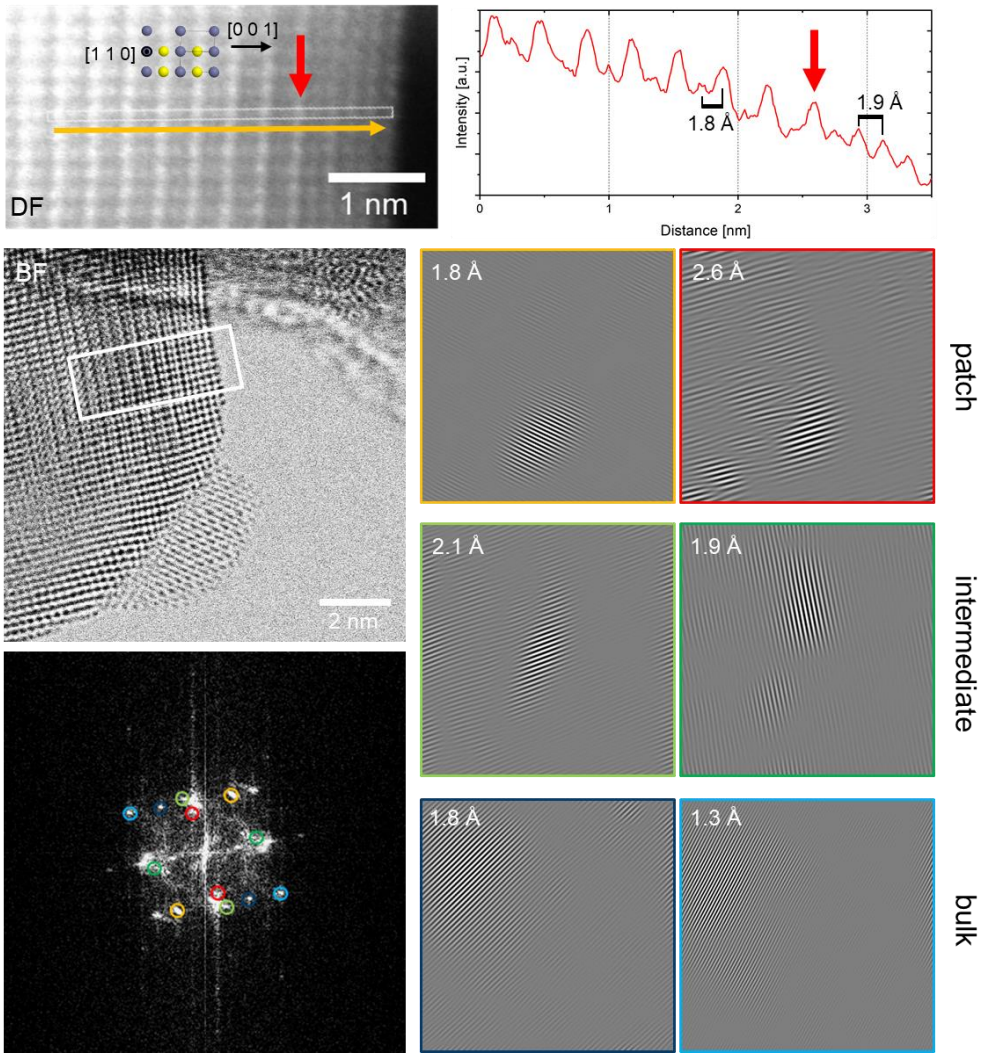

Figure 7.26: DF and BF image, FFT and corresponding inverse FFTs showing different phases of the system. Different colours assign FFT spots to inverse FFTs. 3 different phases are present: The bulk of the nanoparticle, intermediate phase at the edge of the nanoparticle and patch. The white box represents the ROI of the DF image. The graph indicates the DF intensity, where peaks identify the location of an atom column. The red arrow indicates the position of the respective peak in the DF image. The orange arrow indicates the distance shown in the graph.

Figure 7.26. presents an FFT of the BF image (boxed region in Figure 7.22) and inverse FFTs of individual spots. An examination of the inverse FFT images aids the classification of three

distinct structural regions within the system: the patch phase, the intermediate phase and the bulk phase. The patch phase is restricted to superficial decoration on the nanoparticle. As indicated by the red and orange circles in Figure 7.26, the spots in FFT are closer to the centre than those of the other phases, indicating larger interatomic spacings. The bulk phase is located at the centre of the ZnPd nanoparticle, as indicated by the inverse FFTs in blue. Given that a bright DF signal in Figure 7.26 corresponds to Pd, it appears as the bulk phase has a higher Pd content than the intermediate phase, as the Pd lattice periodicity ends at the intermediate phase. The intermediate phase is confined to the edge of the nanoparticle and to the interface with the formed patch, as shown by the inverse FFTs marked in green, and corresponds to tetragonal ZnPd. The intermediate phase exhibits larger interatomic spacings along [0 0 1] than the bulk phase, e.g. 1.8 Å in the bulk and 1.9 Å at the edge, as illustrated by the graph in Figure 7.26.

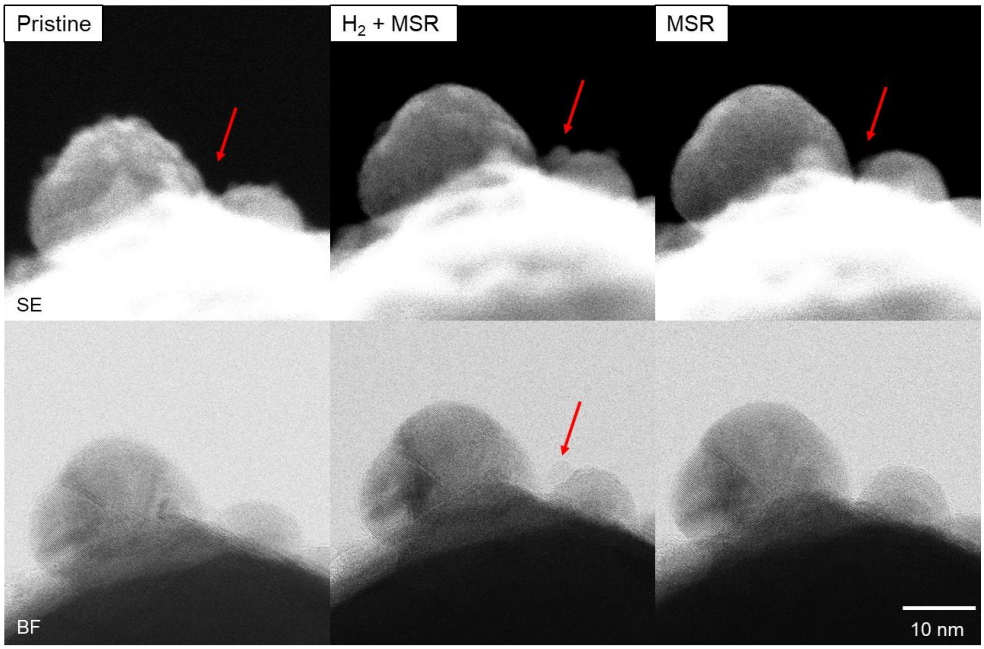

Figure 7.27: SE and DF images of ZnPd nanoparticles taken before (left), after treatment with hydrogen saturated with methanol and water at 200 °C (middle) and after treatment with sole water and methanol steam at 320 °C (right). The reference location was only exposed to the electron beam in vacuum. Red arrows indicate formation and decomposition of a patch.

The sample location, which is shown in Figure 7.23, exhibits similar phases. Here, atom rows with high DF contrast occur predominantly at the bulk, but not at the edge where the patch forms. Surface patches are not formed on all ZnPd nanoparticle, as shown in Figure 7.25. Such

patchless nanoparticles are either covered by a thin amorphous layer or Pd rich, indicated by atom rows with high DF signal.

In a second experimental step, the sample is exposed to pure methanol and water steam at 320 °C, mimicking the conditions applied in chapter 7.5. Different nanoparticles are imaged at reference locations in their pristine state, after treatment with hydrogen enriched with methanol and water at 200 °C, and after treatment in sole water and methanol steam at 320 °C. Such reference locations are only exposed to the electron beam in vacuum and are shown in Figure 7.22 and Figure 7.25. Surface patches, which form during treatment with enriched hydrogen, degrade during the subsequent treatment with only water and methanol steam. This behaviour is shown by the red arrows in Figure 7.27. In addition, other surface features are removed following the pure MSR treatment. The nanoparticle shown in Figure 7.22 loses its faceted morphology and regains a more irregular shape.

Figure 7.28 shows an EDX measurement of a ZnPd nanoparticle after treatment in methanol and water steam at 320 °C. Elemental analysis reveals that Pd is confined to the bulk, while Zn is homogenously distributed. As a result, the edge of the nanoparticle is Pd depleted and Zn enriched, as shown at the arrows at the EDX line scan in Figure 7.28. The oxygen content of the nanoparticle is relatively low and constant.

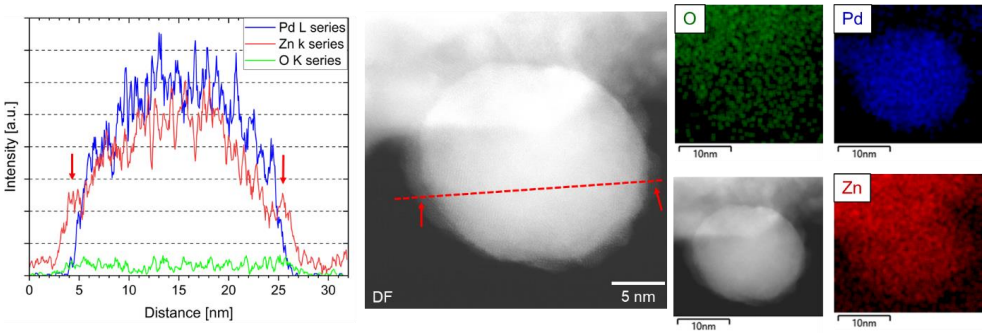

Figure 7.28: EDX measurement of a ZnPd nanoparticle taken after treatment with methanol and water steam at 320 °C. Line scan (left graph) was acquired along the dotted line illustrated in the DF image. Elemental maps (right) were recorded for oxygen (green), palladium (blue) and zinc (red).

7.6.4 Discussions of the Effect of Enriched Hydrogen

The addition of hydrogen has a significant impact on the outcome of *in situ* methanol steam reforming experiments. This chapter presents a discussion of the structural changes in ZnPd nanoparticles that are triggered by a hydrogen-enriched feed.

Formation of Surface Features due to Evolution of Zinc Palladium Nanoparticles

The present *in situ* experiment shows that surface features only form under the right redox conditions. The crystallographic study of the surface features shows good correspondence to zinc peroxide. This is in good agreement with the EDX measurements, which found nanoparticle edges consisting largely of zinc and oxygen. It seems plausible that the exact oxidation state of the Zn species also depends sensitively on the redox conditions, and temperature and may change depending on the water content in the environment. The results are consistent with the findings of Heggen and co-workers[45], who reported the formation of stoichiometric ZnO patches in *ex situ* MSR experiments.

The composition of the feed affects the occurrence of surface features. At the beginning of the gas injection, when the methanol and water contents were high, the conditions were not favourable for the formation of surface features. As the partial pressure of water and methanol decreased, surface features were formed on the ZnPd nanoparticles. At the same time, injection of pure hydrogen does not activate any formation of surface decorations, as deduced in chapter 7.3. Thus, only an interplay of hydrogen, methanol and water in the right ratio generates a redox potential, which allow for the formation of surface features. It is expected that the required hydrogen content is produced during MSR under standard laboratory conditions that are not fully replicated in the *in situ* STEM experiment. High methanol and water contents obstruct the formation and growth of surface features on ZnPd nanoparticles during *in situ* MSR experiments. In these regards, the results, deduced in chapter 7.4, suggest that precise control of the methanol content is decisive for the stability of ZnO, as high methanol contents facilitate its decomposition. Furthermore, the *in situ* experiment shows that surface features, which were initially formed during the reaction, degrade by a subsequent treatment under MSR conditions. This highlights the high dynamic of the system under reaction conditions and its sensitivity to the redox conditions. Therefore, the relative methanol content must not exceed a level that would prevent the formation of surface features. In addition, the low partial pressure, which is present due to the *in situ* conditions, is likely to facilitate the decomposition of the surface features. The present reversibility of the formation of surface features by decomposition indicates the presence of SMSI.

On the other hand, methanol and water also have a positive effect on the formation of surface features, as their presence was found to be essential for their occurrence, underlying that the precise selection of the redox conditions is pivotal to control the dynamic behaviour of the system. As deduced in chapter 7.5, methanol and water trigger changes in morphology and composition that may be crucial for the formation of surface features.

The morphological change involves the formation of crystallographic facets. Formation of surface features on ZnPd nanoparticles was observed on ZnPd (0 0 1) and (1 1 1) facets. This indicates that these ZnPd planes are energetically favourable for the formation of an interface with ZnO. The compositional changes involve segregation and formation of Zn-enriched areas.

As demonstrated in chapter 7.5.1, segregation mechanisms may be triggered by MSR conditions. The FFTs indicate that an intermediate phase forms between bulk and surface feature, creating a Pd gradient from the bulk to the surface of the nanoparticle. This intermediate phase is Zn-enriched, as evidenced by EDX measurements and the absence of periodic Pd planes. Consequently, the formation of surface features is favoured by Zn-enrichment. This is in good agreement with the work of Friedrich and co-workers, who also reported such Zn-enriched surfaces for unsupported ZnPd.[43] In their work Zn segregation on the surface could be topochemically activated and was present on fresh catalysts. However, it supports the idea that Zn enriches favourably on the surface of ZnPd and the presence of compositionally inhomogeneity in the intermetallic compound. Figure 7.29 illustrates the changes in the ZnPd/ZnO system that are triggered by varying redox conditions.

As saturated hydrogen was only injected at 200 °C, but pure MSR experiments were conducted at 320 °C, a temperature effect cannot be ruled out. However, it is expected that the onset temperature for methanol steam reforming is 200 °C and 320 °C enhances the yield. Therefore, both temperatures are supposed to be effective in MSR, but the kinetics is slower at 200 °C.

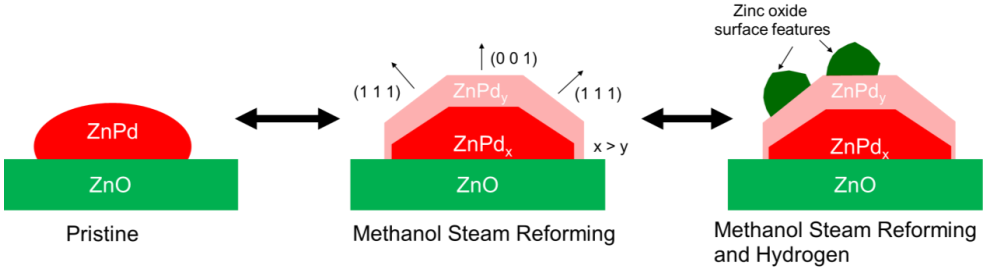

Figure 7.29: Schematic sketch of dynamical, structural changes in composition and morphology of the ZnPd/ZnO system during varying, reactive conditions. Formation of facets and Zn-rich surface are activated by MSR. Under the right redox conditions and in the presence of hydrogen, ZnO_2 surface features are formed on ZnPd.

The named phenomena have been experimentally demonstrated to favour the formation of surface features in their vicinity under suitable redox conditions. They are triggered by a MSR environment and thus occur during catalysis. As the selectivity and activity of the catalyst increase with time at constant temperature, feed and pressure[37], it can be inferred that the catalyst undergoes structural changes. Consequently, it is highly probable that the observed morphological and compositional alterations aid the enhancement in the catalytic performance of ZnPd/ZnO catalysts by enabling the formation of ZnO_2 patches. These results highlight the dynamic mechanisms involved in the catalysis process, offering insights into its fundamental principles. It is important to emphasise that phenomena, which are activated by methanol and water, only affect the nanoparticle, and not the actual formation and growth of surface features.

It is expected that hydrogen plays a pivotal role in these mechanisms and formation is only triggered if the right redox potential is met.

Types of Surface Features

Two distinct types of surface features have been observed during the MSR experiment with additional hydrogen that are referred to as 'patch' and 'coverage layer'.

ZnO patches form predominantly at locations on the support-far side of nanoparticles. As patches were not experimentally found to migrate from the support along the nanoparticle surface, it is expected that they form on the nanoparticle. The following formation mechanism is proposed. As Zn was found to enrich on the nanoparticle edges, surfaces with high Zn contents are formed. Zinc has a high oxidation potential and is partially oxidised by the present reactive conditions, forming ZnO_2 patches on the surface. Formation of ZnO patches on the surface of ZnPd has been discussed in the literature[43,45], but was never proven by *in situ* experiments nor explained through preferential formation on special facets. Hydrogen may support the formation of metallic Zn, which facilitates its oxidation.

In addition to the confined patches, ZnO coverage layers also formed during the present MSR experiments with additional hydrogen. It is likely that the coverage layers originate from the ZnO support and migrate along the surface of the nanoparticle, as shown in Figure 7.19. This migration behaviour is characteristic of SMSI and is driven by the minimisation of the surface free energy of the system. The high degree of wetting and the thin thickness indicate the presence of this particular driving force. Given that zinc peroxide converts to zinc oxide at temperatures < 200 °C[289], the formation of ZnO features may also involve intermediate ZnO_2 formation. Direct *in situ* visualisation may be hampered by a combination of the electron beam-activated temperature increase and the base temperature of 200 °C, which raises the temperature level just above the transformation temperature of ZnO_2.

Both types of surface features occur simultaneously, although they may differ in size, morphology and formation mechanism. Surface features only form under the correct redox conditions, requiring an interplay of hydrogen, water and methanol.

Absence of Structural Changes in Nanoparticles

Some nanoparticles demonstrated resilience to the reactive conditions, exhibiting no obvious structural changes. This suggests a non-uniform behaviour of the nanoparticles towards the applied conditions. Some of the 'resilient' nanoparticles had higher Pd contents. Consequently, a high Pd concentration at the surface appear to have a detrimental effect on formation of surface features and presumably on the catalytic properties. This is in good agreement with the work of Friedrich *et al.* [43], who found a reduced CO_2 selectivity and activity for unsupported ZnPd with high Pd contents at the surface. Other resilient nanoparticles had a thin amorphous surface layer, which apparently obstructed the formation of surface structures. Such surface

layer may hinder oxidation or segregation of Zn. There is no evidence of a size effect of nanoparticles in the formation of surface features.

Conclusions

The *in situ* study of ZnPd nanoparticles supported on ZnO was conducted under a hydrogen atmosphere enriched with methanol and water. The addition of hydrogen to the methanol and water was found to be pivotal for the formation of surface features on ZnPd nanoparticles, generating the redox conditions required. ZnPd evolved compositionally and morphologically due to the formation of (0 0 1) and (1 1 1) facets and a Zn-enriched surface, which generated energetically favourable sites for the subsequent formation of surface features. Two distinct types of zinc oxide surface features were found, which likely exhibit different formation mechanisms. The decomposition of the formed surface features at higher methanol and water contents shows the dynamic behaviour of the system and its reversibility, indicating the presence of SMSI.

The present *in situ* study represents the first experimental evidence of the formation process of such zinc oxide surface features during MSR. It provides valuable information on the dynamical changes in composition and structure that are activated by suitable redox conditions during catalysis. This study reveals the active state of the ZnPd/ZnO system in MSR and offers a plausible explanation for its enhanced selectivity in catalytic properties under reactive conditions.

7.7 In Situ Transmission Electron Microscopy Study of Methanol Steam Reforming Employing a Closed Cell Configuration

In order to study ZnPd nanoparticles supported on ZnO during MSR at a higher pressure, *in situ* TEM experiments were conducted in a closed cell configuration. The experimental set up is given in chapters 3.2.2 and 7.1.

7.7.1 Results of the Pre-reduction of Supported Zinc Palladium Nanoparticles

The ZnPd/ZnO system was monitored during the reduction in a hydrogen atmosphere, as shown in Figure 7.30. The system is largely unaffected by the reduction treatment. In isolated cases, ZnPd nanoparticles show minor changes in morphology. A thin amorphous coverage layer with a thickness of ~10 nm is present on ZnPd nanoparticles and their support. The coverage layer grows slightly during reduction.

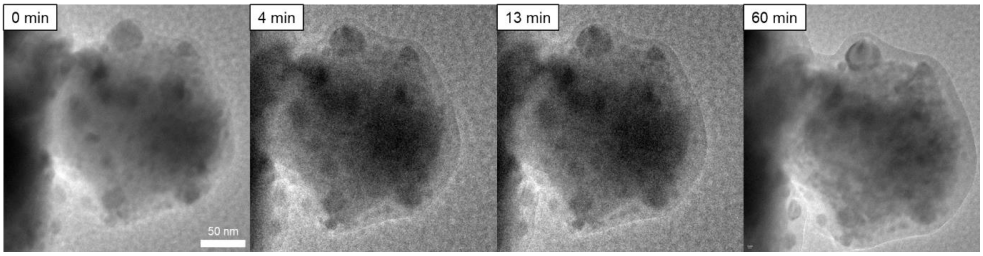

Figure 7.30: Series of HR-TEM images showing the ZnPd/ZnO system during reduction in a hydrogen atmosphere at 200 °C. Time stamps indicate time of reduction.

Figure 7.31 shows HR-TEM images of sample regions of supported ZnPd nanoparticles before and after reduction in a hydrogen atmosphere at 200 °C. These sample regions represent reference locations, which have not been exposed to the electron beam in a hydrogen atmosphere. The reference locations behave similar to regions studied *in situ*, indicating a neglectable beam effect for the reduction only. A coverage layer is not found at the reference locations.

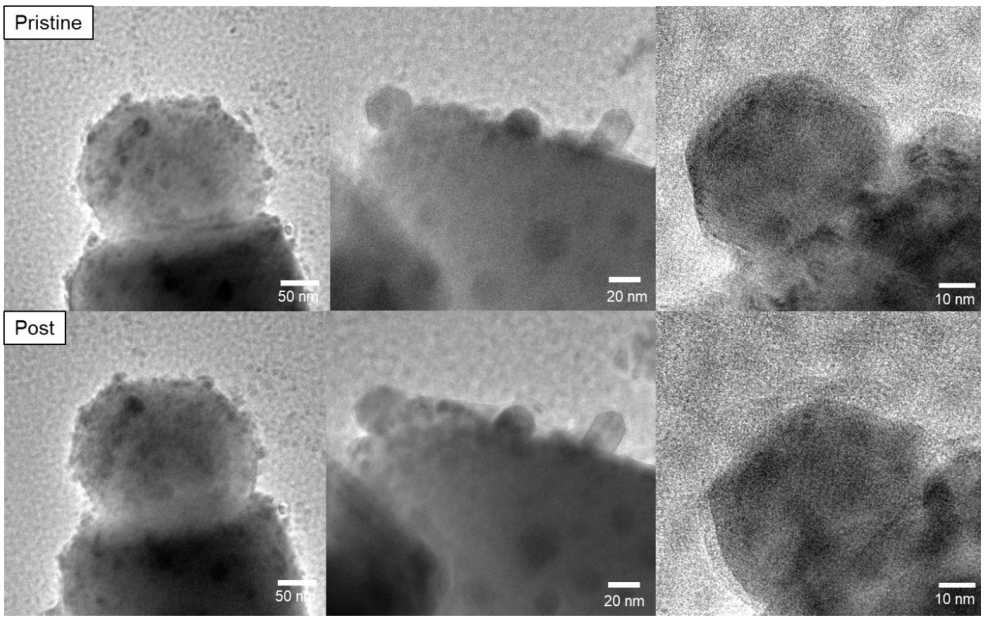

Figure 7.31: HR-TEM of ZnPd nanoparticles before (top row) and after reduction (bottom row) in a hydrogen atmosphere at 200 °C. The system is largely unaffected by the hydrogen treatment.

7.7.2 In Situ Results of the Methanol Steam Reforming Experiment

The ZnPd/ZnO system was observed at both high and low magnifications during methanol steam reforming. Figure 7.32 shows the formation of a new, crystalline feature on a ZnPd nanoparticle at a high magnification during the reference period. The red arrows indicate the formation process, which takes ~ 35 s.

In addition to the formation of novel features, ZnPd nanoparticles also exhibits a different dynamic behaviour, as shown in Figure 7.33. The regions of interest are indicated by the red arrows. In this instance, the contrast of the ZnPd nanoparticle undergoes a dynamic change over a period of ~11 s. Subsequently, the initial contrast of the nanoparticle is restored. As the residual system maintains its initial contrast, it can be concluded that this is a locally restricted phenomenon. Such dynamic changes in contrast are only observed in the case of ZnPd nanoparticles. Such contrast variations are not observed in the case of ZnO. The formation of novel features and the dynamic change in contrast of ZnPd nanoparticles, are observed throughout methanol steam reforming and are found to be independent from the time of the start of the experiment, indicating the presence of a reversible and dynamic mechanism.

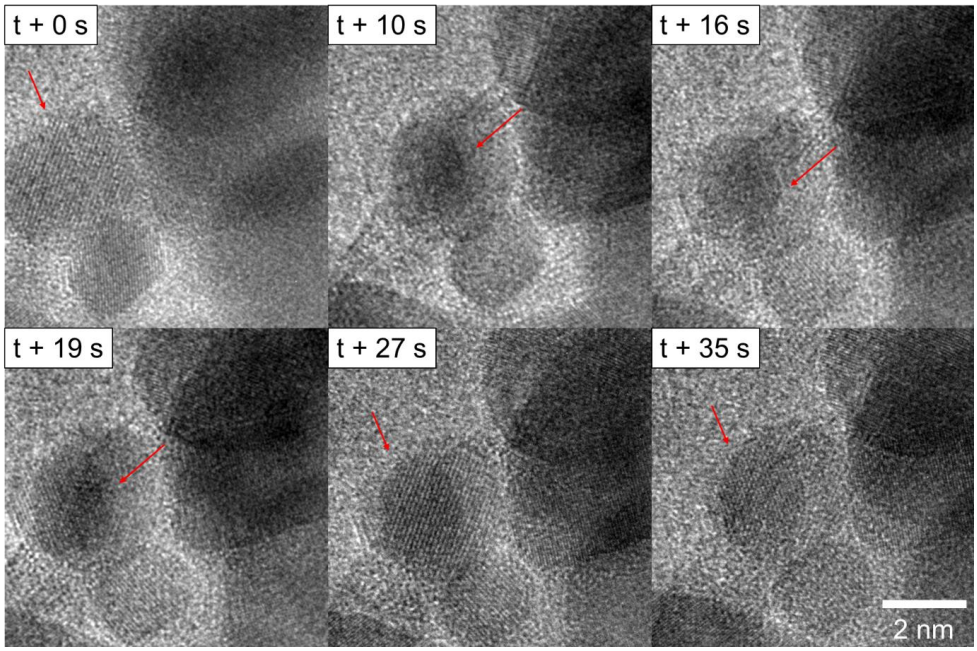

Figure 7.32: Series of HR-TEM images illustrating the formation process of a crystalline feature on a ZnPd nanoparticle.

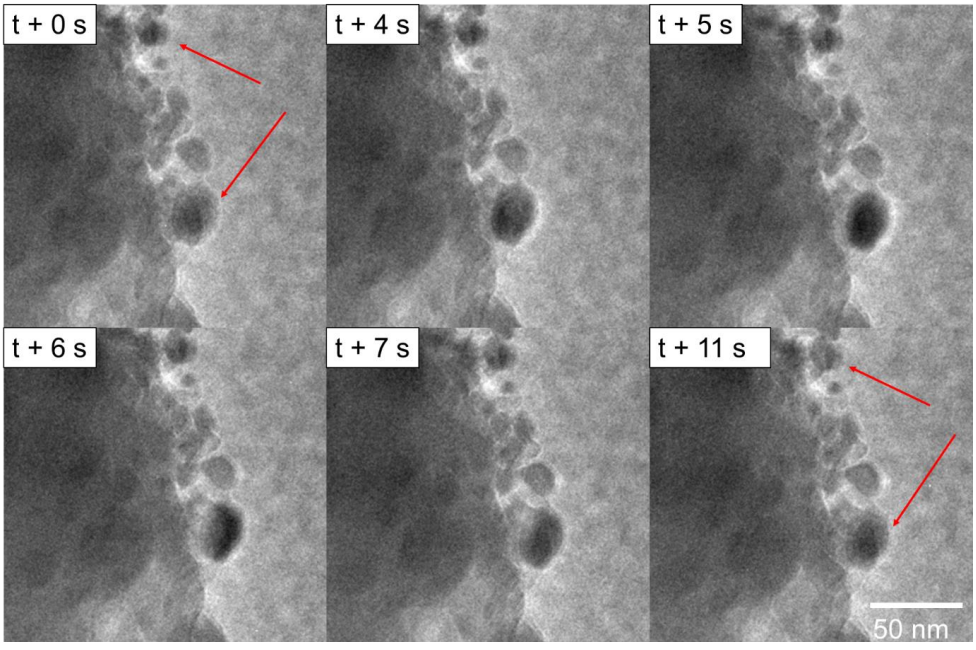

Figure 7.33: Series of HR-TEM images illustrating the dynamic contrast changes of ZnPd nanoparticles. The TEM signal of particles of interest, which are indicated by the red arrows, varied as a function of catalysis time.

Imaging of the same sample location during MSR reveals that the ZnO support undergoes decomposition after 120 s, as illustrated in Figure 7.34. As a result, the nanoparticles aggregate to form a dense cluster. The electron beam effect is qualitatively found to depend on the electron dose. A higher magnification and a more condensed beam accelerate ZnO decomposition. An electron beam effect is only observed in *in situ* TEM, when the sample is simultaneously exposed to MSR conditions and the electron beam for period longer than 120 s.

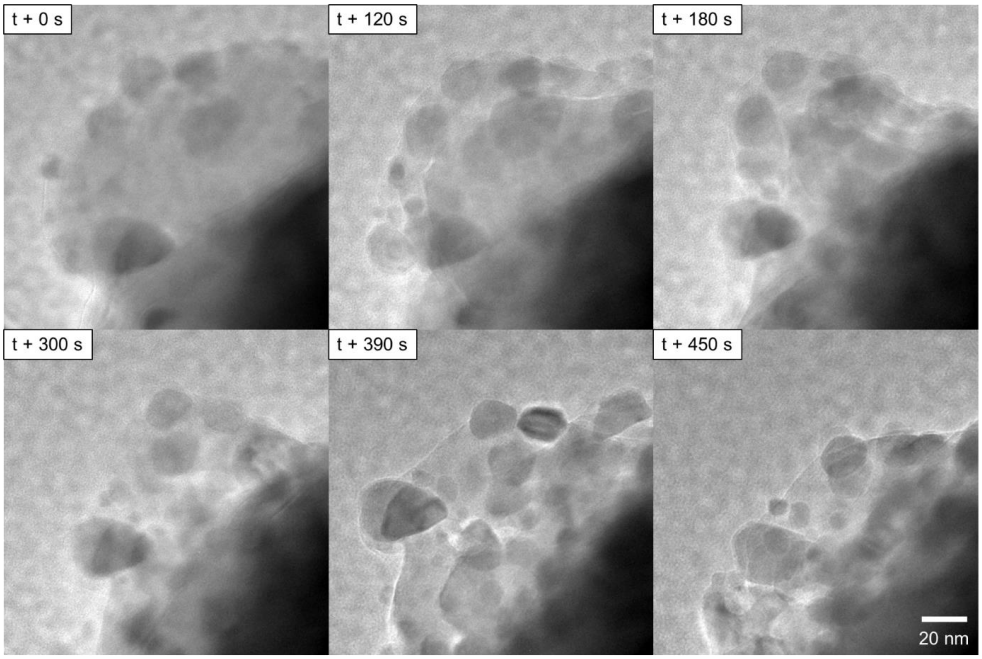

Figure 7.34: Series of HR-TEM images demonstrating an electron beam effect on the system during methanol steam reforming. The ZnO support degrades due to electron beam exposure. Time stamp indicates time of electron beam exposure.

As shown in Figure 7.35, reference locations were imaged both before and after MSR in order to evaluate a potential beam effect on the system. The images were acquired at a temperature of 40 °C in an argon atmosphere. In accordance with the *in situ* data, the contrast of some ZnPd nanoparticle changes during methanol steam reforming, as indicated by the green arrows. The occurrence of such changes appears to be random. Other ZnPd nanoparticles exhibit changes in morphology, as highlighted by the red arrows in Figure 7.35. The observed changes include the formation of facets. An identification of the facet planes is not possible due to absence of lattice information. The decomposition of the ZnO support is not observed at the reference locations.

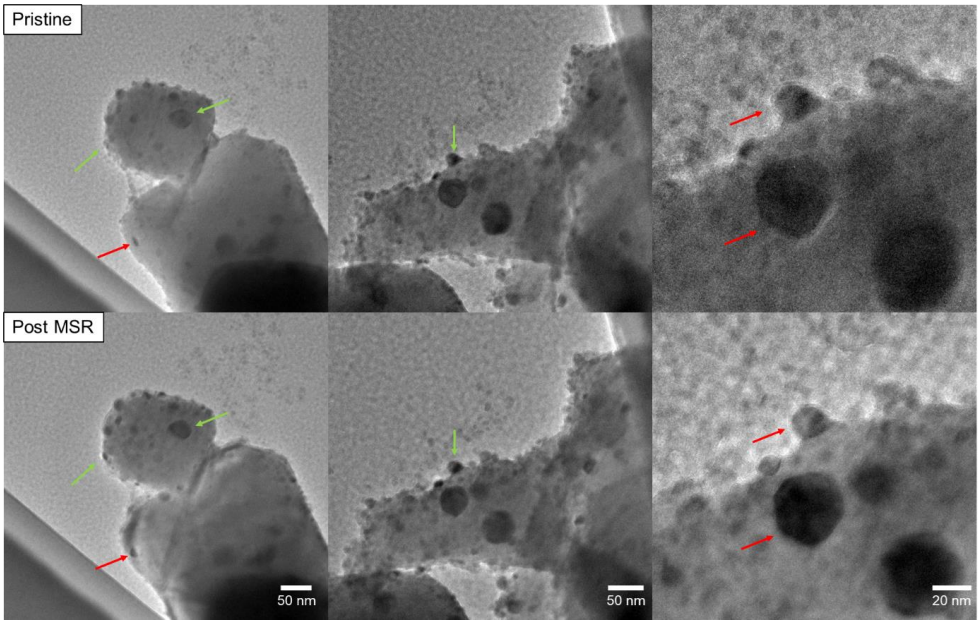

Figure 7.35: HR-TEM images showing reference locations before (top row) and after MSR (bottom row). The green arrows indicate change in contrast of the nanoparticles. The red arrows highlight the change in morphology. Some nanoparticles appear to form facets.

7.7.3 Discussions of Methanol Steam Reforming in situ Experiments by Applying a Closed Cell Configuration

The MSR of ZnPd nanoparticles supported on ZnO was investigated using *in situ* TEM with a closed cell configuration. The results obtained from the closed cell experiments are in accordance with those obtained from the open cell configuration. The system demonstrates resilience to structural and compositional changes during the reduction treatment in a hydrogen atmosphere.

The formation speed of the feature, which forms within seconds on ZnPd in the closed cell configuration, is faster than the formation speed during open cell experiments, which takes several minutes. This finding is in good accordance with the theory of catalysis by Langmuir[290] and Hinshelwood[291], who stated that the chemical potential exerts a direct influence on the kinetics of catalysis, namely the coverage and the reaction speed. It can be concluded that this is also true for changes induced by catalysis, including the formation of surface features, indicating a benchmark for the formation kinetics of catalysis-induced changes.

The dynamic changes in contrast, which occurred for ZnPd nanoparticles, can be attributed to dynamic changes of diffraction conditions due to nanoparticle changes or tilts with respect to

the incident electron beam inherent. As nanoparticles are located on the surface of the support, they are affected strongly by a change in support structure, e.g. decomposition. Lyu and co-workers found a comparable phenomenon in their *in situ* TEM experiments exploring carbon nanofiber growth on nickel catalysts.[292]

Furthermore, the alteration in the morphology of nanoparticles is in accordance with the data obtained from the experiments, using the open cell configuration, particularly the development of facets. These findings support the conclusion that the formation of facets is not attributable to the low partial pressure during the open cell experiments, but rather to the prevailing MSR conditions. This is also the case with regard to the decomposition of ZnO that is initiated by the electron beam. The closed cell experiments indicate that the decomposition of ZnO is based on the beam-induced change in selectivity, rather than the low partial pressure that was present during the open cell experiments.

Conclusions

In conclusion, the results obtained from the experiments, applying the closed cell configuration, are in good agreement with those obtained from the open cell experiments. The utilisation of the closed cell configuration enables the exclusion of intrinsic, experimental parameters inherent to the open cell configuration, such as the low partial pressure of the gas species or the reducing capabilities of the vacuum, which may otherwise act as a driving force for specific phenomena.

7.8 Experimental Challenges in the Quantitative Determination of Gas Compositions

In situ experiments in gas and vapour environments are inherent to many experimental challenges. The nature of such challenges may vary. They may be associated with instrumentation, the environment, chemicals or metrology. While the effect of some challenges is negligible, others have a severe impact on the quality of the experiment. This chapter discusses experimental challenges typically encountered in TEM experiments for *in situ* methanol steam reforming and the errors they cause.

In situ experiments in reactive conditions require a supply system, which introduces the respective medium to the experiment. Such supply systems are typically designed for pure gas or liquid experiments. For steam experiments, an additional vaporiser is required to evaporate the liquid, which represents the stable aggregate state of the chemical under standard conditions. The liquid is classically evaporated by an increase in temperature or reduction of the ambient pressure. Alternatively, a non-condensable carrier gas can be enriched with the liquid by bubbling the gas through the liquid. In *in situ* experiments, using a vapour is challenging as the vapour can condense on the walls of the pipe or reactor. Condensation inside a vertical tube

depends on parameters such as the temperature difference between the wall and the vapor, the presence of a non-condensable gas, the surface condition and the tube wall material.[293–295] Such parameters are typically fixed in an experimental setup and can only be modified to a limited degree. For example, the application of a heating jacket to heat the tube wall would not only be technically difficult, as not all components can be covered in the used setups, but would also change the experiment by increasing the feed temperature. As a result, the catalytic reaction could potentially be performed along the experimental setup due to materials, which may function as a catalyst, e.g. cooper components. In the setups used, the vaporizer unit was connected to the *in situ* cells by steel and polytetrafluoroethylene pipes that had a length of multiple meters due to the experimental design. An increase in pipe lengths promotes the probability of a condensation event and thus makes a precise estimation more challenging.

The interplay between condensation and evaporation plays a crucial role when considering a system of mixed vapours with different vapor pressures, such as methanol and water.[296] Since the evaporation rate is directly linked to the vapour pressure of a reactant, the ratio is expected to shift to the reactant with the higher vapour pressure under the given conditions.[297] A deviation from the given ratio affects the catalytic reactions, as it changes the chemical potential of the reactants and catalytic properties of the system. In the case of methanol steam reforming, methanol has a higher vapour pressure than water, which leads to an excess of methanol through condensation and subsequent evaporation. A higher methanol content facilitates methanol decomposition, which has a detrimental effect on CO_2 selectivity and presumably on the structural evolution of the catalyst. Condensation of mixed vapours is a complex mechanism requiring detailed comprehension of the thermodynamics of fluid mixtures, phase equilibria, heat transfer and mass transfer and the components of the instruments.[296] Many of these parameters can hardly be measured or must be estimated, which hampers an exact quantification.

Turbo molecular pumps (TMP) are most effective when operated within a pressure range of 10^{-7} to 1 mbar, thereby bridging the gap between mechanical and ion getter pumps.[298,299] Such vacuum quality is required for numerous physical measurement techniques, including mass spectroscopy (MS) and TEM. Consequently, TMPs are frequently employed in *in situ* TEM experiments. In the present *in situ* experiments, TMPs evacuate the microscope column by pumping out the injected gas and generate the working vacuum required for MS. TMPs exhibit varying pumping speeds for different chemical substances, sensitively depending on their molecular masses and properties. Generally, the pumping efficiency of an element and molecule decreases with its atomic number.[300] Given that this dependency is valid for methanol and water, it can be concluded that methanol is evacuated less effective than water. Consequently, the initial equilibrium state with equal contents will shift to higher methanol contents during the course of the experiment at a constant vapor supply, resulting in an excess in methanol in a given volume. In an environment where catalytic conditions are attempted to be replicated, this

implies that the catalytic prerequisites are constantly varying and differ from the set value. A comparable problem arises for MS, where the measured feed caused by the characteristics of the used TMP is different from the set feed. In addition, the conditions in the TEM and MS are not identical, as the vacuum pump configurations of the systems differ. The composition of the feed cannot be measured reliably with the requisite temporal resolution in the employed, instrumental system.

Detection of substances via MS is particularly challenging for MSR. Chemical substances of interest are methanol with an atomic number of 32, carbon monoxide with 28 and carbon dioxide. The present atomic numbers are identical with those of molecular oxygen and nitrogen, which are just as carbon dioxide common elements in air. This results in a potential overlap of the signals. This presents a significant obstacle to accurate measurements. Air can only be removed or diluted by a certain extent, so that a residual partial pressure of nitrogen and oxygen must be expected. In order to achieve a reliable measurement, it necessary to allow for longer acquisition times and to perform a calibration of the system for water and methanol. However, the aforementioned characteristics of TMPs present a significant challenge in this regard.

The composition of the feed also depends on the purity of the chemicals used. Anhydrous methanol (99,8 %) was used in the present experiments. However, during the course of its use, water may condense from the air and dissolve in the methanol, resulting in a gradual increase in water content. Consequently, the originally set ratio of water to methanol is obscured by the presence of water in the methanol.

In conclusion, it can be stated that the aforementioned parameters present a significant challenge in quantifying the methanol to water ratio with high precision. A number of assumptions are necessary in order to facilitate a general estimation. This methodology is inadequate for deriving effects based on the composition of the feed. A false bias based on an imprecise estimation may prove more detrimental than a qualitative approach. Consequently, the methanol and water contents are only treated qualitatively, and the results obtained from mass spectroscopy are not used in the analysis of the MSR results.

7.9 Conclusions

In situ STEM experiments in an open cell and closed cell configuration were conducted to examine the effect of methanol and water steam, hydrogen and heat on ZnPd nanoparticles supported on ZnO. The present experiments represent the first *in situ* STEM experiments utilizing a steam mixture of water and methanol, thus establishing a novel methodological approach to the study of methanol steam reforming and the impact of vapours on catalytic nanoparticles in general. *In situ* experiments with the isolated species demonstrated that methanol is a strong reducing agent for ZnO due to the presence of methanol decomposition

and a low experimental partial pressure. The injection of pure hydrogen and water steam had a stabilising effect on the system.

The simultaneous injection of water and methanol steam resulted in the activation of morphological and compositional changes in ZnPd nanoparticles. The morphological changes included the formation of facets, while the compositional changes involved a local enrichment of Zn. ZnO was subjected to strong decomposition when exposed to with the electron beam and the MSR conditions. It seems plausible to suggest that the electron beam changes the selectivity of the reaction, thereby promoting methanol decomposition. The injection of methanol and water steam alone was insufficient to trigger the formation of surface features.

Injection of hydrogen enriched with methanol and water steam activated the formation of surface features, but only under the right redox conditions. The presence of high methanol and water contents impede the growth process, indicating that a precise equilibrium between hydrogen, water and methanol is essential for the growth of ZnO surface features. Zinc oxide patches appeared to preferably grow on ZnPd (0 0 1) and (1 1 1) facets and Zn-enriched areas, which presumably form under MSR conditions. The results represent the first direct *in situ* visualisation of the formation of such ZnO patches. These findings contribute to our understanding of the dynamic changes in the structure and composition of the ZnPd/ZnO system during MSR. In addition, it provides a unique insight into the evolution processes that are triggered by catalytic conditions.

The application of a closed cell configuration allows the investigation of the system at a higher gas pressure. The obtained results are in good agreement with those found during the open cell experiments such as faceting of ZnPd nanoparticles and the minor structural effect of prereduction in a hydrogen atmosphere. The higher pressure accelerates the formation of surface features due to the higher chemical potential.

An evaluation of the challenges associated with measuring the feed composition reveals the complexity of such *in situ* STEM experiments. The used experimental setup cannot facilitate precise quantification of the feed composition. It shows that additional enhancements to the experimental configuration are needed to acquire reliable, compositional data and enable *operando* experiments.

8 Summary and Implications

In this work, the preparation of ZnPd nanoparticles supported on ZnO and their application as catalysts in methanol steam reforming were investigated applying *in situ* transmission electron microscopy. Specific focus was dedicated to the structural and compositional evolution of the system that occurred during the course of the individual reactions. The investigated preparation steps included the calcination of supported palladium nitrate and the reduction of supported palladium oxide.

The results of the *in situ* calcination experiment reveal that palladium nitrate starts to transform into palladium oxide at ~170 °C, triggering the growth of nanoparticles. A calcination treatment at temperatures between 200 and 400 °C creates a stable calcination window in which the nanoparticles resist any substantial increase in size. At temperatures exceeding 460 °C, PdO nanoparticles begin to convert into elemental Pd, accompanied by an increase in particle mobility on the ZnO support surface, particle agglomeration and the formation of ZnO nanorods. Above 660 °C in high vacuum, ZnO is subjected to faceting and decomposition, which is facilitated by the formation and evaporation of elemental zinc and oxygen. Results obtained from *ex situ* calcination experiments and DTA/TG measurements are in accordance with the observations made *in situ*. Consequently, supported palladium nitrate is best calcined at temperatures between 200 and 400 °C for 15 to 120 min.

In the *in situ* reduction experiments, supported PdO was transformed to intermetallic ZnPd, which followed two distinct formation steps, thereby elucidating the mechanism of reactive metal-support interaction. The initial phase of the process involves the activation of the ZnO support through hydrogen spillover, subsequent migration of ZnO to the nanoparticle surface, and an encapsulation of the nanoparticle. The second step comprises the nucleation of the ZnPd phase, its diffusion-controlled growth and the formation of a core-shell structure. The results obtained by a repetition of the reduction experiment at 200 °C demonstrate an acceleration of the observed transformation mechanism. These findings are in good agreement with similar *ex situ* experiments. In light of the experimental conditions, it can be concluded that the electron beam may enhance the effects of the reduction, yet does not appear to be the initiating factor, as evidenced by the stability observed under pure electron beam exposure. Other potential effects based on the formation of hydrogen plasma, temperature differences and the pressure gap, have a minor impact and can be largely disregarded. The findings of the experiments are in accordance with those reported in literature. The results from the present *in situ* reduction experiment illustrate mechanics of the reduction of PdO and the respective RMSI with high temporal and spatial resolution. The mechanism bears resemblance to SMSI; however, there are notable distinctions in the interaction between the nanoparticle and the coverage layer, where an intermetallic phase is formed by RMSI.

In situ STEM experiments with open and closed cell configurations were performed to examine the effect of methanol and water steam, hydrogen and heat on ZnPd nanoparticles supported on ZnO. *In situ* investigation of the single atmosphere species revealed that methanol is a strong reducing agent for ZnO, as demonstrated by the decomposition of the support. In contrast, the injection of pure hydrogen and water steam has a stabilising effect on the system. Simultaneous introduction of water and methanol steam activates an evolution in composition and morphology of ZnPd nanoparticles. The morphological changes comprise faceting of the nanoparticle, while the compositional changes involve a local enrichment of Zn. The simultaneous exposure to the electron beam and MSR conditions facilitate strong decomposition of ZnO, changing the selectivity of the reaction and promoting methanol decomposition. The necessary redox conditions for the formation of surface features are obtained, when hydrogen is added to methanol and water steam. High methanol and water contents impede the formation process, indicating that a precise equilibrium between hydrogen, water and methanol is essential for the growth of zinc oxide surface features. ZnO patches preferentially grow on ZnPd (0 0 1) and (1 1 1) facets and Zn-enriched areas, which form under MSR conditions. The application of a closed cell configuration increases the experimental pressure and accelerates the formation of surface features due to the higher chemical potential. Results obtained from open and closed cell configurations are in good agreement. The results represent the first *in situ* observation of the formation of such zinc oxide patches. These results contribute to our understanding of the dynamic changes in the structure and composition of the ZnPd/ZnO system during MSR. It also provides a unique insight into the dynamic, structural processes that are triggered by catalytic conditions.

The conducted experiments allow direct atomic-scale visualisation and quantification of the dynamic processes occurring in supported ZnPd nanoparticles during their preparation and catalysis. The methanol steam reforming experiments represent the first *in situ* TEM experiments with a steam mixture, offering unique insights into the structural changes of the ZnPd/ZnO system and the formation mechanism of ZnO surface features. This constitutes a significant contribution to the comprehension of catalysts under operational conditions and represent a breakthrough in the utilisation of *in situ* TEM, establishing a methodology for the investigation of catalysts operating in steam environments. The findings are interesting for numerous scientific communities, as they provide unique insights into the design, synthesis and utilisation of a highly active catalytic system.

9 Outlook

Furthermore, it would be interesting to study the quantification of the methanol-to-water ratio of the feed. Given the intrinsic limitation of *in situ* TEM and the used experimental configuration, the impact of the feed could only be analysed qualitatively. However, the quantification of the present redox potential was found to be highly desirable, given that the growth of ZnO surface features was only observed under specific reactive conditions. A more precise quantification of the composition of the feed would require a different experimental configuration. Thermal evaporation of a methanol and water mixture, in conjunction with the application of a carrier gas and heating jackets, are viable approaches to enhance the control of the feed composition. The results and methodology applied in this work form a solid foundation and promising starting point for further exploration of the *in situ* TEM experiment in a steam environment.

Further work that could follow on this point is the study of the catalytic properties of the investigated ZnPd nanoparticles. Despite the sample being prepared according to a well-established protocol, which is known to yield catalytically active ZnPd nanoparticles, the system was not tested under realistic catalytic conditions. Furthermore, the changes that were activated during catalysis cannot be directly linked to the catalytic performance, and thus their effect remains undetermined. Nevertheless, it would be advantageous to conduct such *operando* experiments in order to elucidate the active species of a catalyst. The utilisation of a novel experimental configuration, which employs a residual gas analyser, may facilitate a detailed examination of the catalytic properties, as it allows for the differentiation of molecules with the same atomic number.

Deviations in pressure and time represent factors that may potentially limit the accuracy of *in situ* TEM experiments. Given that catalysts are typically applied for many years, specific activation or deactivation mechanisms may only manifest after a long time frame, which is not technically replicable in a TEM. In open cell configurations, there is a large pressure gap, which affects the kinetics of a chemical reaction. Thus, the same chemical reaction may be accelerated or changed at a higher pressure. The results obtained from experiments conducted in identical locations can be used as a reference point to account for limitations that are inherent to the experimental process.

In conclusion, a natural progression of this work is to quantify the observations made in this study by upgrading the experimental configuration. Given that the present study was the first to explore the use of a catalyst applying *in situ* TEM during methanol steam reforming, it would be interesting to investigate other catalytic systems that are catalytically active in such an environment.

10 References

1. Cornelissen, B., Neumann, P. & Schweiger, O. Global warming promotes biological invasion of a honey bee pest. *Glob. Chang. Biol.* **25**, 3642–3655 (2019).
2. Aguilar, A. & Patermann, C. Biodiplomacy, the new frontier for bioeconomy. *N. Biotechnol.* **59**, 20–25 (2020).
3. Khasnis, A. A. & Nettleman, M. D. Global Warming and Infectious Disease (Review article). *Arch. Med. Res.* **36**, 689–696 (2005).
4. The Federal Constitutional Court. Constitutional complaints against the Federal Climate Change Act partially successful. **2**, 2–5 (2021).
5. Germany, F. S. O. of. Stromerzeugung 2023: 56 % aus erneuerbaren Energieträgern. https://www-genesis.destatis.de/genesis/online?&sequenz=tabelleErgebnis&selectionname=43312-0001#abreadcrumb (2024).
6. Hassan, I. A., Ramadan, H. S., Saleh, M. A. & Hissel, D. Hydrogen storage technologies for stationary and mobile applications: Review, analysis and perspectives. *Renew. Sustain. Energy Rev.* **149**, 111311 (2021).
7. Press and Information Office of the Federal Government. Energy from climate-friendly gas. https://www.bundesregierung.de/breg-en/news/hydrogen-technology-2204238 (2024).
8. Smith, C., Hill, A. K. & Torrente-Murciano, L. Current and future role of Haber-Bosch ammonia in a carbon-free energy landscape. *Energy Environ. Sci.* **13**, 331–344 (2020).
9. Ma, Y. *et al.* Hierarchical nature of hydrogen-based direct reduction of iron oxides. *Scr. Mater.* **213**, 1–7 (2022).
10. Schlapbach, L. & Züttel, A. for Mobile Applications. *Nature* **414**, 353–358 (2001).
11. Deutsches Insitut für Normung. Automotive fuels - Unleaded petrol - Requirements and test methods; German version EN 228:2012+A1:2017. 20 (2017) doi:https://dx.doi.org/10.31030/2669458.
12. Preuster, P., Alekseev, A. & Wasserscheid, P. Hydrogen storage technologies for future energy systems. *Annu. Rev. Chem. Biomol. Eng.* **8**, 445–471 (2017).
13. Roszak, R., Firlej, L., Roszak, S., Pfeifer, P. & Kuchta, B. Hydrogen storage by adsorption in porous materials: Is it possible? *Colloids Surfaces A Physicochem. Eng. Asp.* **496**, 69–76 (2016).
14. Andersson, J. & Grönkvist, S. Large-scale storage of hydrogen. *Int. J. Hydrogen Energy* **44**, 11901–11919 (2019).
15. Usman, M. R. Hydrogen storage methods: Review and current status. *Renew. Sustain. Energy Rev.* **167**, 112743 (2022).
16. Aziz, M., TriWijayanta, A. & Nandiyanto, A. B. D. Ammonia as effective hydrogen storage: A review on production, storage and utilization. *Energies* **13**, 1–25 (2020).
17. Wijayanta, A. T., Oda, T., Purnomo, C. W., Kashiwagi, T. & Aziz, M. Liquid hydrogen, methylcyclohexane, and ammonia as potential hydrogen storage: Comparison review. *Int. J. Hydrogen Energy* **44**, 15026–15044 (2019).

18. Eberle, U., Felderhoff, M. & Schüth, F. Chemical and physical solutions for hydrogen storage. *Angew. Chemie - Int. Ed.* **48**, 6608–6630 (2009).

19. Behrens, M. Chemical hydrogen storage by methanol: Challenges for the catalytic methanol synthesis from CO2. *Recycl. Catal.* **2**, 78–86 (2016).

20. Räuchle, K., Plass, L., Wernicke, H. J. & Bertau, M. Methanol for Renewable Energy Storage and Utilization. *Energy Technol.* **4**, 193–200 (2016).

21. Olah, G. A., Prakash, G. K. S. & Goeppert, A. Anthropogenic chemical carbon cycle for a sustainable future. *J. Am. Chem. Soc.* **133**, 12881–12898 (2011).

22. Olah, G. A., Goeppert, A. & Prakash, G. K. S. *Beyond Oil and Gas: The Methanol Economy*. (Wiley, 2009). doi:10.1002/9783527627806.

23. Avgouropoulos, G. *et al.* Performance evaluation of a proof-of-concept 70 W internal reforming methanol fuel cell system. *J. Power Sources* **307**, 875–882 (2016).

24. Bayrakçeken, A., Türker, L. & Eroğluc, I. Improvement of carbon dioxide tolerance of PEMFC electrocatalyst by using microwave irradiation technique. *Int. J. Hydrogen Energy* **33**, 7527–7537 (2008).

25. Oetjen, H. -F., Schmidt, V. M., Stimming, U. & Trila, F. Performance Data of a Proton Exchange Membrane Fuel Cell Using H 2 / CO as Fuel Gas. *J. Electrochem. Soc.* **143**, 3838–3842 (1996).

26. Shen, J. P. & Song, C. Influence of preparation method on performance of Cu/Zn-based catalysts for low-temperature steam reforming and oxidative steam reforming of methanol for H2 production for fuel cells. *Catal. Today* **77**, 89–98 (2002).

27. Purnama, H. *et al.* CO formation/selectivity for steam reforming of methanol with a commercial CuO/ZnO/Al2O3 catalyst. *Appl. Catal. A Gen.* **259**, 83–94 (2004).

28. CONANT, T. *et al.* Stability of bimetallic Pd–Zn catalysts for the steam reforming of methanol. *J. Catal.* **257**, 64–70 (2008).

29. KARIM, A., CONANT, T. & DATYE, A. The role of PdZn alloy formation and particle size on the selectivity for steam reforming of methanol. *J. Catal.* **243**, 420–427 (2006).

30. Ranganathan, E. S., Bej, S. K. & Thompson, L. T. Methanol steam reforming over Pd/ZnO and Pd/CeO2 catalysts. *Appl. Catal. A Gen.* **289**, 153–162 (2005).

31. Dagle, R. A. *et al.* Carbon dioxide conversion to valuable chemical products over composite catalytic systems. *J. Energy Chem.* **22**, 368–374 (2013).

32. Karim, A. M., Conant, T. & Datye, A. K. Controlling ZnO morphology for improved methanol steam reforming reactivity. *Phys. Chem. Chem. Phys.* **10**, 5584–5590 (2008).

33. Iwasa, N., Masuda, S. & Takezawa, N. Steam reforming of methanol over Ni, Co, Pd and Pt supported on ZnO. *React. Kinet. Catal. Lett.* **55**, 349–353 (1995).

34. Föttinger, K., Van Bokhoven, J. A., Nachtegaal, M. & Rupprechter, G. Dynamic structure of a working methanol steam reforming catalyst: In situ quick-EXAFS on Pd/ZnO nanoparticles. *J. Phys. Chem. Lett.* **2**, 428–433 (2011).

35. Friedrich, M., Teschner, D., Knop-Gericke, A. & Armbrüster, M. Influence of bulk composition of the intermetallic compound ZnPd on surface composition and methanol steam reforming properties. *J. Catal.* **285**, 41–47 (2012).

36. Lorenz, H., Friedrich, M., Armbrüster, M., Klötzer, B. & Penner, S. ZnO is a CO2-selective steam reforming catalyst. *J. Catal.* **297**, 151–154 (2013).

37. Friedrich, M., Penner, S., Heggen, M. & Armbrüster, M. High CO2 selectivity in methanol steam reforming through ZnPd/ZnO teamwork. *Angew. Chemie - Int. Ed.* **52**, 4389–4392 (2013).

38. Armbrüster, M. *et al.* The Intermetallic Compound ZnPd and Its Role in Methanol Steam Reforming. *Catal. Rev.* **55**, 289–367 (2013).

39. Rameshan, C. *et al.* Steam reforming of methanol on PdZn near-surface alloys on Pd(111) and Pd foil studied by in-situ XPS, LEIS and PM-IRAS. *J. Catal.* **276**, 101–113 (2010).

40. Rameshan, C. *et al.* Subsurface-controlled CO2 selectivity of PdZn near-surface alloys in H2 generation by methanol steam reforming. *Angew. Chemie - Int. Ed.* **49**, 3224–3227 (2010).

41. Rameshan, C. *et al.* Hydrogen production by methanol steam reforming on copper boosted by zinc-assisted water activation. *Angew. Chemie - Int. Ed.* **51**, 3002–3006 (2012).

42. Armbrüster, M. *et al.* The intermetallic compound ZnPd and its role in methanol steam reforming. *Catal. Rev. - Sci. Eng.* **55**, 289–367 (2013).

43. Friedrich, M., Teschner, D., Knop-Gericke, A. & Armbrüster, M. Influence of bulk composition of the intermetallic compound ZnPd on surface composition and methanol steam reforming properties. *J. Catal.* **285**, 41–47 (2012).

44. Chee, S. W., Lunkenbein, T., Schlogl, R. & Roldan Cuenya, B. In situ and operando electron microscopy in heterogeneous catalysis-insights into multi-scale chemical dynamics. *J. Phys. Condens. Matter* **33**, (2021).

45. Heggen, M., Penner, S., Friedrich, M., Dunin-Borkowski, R. E. & Armbrüster, M. Formation of ZnO patches on ZnPd/ZnO during methanol steam reforming: A strong metal-support interaction effect? *J. Phys. Chem. C* **120**, 10460–10465 (2016).

46. Peterson, E. J. *et al.* Aerosol synthesis and Rietveld analysis of tetragonal (β1) PdZn. *J. Alloys Compd.* **509**, 1463–1470 (2011).

47. Friedrich, M. Die intermetallischen Verbindungen ZnPd und ZnNi als Modellkatalysatoren in der Methanoldampfreformierung. (Technische Universität Dresden, 2013).

48. Wang, Y., Zhang, J. & Xu, H. Interaction between Pd and ZnO during Reduction of Pd/ZnO Catalyst for Steam Reforming of Methanol to Hydrogen. *Chinese J. Catal.* **27**, 217–222 (2006).

49. Tsai, A. P., Kameoka, S. & Ishii, Y. PdZn = Cu: Can an intermetallic compound replace an element? *J. Phys. Soc. Japan* **73**, 3270–3273 (2004).

50. Chinchen, G. C., Waugh, K. C. & Whan, D. A. The activity and state of the copper surface in methanol synthesis catalysts. *Appl. Catal.* **25**, 101–107 (1986).

51. Breen, J. P. & Ross, J. R. H. Methanol reforming for fuel-cell applications: Development of zirconia-containing Cu-Zn-Al catalysts. *Catal. Today* **51**, 521–533 (1999).

52. Twigg, M. V. & Spencer, M. S. Deactivation of copper metal catalysts for methanol decomposition, methanol steam reforming and methanol synthesis. *Top. Catal.* **22**, 191–203 (2003).

53. Kam, R., Scott, J., Amal, R. & Selomulya, C. Pyrophoricity and stability of copper and platinum based water-gas shift catalysts during oxidative shut-down/start-up operation.

Chem. Eng. Sci. **65**, 6461–6470 (2010).

54. Sá, S., Silva, H., Brandão, L., Sousa, J. M. & Mendes, A. Catalysts for methanol steam reforming-A review. *Appl. Catal. B Environ.* **99**, 43–57 (2010).

55. Gucyi, L., Andras, E. & Armbrüster, M. *Catalysts for Alternative Energy*. *Journal of Chemical Information and Modeling* vol. 53 (2013).

56. Lin, S., Xie, D. & Guo, H. Pathways of methanol steam reforming on pdzn and comparison with Cu. *J. Phys. Chem. C* **115**, 20583–20589 (2011).

57. Armbruster, M. *et al.* Unprecedented catalytic activity and selectivity in methanol steam reforming by reactive transformation of intermetallic in-pt compounds. *J. Phys. Chem. C* **125**, 9809–9817 (2021).

58. Mars, P. & van Krevelen, D. W. Oxidations carried out by means of vanadium oxide catalysts. *Chem. Eng. Sci.* **3**, 41–59 (1954).

59. Speight, J. G. & Ph, D. *1340-1625805401-Qqoazhfj.pdf*.

60. Gibbard, H. F. & Creek, J. L. Vapor Pressure of Methanol from 288.15 to 337.65K. *J. Chem. Eng. Data* **19**, 308–310 (1974).

61. Ovrutsky, A. M., Prokhoda, A. S. & Rasshchupkyna, M. S. Basic Concepts of Theory of Phase Transformations. in *Computational Materials Science* 35–69 (Elsevier, 2014). doi:10.1016/B978-0-12-420143-9.00002-8.

62. Koga, Y. Solution Thermodynamics—Use of the Second and Third Derivatives of G. in *Solution Thermodynamics and its Application to Aqueous Solutions* 27–61 (Elsevier, 2017). doi:10.1016/B978-0-444-63629-4.00002-X.

63. Bredig, G., Bayer, R., Dupre, S., Werte, S. & Siedepunktsbeobachtungen, D. I . Die Dampfdrücke des binären Systems. (1927).

64. Sonntag, D. Important new Values of the Physical Constants of 1986, Vapour Pressure Formulations based on ITS-90, and Psychrometer Formulae. *Zeitschrift für Meteorol.* **40**, 343 (1990).

65. Lunkenbein, T., Schumann, J., Behrens, M., Schlögl, R. & Willinger, M. G. Formation of a ZnO Overlayer in Industrial Cu/ZnO/Al 2 O 3 Catalysts Induced by Strong Metal–Support Interactions . *Angew. Chemie* **127**, 4627–4631 (2015).

66. Bagheri, S., Muhd Julkapli, N. & Bee Abd Hamid, S. Titanium dioxide as a catalyst support in heterogeneous catalysis. *Sci. World J.* **2014**, (2014).

67. Tu, W. *et al.* Gas-Dependent Active Sites on Cu/ZnO Clusters for CH3OH Synthesis. *J. Am. Chem. Soc.* (2022) doi:10.1021/jacs.2c13784.

68. Lykhach, Y. *et al.* Oxide-based nanomaterials for fuel cell catalysis: The interplay between supported single Pt atoms and particles. *Catal. Sci. Technol.* **7**, 4315–4345 (2017).

69. Kong, M., Fei, J., Wang, S., Lu, W. & Zheng, X. Influence of supports on catalytic behavior of nickel catalysts in carbon dioxide reforming of toluene as a model compound of tar from biomass gasification. *Bioresour. Technol.* **102**, 2004–2008 (2011).

70. Wang, W., Qu, Z., Song, L. & Fu, Q. CO2 hydrogenation to methanol over Cu/CeO2 and Cu/ZrO2 catalysts: Tuning methanol selectivity via metal-support interaction. *J. Energy Chem.* **40**, 22–30 (2020).

71. Jenness, G. R. & Schmidt, J. R. Unraveling the role of metal-support interactions in

heterogeneous catalysis: Oxygenate selectivity in Fischer-Tropsch synthesis. *ACS Catal.* **3**, 2881–2890 (2013).

72. Zhang, J. *et al.* Strong Metal-Support Interaction Boosts Activity, Selectivity, and Stability in Electrosynthesis of H2O2. *J. Am. Chem. Soc.* **144**, 2255–2263 (2022).

73. van Deelen, T. W., Hernández Mejía, C. & de Jong, K. P. Control of metal-support interactions in heterogeneous catalysts to enhance activity and selectivity. *Nat. Catal.* **2**, 955–970 (2019).

74. Xiong, M., Gao, Z. & Qin, Y. Spillover in Heterogeneous Catalysis: New Insights and Opportunities. *ACS Catal.* **11**, 3159–3172 (2021).

75. Conner, W. C. & Falconer, J. L. Spillover in Heterogeneous Catalysis. *Chem. Rev.* **95**, 759–788 (1995).

76. Karim, W. *et al.* Catalyst support effects on hydrogen spillover. *Nature* **541**, 68–71 (2017).

77. Kamada, T. *et al.* Ultralong Distance Hydrogen Spillover Enabled by Valence Changes in a Metal Oxide Surface. *J. Am. Chem. Soc.* **145**, 1631–1637 (2023).

78. Shen, H., Li, H., Yang, Z. & Li, C. Magic of hydrogen spillover: Understanding and application. *Green Energy Environ.* **7**, 1161–1198 (2022).

79. Khoobiar, S. Particle to Particle Migration of Hydrogen Atoms on Platinum—Alumina Catalysts from Particle to Neighboring Particles. *J. Phys. Chem.* **68**, 411–412 (1964).

80. Peden, C. H. F. & Goodman, D. W. Model Studies of Copper/Ruthenium Bimetallic Catalysts. *Ind. Eng. Chem. Fundam.* **25**, 58–62 (1986).

81. Fujimoto, K., Uchijima, T., Masai, M. & Inui, T. *New Aspects of Spillover Effect in Catalysis - For Development of Highly Active Catalysts*. (Elsevier Science, 1993).

82. Burch, R., Golunski, S. E. & Spencer, M. S. The role of copper and zinc oxide in methanol synthesis catalysts. *J. Chem. Soc. Faraday Trans.* **86**, 2683–2691 (1990).

83. Dutta, G., Waghmare, U. V., Baidya, T. & Hegde, M. S. Hydrogen spillover on CeO2/Pt: Enhanced storage of active hydrogen. *Chem. Mater.* **19**, 6430–6436 (2007).

84. Platonov, V., Nasriddinov, A. & Rumyantseva, M. Electrospun ZnO/Pd Nanofibers as Extremely Sensitive Material for Hydrogen Detection in Oxygen Free Gas Phase. *Polymers (Basel).* **14**, (2022).

85. Beck, A. *et al.* Hydrogen Interaction with Oxide Supports in the Presence and Absence of Platinum. *J. Phys. Chem. C* **126**, 17589–17597 (2022).

86. Sasikala, R. & Kulshreshtha, S. K. Temperature programmed reduction studies of spillover effect in Pd impregnated metal oxide catalysts. *J. Therm. Anal. Calorim.* **78**, 723–729 (2004).

87. Argyle, M. D. & Bartholomew, C. H. Heterogeneous catalyst deactivation and regeneration: A review. *Catalysts* **5**, 145–269 (2015).

88. Van Deelen, T. W., Nijhuis, J. J., Krans, N. A., Zečević, J. & De Jong, K. P. Preparation of Cobalt Nanocrystals Supported on Metal Oxides to Study Particle Growth in Fischer-Tropsch Catalysts. *ACS Catal.* **8**, 10581–10589 (2018).

89. Penner, S. & Armbrüster, M. Formation of intermetallic compounds by reactive metal-support interaction: A frequently encountered phenomenon in catalysis. *ChemCatChem* **7**, 374–392 (2015).

90. Föttinger, K., Van Bokhoven, J. A., Nachtegaal, M. & Rupprechter, G. Dynamic structure of a working methanol steam reforming catalyst: In situ quick-EXAFS on Pd/ZnO nanoparticles. *J. Phys. Chem. Lett.* **2**, 428–433 (2011).

91. Chin, Y. H., Dagle, R., Hu, J., Dohnalkova, A. C. & Wang, Y. Steam reforming of methanol over highly active Pd/ZnO catalyst. *Catal. Today* **77**, 79–88 (2002).

92. Iwasa, N. & Takezawa, N. New supported Pd and Pt alloy catalysts for steam reforming and dehydrogenation of methanol. *Top. Catal.* **22**, 215–224 (2003).

93. Chin, Y. H., Wang, Y., Dagle, R. A. & Li, X. S. Methanol steam reforming over Pd/ZnO: Catalyst preparation and pretreatment studies. *Fuel Process. Technol.* **83**, 193–201 (2003).

94. Kriegel, R., Ivarsson, D. C. A. & Armbrüster, M. Formic Acid Decomposition over ZnPd—Implications for Methanol Steam Reforming. *ChemCatChem* **10**, 2664–2672 (2018).

95. Martin, N. M. *et al.* Dissociative adsorption of hydrogen on PdO(101) studied by HRCLS and DFT. *J. Phys. Chem. C* **117**, 13510–13519 (2013).

96. Iwasa, N., Suzuki, H., MasaoTerashita, Arai, M. & Takezawa, N. Methanol synthesis from CO2 under atmospheric pressure over supported Pd catalysts. *Catal. Letters* **96**, 75–78 (2004).

97. Bowker, M. *et al.* The Critical Role of βpdZn Alloy in Pd/ZnO Catalysts for the Hydrogenation of Carbon Dioxide to Methanol. *ACS Catal.* **12**, 5371–5379 (2022).

98. Shen, L. *et al.* PdZn intermetallic on a CN@ZnO hybrid as an efficient catalyst for the semihydrogenation of alkynols. *J. Catal.* **350**, 13–20 (2017).

99. Fujita, S. *et al.* Pd and PdZn supported on ZnO as catalysts for the hydrogenation of cinnamaldehyde to hydrocinnamyl alcohol. *Mol. Catal.* **442**, 12–19 (2017).

100. Lamber, R., Jaeger, N. & Schulz-Ekloff, G. On the metal-support interaction in the Ni-SiO2 system. *Surf. Sci.* **227**, 268–272 (1990).

101. Li, X., Zhao, J. & Su, D. Structural Changes of Intermetallic Catalysts under Reaction Conditions. *Small Struct.* **2**, 1–22 (2021).

102. Gebauer-Henke, E., Touroude, R. & Rynkowski, J. Catalytic and physicochemical properties of Pt/α-GeO2 systems in reaction of selective hydrogenation of α,β-unsaturated aldehydes in a gas phase. *Kinet. Catal.* **48**, 562–566 (2007).

103. Okanishi, T., Matsui, T., Takeguchi, T., Kikuchi, R. & Eguchi, K. Chemical interaction between Pt and SnO2 and influence on adsorptive properties of carbon monoxide. *Appl. Catal. A Gen.* **298**, 181–187 (2006).

104. Resasco, D. E., Weber, R. S., Sakellson, S., McMillan, M. & Haller, G. L. X-RAY ABSORPTION NEAR-EDGE STRUCTURE EVIDENCE FOR DIRECT METAL-METAL BONDING AND ELECTRON TRANSFER IN REDUCED Rh/TiO2 CATALYSTS. *J. Phys. Chem.* **92**, 189–193 (1988).

105. Karpiński, Z. Catalysis by Supported, Unsupported, and Electron-Deficient Palladium. in 45–100 (1990). doi:10.1016/S0360-0564(08)60363-6.

106. Juszczyk, W. & Karpiński, Z. Characterization of supported palladium catalysts. II. Pd SiO2. *J. Catal.* **117**, 519–532 (1989).

107. Iwasa, N., Mayanagi, T., Ogawa, N., Sakata, K. & Takezawa, N. New catalytic functions

of Pd–Zn, Pd–Ga, Pd–In, Pt–Zn, Pt–Ga.pdf. *Catal. Letters* **54**, 119–123 (1998).

108. Penner, S. *et al.* Growth and structural stability of well-ordered PdZn alloy nanoparticles. *J. Catal.* **241**, 14–19 (2006).

109. Penner, S. *et al.* Platinum nanocrystals supported by silica, alumina and ceria: Metal-support interaction due to high-temperature reduction in hydrogen. *Surf. Sci.* **532**–**535**, 276–280 (2003).

110. Sadi, F., Duprez, D., Gérard, F., Rossignol, S. & Miloudi, A. Morphological and structural changes in reducing and steam atmospheres of SiO2-supported Rh catalysts. *Catal. Letters* **44**, 221–228 (1997).

111. Lorenz, H. *et al.* Pd-In2O3 interaction due to reduction in hydrogen: Consequences for methanol steam reforming. *Appl. Catal. A Gen.* **374**, 180–188 (2010).

112. Fu, Q. & Wagner, T. Interaction of nanostructured metal overlayers with oxide surfaces. *Surf. Sci. Rep.* **62**, 431–498 (2007).

113. MOSS, R. The structure and activity of supported metal catalysts VIII. Chemisorption and benzene hydrogenation on palladium/silica catalysts. *J. Catal.* **58**, 206–219 (1979).

114. Yamaguchi, N., Kamiuchi, N., Muroyama, H., Matsui, T. & Eguchi, K. Effect of reduction treatment on CO oxidation over Pt/SnO2 catalyst. *Catal. Today* **164**, 169–175 (2011).

115. Tauster, S. J., Fung, S. C. & Garten, R. L. Strong metal-support interactions. Group 8 noble metals supported on titanium dioxide. *J. Am. Chem. Soc.* **100**, 170–175 (1978).

116. Sakellson, S., McMillan, M. & Haller, G. L. EXAFS evidence for direct metal-metal bonding in reduced rhodium/titania catalysts. *J. Phys. Chem.* **90**, 1733–1736 (1986).

117. Luo, Z., Zhao, G., Pan, H. & Sun, W. Strong Metal–Support Interaction in Heterogeneous Catalysts. *Adv. Energy Mater.* **12**, 1–15 (2022).

118. Beck, A. *et al.* The dynamics of overlayer formation on catalyst nanoparticles and strong metal-support interaction. *Nat. Commun.* **11**, 1–8 (2020).

119. Resasco, D. E., Fenoglio, R. J., Suarez, M. P. & Cechini, J. O. Different strong metal-support interaction effects on Rh/TiO2 and Pt/TiO2 catalysts. *J. Phys. Chem.* ® **90**, 4330–4333 (1986).

120. Horsley, J. A. A Molecular Orbital Study of Strong Metal-Support Interaction between Platinum and Titanium Dioxide. *J. Am. Chem. Soc.* **101**, 2870–2874 (1979).

121. Hsieh, B. J. *et al.* Tuning metal support interactions enhances the activity and durability of TiO2-supported Pt nanocatalysts. *Electrochim. Acta* **224**, 452–459 (2017).

122. Kumar, A. & Ramani, V. Strong metal-support interactions enhance the activity and durability of platinum supported on tantalum-modified titanium dioxide electrocatalysts. *ACS Catal.* **4**, 1516–1525 (2014).

123. Chen, B. H. & White, J. M. Properties of platinum supported on oxides of titanium. *J. Phys. Chem.* **86**, 3534–3541 (1982).

124. Sanchez, M. G. & Gazquez, J. L. Oxygen vacancy model in strong metal-support interaction. *J. Catal.* **104**, 120–135 (1987).

125. Fu, Q., Wagner, T., Olliges, S. & Carstanjen, H. D. Metal-oxide interfacial reactions: Encapsulation of Pd on TiO2 (110). *J. Phys. Chem. B* **109**, 944–951 (2005).

126. Bally, A. Electronic properties of nano-crystalline titanium dioxide thin films. **2094**, 140 (1999).

127. Labich, S., Taglauer, E. & Knözinger, H. Metal-support interactions on rhodium model catalysts. *Top. Catal.* **14**, 153–161 (2000).

128. Diebold, U. The surface science of titanium dioxide. *Surf. Sci. Rep.* **48**, 53–229 (2003).

129. Tang, H. *et al.* Classical strong metal–support interactions between gold nanoparticles and titanium dioxide. *Sci. Adv.* **3**, 1–8 (2017).

130. Du, X. *et al.* Size-dependent strong metal-support interaction in TiO2 supported Au nanocatalysts. *Nat. Commun.* **11**, 1–8 (2020).

131. Rieboldt, F. *et al.* Nucleation and growth of Pt nanoparticles on reduced and oxidized rutile TiO2 (110). *J. Chem. Phys.* **141**, (2014).

132. Deng, L. *et al.* Strong metal-support interaction between Pt and SiO2 following high-temperature reduction: A catalytic interface for propane dehydrogenation. *Chem. Commun.* **53**, 6937–6940 (2017).

133. Wang, J. *et al.* Thin porous alumina sheets as supports for stabilizing gold nanoparticles. *ACS Nano* **7**, 4902–4910 (2013).

134. Fu, Q. *et al.* Reaction-induced strong metal-support interactions between metals and inert boron nitride nanosheets. *J. Am. Chem. Soc.* **142**, 17167–17174 (2020).

135. Tang, H. *et al.* Strong Metal-Support Interactions between Gold Nanoparticles and Nonoxides. *J. Am. Chem. Soc.* **138**, 56–59 (2016).

136. Liu, X. *et al.* Strong Metal–Support Interactions between Gold Nanoparticles and ZnO Nanorods in CO Oxidation. *J. Am. Chem. Soc.* **134**, 10251–10258 (2012).

137. Matsubu, J. C. *et al.* Adsorbate-mediated strong metal-support interactions in oxide-supported Rh catalysts. *Nat. Chem.* **9**, 120–127 (2017).

138. Zhang, J. *et al.* Wet-Chemistry Strong Metal-Support Interactions in Titania-Supported Au Catalysts. *J. Am. Chem. Soc.* **141**, 2975–2983 (2019).

139. Gao, Y., Liang, Y. & Chambers, S. A. Thermal stability and the role of oxygen vacancy defects in strong metal support interaction - Pt on Nb-doped TiO2(100). *Surf. Sci.* **365**, 638–648 (1996).

140. Zhang, J., Zhu, D., Yan, J. & Wang, C. A. Strong metal-support interactions induced by an ultrafast laser. *Nat. Commun.* **12**, 1–10 (2021).

141. Iwasa, N., Kudo, S., Takahashi, H., Masuda, S. & Takezawa, N. Highly selective supported Pd catalysts for steam reforming of methanol. *Catal. Letters* **19**, 211–216 (1993).

142. Xu, M. *et al.* TiO2-x-Modified Ni Nanocatalyst with Tunable Metal-Support Interaction for Water-Gas Shift Reaction. *ACS Catal.* **7**, 7600–7609 (2017).

143. Twigg, M. V. & Spencer, M. S. Deactivation of supported copper metal catalysts for hydrogenation reactions. *Appl. Catal. A Gen.* **212**, 161–174 (2001).

144. Li, D. *et al.* Induced activation of the commercial Cu/ZnO/Al2O3 catalyst for the steam reforming of methanol. *Nat. Catal.* **5**, 99–108 (2022).

145. Valdés-López, V. F., Mason, T., Shearing, P. R. & Brett, D. J. L. Carbon monoxide poisoning and mitigation strategies for polymer electrolyte membrane fuel cells – A

review. *Prog. Energy Combust. Sci.* **79**, (2020).

146. Leyrer, J., Margraf, R., Taglauer, E. & Knözinger, H. Solid-solid wetting and formation of monolayers in supported oxide systems. *Surf. Sci.* **201**, 603–623 (1988).

147. Xie, Y. C. & Tang, Y. Q. Spontaneous Monolayer Dispersion of Oxides and Salts onto Surfaces of Supports: Applications to Heterogeneous Catalysis. *Adv. Catal.* **37**, 1–43 (1990).

148. Taglauer, E. & Knözinger, H. Characterization of Supported Catalyst Systems with Surface Spectroscopies. *Phys. Status Solidi* **192**, 465–475 (1995).

149. Tammann, G. Die Temperatur des Beginns innerer Diffusion in Kristallen. *Zeitschrift für Anorg. und Allg. Chemie* **157**, 321–325 (1926).

150. Michaelson, H. B., Sylvania Electric Products, I. & Commission., U. S. A. E. The theories of the sintering process: a guide to the literature (1931-1951). 41 pages (1951).

151. Wang, G., Yang, Y., Han, D. & Li, Y. Oxygen defective metal oxides for energy conversion and storage. *Nano Today* **13**, 23–39 (2017).

152. Hasegawa, M. *Ellingham Diagram*. *Treatise on Process Metallurgy* vol. 1 (Elsevier Ltd., 2013).

153. Sabat, K. C., Rajput, P., Paramguru, R. K., Bhoi, B. & Mishra, B. K. Reduction of oxide minerals by hydrogen plasma: An overview. *Plasma Chem. Plasma Process.* **34**, 1–23 (2014).

154. ELLINGHAM, H. J. T. Transactions and Communications. *J. Soc. Chem. Ind.* **63**, 125–160 (1944).

155. Epifano, E. & Monceau, D. Ellingham diagram: A new look at an old tool. *Corros. Sci.* **217**, 111113 (2023).

156. Yeşiltepe, S. & Şeşen, M. K. Production of composite pellets from waste coffee grounds, mill scale and waste primary battery to produce ferromanganese; a zero waste approach. *Acta Metall. Slovaca* **26**, 45–48 (2020).

157. Burja, J., Tehovnik, F., Lamut, J. & Knap, M. Alumothermic reduction of ilmenite in a steel melt. *Mater. Tehnol.* **47**, 217–222 (2013).

158. Pennycook, S. J. *et al.* Aberration-corrected scanning transmission electron microscopy: The potential for nano- and interface science. *Zeitschrift fuer Met. Res. Adv. Tech.* **94**, 350–357 (2003).

159. Williams, D. B. & Carter, C. B. *Lenses, Apertures, and Resolution*. *Transmission Electron Microscopy* (2009). doi:10.1007/978-1-4757-2519-3.

160. Yoshimura, N. *Vacuum Technology Practice for Scientific Instruments*. vol. 19 (2008).

161. Houdellier, F. *et al.* Developments of high brightness cold field emission source for TEM and SEM applications. 5–6 (2015).

162. Kohl, H. & Reimer, L. *Transmission Electron Microscopy*. vol. 36 (Springer New York, 2008).

163. Kirkland, E. J. On the optimum probe in aberration corrected ADF-STEM. *Ultramicroscopy* **111**, 1523–1530 (2011).

164. Nellist, P. D. *Scanning transmission electron microscopy*. *Springer Handbooks* (2019). doi:10.1007/978-3-030-00069-1_2.

165. Jose Chirayil, C., Abraham, J., Kumar Mishra, R., George, S. C. & Thomas, S. Instrumental Techniques for the Characterization of Nanoparticles. in *Thermal and Rheological Measurement Techniques for Nanomaterials Characterization* 1–36 (Elsevier, 2017). doi:10.1016/B978-0-323-46139-9.00001-3.

166. Yater, J. E. Secondary electron emission and vacuum electronics. *J. Appl. Phys.* **133**, (2023).

167. Bethe, H. Theorie der Beugung von Elektronen an Kristallen. *Ann. Phys.* **392**, 55–129 (1928).

168. Bloch, F. Über die Quantenmechanik der Elektronen in Kristallgittern. *Zeitschrift für Phys.* **52**, 555–600 (1929).

169. Cowley, J. M. & Moodie, A. F. The scattering of electrons by atoms and crystals. I. A new theoretical approach. *Acta Crystallogr.* **10**, 609–619 (1957).

170. De Graef, M. *Introduction to Conventional Transmission Electron Microscopy*. *Materials Research Bulletin* vol. 38 (Cambridge University Press, 2003).

171. Winkler, F. Absolute scale off-axis electron holography of thin dichalcogenide crystals at atomic resolution. vol. 191 (RWTH Aachen, 2018).

172. Scherzer, O. The Theoretical Resolution Limit of the Electron Microscope. *J. Appl. Phys.* **20**, 20–29 (1949).

173. Haider, M. *et al.* Electron microscopy image enhanced [7]. *Nature* **392**, 768–769 (1998).

174. Lentzen, M. *et al.* High-resolution imaging with an aberration-corrected transmission electron microscope. *Ultramicroscopy* **92**, 233–242 (2002).

175. Jia, C. L., Houben, L., Thust, A. & Barthel, J. On the benefit of the negative-spherical-aberration imaging technique for quantitative HRTEM. *Ultramicroscopy* **110**, 500–505 (2010).

176. Jia, C. L., Lentzen, M. & Urban, K. Atomic-resolution imaging of oxygen in perovskite ceramics. *Science (80-.).* **299**, 870–873 (2003).

177. Kondrat, S. A. & van Bokhoven, J. A. A Perspective on Counting Catalytic Active Sites and Rates of Reaction Using X-Ray Spectroscopy. *Top. Catal.* **62**, 1218–1227 (2019).

178. Yaguchi, T., San Gabriel, M. L., Hashimoto, A. & Howe, J. Y. In-situ TEM study from the perspective of holders. *Microscopy* **73**, 117–132 (2024).

179. Plodinec, M. *et al.* Versatile Homebuilt Gas Feed and Analysis System for Operando TEM of Catalysts at Work. *Microsc. Microanal.* **26**, 220–228 (2020).

180. Xin, H. L., Niu, K., Alsem, D. H. & Zheng, H. In situ TEM study of catalytic nanoparticle reactions in atmospheric pressure gas environment. *Microsc. Microanal.* **19**, 1558–1568 (2013).

181. Jinschek, J. R. Advances in the environmental transmission electron microscope (ETEM) for nanoscale in situ studies of gas-solid interactions. *Chem. Commun.* **50**, 2696–2706 (2014).

182. Paredes, A. M. MICROSCOPY | Scanning Electron Microscopy. in *Encyclopedia of Food Microbiology* 693–701 (Elsevier, 2014). doi:10.1016/B978-0-12-384730-0.00215-9.

183. Mitchell, D. R. G. Contamination mitigation strategies for scanning transmission electron microscopy. *Micron* **73**, 36–46 (2015).

184. Iwasa, N., Masuda, S., Ogawa, N. & Takezawa, N. Steam reforming of methanol over Pd/ZnO: Effect of the formation of PdZn alloys upon the reaction. *Appl. Catal. A, Gen.* **125**, 145–157 (1995).

185. Daněk, V. Phase Equilibria. in *Physico-Chemical Analysis of Molten Electrolytes* 107–219 (Elsevier, 2006). doi:10.1016/B978-044452116-3/50004-0.

186. Ghasemi, A. Ferrite characterization techniques. in *Magnetic Ferrites and Related Nanocomposites* 49–124 (Elsevier, 2022). doi:10.1016/B978-0-12-824014-4.00002-0.

187. Gao, L. *et al.* Effect of alloying elements on properties and microstructures of SnAgCu solders. *Microelectron. Eng.* **87**, 2025–2034 (2010).

188. Chen, X., Zhang, Y., Hui, D., Chen, M. & Wu, Z. Study of melting properties of basalt based on their mineral components. *Compos. Part B Eng.* **116**, 53–60 (2017).

189. Plante, A. F., Fernández, J. M. & Leifeld, J. Application of thermal analysis techniques in soil science. *Geoderma* **153**, 1–10 (2009).

190. de la Guardia, M. & Armenta, S. Multianalyte Determination Versus One-at-a-Time Methodologies. in 121–156 (2011). doi:10.1016/B978-0-444-53709-6.00006-9.

191. Douvris, C., Vaughan, T., Bussan, D., Bartzas, G. & Thomas, R. How ICP-OES changed the face of trace element analysis: Review of the global application landscape. *Sci. Total Environ.* **905**, 167242 (2023).

192. Gottstein, G. *Physikalische Grundlagen der Materialkunde*. (Springer Berlin Heidelberg, 2007). doi:10.1007/978-3-540-71105-6.

193. Bragg, P. W. H. & Bragg, W. L. Downloaded from https://royalsocietypublishing.org/ on 19 July 2024. **17**, 428–438 (1913).

194. Hitachi High-Tech Canada. MHS-5000 Single Tilt MEMS Heating Holder for HF5000 Hitachi STEM. (2022).

195. DENSsolutions. Climate. https://denssolutions.com/products/climate/ (2024).

196. Thust, A., Barthel, J. & Tillmann, K. FEI Titan 80-300 TEM. *J. large-scale Res. Facil. JLSRF* **2**, A41 (2016).

197. Smith, D. J. & McCartney, M. R. Microscopy Applications - Semiconductors. *Encycl. Anal. Sci. Second Ed.* 84–91 (2004) doi:10.1016/B0-12-369397-7/00394-0.

198. Tshabalala, Z. P., Oosthuizen, D. N., Swart, H. C. & Motaung, D. E. Tools and techniques for characterization and evaluation of nanosensors. in *Nanosensors for Smart Cities* 85–110 (Elsevier, 2020). doi:10.1016/B978-0-12-819870-4.00005-0.

199. Egerton, R. F. Dose measurement in the TEM and STEM. *Ultramicroscopy* **229**, (2021).

200. Meise, A., Heggen, M., Dunin-Borkowski, R. E. & Armbrüster, M. In Situ Scanning Transmission Electron Microscopy Calcination of Palladium Nitrate Supported on Zinc Oxide. *Small Sci.* **2400048**, 1–10 (2024).

201. Pei, Z., Xu, H. & Zhang, Y. Preparation of Cr2O3 nanoparticles via C2H5OH hydrothermal reduction. *J. Alloys Compd.* **468**, 2007–2010 (2009).

202. Van Dillen, A. J., Terörde, R. J. A. M., Lensveld, D. J., Geus, J. W. & De Jong, K. P. Synthesis of supported catalysts by impregnation and drying using aqueous chelated metal complexes. *J. Catal.* **216**, 257–264 (2003).

203. Zhao, T. *et al.* Synthesis of supported catalysts by impregnation and calcination of Low-

temperature polymerizable metal-complexes. *Top. Catal.* **54**, 1163–1174 (2011).

204. Munnik, P., De Jongh, P. E. & De Jong, K. P. Recent Developments in the Synthesis of Supported Catalysts. *Chem. Rev.* **115**, 6687–6718 (2015).

205. Al-Hada, N. M. *et al.* A facile thermal-treatment route to synthesize the semiconductor CdO nanoparticles and effect of calcination. *Mater. Sci. Semicond. Process.* **26**, 460–466 (2014).

206. Bryant, K., West, C. W. & Saunders, S. R. Impacts of calcination on surface-clean supported nanoparticle catalysts. *Appl. Catal. A Gen.* **579**, 58–64 (2019).

207. Purnama, B., Wijayanta, A. T. & Suharyana. Effect of calcination temperature on structural and magnetic properties in cobalt ferrite nano particles. *J. King Saud Univ. - Sci.* **31**, 956–960 (2019).

208. Ashraf, R., Riaz, S., Kayani, Z. N. & Naseem, S. *Effect of Calcination on Properties of ZnO Nanoparticles*. *Materials Today: Proceedings* vol. 2 (Elsevier Ltd., 2015).

209. Ravi, S. & Karthikeyan, A. Effect of calcination temperature on La0.7Sr0.3MnO3 nanoparticles synthesized with modified sol-gel route. *Phys. Procedia* **54**, 45–54 (2014).

210. Shoaib, A. *et al.* Noble metal nanoclusters and their in situ calcination to nanocrystals: Precise control of their size and interface with TiO2 nanosheets and their versatile catalysis applications. *Nano Res.* **9**, 1763–1774 (2016).

211. Epicier, T. *et al.* 2D & 3D in situ study of the calcination of Pd nanocatalysts supported on delta-Alumina in an Environmental Transmission Electron Microscope. *Catal. Today* **334**, 68–78 (2019).

212. Huang, R., Kim, K., Kim, H. J., Jang, M. G. & Han, J. W. Size-Controlled Pd Nanoparticles Loaded on Co3O4 Nanoparticles by Calcination for Enhanced CO Oxidation. *ACS Appl. Nano Mater.* **3**, 486–495 (2020).

213. Simonsen, S. B., Shao, J. & Zhang, W. Structural evolution during calcination and. *Nanotechnology* **28**, 265402 (2017).

214. Yeh, Y. T. *et al.* In Situ TEM Observation of (Cr, Mn, Fe, Co, and Ni)3O4 High-Entropy Spinel Oxide Formation During Calcination at Atomic Scale. *Small* **2307284**, 1–11 (2023).

215. Zhou, Y. *et al.* Cooperative Characterization of In Situ TEM and Cantilever-TGA to Optimize Calcination Conditions of MnO2 Nanowire Precursors. *Nano Lett.* **23**, 2412–2420 (2023).

216. Fiordaliso, E. M. *et al.* Intermetallic GaPd2 Nanoparticles on SiO2 for Low-Pressure CO2 Hydrogenation to Methanol: Catalytic Performance and in Situ Characterization. *ACS Catal.* **5**, 5827–5836 (2015).

217. Zhang, S. *et al.* Dynamic structural evolution of supported palladium-ceria core-shell catalysts revealed by in situ electron microscopy. *Nat. Commun.* **6**, 1–6 (2015).

218. Lebarbier, V., Dagle, R., Datye, A. & Wang, Y. The effect of PdZn particle size on reverse-water-gas-shift reaction. *Appl. Catal. A Gen.* **379**, 3–6 (2010).

219. Griffiths, A. J. V. & Walther, T. Quantification of carbon contamination under electron beam irradiation in a scanning transmission electron microscope and its suppression by plasma cleaning. *J. Phys. Conf. Ser.* **241**, 4–8 (2010).

220. Bruns, J., Klüner, T. & Wickleder, M. S. Oxoanionic noble metal compounds from

fuming nitric acid: The palladium examples Pd(NO3)2 and Pd(CH3SO3)2. *Chem. - A Eur. J.* **21**, 1294–1301 (2015).

221. Khranenko, S. P., Baidina, I. A. & Gromilov, S. A. Crystal structure refinement for trans-[Pd(NO3) 2(H2O)2]. *J. Struct. Chem.* **48**, 1152–1155 (2007).

222. Glemser, O. & Peuschel, G. Beitrag zur Kenntnis des Systems PdO/H2O. *Zeitschrift für Anorg. und Allg. Chemie* **281**, 44–53 (1955).

223. Loebich, O. & Raub, C. J. Das zustandsdiagramm lithium-palladium und die magnetischen eigenschaften der Li-Pd-Legierungen. *J. Less Common Met.* **55**, 67–76 (1977).

224. Li, X. *et al.* Efficient conversion of glycerol to 1, 2-propenadiol over ZnPd/ZnO-3Al catalyst: The significant influences of calcination temperature. *Catal. Today* **302**, 210–216 (2018).

225. Li, X. *et al.* A study on the oxygen vacancies in ZnPd/ZnO-Al and their promoting role in glycerol hydrogenolysis. *ChemCatChem* **7**, 1322–1328 (2015).

226. Kuo, S. T. *et al.* Investigation into the interactions between Bi2O3-doped ZnO and AgPd electrode. *J. Eur. Ceram. Soc.* **28**, 2557–2562 (2008).

227. Penner, S. *et al.* Growth and decomposition of aligned and ordered PdO nanoparticles. *J. Chem. Phys.* **125**, (2006).

228. Engels, V. *et al.* Nanoparticulate PdZn as a novel catalyst for ZnO nanowire growth. *Nanoscale Res. Lett.* **5**, 904–907 (2010).

229. Dalal, S. H. *et al.* Controllable growth of vertically aligned zinc oxide nanowires using vapour deposition. *Nanotechnology* **17**, 4811–4818 (2006).

230. Chien, F. S. Sen *et al.* Fast-response ozone sensor with ZnO nanorods grown by chemical vapor deposition. *Sensors Actuators, B Chem.* **144**, 120–125 (2010).

231. Wu, J. J. & Liu, S. C. Low-temperature growth of well-aligned ZnO nanorods by chemical vapor deposition. *Adv. Mater.* **14**, 215–218 (2002).

232. Wu, C. L. *et al.* Growth and characterization of chemical-vapor-deposited zinc oxide nanorods. *Thin Solid Films* **498**, 137–141 (2006).

233. Ye, Z., Wang, T., Wu, S., Ji, X. & Zhang, Q. Na-doped ZnO nanorods fabricated by chemical vapor deposition and their optoelectrical properties. *J. Alloys Compd.* **690**, 189–194 (2017).

234. Liu, X., Wu, X., Cao, H. & Chang, R. P. H. Growth mechanism and properties of ZnO nanorods synthesized by plasma-enhanced chemical vapor deposition. *J. Appl. Phys.* **95**, 3141–3147 (2004).

235. Hu, M., Giapis, K. P. & Poulikakos, D. Interfacial mixing during annealing of zinc oxide nanoparticle junctions. *Appl. Phys. Lett.* **98**, (2011).

236. Anthrop, D. F. & Searcy, A. W. Sublimation and thermodynamic properties of zinc oxide. *J. Phys. Chem.* **68**, 2335–2342 (1964).

237. Nuss, J., Wedig, U., Kirfel, A. & Jansen, M. The Structural Anomaly of Zinc: Evolution of Lattice Constants and Parameters of Thermal Motion in the Temperature Range of 40 to 500 K. *Zeitschrift für Anorg. und Allg. Chemie* **636**, 309–313 (2010).

238. Šarić, A. *et al.* Insight into the Growth Mechanism and Photocatalytic Behavior of Tubular Hierarchical ZnO Structures: An Integrated Experimental and Theoretical

Approach. *Inorg. Chem.* **61**, 2962–2979 (2022).

239. Wallinga, J., Arnoldbik, W. M., Vredenberg, A. M., Schropp, R. E. I. & Van Der Weg, W. F. Reduction of tin oxide by hydrogen radicals. *J. Phys. Chem. B* **102**, 6219–6224 (1998).

240. Hi, J. H. T. & Science, C. We have exposed films of various conductive transparent oxides (CTOs) such as SnO2 and indium tin oxide to hydrogen plasmas in d . c . and r . f . discharges and have measured the white light optical transmission , the room air work function and the she. **117**, 149–155 (1984).

241. Niu, Y. *et al.* Visualizing Formation of Intermetallic PdZn in a Palladium/Zinc Oxide Catalyst: Interfacial Fertilization by PdH x. *Angew. Chemie - Int. Ed.* **58**, 4232–4237 (2019).

242. Zenou, V. Y. *et al.* Redox and phase behavior of Pd-substituted (La,Sr)CrO3 perovskite solid oxide fuel cell anodes. *Solid State Ionics* **296**, 90–105 (2016).

243. Park, K., Hakeem, D. A., Pi, J. W. & Jung, G. W. Emission enhancement of Eu3+-doped ZnO by adding charge compensators. *J. Alloys Compd.* **772**, 1040–1051 (2019).

244. Glemser, O. & Peuschel, G. Beitrag zur Kenntnis des Systems PdO/H 2 O. *Zeitschrift für Anorg. und Allg. Chemie* **281**, 44–53 (1955).

245. Neyts, E. C., Ostrikov, K., Sunkara, M. K. & Bogaerts, A. Plasma Catalysis: Synergistic Effects at the Nanoscale. *Chem. Rev.* **115**, 13408–13446 (2015).

246. Prins, R. Hydrogen spillover. Facts and fiction. *Chem. Rev.* **112**, 2714–2738 (2012).

247. Rogal, J., Reuter, K. & Scheffler, M. Thermodynamic stability of PdO surfaces. *Phys. Rev. B - Condens. Matter Mater. Phys.* **69**, (2004).

248. Vitos, L., Ruban, A. V., Skriver, H. L. & Kollár, J. The surface energy of metals. *Surf. Sci.* **411**, 186–202 (1998).

249. Na, S. H. & Park, C. H. First-principles study of the surface of wurtzite ZnO and ZnS - Implications for nanostructure formation. *J. Korean Phys. Soc.* **54**, 867–872 (2009).

250. Tew, M. W., Miller, J. T. & Van Bokhoven, J. A. Particle size effect of hydride formation and surface hydrogen adsorption of nanosized palladium catalysts: L3 Edge vs K Edge X-ray absorption spectroscopy. *J. Phys. Chem. C* **113**, 15140–15147 (2009).

251. Chen, Z. X., Neyman, K. M. & Rösch, N. Theoretical study of segregation of Zn and Pd in Pd-Zn alloys. *Surf. Sci.* **548**, 291–300 (2004).

252. Kou, S. & Chang, Y. . Thermodynamics of ordered β1-pdZn alloys. *Acta Metall.* **23**, 1185–1190 (1975).

253. Khort, A., Roslyakov, S. & Loginov, P. Solution combustion synthesis of single-phase bimetallic nanomaterials. *Nano-Structures and Nano-Objects* **26**, 100727 (2021).

254. Owen, E. A. & Yates, E. L. XLI. Precision measurements of crystal parameters . *London, Edinburgh, Dublin Philos. Mag. J. Sci.* **15**, 472–488 (1933).

255. Kuper, A. B., Lazarus, D., Manning, J. R. & Tomizuka, C. T. Diffusion in Ordered and Disordered Copper-Zinc. *Phys. Rev.* **104**, 1536–1541 (1956).

256. Eastman, C. M., Zhang, Q. & Zhao, J. C. Diffusion Coefficients and Phase Equilibria of the Cu-Zn Binary System Studied Using Diffusion Couples. *J. Phase Equilibria Diffus.* **41**, 642–653 (2020).

257. López-Salazar, P. *et al.* Determination of diffusion coefficient of copper in ZnO (001) single crystals at 1000 °C. *Crystals* **9**, 1–6 (2019).

258. Liu, J. *et al.* Reversed Nanoscale Kirkendall Effect in Au-InAs Hybrid Nanoparticles. *Chem. Mater.* **28**, 8032–8043 (2016).

259. Iwasa, N., Ogawa, N., Masuda, S. & Takezawa, N. Selective PdZn Alloy Formation in the Reduction of Pd/ZnO Catalysts. *Bull. Chem. Soc. Jpn.* **71**, 1451–1455 (1998).

260. Moezzi, A., McDonagh, A. M. & Cortie, M. B. Zinc oxide particles: Synthesis, properties and applications. *Chem. Eng. J.* **185**–**186**, 1–22 (2012).

261. Kim, J. H., Mirzaei, A., Woo Kim, H. & Kim, S. S. Combination of Pd loading and electron beam irradiation for superior hydrogen sensing of electrospun ZnO nanofibers. *Sensors Actuators, B Chem.* **284**, 628–637 (2019).

262. Su, D. S. Electron beam induced changes in transition metal oxides. *Anal. Bioanal. Chem.* **374**, 732–735 (2002).

263. Frenkel, J. Über die Wärmebewegung in festen und flüssigen Körpern. *Zeitschrift für Phys.* **35**, 652–669 (1926).

264. Phan, D. T. & Chung, G. S. Effects of defects in Ga-doped ZnO nanorods formed by a hydrothermal method on CO sensing properties. *Sensors Actuators, B Chem.* **187**, 191–197 (2013).

265. Sundara Venkatesh, P., Dharmaraj, P., Purushothaman, V., Ramakrishnan, V. & Jeganathan, K. Point defects assisted NH3 gas sensing properties in ZnO nanostructures. *Sensors Actuators, B Chem.* **212**, 10–17 (2015).

266. Liao, L. *et al.* Size dependence of gas sensitivity of ZnO nanorods. *J. Phys. Chem. C* **111**, 1900–1903 (2007).

267. Hettler, S. *et al.* Charging of carbon thin films in scanning and phase-plate transmission electron microscopy. *Ultramicroscopy* **184**, 252–266 (2018).

268. Wang, L. *et al.* Dynamics of the charging-induced imaging instability in transmission electron microscopy. *Nanoscale Adv.* **3**, 3035–3040 (2021).

269. Kryshtal, A., Mielczarek, M. & Pawlak, J. Effect of electron beam irradiation on the temperature of single AuGe nanoparticles in a TEM. *Ultramicroscopy* **233**, 113459 (2022).

270. Nuñez Valencia, C., Lomholdt, W. B., Leth Larsen, M. H., Hansen, T. W. & Schiøtz, J. Beam induced heating in electron microscopy modeled with machine learning interatomic potentials. *Nanoscale* **16**, 5750–5759 (2024).

271. Park, J. *et al.* Direct Quantification of Heat Generation Due to Inelastic Scattering of Electrons Using a Nanocalorimeter. *Adv. Sci.* **8**, 1–6 (2021).

272. Langmuir, I. The mechanism of the catalytic action of platinum in the reactions 2Co + O2= 2Co2 and 2H2+ O2= 2H2O. *Trans. Faraday Soc.* **17**, 621 (1922).

273. Schlögl, R. Heterogene Katalysatoren – fundamental betrachtet. *Angew. Chemie* **127**, 3531–3589 (2015).

274. Gabasch, H. *et al.* Zn adsorption on Pd(111): ZnO and PdZn alloy formation. *J. Phys. Chem. B* **110**, 11391–11398 (2006).

275. MacArthur, K. E. *et al.* Post-Synthesis Heat Treatment of Doped PtNi-Alloy Fuel-Cell Catalyst Nanoparticles Studied by In-Situ Electron Microscopy. *ACS Appl. Energy*

Mater. **6**, 5959–5967 (2023).

276. Liu, T., Zhang, Q. & Zhao, Q. Theoretical insight into the anion vacancy healing process during the oxygen evolution reaction on TaON and Ta3N5. *Phys. Chem. Chem. Phys.* **24**, 13999–14006 (2022).

277. Badreldin, A., Abusrafa, A. E. & Abdel-Wahab, A. Oxygen-deficient perovskites for oxygen evolution reaction in alkaline media: a review. *Emergent Mater.* **3**, 567–590 (2020).

278. Badreldin, A., Abusrafa, A. E. & Abdel-Wahab, A. Oxygen-Deficient Cobalt-Based Oxides for Electrocatalytic Water Splitting. *ChemSusChem* **14**, 10–32 (2021).

279. Lejček, P. Approaches to Study Grain Boundary Segregation. *Springer Ser. Mater. Sci.* **136**, 25–49 (2010).

280. Ojo, O. A. & Richards, N. L. *Heat-affected zone cracking in welded nickel superalloys*. *Welding and Joining of Aerospace Materials* (Woodhead Publishing Limited, 2012). doi:10.1533/9780857095169.1.142.

281. Harries, D. R. & Marwick, A. D. Non-equilibrium segregation in metals and alloys. *Philos. Trans. R. Soc. London. Ser. A, Math. Phys. Sci.* **295**, 197–207 (1980).

282. Ivarsson, D. C. A., Burkhardt, U., Heggen, M., Ormeci, A. & Armbrüster, M. On the twinning in ZnPd. *Phys. Chem. Chem. Phys.* **19**, 5778–5785 (2017).

283. Dahale, C., Goverapet Srinivasan, S. & Rai, B. Effects of Segregation on the Catalytic Properties of AgAuCuPdPt High-Entropy Alloy for CO Reduction Reaction. *ACS Appl. Mater. Interfaces* (2023) doi:10.1021/acsami.3c12775.

284. Tang, C. *et al.* Co2 reduction on copper's twin boundary. *ACS Catal.* **10**, 2026–2032 (2020).

285. Ni, B. & Wang, X. Face the Edges: Catalytic Active Sites of Nanomaterials. *Adv. Sci.* **2**, 1–22 (2015).

286. Akella, J., Ganguly, J., Grover, R. & Kennedy, G. Melting of lead and zinc to 60 kbar. *J. Phys. Chem. Solids* **34**, 631–636 (1973).

287. Šarić, A. *et al.* Insight into the Growth Mechanism and Photocatalytic Behavior of Tubular Hierarchical ZnO Structures: An Integrated Experimental and Theoretical Approach. *Inorg. Chem.* **61**, 2962–2979 (2022).

288. Bocharov, D. *et al.* A comprehensive study of structure and properties of nanocrystalline zinc peroxide. *J. Phys. Chem. Solids* **160**, 110318 (2022).

289. Uekawa, N. *et al.* Nonstoichiometric properties of zinc oxide nanoparticles prepared by decomposition of zinc peroxide. *Phys. Chem. Chem. Phys.* **5**, 929–934 (2003).

290. Langmuir, I. The mechanism of the catalytic action of platinum in the reactions 2Co + O2= 2Co2 and 2H2+ O2= 2H2O. *Trans. Faraday Soc.* **17**, 621 (1922).

291. Donnelly, R. P. & Hinshelwood, C. N. CCXXVIII.—The combination of hydrogen and oxygen on the surface of platinum. *J. Chem. Soc.* 1727–1733 (1929) doi:10.1039/JR9290001727.

292. Lyu, Y. *et al.* Tracing the Active Phase and Dynamics for Carbon Nanofiber Growth on Nickel Catalyst Using Environmental Transmission Electron Microscopy. *Small Methods* **6**, 1–9 (2022).

293. Mills, A. F., Hubbard, G. L., James, R. K. & Tan, C. Experimental study of film

condensation on horizontal grooved tubes. *Desalination* **16**, 121–133 (1975).

294. Rose, J. W. Effect of condenser tube material on heat transfer during dropwise condensation of steam. *Int. J. Heat Mass Transf.* **21**, 835–840 (1978).

295. Hammami, Y. El, Feddaoui, M., Mediouni, T. & Mir, A. Numerical study of condensing a small concentration of vapour inside a vertical tube. *Heat Mass Transf. und Stoffuebertragung* **48**, 1675–1685 (2012).

296. Vuddagiri, S. R. & Eubank, P. T. Condensation of mixed vapors and thermodynamics. *AIChE J.* **44**, 2526–2541 (1998).

297. Langmuir, I. Vapor pressures, evaporation, condensation and adsorption. *J. Am. Chem. Soc.* **54**, 2798–2832 (1932).

298. Knapp, W. Vacuum technology. *Vac. Electron. Components Devices* 483–520 (2008) doi:10.1007/978-3-540-71929-8_11.

299. Retired, M. H. Technology of Vacuum Pumps — An Overview.

300. Vacuum, P. Working With Turbo Pumps. (2003).

301. Kaurova, I. A., Kuz'Micheva, G. M., Rybakov, V. B., Cousson, A. & Gayvoronsky, V. Y. Structural peculiarities and point defects of bulk-ZnO single crystals. *J. Alloys Compd.* **616**, 71–75 (2014).

11 Supporting Information

Figure 11.1: Laboratory closed cell setup enabling *in situ* gas experiments. A schematic illustration of the setup is given in Figure 3.6.

Figure 11.2: Optical microscopical image of MEMS heating chips. Left: SiN membranes centred in heating spiral (5x magnification). Right: SiN-windows loaded with $Pd(NO_3)_2$ supported on ZnO, which is visible as dark particles (50x magnification). Figure is taken with permission from reference[200].

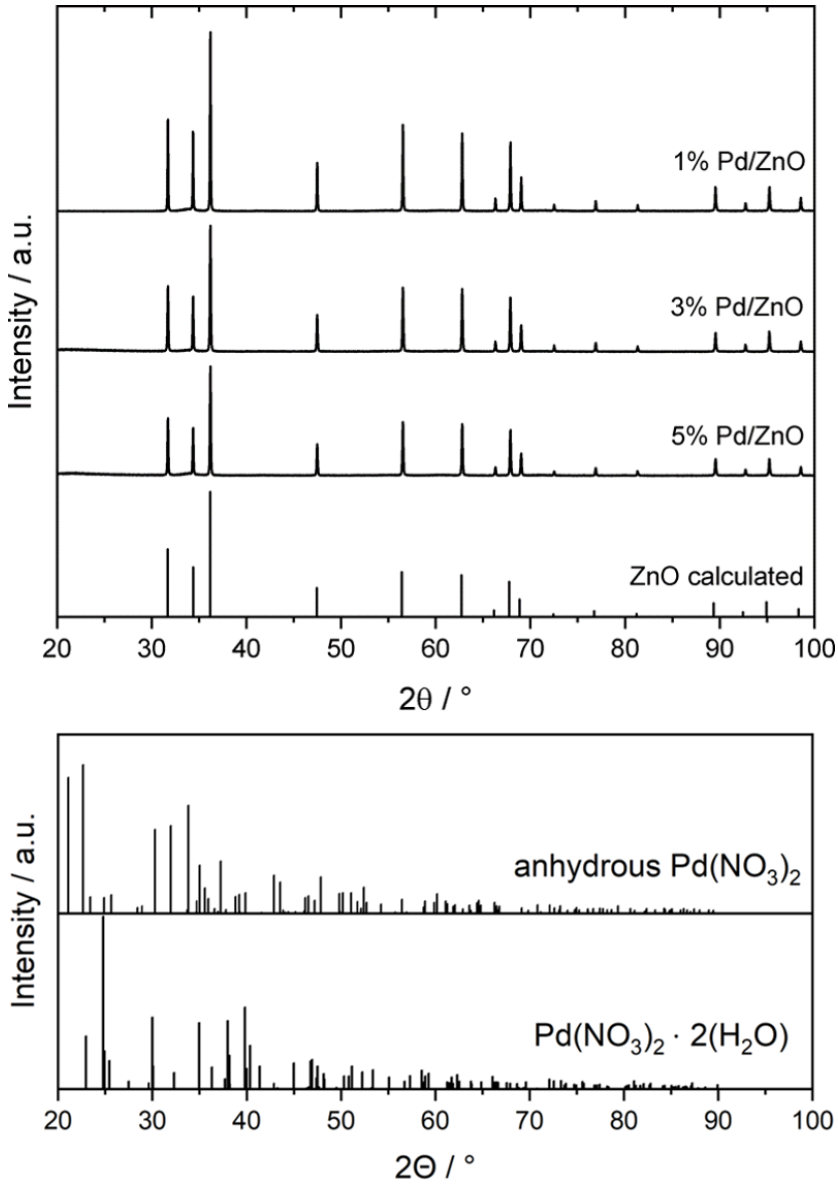

Figure 11.3: XRD results of different Pd-loading on ZnO (1%, 3% and 5%); calculated ZnO reflections are given for reference[301]. Missing PdO reflections are due to small crystallite size and/or bad crystallinity. Diffraction patterns of anhydrous and water containing palladium nitrate are added for reference.[220,221] Figure is taken with permission from reference[200].

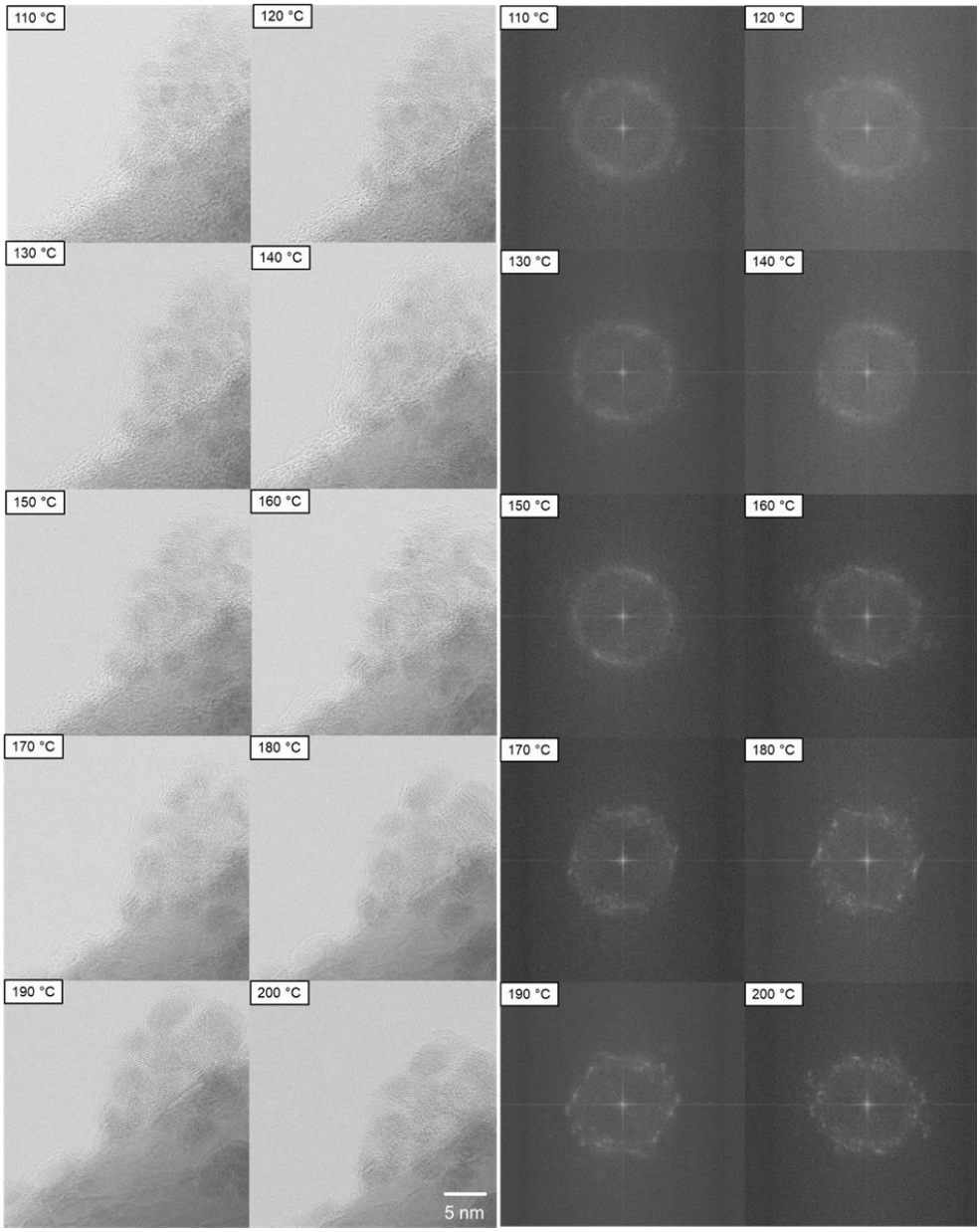

Figure 11.4: E-STEM series of BF images and the corresponding FFTs of an *in situ* calcination experiment demonstrate the structural transformation of $Pd(NO_3)_2$/ZnO to PdO/ZnO in oxygen. Figure is taken with permission from reference[200].

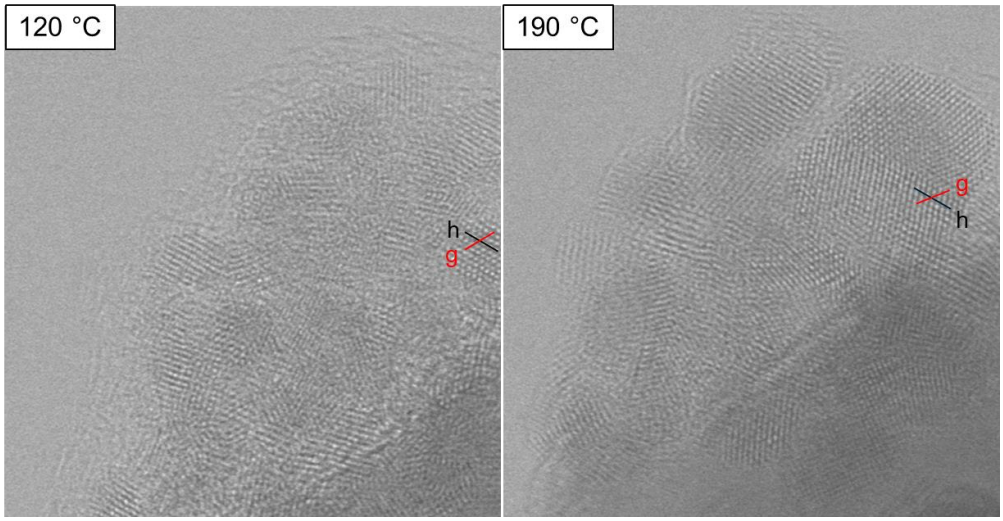

Figure 11.5: Measurements of interatomic spacings in two directions labelled h and g on the same nanoparticle at 120°C and 190°C. Figure is taken with permission from reference[200].

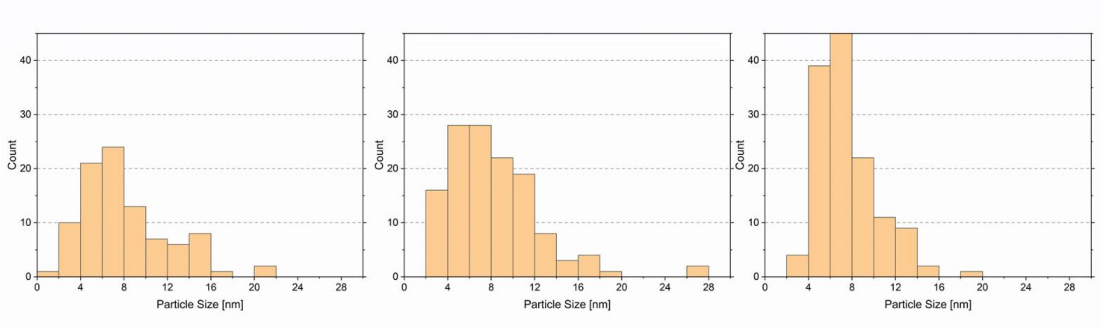

Figure 11.6: Histograms of *ex situ* calcinated PdO on ZnO with different loadings (left to right: 1%, 3%, 5%) performed under identical, ambient lab conditions (500°C, 180 min dwell time, ambient air pressure). Figure is taken with permission from reference[200].

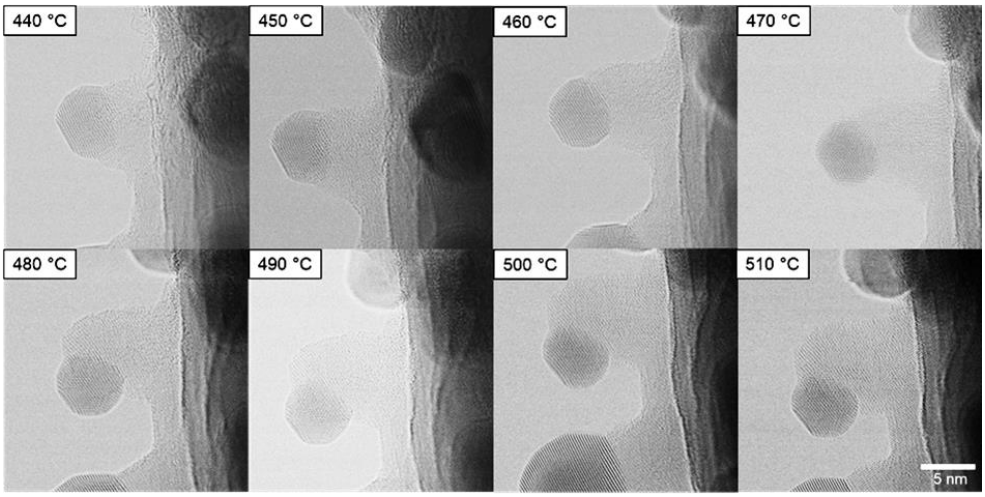

Figure 11.7: High resolution BF image series of single particle evolution during a calcination treatment between 400 and 500 °C. Formation of nanorods are visible. Figure is taken with permission from reference[200].

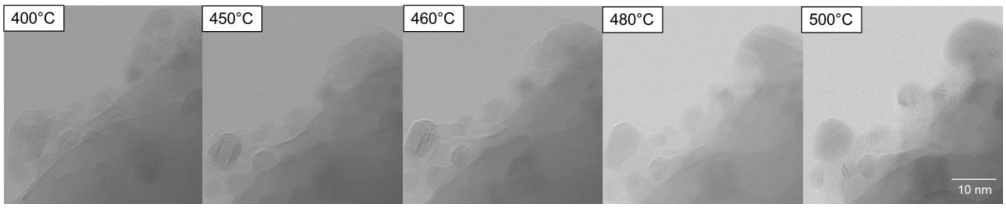

Figure 11.8: BF images series of particle evolution during a calcination treatment between 400 and 500 °C. Figure is taken with permission from reference[200].

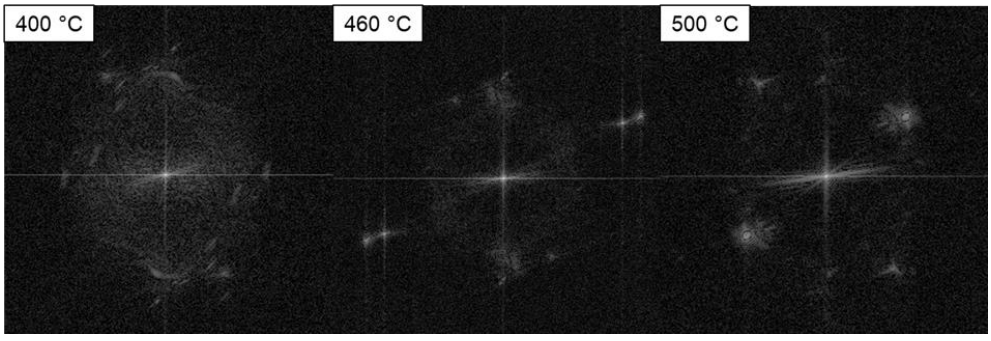

Figure 11.9: Series of FFTs based on images, which are shown in Figure 4.13. Figure is taken with permission from reference[200].

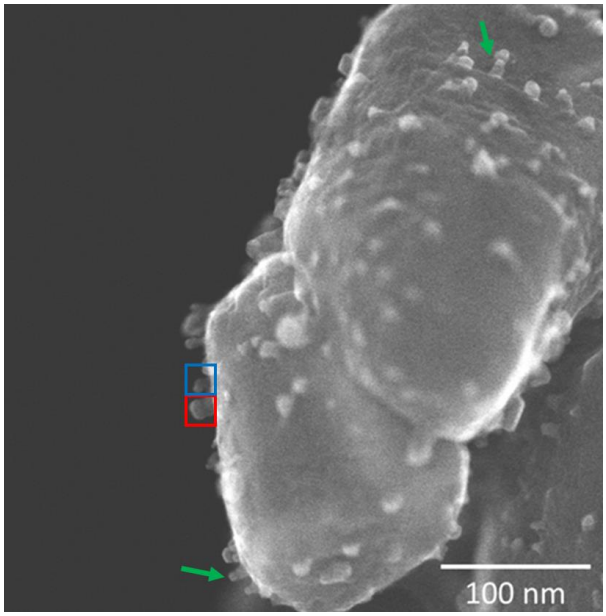

Figure 11.10: SE E-STEM overview image illustrating the distribution of nanorods anchored to nanoparticles. Red ROI marks the region that is displayed in Figure 4.12 and Figure 4.13. Blue ROI highlights the region that is represented in Figure 11.7. Green arrows mark ZnO nanorods, which have not been imaged *in situ*. Figure is taken with permission from reference[200].

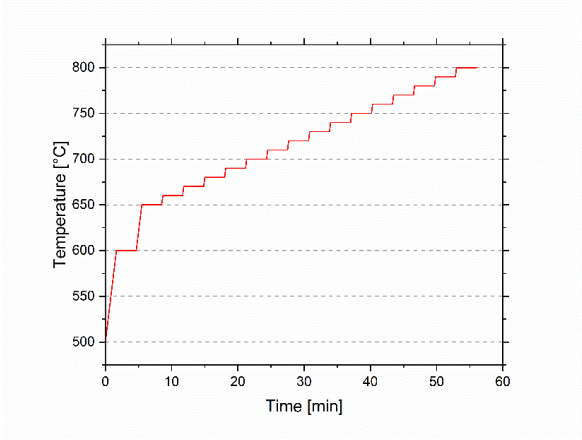

Figure 11.11: Illustration of heating ramp between 500 and 800 °C during imaging of high temperature behaviour of PdO/ZnO system.

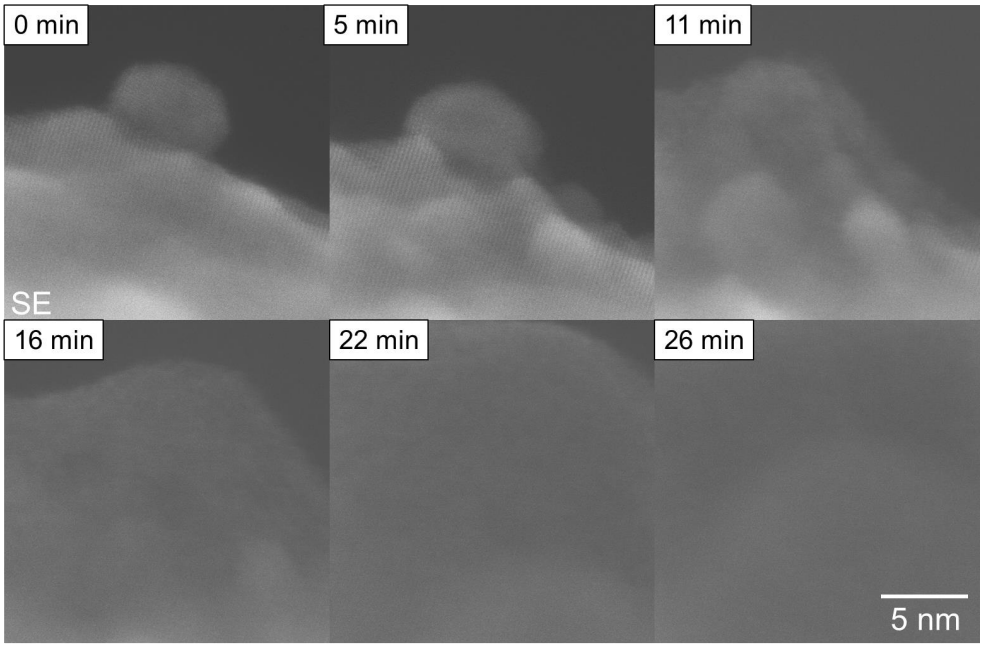

Figure 11.12: Series of SE images that show formation of contamination over time during reduction in a hydrogen atmosphere at room temperature. Specimen structures cannot be resolved after 22 min.

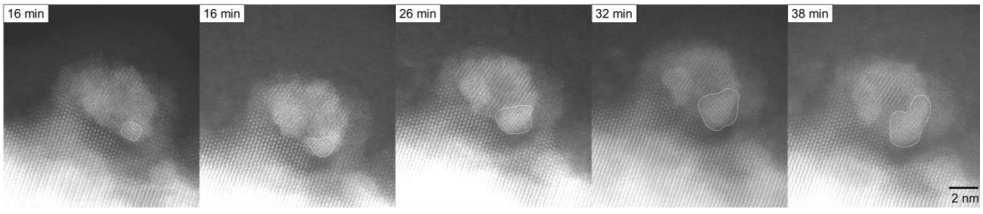

Figure 11.13: Series of DF images illustrating the phase growth during reduction. The time stamps identify time of reduction. The corresponding measurements are displayed in Figure 6.7.

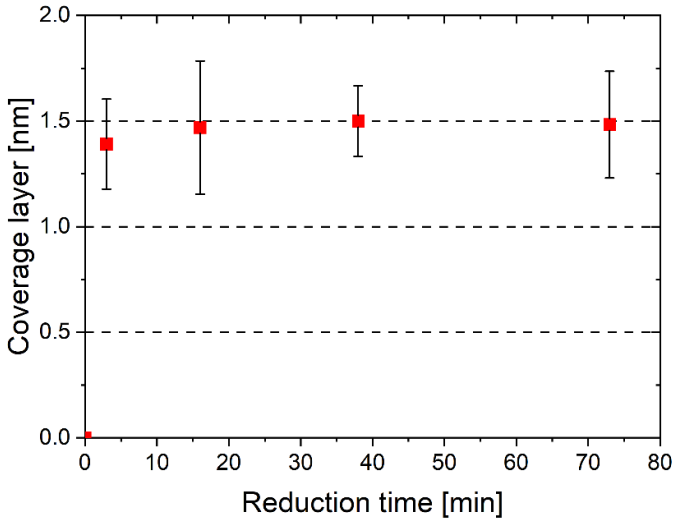

Figure 11.14: The change in thickness of the coverage layer is shown as a function of reduction time. The coverage layer converges to a thickness of ~1.5 nm, after it is formed. The corresponding covered nanoparticle is displayed in Figure 6.11. At each reduction time, the layer thickness was measured at 9 different locations and averaged.

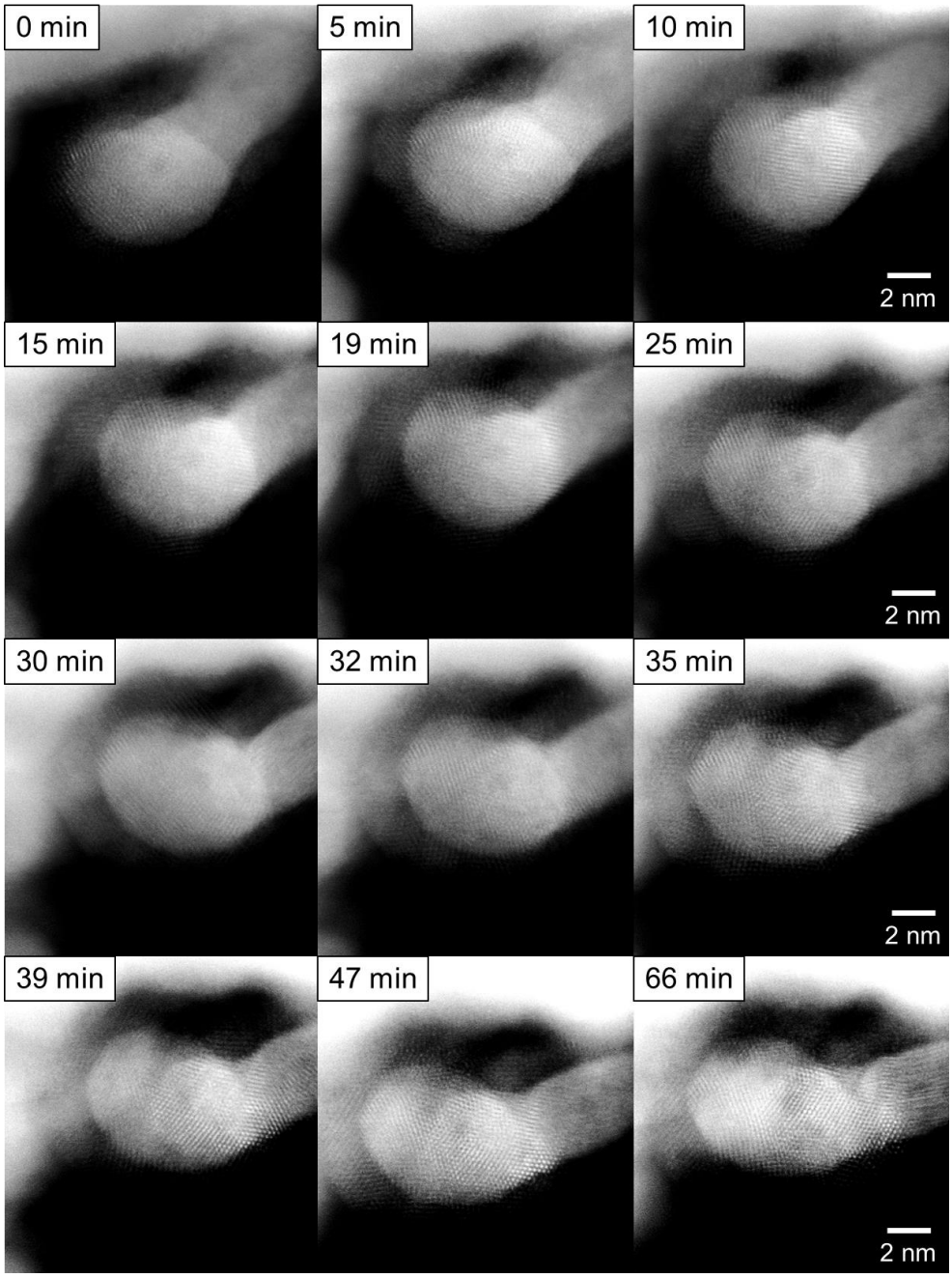

Figure 11.15: Series of DF images during reduction of PdO at room temperature after a pre-treatment at 200 °C. Time stamp indicates reduction time. ZnO is activated within the first 5 min. After interaction between nanoparticle and support, structural changes in the nanoparticle are observed.

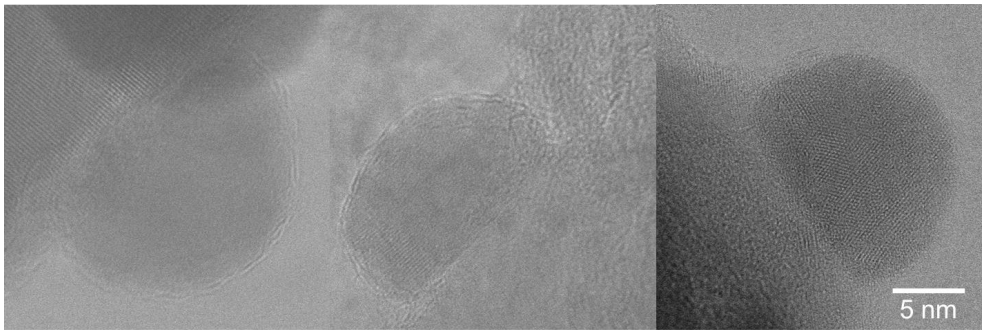

Figure 11.16: BF images series of ZnPd nanoparticles imaged after prereduction at 200 °C.

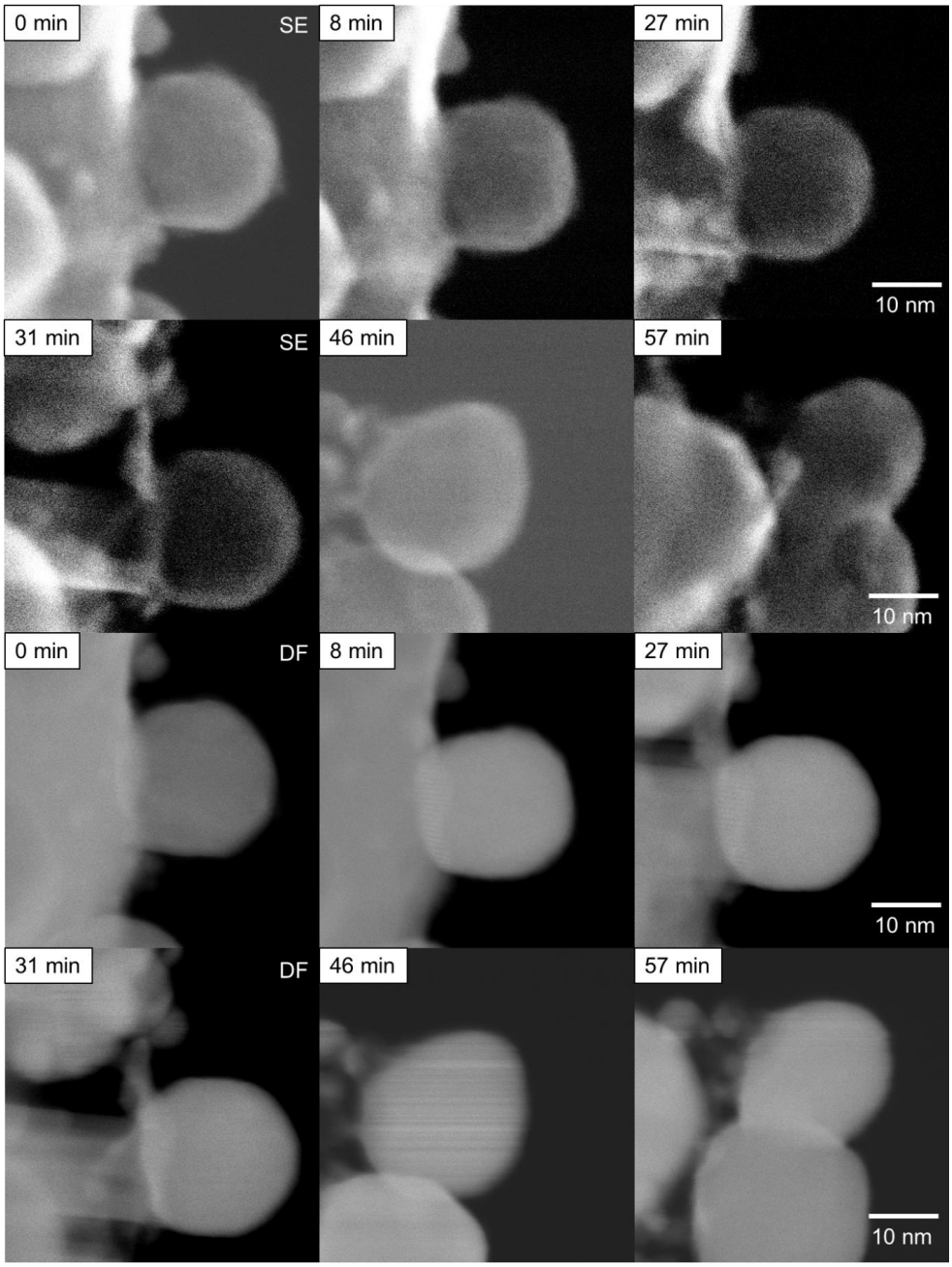

Figure 11.17: Series of SE (top) and DF (bottom) images of a supported ZnPd nanoparticle exposed to methanol steam. The corresponding *in situ* experiment is discussed in chapter 7.4.2.

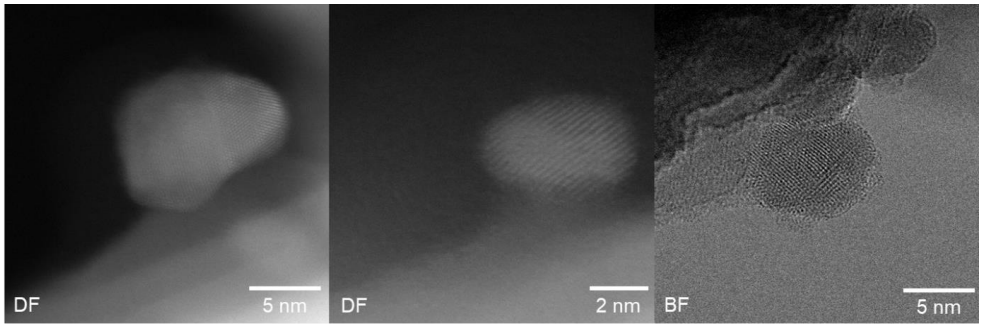

Figure 11.18: DF and BF images of pristine ZnPd nanoparticles acquired before exposure to MSR conditions and discussed in chapter 7.5. DF images represent reference locations. Post MSR states are shown in Figure 7.14.

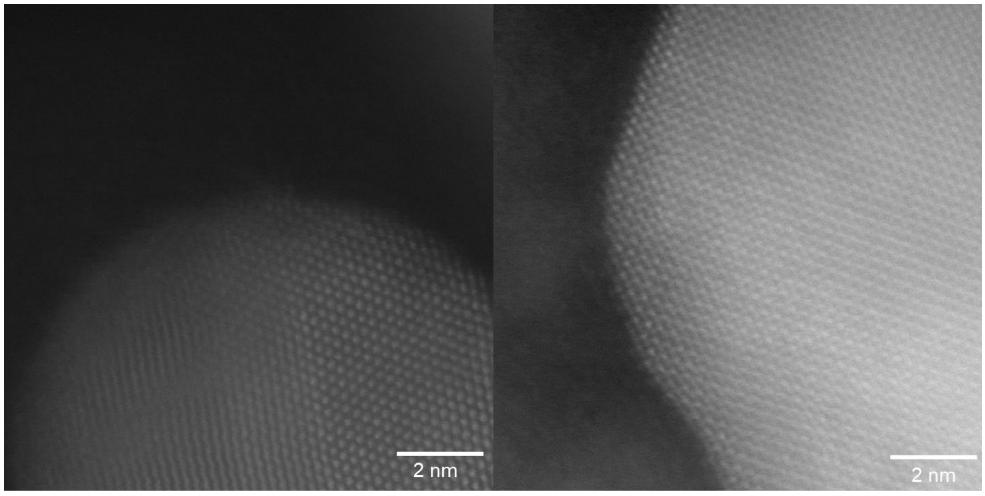

Figure 11.19: High resolution DF images of ZnPd nanoparticles acquired after MSR exposure. Crystal structure is identified and shown in Figure 7.14. Different species can be distinguished in the right image. Atom columns with high DF signal correspond to Pd and with low to Zn.

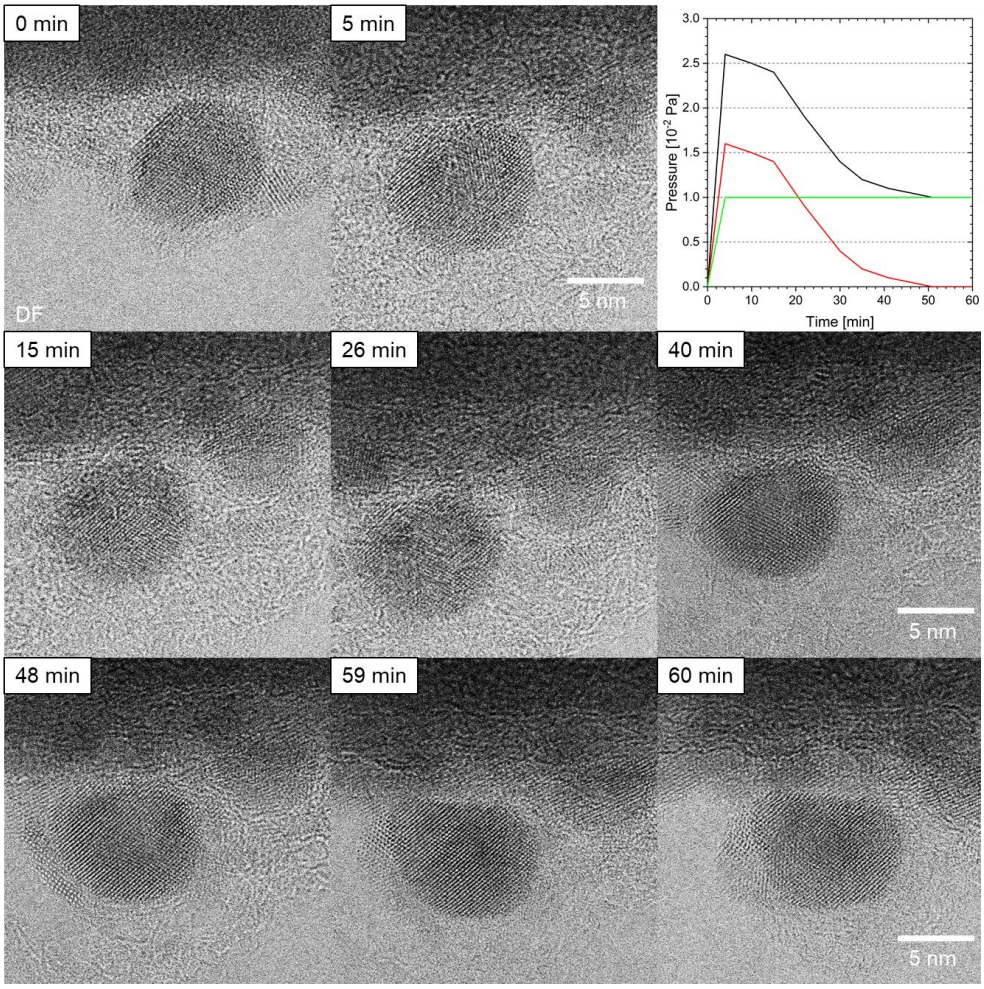

Figure 11.20: Series of BF images of ZnPd nanoparticle exposed to methanol steam, water steam and hydrogen at 200 °C. Column pressure (black), partial pressure of methanol and water (red) and hydrogen partial pressure (green) are illustrated as a function of injection time.

Acknowledgements

Literature and tools only help you so far. Many skills, results and wisdom have only been gained with the constant help of my dear colleagues. In this respect, I have to give special praise to the many smart and kind people I have met during my PhD journey, who have supported me from day one. It has been a great pleasure to work with you! I am happy to acknowledge:

- My supervisor Prof. Dr. Rafal E. Dunin-Borkowski, for providing me with the opportunity to pursue my PhD and establishing an outstanding working environment that allows for open, free and challenging research. His accessibility, detailed and helpful comments to any submission, and on-going support are highly appreciated.
- Prof. Dr. Joachim Mayer, for introducing me to the exciting field of electron microscopy in the first place and for accepting the role as co-assessor of this dissertation.
- Prof. Dr. Matthias Wuttig and Prof. Dr. Volker Meden for participating as chair and additional examiner in my doctoral examination.
- Dr. Marc Heggen, for his daily support, fruitful discussions, constant encouragement and patience in answering silly questions. I am grateful for his supportive attitude towards a healthy workload and a self-organised way of working.
- Prof. Dr. Marc Armbrüster, for his educational and detail-oriented character. His chemical and thoughtful perspective in discussions is much respected.
- My group at FZJ, including Dr. Paul Paciok, Dr. Kateryna Loza, Dr. Shibrata Baska, Dr. Pengfei Cao, Dr. Katherine MacArthur, Dr. Juri Barthel and Robert Zandonella, who always gave me great advice and perspective. Their support during the set up and conduction of challenging and tedious *in situ* experiments is highly appreciated.
- The members of the Ross gang at MIT for their unwavering support, their constant curiosity and thought-provoking discussions. I would like to thank Prof. Dr. Frances Ross for giving me the opportunity to be a part of her inspiring group and for the unique experience I have had.
- Lidia Kibkalo, Marie Göcking, Alexander Müller and René Borowski, for their constant support with scientific and non-scientific challenges, endless supply of office supplies and entertaining stories. I am especially grateful that they saved me many hours of work and nerves by knowing who to call or what to do.
- Dr. Dylan Jennings, Dr. Moritz Kindelmann, Vita Mergner and all the others I have laughed and lunched with. You made the daily work truly enjoyable.
- My friends, family and handball team, for their support, distraction and balancing the daily life of a doctoral student.

List of Publications

I gratefully acknowledge the funding provided by the Deutsche Forschungsgemeinschaft (DFG) within grant no. 441718867. I am grateful for the financial support provided for this dissertation, which enabled me to contribute to the following publications.

1. Vennewald, M. et al. Dynamics of palladium single-atoms on graphitic carbon nitride during ethylene hydrogenation. J. Catal. 421, 134–144 (2023).
2. Ahmadi, M. et al. Atomically Resolved Phase Coexistence in VO 2 Thin Films. ACS Nano (2024) doi:10.1021/acsnano.3c10745.
3. Meise, A., Heggen, M., Dunin-Borkowski, R. E. & Armbrüster, M. In Situ Scanning Transmission Electron Microscopy Calcination of Palladium Nitrate Supported on Zinc Oxide. Small Sci. 2400048, 1–10 (2024).
4. Eberst, A. et al. Advanced Physics Research Deeper Insight into the Mechanisms behind Sputter Damage in Silicon Solar Cells based on the Example of Nanocrystalline Silicon Carbide. 2400036, (2024).
5. P. K. Chakraborty et al. Unveiling the exsolution mechanisms and investigation of the catalytic processes of Sr2FeMo0.65Ni0.35O6-δ using in situ transmission electron microscopy, Nano Today (2025)
6. K. V. A. Birkelbach et al. An Immobilized Rh-based Solid Molecular Catalyst for the Reductive Hydroformylation of 1-Octene, Angew. Chemie (2025)
7. J. C. Baums et al. Additive-Free, Aqueous CO2 Hydrogenation with Ru/Polyphosphine-Based Solid Molecular Catalysts, ChemCatChem (2025)

Eidesstaatliche Erklärung

Ansgar Meise erklärt hiermit, dass diese Dissertation und die darin dargelegten Inhalte die eigenen sind und selbstständig, als Ergebnis der eigenen originären Forschung, generiert wurden.

Hiermit erkläre ich an Eides statt:

1. Diese Arbeit wurde vollständig oder größtenteils in der Phase als Doktorand dieser Fakultät und Universität angefertigt;

2. Sofern irgendein Bestandteil dieser Dissertation zuvor für einen akademischen Abschluss oder eine andere Qualifikation an dieser oder einer anderen Institution verwendet wurde, wurde dies klar angezeigt;

3. Wenn immer andere eigene- oder Veröffentlichungen Dritter herangezogen wurden, wurden diese klar benannt;

4. Wenn aus anderen eigenen- oder Veröffentlichungen Dritter zitiert wurde, wurde stets die Quelle hierfür angegeben. Diese Dissertation ist vollständig meine eigene Arbeit, mit der Ausnahme solcher Zitate;

5. Alle wesentlichen Quellen von Unterstützung wurden benannt;

6. Wenn immer ein Teil dieser Dissertation auf der Zusammenarbeit mit anderen basiert, wurde von mir klar gekennzeichnet, was von anderen und was von mir selbst erarbeitet wurde;

7. Ein Teil oder Teile dieser Arbeit wurden zuvor veröffentlicht und zwar in Kapitel 4 im Journal „Small Science“ unter dem Titel „In Situ Scanning Transmission Electron Microscopy Calcination of Palladium Nitrate Supported on Zinc Oxide“.

Köln, 23. Juni 2025

Ansgar Meise

Band / Volume 656
Oxide-based All-Solid-State Batteries for and from Recycling Processes
V. M. Kiyek (2025), viii, 128 pp, xix
ISBN: 978-3-95806-806-3

Band / Volume 657
Investigation of current and future anthropogenic chemical regimes in simulation chamber experiments
M. Färber (2025), 213 pp
ISBN: 978-3-95806-809-4

Band / Volume 658
Dynamischer Betrieb von Polymer-Elektrolyt-Membran Wasserelektrolyseuren
E. Rauls (2025), XIV, 239 pp
ISBN: 978-3-95806-811-7

Band / Volume 659
Pore-scale reactive transport modeling in cementitious materials: Development and application of a high-performance computing code based on the Lattice-Boltzmann method
S. Rohmen (2025), X, 295 pp
ISBN: 978-3-95806-812-4

Band / Volume 660
Recyclingmöglichkeiten für die Keramikkomponenten einer Festoxidzelle
S. Sarner (2025), VIII, 122 pp
ISBN: 978-3-95806-816-2

Band / Volume 661
Methodological Approach Enabling the Two-phase Flow Investigation in Alkaline Electrolysis under Demanding Conditions
S. Renz (2025), IX, 252 pp
ISBN: 978-3-95806-821-6

Band / Volume 662
Variable renewable energy potential estimates based on high-resolution regional atmospheric modelling over southern Africa
S. Chen (2025), XIII, 141 pp
ISBN: 978-3-95806-822-3

Band / Volume 663
Advances in Understanding Nitrate Aerosol Formation and the Implications for Atmospheric Radiative Balance
A. Milousis (2025), 195 pp
ISBN: 978-3-95806-823-0

Band / Volume 664
Optimization of NaSICON-type lithium- ion conductors for solid-state batteries
A. Loutati (2025), viii, 104 pp
ISBN: 978-3-95806-824-7

Band / Volume 665
Innovative Plasma Sprayed Thermal Barrier Coatings for Enhanced Flexibility in Gas Turbine Operation
J. Igel (2025), V, 153, XXXVI pp
ISBN: 978-3-95806-827-8

Band / Volume 666
Techno- ökonomisches Potenzial dezentraler und autarker Energiesysteme
S. K. A. Risch (2025), xxiii, 210 pp
ISBN: 978-3-95806-829-2

Band / Volume 667
Reactive Field Assisted Sintering of Novel Rare Earth Garnets for Plasma Etching Applications
C. Stern (2025), VII, 101, XXVIII pp
ISBN: 978-3-95806-833-9

Band / Volume 668
Effects of mucilage and extracellular polymeric substances on soil gas diffusion
A. Haupenthal (2025), v, 99 pp
ISBN: 978-3-95806-834-6

Band / Volume 669
Quantifying Recombination Losses and Charge Extraction in Halide Perovskite Solar Cells
L. Krückemeier (2025), vi, 286 pp
ISBN: 978-3-95806-835-3

Band / Volume 670
Investigation of Dynamic Material Changes During the Preparation of ZnPd Nanoparticles Supported on ZnO and their Catalytic Application in Methanol Steam Reforming on the Atomic Level
A. Meise (2025), xviii, 175 pp
ISBN: 978-3-95806-838-4

Energie & Umwelt / Energy & Environment
Band / Volume 670
ISBN 978-3-95806-838-4

Mitglied der Helmholtz-Gemeinschaft

JÜLICH
Forschungszentrum